

ISSN 2071-4726
2071-0305

Инженерно-строительный журнал

НАУЧНОЕ ИЗДАНИЕ

№7(91) 2019





ПОЛИТЕХ
Санкт-Петербургский
политехнический университет
Петра Великого

Инженерно-строительный институт
Центр дополнительных профессиональных программ
195251, г. Санкт-Петербург, Политехническая ул., 29,
тел/факс: 552-94-60, www.stroikursi.spbstu.ru,
stroikursi@mail.ru

**Приглашает специалистов организаций, вступающих в СРО,
на курсы повышения квалификации (72 часа)**

Код	Наименование программы	Виды работ*
Курсы по строительству		
БС-01-04	«Безопасность и качество выполнения общестроительных работ»	п.1,2, 3, 5, 6, 7, 9, 10, 11, 12, 13, 14
БС-01	«Безопасность и качество выполнения геодезических, подготовительных и земляных работ, устройства оснований и фундаментов»	1,2,3,5
БС-02	«Безопасность и качество возведения бетонных и железобетонных конструкций»	6,7
БС-03	«Безопасность и качество возведения металлических, каменных и деревянных конструкций»	9,10,11
БС-04	«Безопасность и качество выполнения фасадных работ, устройства кровель, защиты строительных конструкций, трубопроводов и оборудования»	12,13,14
БС-05	«Безопасность и качество устройства инженерных сетей и систем»	15,16,17,18,19
БС-06	«Безопасность и качество устройства электрических сетей и линий связи»	20,21
БС-08	«Безопасность и качество выполнения монтажных и пусконаладочных работ»	23,24
БС-12	«Безопасность и качество устройства мостов, эстакад и путепроводов»	29
БС-13	«Безопасность и качество выполнения гидротехнических, водолазных работ»	30
БС-14	«Безопасность и качество устройства промышленных печей и дымовых труб»	31
БС-15	«Осуществление строительного контроля»	32
БС-16	«Организация строительства, реконструкции и капитального ремонта. Выполнение функций технического заказчика и генерального подрядчика»	33
Курсы по проектированию		
БП-01	«Разработка схемы планировочной организации земельного участка, архитектурных решений, мероприятий по обеспечению доступа маломобильных групп населения»	1,2,11
БП-02	«Разработка конструктивных и объемно-планировочных решений зданий и сооружений»	3
БП-03	«Проектирование внутренних сетей инженерно-технического обеспечения»	4
БП-04	«Проектирование наружных сетей инженерно-технического обеспечения»	5
БП-05	«Разработка технологических решений при проектировании зданий и сооружений»	6
БП-06	«Разработка специальных разделов проектной документации»	7
БП-07	«Разработка проектов организации строительства»	8
БП-08	«Проектные решения по охране окружающей среды»	9
БП-09	«Проектные решения по обеспечению пожарной безопасности»	10
БП-10	«Обследование строительных конструкций и грунтов основания зданий и сооружений»	12
БП-11	«Организация проектных работ. Выполнение функций генерального проектировщика»	13
Э-01	«Проведение энергетических обследований с целью повышения энергетической эффективности и энергосбережения»	
Курсы по инженерным изысканиям		
И-01	«Инженерно-геодезические изыскания в строительстве»	1
И-02	«Инженерно-геологические изыскания в строительстве»	2,5
И-03	«Инженерно-гидрометеорологические изыскания в строительстве»	3
И-04	«Инженерно-экологические изыскания в строительстве»	4
И-05	«Организация работ по инженерным изысканиям»	7

*(согласно приказам Минрегионразвития РФ N 624 от 30 декабря 2009 г.)

**По окончании курса слушателю выдается удостоверение о краткосрочном повышении
квалификации установленного образца (72 ак. часа)**

Для регистрации на курс необходимо выслать заявку на участие, и копию диплома об образовании по телефону/факсу: 8(812) 552-94-60, 535-79-92, , e-mail: stroikursi@mail.ru.

Инженерно-строительный журнал

НАУЧНОЕ ИЗДАНИЕ

ISSN 2071-4726, 2071-0305

Свидетельство о государственной регистрации: ПИ №ФС77-38070, выдано Роскомнадзором

Специализированный научный журнал. Выходит с 09.2008.

Включен в Перечень ведущих периодических изданий ВАК РФ

Периодичность: 8 раз в год

Учредитель и издатель:

Санкт-Петербургский политехнический университет Петра Великого

Адрес редакции:

195251, СПб, ул. Политехническая, д. 29, Гидрокорпус-2, ауд. 245

Главный редактор:

Екатерина Александровна Линник

Научный редактор:

Николай Иванович Ватин

Выпускающий редактор:

Анастасия Крупина

Редакционная коллегия:

д.ф.-м.н., доцент Р.А. Абдикаримов;
 д.т.н., проф. В.В. Бабков;
 к.т.н., проф. А.И. Боровков;
 д.т.н., проф. А. Бородинец;
 д.т.н., проф. Н.И. Ватин;
 PhD, проф. М. Вельжкович;
 к.т.н., М.Р. Гарифуллин;
 д.т.н., проф. Э.К. Завадскас;
 д.ф.-м.н., проф. М.Н. Кирсанов;
 D.Sc., проф. М. Кнежевич;
 д.т.н., проф. В.В. Лалин;
 д.т.н., проф. Б.Е. Мельников;
 д.т.н., академик М.М. Мирсаидов;
 д.т.н., проф. Р.Б. Орлович;
 Dr. Sc. Ing., professor
 Л. Пакрастиньш;
 Dr.-Ing. Habil., professor
 Х. Пастернак;
 д.т.н., проф. А.В. Перельмутер;
 д.т.н., проф. М.Р. Петриченко;
 д.т.н., проф. В.В. Сергеев;
 д.ф.-м.н., проф. М.Х. Стрелец;
 д.т.н., проф. О.В. Тараканов;
 д.т.н., проф. Б.Б. Телтаев;
 д.т.н., проф. В.И. Травуш;
 д.т.н., проф. Д. Унгерман;
 д.т.н., проф. С.В. Федосов

Дата выхода: 29.11.2019

Содержание

Алексейцев А.В., Гейли Л., Друкис П. Оптимизация балочных конструкций каркасных зданий с учетом требований к их безопасности	3
Юсуф М.О. Синергетический эффект железных опилок и микрокремнезёма на поглощающую способность и усадку цементного теста	16
Аль Раджаб Ю.С., Тамини М.Ф. Теплопередача и тепловой удар переработанного стеклобетона	27
Ходжаев Д.А., Абдикаримов Р.А., Мирсаидов М.М. Динамика физически нелинейной вязкоупругой цилиндрической оболочки с сосредоточенными массами	39
Аль-Рушан Р. Влияние расстояния между тросами на поведение вантовых мостов	49
Шаронова О.М., Юмашев В.В., Соловьев Л.А., Аншиц А.Г. Тонкодисперсная высококальциевая летучая зола как основа композитного цементирующего материала	60
Хатиб Дж., Джахами А., Элкорди А., Баалбаки О. Конструктивные характеристики железобетонных балок, содержащих отходы пластика	73
Тюкалов Ю.Я. Равновесные конечные элементы для плоских задач теории упругости	80
Сиддиг Е., Ченг П., Ли Ю. Влияние модифицированной полимером наноглины на характеристики асфальтобетонной смеси	98
Урханова Л.А., Лхасаранов С.А., Буянтуев С.Л., Федюк Р.С., Таскин А.В. Снижение щелочной коррозии базальтовой фибры в бетоне	112
Лиу Ч.-К., Чанг Дж., Ли Ф., Джин Х.-П., Чонг Ч.-Ю. Мембранный элемент для высотных зданий связевой системы	121
Травуш В.И., Гордон В.А., Колчунов В.И., Леонтьев Е.В. Динамическое деформирование балки при внезапном структурном изменении упругого основания	129

© ФГАОУ ВО СПбГУ, 2019

© Иллюстрация на обложке: Илья Смагин

Контакты:

E-mail: mce@spbstu.ru

Web: <http://www.engstroy.spbstu.ru>

Magazine of Civil Engineering

SCHOLAR JOURNAL

ISSN 2071-4726, 2071-0305

Peer-reviewed scientific journal

Start date: 2008/09

8 issues per year

Publisher:Peter the Great St. Petersburg
Polytechnic University**Indexing:**Scopus, Russian Science Citation
Index (WoS), Compendex, DOAJ,
EBSCO, Google Academia, Index
Copernicus, ProQuest, Ulrich's Serials
Analysis System, CNKI**Corresponding address:**245 Hydro Building, 29
Polytechnicheskaya st., Saint-
Petersburg, 195251, Russia**Editor-in-chief:**

Ekaterina A. Linnik

Science editor:

Nikolay I. Vatin

Technical editor:

Anastasia Krupina

Editorial board:R.A. Abdikarimov, D.Sc., associate
professor

V.V. Babkov, D.Sc., professor

A.I. Borovkov, PhD, professor

A. Borodinecs, Dr.Sc.Ing., professor

M. Veljkovic, PhD, professor

M. Garifullin, PhD, postdoctorant

E.K. Zavadskas, D.Sc., professor

M.N. Kirsanov, D.Sc., professor

M. Knezevic, D.Sc., professor

V.V. Lalin, D.Sc., professor

B.E. Melnikov, D.Sc., professor

M.M. Mirsaidov, D.Sc., professor

R.B. Orlovich, D.Sc., professor

L. Pakrastinsh, Dr.Sc.Ing., professor

H. Pasternak, Dr.-Ing.habil.,
professor

A.V. Perelmuter, D.Sc., professor

M.R. Petrichenko, D.Sc., professor

V.V. Sergeev, D.Sc., professor

M.Kh. Strelets, D.Sc., professor

O.V. Tarakanov, D.Sc., professor

B.B. Teltayev, D.Sc., professor

V.I. Travush, D.Sc., professor

S.V. Fedosov, D.Sc., professor

Date of issue: 29.11.2019

Contents

Alekseytsev, A.V., Gaile L., Drukis, P. Optimization of steel beam structures for frame buildings subject to their safety requirements	3
Yusuf, M.O. Synergistic-effect of iron-filing and silica-fume on the absorption and shrinkage of cement paste	16
Al Rjoub, Y.S., Tamimi, M.F. Heat transfer and thermal shock of recycled glass concrete	27
Khodzhaev, D.A., Abdikarimov, R.A., Mirsaidov, M.M. Dynamics of a physically nonlinear viscoelastic cylindrical shell with a concentrated mass	39
Al-Rousan, R. The impact of cable spacing on the behavior of cable-stayed bridges	49
Sharonova, O.M., Yumashev, V.V., Solovyov, L.A., Anshits, A.G. The fine high-calcium fly ash as the basis of composite cementing material	60
Khatib, J., Jahami, A., Elkordi, A., Baalbaki, O. Structural performance of reinforced concrete beams containing plastic waste caps	73
Tyukalov, Yu.Ya. Equilibrium finite elements for plane problems of the elasticity theory	80
Siddig, E., Cheng, P., Li, Y. Effects of polymer modified nanoclay on the performance of asphalt mixture	98
Urkhanova, L.A., Lkhasaranov, S.A., Buyantuev, S.L., Fediuk, R.S., Taskin, A.V. Reducing alkaline corrosion of basalt fiber in concrete	112
Liu, Z.-Q., Zhang, J., Li, F., Jin, H.-P., Zong, Z.-Y. An improved membrane element for high-rise building with shear walls	121
Travush, V.I., Gordon, V.A., Kolchunov, V.I., Leontiev, E.V. Dynamic deformation of a beam at sudden structural transformation of foundation	129

© Peter the Great St. Petersburg Polytechnic University. All rights reserved.

© Coverpicture – Ilya Smagin

E-mail: mce@spbstu.ruWeb: <https://engstroy.spbstu.ru/en/>



DOI: 10.18720/MCE.91.1

Optimization of steel beam structures for frame buildings subject to their safety requirements

A.V. Alekseytsev^{a*}, L. Gaile^b, P. Drukis^b

^a National Research Moscow State Civil Engineering University, Moscow, Russia

^b Riga Technical University, Riga, Latvia

* E-mail: aalexw@mail.ru

Keywords: building structures, construction safety, column collapse risk, ceiling optimization, buildings durability, steel beams, local damages, emergency actions, transformable structures, evolutionary modelling

Abstract. A method for finding design solutions for discrete sets of design parameters, including a single two-cycle iterative process, has been developed. The evolutionary procedure is a first cycle. Within the framework of this process, a second recurrent cycle is used to calculate the structure in a static nonlinear arrangement. The coefficients are used for correction of the object loading as part of its static analysis to take into account the dynamic effect. Risk assessment for the structure variant also takes part within the framework of the evolutionary procedure. The proposed algorithm has been developed for the structures of buildings of a higher criticality rating, which will allow to increase the mechanical safety of construction objects with the simultaneous rational saving of material costs. As an example of design, a transformed beam structure, equipped with an adaptation system for beyond design effects, is considered. It is shown that during the synthesis of structures of increased durability, the use of adaptation systems in the form of safety elements has an advantage compared to an ordinary increase of the cross section.

1. Introduction

The tasks of optimal design of bearing structures are relevant for construction science. At the same time, in a number of research tasks, they do not take into account the risks of the occurrence of emergencies [1, 2]. This can significantly affect the safety of the object during operation. One of the measures to obtain the most rational design project from the standpoint of estimating the cost of ensuring the safety of buildings and structures is to use approaches based on the risk of material losses during the operation of structures [3–11]. In many studies devoted to this topic, problem statements has been considered, which make it possible to take into account the reliability of the structure, the risks associated with design errors, the level of loading of the object, the nature of loading, etc. Such issues were considered for mechanically [9, 12–14] and exothermically [15, 16] damaged reinforced concrete structures, steel structures under climatic temperature effects [17], and other supporting systems. In some cases, the calculations took into account the full life cycle of the structure [18]. In addition, of interest is the analysis of the risks of material losses with significant wind pressure [10], seismic activity [4–6, 14], floods [7] and other special loads and impacts. Separate attention to the issue of assessing the safety of systems that have damage accumulated during operation is given in [19].

In modern socio-economic conditions, the problem of ensuring the safety of structures comes to the fore. First, this applies to objects of a high level of responsibility. For the supporting structures of such objects, the risks associated with ensuring safety should be reduced to a rational minimum.

In this regard, the solution to the problem of the yield of design solutions to the optimal cost-risk ratio seems to be particularly relevant. It should be noted that so far this problem has not been given enough attention. The reason is the absence, until recently, of both effective methods for optimizing building support

Alekseytsev, A.V., Gaile L., Drukis, P. Optimization of steel beam structures for frame buildings subject to their safety requirements. Magazine of Civil Engineering. 2019. 91(7). Pp. 3–15. DOI: 10.18720/MCE.91.1

Алексейцев А.В., Гейли Л., Друкис П. Оптимизация балочных конструкций каркасных зданий с учетом требований к их безопасности // Инженерно-строительный журнал. 2019. № 7(91). С. 3–15. DOI: 10.18720/MCE.91.1



This work is licensed under a [CC BY-NC 4.0](https://creativecommons.org/licenses/by-nc/4.0/)

structures and the computing power of computers that implement them. One of the approaches that allow significant progress in solving this problem is evolutionary modeling or genetic algorithms.

Now they are used in solving problems of assessing the reliability of structures [20–23], searching for parameters for structures of various types, including frames [22], trusses [23], cable-stayed bridges [24], domes and vaults [25], laminates with high energy absorption capacity [26] and many other objects.

The issues of mechanical safety of beam building structures occupy important place herein. Mechanical safety enhancement in case of local damages in the form of emergency actions from the point of view of a design solution can be achieved in two main ways:

– redistribution of internal forces flows generated by abnormal dynamic additional loadings. This can be achieved by the preventive opportunities of modifying the object's structural layout based on the predicted change of the mode of operation of the joint connections, by increasing the cross sections of certain elements, and by introducing additional reinforcement;

– installation of a system of additional safety elements and arrangements actuated by deformable structures or mechanical actuators at the building accident, and redistributing additional loadings from abnormal loads to other structures or foundation. In this case, the safety elements can be destroyed, damping the impact effects.

In a series of contributions about the optimization of building structures, for example [27], the problem of finding the minimum mass, volume, or cost of objects was solved taking into account various factors that did not include risk analysis. In this case, conditions of normal operation were most often considered, some works are devoted to the optimization of structures during emergency action. Researches show that a rational distribution of the material of a structure, which is sought for in optimization problems, in some cases leads to a significant reduction in the safety margins. When considering the actual design conditions (the quality of construction materials, inaccuracies during installation, arrangement of joint connections, improper operation), a reduction in safety margins can create an increased risk of accident and lead to severe economic and social consequences. Therefore, an optimization criterion based only on cost minimization seems to be biased. In this regard, it is necessary to develop approaches related to the risks assessment of accidents and material losses, which will increase the safety of design solutions. It is not consider social losses due to the complexity and individuality of specific cases.

This article discusses the approach to the optimal synthesis of design solutions for beam ceiling and roof structures of increased durability with safety elements from the perspective of minimizing the risks associated with accidental impacts. At the same time, the search for variants of the design solution is carried out taking into account the rational minimum of costs for the supply and construction of these structures.

2. Methods

2.1. Formulation of the problem

It is considered a deformable beam structure of the building having a mechanism for adapting to emergency actions (a safety system), providing or at least enhancing the durability of the system in an accident. Risks from a possible accident are considered only at the stage of operation of the structure. The task of finding the optimal solution for any variant of such a structure depends on the levels of local damage. Here are these damage levels:

– normal level of damage (NLD), when local damage does not create any significant risk of loss of the durability of the object during the operation of the safety system of the structure.

– higher level of damage (HLD), when the safety elements system with a high probability will not be able to prevent the destruction of the structure in all possible damage cases.

In this case, the optimization task falls into two subtasks. For the NLD formulation, the design parameters should be chosen in such a way as to deliver at least the following functionality:

$$C + C_s(y_s) - R(y_s, p) \rightarrow \min, \quad R = pU(y_s), \quad (1)$$

where C is the initial cost of the structure without safety system;

C_s is a cost of the safety system;

R is the absolute risk factor of an accident with the material losses;

y_s is a discrete set of variable design parameters of the safety system;

p is a failure probability of the structure under the condition of accident;

U is damage from material losses in monetary terms.

For HLD formulation the optimization problem can be formulated as:

$$C(y) + C_s(y_s) - R(y, y_s, p) \rightarrow \min, \quad R = pU(y, y_s), \quad (2)$$

where y is a discrete set of variable design parameters of the structure, excluding the elements of the safety system, values U, C, C_s, y_s, R, p are the same as in the formula (1).

Active (checkable during the iterative process) constraints in solving extreme problems (1), (2) are:

- the condition of durability, it is interpreted for the structures under consideration as a prohibition of significant changes in geometry during the accident;
- the condition for the prevention of local destruction of the material of structural elements, leading to a general destruction along critical sections with their dynamic additional loadings.

As passive constraints (checkable after the iterative process of finding a solution), it is considered the restrictions on limit states regulated by the relevant standards (codes, state standards) for various types of structures. It also fulfils the design requirements for ensuring local strength, flexibility, support conditions, etc.

The modular system for dimensions coordinating in construction and the design of beam structures require the definition of design parameters in the form of discrete sets:

$$y = \{\bar{y}_1, \bar{y}_2, \dots, \bar{y}_n\}, \quad y_s = \{\bar{y}_{s1}, \bar{y}_{s2}, \dots, \bar{y}_{sm}\}, \quad (3)$$

where $\bar{y}_i, i \in [1..n]$ is the vector of i -th variable design parameter, specified by the components from the range of acceptable values for the values selection used in solving the problem;

$\bar{y}_{sj}, j \in [1..m]$ is similar, but for the safety system;

n, m are the numbers of variable parameters for the structure and its safety system, respectively. For example, for steel beam structure, vector \bar{y}_1 , bonded to a specific beam structural element can be represented in the following form:

$$\bar{y}_1 = (\{A\}_1, \{J_x\}_1, \{J_y\}_1, \{J_z\}_1, \{X\}_1, \{Y\}_1), \quad (4)$$

where A, J_x, J_y, J_z, X, Y are respectively, the area, the moments of inertia and the coordinates of critical points in sections in the local coordinate system of the element. The sizes of the sets of areas and moments of inertia are determined by the number G of variable values for the considered parameter, and the dimensions of the coordinate sets X, Y – by the number P of considered critical points for the cross section, otherwise the set $\{A\} = \{A_1, \dots, A_G\}$, $X = \{X_1, \dots, X_G\}$, $X_1 = \{x_1, \dots, x_P\}$. The other sets have a similar view.

Structure calculations will be performed on the basis of the finite element analysis. The review of modern methods for the optimal design of technical objects for discrete sets of design parameters allows choosing the most effective approach to solve the problems posed, based on the evolutionary search.

2.2. Constraints

The time of the normal operation period for steel structure is considered. The strength of the ceiling (or roof) bearing beams of the first stress-strain state class (with the avoidance of plastic deformation for use in floors or coatings) [28]:

$$\frac{M}{W_n R_y \gamma_c} \leq 1; \quad \frac{QS}{Jt R_s \gamma_c} \leq 1, \quad (5)$$

where M is a bending moment;

W_n is the section net resistance;

R_y is the design bending resistance;

γ_c is the working conditions factor of the structure;

Q is a shear force;

S is the static moment of the shear part of the cross section;

J is the moment of inertia in the bending plane;

t is the thickness of the shear part section;

R_s is the design shear resistance.

Strength of second and third stress-strain state classes for beams (assuming plastic strain) is determined [28]:

$$\frac{M}{c_x \beta W_n R_y \gamma_c} \leq 1; \quad \frac{Q}{A_w R_s \gamma_c} \leq 1, \quad (6)$$

where c_x, β are coefficients, that take into account the cross section shape and the level of tangential bending stresses respectively;

A_w is the shear area.

Beam stiffness due to structural safety and aesthetic requirements

$$f / L \leq \Omega_L, \quad (5)$$

where f is a deflection of the structure;

L is the span;

Ω_L is the coefficient determined by the L value. For example, for $L = 6$ m, it is assumed $\Omega_{LL} = 0.005$, for $L = 12$ m, $\Omega_L = 0.004$, and so on.

General and local sustainability conditions are met by design requirements. For this purpose, the shape of the section, the setting of stiffeners, the fixing from the plane of bending are specially set.

For the conditions of an accident, the presence of plastic stress σ_{yield} is allowed, the value of which does not exceed the limit values σ_{lim} corresponding to the formation of cracks or rupture of structural steel:

$$\frac{\sigma_{yield}}{\sigma_{lim}} \leq 1. \quad (7)$$

Limiting the deflection of the transformed system. In an accident, after the mechanical safety system is activated, the transformed frame structure is deformed. The deflections f_e of this system should not exceed the allowable values f_{ult} sufficient for the safe evacuation of people and equipment from the building. The value f_{ult} is taken as $f_{ult} = 0.7H$, where H is the height of the floor, but not less than 2 m.

This constraint is used as an active for simplified evaluation of design structures. At the same time, for the final design solution, a calculation must be performed taking into account geometric nonlinearity, in particular, the proposed V.F. Mushchanov et al. [27, 28], as well as monitoring the rationality of the resulting geometry to ensure the evacuation of people and equipment [29].

2.3. Method for solving the problem

The general scheme of the computational process is presented in Figure 1. Such stages of the computing iterative process are carried out.

2.3.1. Construction of a finite element model and the formation of sets of variable parameters. At this stage, the information on the discretized model of the object, including the topology, material, loads, and reference restrictions is entered. Sets of varying parameters and identifiers are represented in the form of matrices, connecting these sets with the finite element model of the system.

2.3.2. Formation of initial sets of variants of structures in the form of data arrays. First set V is current and contains a description of the variants of structures represented in a coded variable I :

$$V = \{I_1, I_2, \dots, I_N\}, \quad I_1 = \{a_{11}, a_{12}, \dots, a_{1n}\}, \dots, I_N = \{a_{N1}, a_{N2}, \dots, a_{Nn}\}, \quad (8)$$

where N is the number of structures in the set;

a_{ij} is the value number of j -th parameter of variant i , ($i \in [1..N]$, $j \in [1..n]$), determining the characteristics of a parameter from the sets $\{A\}_j$, $\{J_x\}_j$, $\{J_y\}_j$, $\{J_z\}_j$, $\{X\}_j$, $\{Y\}_j$. That is, if $a_{11} = 3$ for the rod, associated with variable parameter 1 of the first variant of (I_1) structure from the set V , the characteristics $\{A_3\}_1$, $\{J_{x3}\}_1$, $\{J_{y3}\}_1$, $\{J_{z3}\}_1$, $\{X_3\}_1$, $\{Y_3\}_1$ will be assigned.

The variants of structures for the initial set V are formed according to the principle of decreasing identifier numbers a_{ij} , with the components of the vectors \bar{y} to be sorted by ascending values of geometric characteristics. At the same stage, similar to the set structure V the V_{best} data set structure is formed, which will be used to save the best solutions. The size of this set usually contains 15–20 structures variants. Initial set V_{best} is empty.

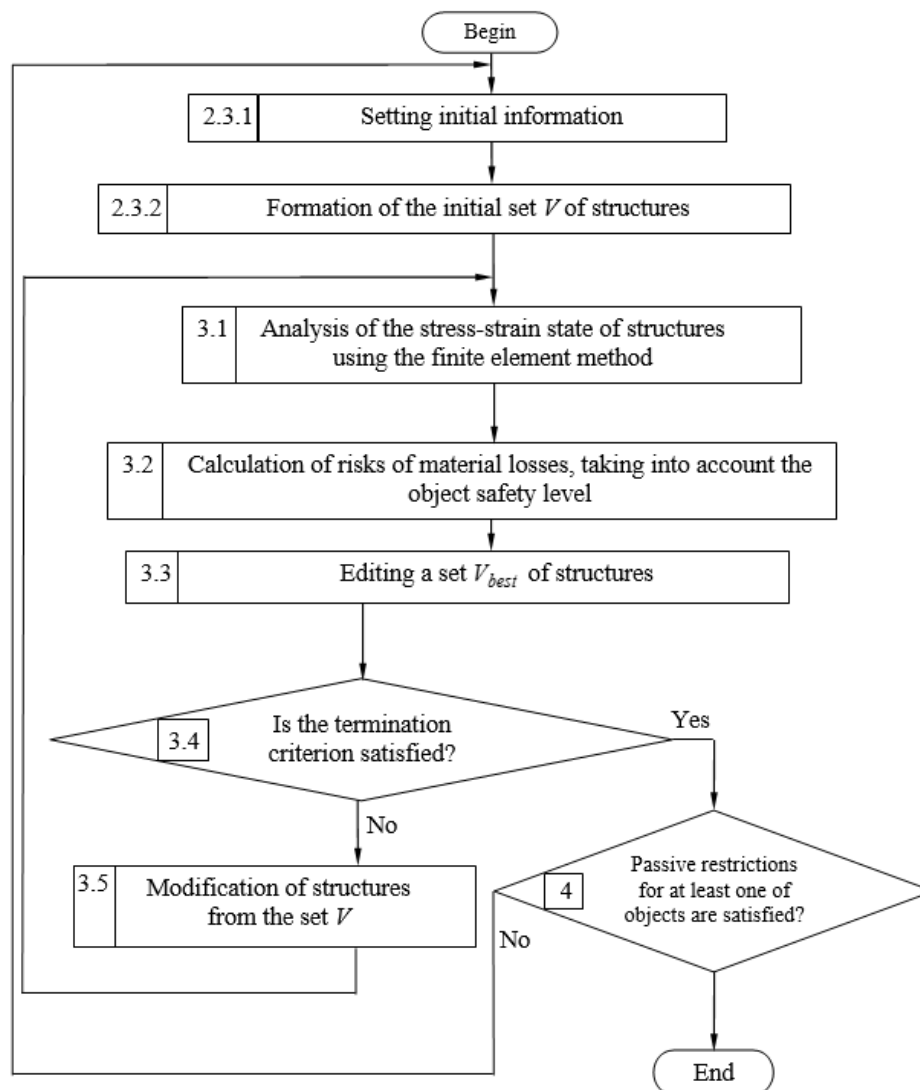


Figure 1. The sequence of finding the optimal solution.

2.4. Iterative process of finding solutions

2.4.1. Calculation of structures variants. Since the considered systems can have local damages, their calculation should be performed in a formulation that takes into account both physically and structurally nonlinear effects, as well as large displacements. Since the analysis of the structure in the dynamic formulation within the framework of the evolutionary approach is not possible due to the very high computational capacity of the process, we will use the simplified approach, which consists in a quasistatic nonlinear calculation with internal iteration cycles not related to the external cycles of the evolutionary algorithm. Dynamic effects in this calculation will be approximately taken into account by dynamic coefficients, the magnitude of which increases the loading level of the system. For this calculation, you can use the algorithm from the [30] or the NX Nastran solver. In this case, we consider the final position of the adaptation system, corresponding to the maximum activation after local damage to the system.

In the genetic algorithm for the analysis of the stress-strain state, the elements of the “Beam” type (NX Nastran) are used, which provide for the possibility of taking into account the plastic flow of the material with hardening. At the end of the search process, for the analysis of the resulting system, single-layer shell elements (“Plate”) are used.

It is defined dynamic coefficients outside the evolutionary search process as follows. For each variant of accident effect, we perform calculations of the damaged system in dynamic and static arrangement, determining the maximum equivalent stresses σ_D and σ_S respectively. We take into account the physically

and geometrically nonlinear behaviour of the object. We do not consider the transient dynamic process of the adaptation system activation. As a result, the dynamic coefficient $k_D = \sigma_D / \sigma_S$.

If, as a result of the calculation, it is determined that the structure has durability, then we consider it at the next stage of the iterative process. If, based on the results of the calculation, it is determined that none of the structure variants is durable, then we go to the stage 1.

2.4.2. Calculation of the building fail risks of an accident. For the automated calculation of the risks associated with material damage from accidental effect, we introduce the following data sets:

$$S = (\{N_s, \{N_e\}, L, D\}_1, \dots, \{N_s, \{N_e\}, L, D\}_{ns}), \quad (9)$$

where S is the array of information about structural elements, the number of which is ns , and each element of which contains the number of the structural element N_s and a list $\{N_e\}$ of the numbers of finite elements constituting this structural element, the length of the structural element L and binary damage identifier D . If in any finite element we detect stresses equal to or exceeding a certain critical level (for example, for steel this is the yield strength), then we consider the structural element to be damaged, and $D = 1$, otherwise $D = 0$. Within the same structural element, the sections of all finite elements are assumed to be similar.

Thus, the loss U_s from the failure of the structure rods and the safety system, can be determined by selecting all structural elements having damage from the array S :

$$\forall S_i | D = 1: U_{si} = k_w C_s L_i A_i \rho_i, \quad U_s = \sum_{S_i | D=1} U_{si}, \quad i \in [1 \dots ns], \quad (10)$$

where U_{si} , C_s , L_i , A_i , ρ_i are respectively loss from damage of i -th structural element, the cost of its unit of mass, length, cross-sectional area and density of the material;

$k_w = 1,02 \dots 1,1$ is the coefficient taking into account the cost of welding.

The loss $U_{\tilde{s}p}$ from the failure of equipment and floor structures (coatings) can be determined based on the selection of data from the array \tilde{S} :

$$\tilde{S} = \{\{N_p, \{N_k\}, C_{\tilde{s}}, C_p\}_1, \dots, \{N_p, \{N_k\}, C_{\tilde{s}}, C_p\}_{np}\}, \quad (11)$$

where N_p is the number of span in which the damaged structure is located;

$\{N_k\}$ is a list of structural elements limiting this span;

$C_{\tilde{s}}$, C_p are the costs of equipment and floors that were exposed to emergency actions, before they are damaged. If we consider a multi-storey object, the spans are numbered on each floor. If there are damaged structural elements in span N_p from the list $\{N_k\}$, we also consider the equipment and floors as damaged, otherwise we assume $C_{\tilde{s}} = 0$, $C_p = 0$.

Thus

$$\forall \tilde{S}_i | \{C_{\tilde{s}} \neq 0\} \vee (C_p \neq 0): U_{\tilde{s}p} = \sum_{np} C_{\tilde{s}i} + C_{pi}, \quad i \in [1 \dots np], \quad (12)$$

where np is the number of spans.

The total material loss will be:

$$U = U_s + U_{\tilde{s}p}. \quad (13)$$

The risks of damage from an accident are divided into two groups. The first group (I) is associated with the failure of the structure in normal operating conditions, the second – with failures during emergency actions. When calculating the probability p_I of failures of the first group we take into account the variation of mechanical characteristics and loads due to their statistical variability. This probability of failure is calculated based on a well-known approach using the Laplace formula under the assumption that random variables are distributed according to normal rule. This probability of failure significantly depends on the actual safety margin of the elements [31, 32] and nodal joints [33]. The probability p_{II} of risk of damage of the second group (II) is determined based on the analysis of statistics of accidents and disasters at construction sites.

Thus, the total risk of material loss at the stage of operation of the structure will be defined as:

$$R = R_I + R_{II} = U_s p_I + U_{sp} p_{II}. \quad (14)$$

Further, depending on the levels of local damages NLD and HLD, for each structure considered at this stage of the evolutionary algorithm, we calculate the value of the objective function $C(I)$ according to the formula (1), (2).

2.4.3. Filling the set V_{best} . All structures considered at the previous stage are checked for compliance with the conditions of fitting the set V_{best} in accordance with the strategy of "elitism" known in genetic algorithms. Any variant from the set V , if it is not in the set V_{best} , fit into it provided that $C(I \in V) \leq C(I \in V_{best})$.

2.4.4. Termination the end condition of iterations [1]. If during a certain number of iterations there are no changes in the set V_{best} , it means termination of the evolutionary cycle. This number of iterations depends on the number of variable parameters and the number of values of these parameters allowed for use in the search process. It is determined empirically at the stage of formal problem solving.

2.4.5. Editing the set V . Those structure variants that do not have the property of durability are replaced by randomly generated new variants. Half of the variants, for which the durability condition is satisfied are edited using the following statements:

– random change of parameter value. Let's consider a structure variant presented in coded form (8): $I_1 = \{a_{11}, a_{12}, \dots, a_{1n}\}$. The work of the function is as follows. The parameter number for changes is randomly selected, and then the number of the parameter value is also random. In evolutionary modelling terminology, this function is called a simple single-point mutation. For definiteness, we consider the number of variable parameters equal to 3, and the ranges of change codes as $a_1 = \{1, 2, 3\}$, $a_2 = \{1, 2\}$, $a_3 = \{1, 2, 3, 4\}$. When changing the original structure variant $I = \{3, 2, 1\}$ with this function, the following variants may occur: $\tilde{I}_1 = \{1, 2, 3\}$, $\tilde{I}_2 = \{2, 2, 4\}$, $\tilde{I}_3 = \{3, 1, 4\}$, $\tilde{I}_4 = \{3, 2, 1\}$ and etc. In the first two variants, the value of the first parameter randomly changed, in the third – of the second, in the last – of the third;

– exchange of parameters (crossover) [1]. To implement it, you must select two variants for the object. The work of the function consists of two stages. First stage: randomly select the parameter number, for which the exchange will take place, the second stage is the exchange of parameters. In the terminology of evolutionary modelling, this function is called single point crossover. To illustrate the work of the function, we give an example presented in the table. Here, parameter 3 is initially selected, with respect to which the exchange is performed.

Table 1. An example of the parameter exchange function.

Before exchange	After exchange
$I_1 = \{a_1, a_2, a_3, a_4, a_5, a_6, \}$	$\tilde{I}_1 = \{a_1, a_2, a_3, b_4, b_5, b_6, \}$
$I_2 = \{b_1, b_2, b_3, b_4, b_5, b_6, \}$	$\tilde{I}_2 = \{b_1, b_2, b_3, a_4, a_5, a_6, \}$

The other half of the structure variants, for which the durability condition is satisfied, is replaced with the variants from the set V_{best} , selected in ascending order of the objective function C and edited only by the random change function of the parameter value.

4. Check of passive constraints. If the passive constraints are satisfied, then the solution is obtained; if not, then you can check their satisfaction for the structure variants obtained as a result of the search that are closest in terms of the objective function value.

As a result of the algorithm, we obtain several best solutions by criterion (1) or (2), which means optimality in terms of the cost-risk ratio. If it is required to maximize the safety of the structure, then this algorithm can be used by specifying such a formulation of the objective function:

$$\begin{cases} R \rightarrow \min \\ C(y) + C_s(y_s) \rightarrow \min \end{cases} \quad \text{or} \quad ((C(y) + C_s(y_s))k_1 + Rk_2) \rightarrow \min, \quad (15)$$

where k_1, k_2 are coefficients that are defined as unit fractions, which determine the degree of importance of taking material loss risk into account.

The designer when agreed with the project investor assigns these coefficients. If an investor wants to insure himself against potential risks, then $k_1 > 1$, the value of k_1 is assigned large if the investor does not need a safety system $k_2 = 0$.

If risk consideration for a designer does not seem significant (for example, at low cost, quality assurance of construction materials and low probability of accidents), then the problem of structural optimization can be solved using evolutionary modelling based on [34].

3. Results and Discussion

3.1. Results of steel ceiling beam optimization

The design of a beam structure with an adaptation system for emergency actions, the concept of which by a patent for an invention is protected (pat. No. 2556761 RF, MPK E04B 1/24, Figure 2).

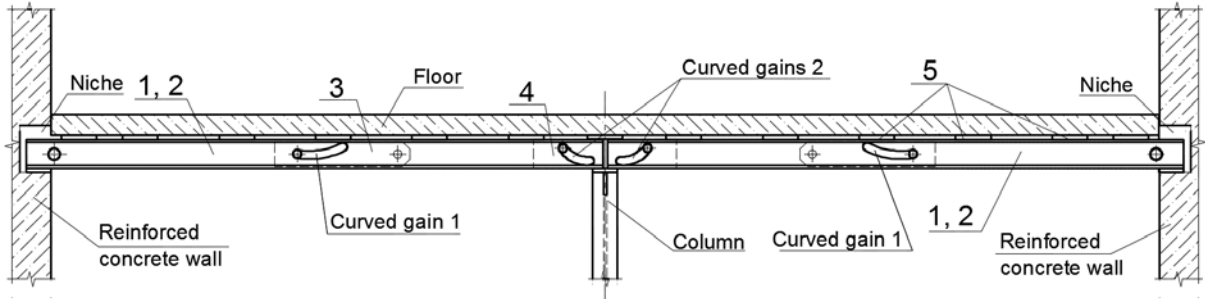
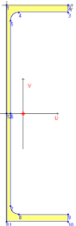
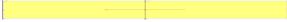
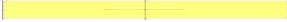


Figure 2. The ceiling beam and preventive safety system.

In the figure, the following designations are introduced: 1, 2 – are continuous and split channel beams; 3, 4 – plates, 5 – ties, welded to a continuous channel beam. The beam is made of structural steel C245. Spans are 3 m. Support joints are hinge-fixed, with the possibility of free rotation of the split channel beam in a niche. In case of accident removal of the middle support, the system is transformed into a frame structure. Running load $q=30$ kN/m. The dimensions of the standard profiles of the rods of channel beams 1 and 2, and the cross sections of plates 3 and 4 were varied independently. The durability condition in this case involves the transformation of the structure into a frame system and ensuring the condition of not exceeding the maximum deflection, which it is assumed to be 6 cm. Strength conditions were taken into account in accordance with the requirements of [31]. The structure is attributed to the 3rd class of the stress-strain state, under which the formation of conditional plastic hinges is allowed during the deformation. The characteristics of variable parameters for the structure and its adaptation system to accident are presented in the Table. 2.

The calculation is made by the finite element method using spatial rods, while taking into account the effect of buckling of the flat shape of the bend. Statistical data on the variation of the mechanical characteristics of structural steel and loads are taken from [34]. Design requirements were imposed on the dimensions of the plates and channel beams, consisting in coordinating the heights of these elements to ensure the operation of the adaptation mechanism.

Table 2. Allowable combinations of cross-sectional column dimensions.

Element in the Figure 1	Section shape	Profile grades and plate dimensions, m
Channel beams 1 and 2 (S1)		Channel beam with parallel edges of the rims according to GOST 8240–97: 1) 20P; 2) 24P; 3) 30P; 4) 36P; 5) 40P.
Plate 3 (P1)		1) 1.0×0.2×0.008; 2) 1.0×0.24×0.01; 3) 1.0×0.3×0.01; 4) 1.0×0.4×0.01;
Plates 4 (P2)		1) 1.2×0.2×0.02; 2) 1.2×0.24×0.02; 3) 1.2×0.3×0.03; 4) 1.2×0.4×0.04;

Analysis of the dynamic effect in case of local damage to the middle support was calculated “extensive” for a fully transformed state of the system (Figure 3) without taking into account its damping properties during transformation. The coefficient of the beam dynamics without adaptation mechanism when removing its middle

support turned out to be equal to 1.95. In the presence of a transforming safety system to be equal to 1.52. These coefficients were obtained based on the energy approach of G.A. Geniev. The coefficient of dynamics in this case is calculated as $k = 2D - S$, D is the value of the maximum dynamic stress in the cross section of the transformed system with local damage; S is the value of this stress obtained in a static finite element analysis.

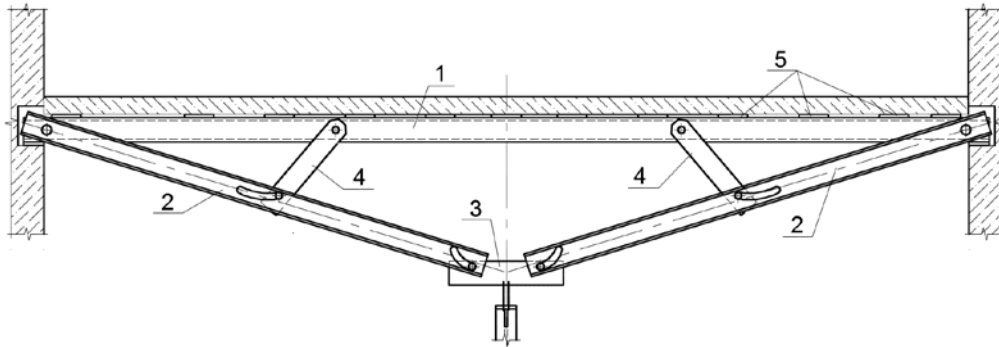


Figure 3. Beam system diagram transformed into a frame system.

When calculating the material loss, the cost of damaged elements of the beam and equipment worth 500 th. cu was taken into account. The cost of the material of beams, elements and parts of the safety system, taking into account the welding work, was assumed to be 60 th. cu per 1 ton. When calculating the risk of loss as a result of emergency actions, the probability of its occurrence was taken to be 0.01. In sets V , V_{best} 5 structure variants were used. The search process took not more than 20 iterations. Search results are shown in the Table. 3.

Table 3. The solutions obtained are similar to objective function.

Project No.	Codes of parameter values from the Table 1.			Objective function $C(I)$
	S1	P2	P1	
D1	1	1	3	7106
D2	1	2	3	7334
D3	1	3	3	7825

In the absence of an accident prevention system and ensuring the durability of the structure during an accident (with the same deflection of the damaged system) for the beam, it is necessary to use a section having a profile 36 P of channel beam. Table 4 shows a comparison of the obtained design solutions for structures with the presence and absence of an accident prevention system. The cost of these structures differs 1.3 times. The risk of material loss for them within the error of 13 % is similar.

Table 4. Comparison of the results of the structure synthesis.

Project No.	Structure cost \tilde{C} , cu	Risk of material loss, cu	Codes of parameter values from the Table 1.		
		R	S1	P2	P1
D1	12730	5624	1	1	3
D*	16555	5012	4*	–	–

* Project for a beam without a safety system.

3.2. Discussion

The issues of adaptation and improvement of genetic algorithms for solving the considered problems are also investigated. This is primarily an increase in the effectiveness of the search for a solution at the initial stages of the iterative process [35], the use of a combined scheme of constraints accounting [36]. The concepts of genetic algorithms that use the basics of game theory to search for solutions on several optimality criteria, in particular based on D. Nash equilibrium, G. Stackelberg game models and optimality by V. Pareto [37] are promising.

The dynamics coefficients obtained in this example can be found more accurately, based on the provisions of [38]. The proposed iterative procedure can be implemented for other types of thin-walled structures, for example, [39]. However, when assessing the bearing capacity of objects, various features of deformation and types of such systems should be taken into account: these are non-uniform torsion [40], types of profiles [41], strength and stability of nodes [42], as well as the value of welding stresses [43]. A separate issue is the applicability of such an iterative scheme to the optimization of concrete and reinforced concrete structures [44].

It should be noted that the proposed approach to estimating the life cycle cost of operating structures is somewhat simplified. This is primarily due to the significant difference in the complete data on the provision of normal operating conditions for structures of various types. For example, to estimate operating costs for lattice structures, one can use the results of work [45]. But these results may not be fully used for other systems. For constructions of new types such data are practically absent.

4. Conclusions

1. A method to search for design solutions for frame building structures based on the joint use of evolutionary modelling, risk theory and calculations in a physically and geometrically non-linear formulation, which makes it possible to obtain cost-effective and safe systems based on sets of design parameters specified in a discrete form, has been developed.

2. The proposed method allows to take into account the peculiarities of the design of building structures related to the availability for production in specific conditions of standard sizes of rod profiles, the use of certain materials and to consider both one and several stages of the structure life cycle.

3. The considered example of design a ceiling beam system of increased durability shows that the arrangement of prevention safety systems, includes allowing the structure transformation, is more preferable from the point of achieving safety and economy goals.

4. The considered algorithm has limitations on the use in terms of estimating operating costs for various types of structures. Overcoming these limitations requires additional research, reflecting the features of operation, maintain measures, general repairs and reconstruction of these systems.

References

1. Alekseytsev, A.V., Akhremenko, S.A. Evolutionary optimization of prestressed steel frames. Magazine of Civil Engineering. 2018. 81(5). Pp. 32–42. doi: 10.18720/MCE.81.4
2. Alekseytsev, A.V. Evolutionary optimization of steel trusses with the nodal joints of rods. Magazine of Civil Engineering. 2013. 40(5). Pp. 28–37. DOI: 10.5862/MCE.40.3
3. Schacht, G., Kaeding, M., Bolle, G., Concepts for the assessment of bridges with the risk of stress corrosion cracking. Beton- und Stahlbetonbau. 2019. No. 2(114). Pp. 85–94.
4. Veismoradi, S., Cheraghi, A., Darvishan, E. Probabilistic mainshock-aftershock collapse risk assessment of buckling restrained braced frames. Soil Dynamics And Earthquake Engineering. 2018. No. 115. Pp. 205–216.
5. Martins, L., Silva, V., Bazzurro, P. Advances in the derivation of fragility functions for the development of risk-targeted hazard maps. Engineering Structures. 2018. No. 173. Pp. 669–680.
6. Shokrgozar, H.R., Mansouri, I., Hu, J.W. Comparison of Seismic Reliability and Risk Assessment for Special and Intermediate Steel Moment Frames. KSCE Journal of Civil Engineering. 2018. No. 9 (22). Pp. 3452–3461.
7. Lonetti, P., Maletta, R. Dynamic impact analysis of masonry buildings subjected to flood actions. Engineering Structures. 2018. No. 167. Pp. 445–458.
8. Muntasir, Billah, A.H.M., Alam, M.S. Probabilistic seismic risk assessment of concrete bridge piers reinforced with different types of shape memory alloys. Engineering Structures. 2018. No. 162. Pp. 97–108.
9. Droogne, D., Botte, W., Caspeele, R. A multilevel calculation scheme for risk-based robustness quantification of reinforced concrete frames. Engineering Structures. 2018. No. 160. Pp. 56–70.
10. Vanmarcke, E., Lin, N., Yau, S.-C. Quantitative risk analysis of damage to structures during windstorms: some multi-scale and system-reliability effects. Structure and Infrastructure Engineering. 2013. No. 10. Pp. 1311–1319.
11. Bezabeh, M.A., Tesfamariam, S., Popovski, M., Goda, K. Stierner, S.F. Seismic base shear modification factors for timber-steel hybrid structure: collapse risk assessment approach. Journal of Structural Engineering. 2017. No. 10(143) 04017136.
12. Tampazyan, A.G., Zubareva, S. Optimal design of reinforced concrete structures taking into account the particular calculation for progressive destruction. MATEC Web of Conferences. 2017. No. 117, 00163.
13. Amiri, S., Saffari, H., Mashhadi, J., Assessment of dynamic increase factor for progressive collapse analysis of RC structures. Engineering Failure Analysis. 2018. No. 84. Pp. 300–310.
14. Sattar, S., Liel, A.B. Collapse indicators for existing nonductile concrete frame buildings with varying column and frame characteristics. Engineering Structures. 2017. No. 152. Pp. 188–201.
15. Tampazyan, A.G. Calculation of reinforced concrete plates with hole at long-term loading. IOP Conf. Series: Materials Science and Engineering. 2018. No. 365, 052021.
16. Tamrazyan, A.G., Avetisyan, L.A. Behavior of compressed reinforced concrete columns under thermodynamic influences taking into account increased concrete deformability. IOP Conf. Series: Materials Science and Engineering. 2018. No. 365, 052034.
17. Arabi, S., Shafei, B., Phares, B.M. Investigation of fatigue in steel sign-support structures under diurnal temperature changes [Online]. Journal of Constructional Steel Research. 2019. No. 153. Pp. 286–297. URL: <https://doi.org/10.1016/j.jcsr.2018.09.024>
18. Barone, G., Frangopol, D.M. Life-cycle maintenance of deteriorating structures by multi-objective optimization involving reliability, risk, availability, hazard and cost. Structural Safety. 2014. No. 48. Pp. 40–50.
19. Liu, Y.-F., Liu, X.-G., Fan, J.-S. Refined safety assessment of steel grid structures with crooked tubular members. Automation in Construction. 2019. No. 99. Pp. 249–264.
20. Truong, V.-H., Kim, S.-E. Reliability-based design optimization of nonlinear inelastic trusses using improved differential evolution algorithm. Advances in Engineering Software. 2018. No. 121. Pp. 59–74.

21. Saad, L., Chateaufneuf, A., Raphael, W. Robust formulation for Reliability-based design optimization of structures. *Structural and Multidisciplinary Optimization*. 2018. No. 6(57). Pp. 2233–2248.
22. Le, L.A., Bui-Vinh, T., Ho-Huu, V. An efficient coupled numerical method for reliability-based design optimization of steel frames. *Journal Of Constructional Steel Research*. 2017. No. 138. Pp. 389–400.
23. Azad, S.K Seeding the initial population with feasible solutions in metaheuristic optimization of steel trusses. *Engineering Optimization*. 2018. No. 1(50). Pp. 89–105.
24. Ferreira, F., Simoes, L. Optimum design of a cable-stayed steel footbridge with three dimensional modelling and control devices. *Engineering Structures*. 2019. No. 180. Pp. 510–523.
25. Babaei, M., Sheidaii, M.R. Desirability-Based Design of Space Structures Using Genetic Algorithm and Fuzzy Logic. *International Journal of Civil Engineering*. 2017. No. 2A(15). Pp. 231–245.
26. Karen, I., Yazici, M., Shukla, A. Designing foam filled sandwich panels for blast mitigation using a hybrid evolutionary optimization algorithm. *Composite Structures*. 2016. No. 158. Pp. 72–82.
27. Mushchanov, V.F., Demidov, A.I., Orzhekhovskiy, A.N. Uchet geometricheskoy nelineynosti v chislennykh metodakh rascheta stroitelnykh konstruksiy [Accounting of geometric nonlinearity in numerical methods for calculating building structures]. *Vestnik Donbasskoy natsionalnoy akademii stroitelstva i arkhitektury*. 2018. Vol. 1. No. 4 (132). Pp. 87–91.
28. Gorokhov, Ye.V., Mushchanov, V.F., Romenskiy, I.V., Mushchanov, A.V. Vliyaniye geometricheskikh parametrov na napryazhenno-deformirovannoye sostoyaniye strukturnogo pokrytiya na pryamougolnom plane [The influence of geometric parameters on the stress-strain state of the structural coating on a rectangular plan]. *Metallicheskiye konstruksii*. 2015. T. 21. No. 4. Pp. 191–206.
29. Mushchanov, V., Protopopov, I., Korsun, O., Garifullin, M. in (2015) *Procedia Eng*. DOI: 10.1016/j.proeng.2015.08.209
30. Serpik, I.N., Alekseytsev, A.V. Optimization of flat steel frame and foundation posts system. *Magazine of Civil Engineering*. 2016. 61(1). Pp. 14–24. DOI: 10.5862/MCE.61.2
31. Rulebook. SP 16.13330.2017 Steel structures. Updated version. Ministry of Construction of the Russian Federation, 2017 [Online]. URL: <http://www.minstroyrf.ru/docs/14474/>
32. Raizer, V.D. *Reliability of Structures: Analysis and Applications*. USA, Backbone Publishing Company, 2009 146 p.
33. Priadko, I.N., Mushchanov, V.P., Bartolo, H., Vatin, N.I., Rudnieva, I.N. Improved numerical methods in reliability analysis of suspension roof joints. *Magazine of Civil Engineering*. 2016. DOI: 10.5862/MCE.65.3
34. Serpik, I., Alekseytsev, A. IOP Conf. Ser. Mater. Sci. Eng. 2018. DOI: 10.1088/1757-899X/365/5/052003
35. Lu, M., Ye, J. Guided genetic algorithm for dome optimization against instability with discrete variables. *Journal Of Constructional Steel Research*. 2017. No. 139. Pp. 149–156.
36. Serpik, I.N., Alekseytsev, A.V., Balabin, P.Yu., Kurchenko, N.S. Flat rod systems: optimization with overall stability control. *Magazine of Civil Engineering*. 2017. No. 8. Pp. 181–192.
37. Greiner, D., Periaux, J., Emperador, J.M. Game Theory Based Evolutionary Algorithms: A Review with Nash Applications in Structural Engineering Optimization Problems. *Archives of Computational Methods in Engineering*. 2017. No. 4(24). Pp. 703–750.
38. Tusnin, A. Dynamic factors in case of damaging continuous beam supports. *Magazine of Civil Engineering*. 2018. 78(2). Pp. 47–64. DOI: 10.18720/MCE.78.4
39. Rybakov, V.A., Al Ali, M., Panteleev, A.P., Fedotova, K.A., Smirnov, A.V. Bearing capacity of rafter systems made of steel thin-walled structures in attic roofs. *Magazine of Civil Engineering*. 2017. 76(8). Pp. 28–39. DOI: 10.18720/MCE.76.3
40. Pavlenko, A.D., Rybakov, V.A., Pikht, A.V., Mikhailov, E.S. Non-uniform torsion of thin-walled open-section multi-span beams. *Magazine of Civil Engineering*. 2016. 67(7). Pp. 55–69. DOI: 10.5862/MCE.67.6
41. Vatin, N.I., Nazmeeva, T., Guslinsky, R. Problems of cold-bent notched c-shaped profile members. *Advanced Materials Research*. 2014. 941–944. Pp. 1871–1875. DOI: 10.4028/www.scientific.net/AMR.941-944.1871
42. Atavin, I.V., Melnikov, B.E., Semenov, A.S., Chernysheva, N.V., Yakovleva, E.L. Influence of stiffness of node on stability and strength of thin-walled structure. *Magazine of Civil Engineering*. 2018. 80(4). Pp. 48–61. DOI: 10.18720/MCE.80.5
43. Al Ali, M., Isaev, S.A., Vatin, N.I. Development of Modified formulae for detection of the welding stresses in the welded steel cross-sections [Online]. *Materials Physics and Mechanics*. 2016. 26 (1). Pp. 9–15. URL: <https://www.scopus.com/inward/record.uri?eid=2-s2.0-84963975944&partnerID=40&md5=172ea7080590b2dd71fef166d3a24fe0>
44. Kafi, M.A., Kachooee, A. The behavior of concentric brace with bounded fuse. *Magazine of Civil Engineering*. 2018. 78(2). Pp. 16–29. DOI: 10.18720/MCE.78.2
45. Gubanov, V.V. Ensuring the durability of lattice towers. Abstract of PhD dissertation in Engineering / Donbass National Academy of Civil Engineering and Architecture, Makeevka [Online], 1995. URL: <https://dlib.rsl.ru/01000775429>

Contacts:

Anatoly Alekseytsev, +7(960)5643358; aalexw@mail.ru
Liga Gaile, +37122 169545; liga.gaile@gmail.com
Peteris Drukis, +37124332827; peteris.drukis@gmail.com

© Alekseytsev, A.V., Gaile L., Drukis, P., 2019



DOI: 10.18720/MCE.91.1

Оптимизация балочных конструкций каркасных зданий с учетом требований к их безопасности

А.В. Алексейцев^а, Л. Гейли^б, П. Друкис^б

^а *Национальный исследовательский Московский государственный строительный университет, г. Москва, Россия*

^б *Рижский технический университет, г. Рига, Латвия*

* E-mail: aalexw@mail.ru

Ключевые слова: строительные конструкции, оптимизация, механическая безопасность, риск, живучесть, локальные повреждения, запроектные воздействия

Аннотация. Разработан метод поиска проектных решений на дискретных множествах параметров проектирования, учитывающий риски материальных потерь при авариях и начальную стоимость конструкции и включающий единый двухцикловый итерационный процесс. Первым циклом является генетическая итерационная процедура. В рамках этого процесса вводится многократно повторяющийся второй цикл, используемый для расчета конструкции в статической нелинейной постановке. Для учета динамического эффекта используются коэффициенты, вычисляемые с использованием методов прямого интегрирования уравнений движения поврежденной системы, с помощью которых корректируется нагруженность объекта. Оценка рисков для варианта конструкции происходит также в рамках эволюционной процедуры. Предлагаемый алгоритм предусматривает возможность учета степени безопасности объекта, что позволит повысить до необходимого уровня сопротивляемость авариям несущих конструкций с одновременной рациональной экономией материальных затрат. В качестве примера проектирования рассмотрена трансформируемая балочная конструкция, оборудованная системой адаптации к запроектным воздействиям. Показывается, что при синтезе конструкций повышенной живучести использование систем адаптации в виде страховочных элементов имеет преимущество по сравнению с простым увеличением сечений элементов.

Литература

1. Алексейцев А.В., Ахременко С.А. Эволюционная оптимизация предварительно напряженных стальных рам // Инженерно-строительный журнал. 2018. № 5(81). С. 32–42. doi: 10.18720/MCE.81.4
2. Алексейцев А.В. Эволюционная оптимизация стальных ферм с учетом узловых соединений стержней // Инженерно-строительный журнал. 2013. № 5(40). С. 28–37. DOI: 10.5862/MCE.40.3
3. Schacht G., Kaeding M., Bolle G., Concepts for the assessment of bridges with the risk of stress corrosion cracking // Beton- und Stahlbetonbau. 2019. No. 2(114). Pp. 85–94.
4. Veismoradi S., Cheraghi A., Darvishan E. Probabilistic mainshock-aftershock collapse risk assessment of buckling restrained braced frames // Soil Dynamics And Earthquake Engineering. 2018. No. 115. Pp. 205–216.
5. Martins L., Silva V., Bazzurro P. Advances in the derivation of fragility functions for the development of risk-targeted hazard maps // Engineering Structures. 2018. No. 173. Pp. 669–680.
6. Shokrgozar H.R., Mansouri I., Hu J.W. Comparison of Seismic Reliability and Risk Assessment for Special and Intermediate Steel Moment Frames // KSCE Journal of Civil Engineering. 2018. No. 9 (22). Pp. 3452–3461.
7. Lonetti P., Maletta R. Dynamic impact analysis of masonry buildings subjected to flood actions // Engineering Structures. 2018. No. 167. Pp. 445–458.
8. Muntasir Billah A. H. M., Alam M. S. Probabilistic seismic risk assessment of concrete bridge piers reinforced with different types of shape memory alloys // Engineering Structures. 2018. No. 162. Pp. 97–108.
9. Droogne D., Botte W., Caspeepe R. A multilevel calculation scheme for risk-based robustness quantification of reinforced concrete frames // Engineering Structures. 2018. No. 160. Pp. 56–70.
10. Vanmarcke E., Lin N., Yau S.-C. Quantitative risk analysis of damage to structures during windstorms: some multi-scale and system-reliability effects // Structure and Infrastructure Engineering. 2013. No. 10. Pp. 1311–1319.
11. Bezabeh M.A., Tesfamariam S., Popovski M., Goda K., Stiemer S.F. Seismic base shear modification factors for timber-steel hybrid structure: collapse risk assessment approach // Journal of Structural Engineering. 2017. No. 10(143), 04017136.
12. Tampazyan A.G., Zubareva S. Optimal design of reinforced concrete structures taking into account the particular calculation for progressive destruction // MATEC Web of Conferences, 2017. No. 117, 00163.
13. Amiri S., Saffari H., Mashhadi J., Assessment of dynamic increase factor for progressive collapse analysis of RC structures // Engineering Failure Analysis. 2018. No. 84. Pp. 300–310.
14. Sattar S., Liel A.B. Collapse indicators for existing nonductile concrete frame buildings with varying column and frame characteristics // Engineering Structures. 2017. No. 152. Pp. 188–201.

15. Tampazyan A.G. Calculation of reinforced concrete plates with hole at long-term loading // IOP Conf. Series: Materials Science and Engineering. 2018. No. 365 052021.
16. Tamrazyan A.G., Avetisyan L.A. Behavior of compressed reinforced concrete columns under thermodynamic influences taking into account increased concrete deformability // IOP Conf. Series: Materials Science and Engineering. 2018. No. 365, 052034.
17. Arabi S., Shafei B., Phares B.M. Investigation of fatigue in steel sign-support structures under diurnal temperature changes [Электронный ресурс] // Journal of Constructional Steel Research. 2019. No. 153. Pp. 286–297. URL: <https://doi.org/10.1016/j.jcsr.2018.09.024>
18. Barone G., Frangopol D.M. Life-cycle maintenance of deteriorating structures by multi-objective optimization involving reliability, risk, availability, hazard and cost // Structural Safety. 2014. No. 48. Pp. 40–50.
19. Liu Y.-F., Liu X.-G., Fan J.-S. Refined safety assessment of steel grid structures with crooked tubular members // Automation in Construction. 2019. No. 99. Pp. 249–264.
20. Truong V.-H., Kim S.-E. Reliability-based design optimization of nonlinear inelastic trusses using improved differ-ential evolution algorithm // Advances in Engineering Software. 2018. No. 121. Pp. 59–74.
21. Saad L., Chateaufneuf A., Raphael W. Robust formulation for Reliability-based design optimization of structures // Structural and Multidisciplinary Optimization. 2018. No. 6(57). Pp. 2233–2248.
22. Le L.A., Bui-Vinh T., Ho-Huu V. An efficient coupled numerical method for reliability-based design optimization of steel frames // Journal Of Constructional Steel Research. 2017. No. 138. Pp. 389–400.
23. Azad S.K. Seeding the initial population with feasible solutions in metaheuristic optimization of steel trusses // Engineering Optimization. 2018. No. 1(50). Pp. 89–105.
24. Ferreira F., Simoes L. Optimum design of a cable-stayed steel footbridge with three dimensional modelling and control devices // Engineering Structures. 2019. No. 180. Pp. 510–523.
25. Babaei M., Sheidaii M.R. Desirability-Based Design of Space Structures Using Genetic Algorithm and Fuzzy Logic // International Journal of Civil Engineering. 2017. No. 2A(15). Pp. 231–245.
26. Karen I., Yazici M., Shukla A. Designing foam filled sandwich panels for blast mitigation using a hybrid evolutionary optimization algorithm // Composite Structures. 2016. No. 158. Pp. 72–82.
27. Мушанов В.Ф., Демидов А.И., Оржеховский А.Н. Учет геометрической нелинейности в численных методах расчета строительных конструкций // Вестник Донбасской национальной академии строительства и архитектуры. 2018. Т. 1. № 4 (132). С. 87–91.
28. Горохов Е.В., Мушанов В.Ф., Роменский И.В., Мушанов А.В. Влияние геометрических параметров на напряженно-деформированное состояние структурного покрытия на прямоугольном плане // Металлические конструкции. 2015. Т. 21. № 4. С. 191–206.
29. Mushchanov V., Protopopov I., Korsun O., Garifullin M. Procedia Eng. 2015. DOI: 10.1016/j.proeng.2015.08.209
30. Серпик И.Н., Алексейцев А.В. Оптимизация системы стальной плоской рамы и столбчатых фундаментов // Инженерно-строительный журнал. 2016. № 1(61). С. 14–24. DOI: 10.5862/MCE.61.2
31. Rulebook. SP 16.13330.2017 Steel structures. Updated version. Ministry of Construction of the Russian Federation, 2017 [Электронный ресурс]. URL: <http://www.minstroyrf.ru/docs/14474/>
32. Raizer V.D. Reliability of Structures: Analysis and Applications. USA, Backbone Publishing Company, 2009. 146 p.
33. Priadko I.N., Mushchanov V.P., Bartolo H., Vatin N.I., Rudnieva I.N. Improved numerical methods in reliability analysis of suspension roof joints // Magazine of Civil Engineering. 2016. DOI: 10.5862/MCE.65.3
34. Serpik I., Alekseytsev A. IOP Conf. Ser. Mater. Sci. Eng. 2018. DOI: 10.1088/1757-899X/365/5/052003
35. Lu M., Ye J. Guided genetic algorithm for dome optimization against instability with discrete variables // Journal Of Constructional Steel Research. 2017. No. 139. Pp. 149–156.
36. Serpik I.N., Alekseytsev A.V., Balabin P.Yu., Kurchenko N.S. Flat rod systems: optimization with overall stability control // Magazine of Civil Engineering. 2017. No. 8. Pp. 181–192.
37. Greiner D., Periaux J., Emperador J.M. Game Theory Based Evolutionary Algorithms: A Review with Nash Applications in Structural Engineering Optimization Problems // Archives of Computational Methods in Engineering. 2017. No. 4(24). Pp. 703–750.
38. Туснин А.Р. Коэффициенты динамичности при повреждении опор неразрезных балок // Инженерно-строительный журнал. 2018. № 2(78). С. 47–64. doi: 10.18720/MCE.78.4
39. Рыбаков В.А., Ал Али М., Пантелеев А.П., Федотова К.А., Смирнов А.В. Несущая способность стропильных систем из стальных тонкостенных конструкций в чердачных крышах // Инженерно-строительный журнал. 2018. № 8(76). С. 28–39. doi: 10.18720/MCE.76.3
40. Павленко А.Д., Рыбаков В.А., Пихт А.В., Михайлов Е.С. Стесненное кручение многопролетных тонкостенных балок открытого профиля // Инженерно-строительный журнал. 2016. № 7(67). С. 55–69. DOI: 10.5862/MCE.67.6
41. Vatin N.I., Nazmeeva T., Guslinsky R. Problems of cold-bent notched c-shaped profile members // Advanced Materials Research. 2014. 941–944. Pp. 1871–1875. DOI: 10.4028/www.scientific.net/AMR.941-944.1871
42. Атавин И.В., Мельников Б.Е., Семенов А.С., Чернышева Н.В., Яковлева Е.Л. Влияние жесткости узловых соединений на устойчивость и прочность тонкостенных конструкций // Инженерно-строительный журнал. 2018. № 4(80). С. 48–61. doi: 10.18720/MCE.80.5
43. Al Ali M., Isaev S.A., Vatin N.I. Development of Modified formulae for detection the welding stresses in the welded steel cross-sections [Электронный ресурс] // Materials Physics and Mechanics. 2016. 26 (1). Pp. 9–15. URL: <https://www.scopus.com/inward/record.uri?eid=2-s2.0-84963975944&partnerID=40&md5=172ea7080590b2dd71fef166d3a24fe0>.
44. Кафя М.А., Качуй А. Поведение концентрических расколов с встроенным предохранителем по сжимающей нагрузке // Инженерно-строительный журнал. 2018. № 2(78). С. 16–29. doi: 10.18720/MCE.78.2
45. Губанов В.В. Обеспечение долговечности решетчатых башен: автореф. дис. ... канд. техн. наук [Электронный ресурс] / Донбасская национальная академия строительства и архитектуры, Макеевка, 1995. URL: <https://dlib.rsl.ru/01000775429>

Контактные данные:

*Анатолий Викторович Алексейцев, +7(960)5643358; эл. почта: aalexw@mail.ru
Лига Гейли, 37122169545; эл. почта: liga.gaile@gmail.com
Петерис Друкис, 37124332827; эл. почта: peteris.drukis@gmail.com*



DOI: 10.18720/MCE.91.2

Synergistic-effect of iron-filing and silica-fume on the absorption and shrinkage of cement paste

M.O. Yusuf*

University of Hafr Al Batin, Hafr Al Batin, Saudi Arabia

* E-mail: moruf@uhb.edu.sa

Keywords: iron-filing, silica fume, water absorption, shrinkage, workability, paste

Abstract. This study investigated workability, water absorption, and drying shrinkage performances of the synergy of iron filing (IF) with silica fume (SF) in the ordinary Portland (OPC) cement paste. IF varied from 0 to 15wt. % while SF was kept constant at 10wt % of the binder. The finding revealed that at low water/binder (w/b) ratio of 0.25, the synergistic effects of the combination of IF and SF reduced the workability and shrinkage of the paste exponentially but increased water absorption. Besides, an increase in absorption was due to non-absorbent nature of IF and proliferation of interfacial transition zones (ITZ) within the matrix while addition of SF caused the increase in pore tortuosity through secondary pozzolanic reaction accompanied by its micro-filling effects. Moreover, bond characterization showed that drying shrinkage reduction was due to IF retention of evaporable water within the matrix, and the removal of hydroxyl precipitated together with an improved polymerized units of silicate. Scanning electron micrograph indicated the improvement in the microstructural density due to the formation of CASH or CSH and restriction of internal strain deformation due to the formation of Fe-infused product (CAFSH). The least shrinkage value was observed at the IF substitution level of 15% with the SF of 10%. Therefore, synergistic effects of SF and IF could enhance production of more durable concrete more especially in the hot weather climate.

1. Introduction

Iron-filings (IF) are mostly a waste product obtained from metal cutting, grinding, filing, or milling of finished iron products especially in workshops and foundry [1]. This waste (iron filing) in addition to blast furnace slag is attached to chain of iron utilization as a product or dominant component of steel alloy. There have been some studies on the uses of IF as an additive or partial supplement for sand in paste, mortar or concrete products [2]. Alserai et al. [1] conducted research on the contribution of iron filing (IF) when used together with recycled aggregates and reported its contribution to concrete mechanical properties. Alzaed [2] also reported that up to 10 % of IF could be used to improve the concrete strength while Familusi et al. [3] stated that quarry-dust used in binary could produce a concrete of better strength especially when the constituent waste materials utilized are not in excess 50 % of the total mixture.

Moreover, the increase in strength of concrete when IF is utilized has been adduced to pore blockage that enhanced reduction in porosity [4]. Olutoge et al. [5] also asserted that 20 % sand replacement could bring about 13.5 % gain in strength, and this is in consonance with the finding published by Ghannam et al. [6]. Noori and Ibrahim [7] reported a slight variation of 12 %. However, Vasudevan [8] observed decreasing in slump value and the strength with addition 5 % of IF. The difference in the percentage reported could be due to oxide composition together with impurities as many of the authors could not present the x-ray florescence (XRF) of the IF used.

Furthermore, there are several studies on shrinkage characteristics of OPC paste. For instance, Ahmad et al. [9] identified water/binder ratio as the most important factors controlling the shrinkage OPC based binder. This is followed by cement content and the presence of pozzolanic materials such as silica fume and fly-ash

Yusuf, M.O. Synergistic-effect of iron-filing and silica-fume on the absorption and shrinkage of cement paste. Magazine of Civil Engineering. 2019. 91(7). Pp. 16–26. DOI: 10.18720/MCE.91.2

Юсуф М.О. Синергетический эффект железных опилок и микрокремнезёма на поглощающую способности и усадку цементного теста // Инженерно-строительный журнал. 2019. № 7(91). С. 16–26. DOI: 10.18720/MCE.91.2



This work is licensed under a [CC BY-NC 4.0](https://creativecommons.org/licenses/by-nc/4.0/)

contents among other factors. Bagheri et al. [10] used the silica fume in ternary blending with blast furnace slag to improve the mechanical and durability of concrete by reducing the permeability and increasing the compressive strength of the binder. Almusallam et al. [11] identified that, in the hot climate, lean-stiff concrete has higher resistance to plastic shrinkage compare to rich concrete due to the presence of more cement in the latter. The rate of evaporation and bleeding could be reduced in the concrete that contains silica fume even at the expense of the workability of the mixture. In the same manner with silica fume, Brooks and Megat Johari [12] and Guneiyisi et al. [13] pointed to the fact that inclusion of metakaolin – due to its pozzolanicity and ability to proceed on secondary hydrations – could also reduce creep, autogenous and drying shrinkage.

It has been reported that carbonation of paste and pore diameter could contribute to larger autogenous shrinkage than moisture content in alkali activated slag [14]. This is possible due to large proportion of pore sizes and radius within the slag mesoporous region [15]. Jankovic [16] used environmental scanning electron microscope (ESEM) to study interfacial transition zone (ITZ) of cement paste with a view to determining the shrinkage strain and its non-linearity with relative humidity. He concluded that type of cement, admixture and water-cement (w/c) ratio could affect the shrinkage of cement paste while wet condition of the sample could cause capillary mechanism to have significant impact. The amount of cement in the mixture could also influence the chemical and drying shrinkage in the resulting concrete. This is highlighted in the analysis of high performance concrete (HPC) used in Iowa bridge construction [17].

Moreover, Jin et al. [18] investigated the reduction of the shrinkage of AAS by using MgO and concluded that the level of reactivity of MgO together with curing condition could influence how the strength and shrinkage characteristics of alkaline activated slag (AAS) could be described. Heat-curing together with silica modulus ($\text{SiO}_2/\text{Na}_2\text{O}$) after 7-day of pre-curing was reported to be more effective in reducing drying shrinkage in geopolymer binder [19, 20]. The depth of the drying surface could also affect the internal drying shrinkage of concrete [21]. Slowik et al. [22] emphasized that shrinkage in plastic state of wet mortar or concrete could affect the durability performance of concrete in its hardened state. Tam et. al [23] stated that water to binder ratio could also have significant effects on the shrinkage and permeability of concrete. The use of palm oil fuel ash (POFA) up to 30 % as an additive was reported to reduce the drying shrinkage of concrete due to its high silica content that led to lower permeability of the product [24].

Meanwhile, despite these studies, no studies have addressed the water absorption, and shrinkage performance of addition of IF and SF into ordinary Portland cement paste sample with a view to understanding the bond characteristics, interaction within the microstructure, absorption and the shrinkage characteristic of the resultant product. The benefit of this study is to improve the durability characteristics (shrinkage) of concrete, promote waste valorization through utilization of more industrial waste products such as iron-filing, and to reduce the cost of green concrete production (by minimizing OPC content) which favours environmental sustainability.

2. Materials and Methods

2.1. Materials

2.1.1. Ordinary Portland cement

The cement used in the study satisfies the requirement of ASTM C 150 [25]. The oxide compositions were determined by X-ray fluorescence (XRF) technique and the results are as shown in Table 1 while the particle size distribution is as shown in Figure 1.

Table 1. Oxides composition of Ordinary Portland and Iron filling Oxides.

Oxides	OPC, %	Iron filing, %	Silica Fume, %
SiO_2	19.01	1.38	95.85
Al_2O_3	4.68	0.61	0.26
Fe_2O_3	3.20	96.5	0.05
CaO	66.89	0.02	0.21
MgO	0.81	–	0.45
Na_2O	0.09	–	–
TiO_2	0.22	0.03	–
K_2O	1.17	0.13	–
P_2O_5	0.08	0.05	–
SO_3	3.66	0.23	1.00
MnO	0.19	0.5	–
Cl	–	0.05	–
Cr_2O_3	–	0.11	–
ZnO	–	0.07	–
SnO	–	0.08	–
SrO2	–	0.02	–
CuO	–	0.22	–
LOI	2.48	–	2.80
$\text{SiO}_2 + \text{Al}_2\text{O}_3 + \text{Fe}_2\text{O}_3$	26.89	98.49	96.16
Moisture content	–	–	0.85

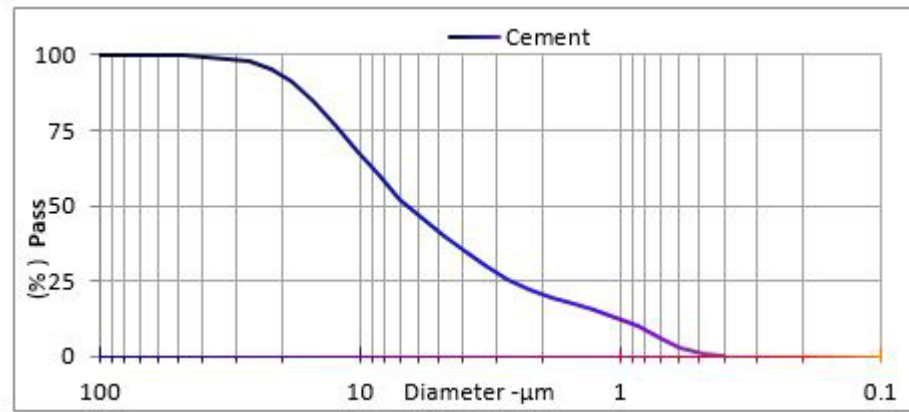


Figure 1. Particle size distribution of the ordinary Portland cement.

2.1.2. Fine aggregate

It consists of dune sand with fineness modulus of 1.85. The specific gravity in saturated dry condition was 2.62 with the absorption capacity of 0.65 %.

2.1.3. Iron-filing

The material is collected at mechanical lathe machine and brake disc grinding workshops at Senaiya Hafr Al Batin in the Eastern province of Saudi Arabia. It has the fineness modulus of 2.89 while its particle size distribution is shown in Figure 2. Its oxide composition shown in Table 1 reflects the dominance of iron oxide. The physical properties of OPC, IF powder and fine aggregates are as shown in Table 2.

Table 2. Physical properties of fine aggregates and iron filing.

Physical Properties	Sand	Iron Filing	OPC	Silica fume
Bulk Density (kg/m ³)	1699	1932	3100	630
Specific gravity	2.67	6.85	3.41	2.25
Specific surface area (m ² /kg)		13.73	331.0	18000
Fineness modulus	3.3	2.89	2.84	–
Average diameter, D50 (µm)	–	250	6.69	0.15

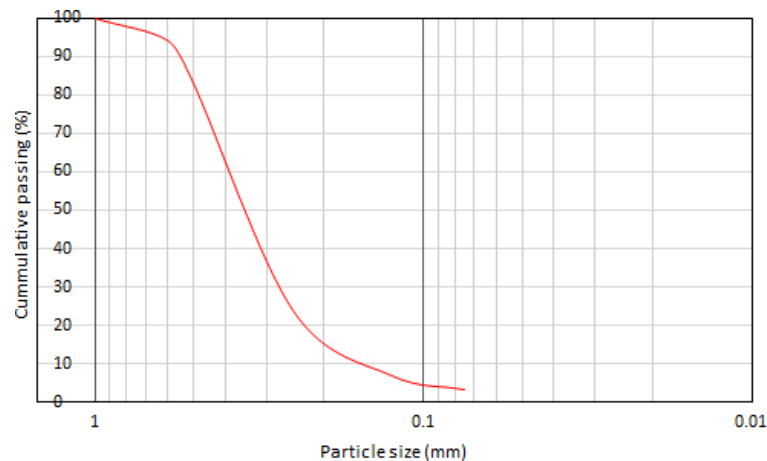


Figure 2. Particle size distribution curve of iron-filing powder.

2.1.4. Silica fume

This is a densified silica fume (SF) produced by Xiamen All Carbon Corporation, Xiamen, China and supplied by Al-Rashed Cement Co, Saudi Arabia. The material has the specific surface area of 18000 m²/kg, and bulk density of 630 kg/m³. Other materials physical properties are shown in Table 2 while its oxide compositions are also shown in Table 1.

2.2. Research Methodology

Mix design was conducted such that the percentage composition of the IF and SF in paste varied as 5, 10 and 15 % with addition of 10wt. % SF in all the mixtures while the water/binder (w/b) ratio was maintained as 0.25. The workability of the mixture was determined to understand the contribution of IF and SF in synergy to the consistency of the mixture. Thereafter, the hardened paste was exposed to water to study the water

absorption and shrinkage of the products due to the synergistic-effect of IF and SF. Fourier transform infrared (FTIR) spectroscopy was used to determine the impact of SF and IF on the bond characteristics of the binders. The microstructures of the samples were also examined to study the impact or contribution of IF to the densification of the paste.

2.2.1. Microstructural and Fourier infrared spectroscopic analyses

The JEOL scanning electron microscopy coupled with energy dispersive spectroscopy (SEM + EDS) model 5800 LV, was used to test the morphology of the 28-day sample paste obtained from solid sample by first coating it with gold thin fume [26, 27]. The pulverized sample was used for the FTIR spectroscopy in order to characterize the bonds that exist between the molecular compounds. FTIR was conducted using Perking Elmer 880 spectrometer using the technique of attenuated total reflection (ATR).

2.2.2. Mix proportion

Mix design was conducted such that the percentage composition of the IF varied as 0, 5, 10 and 15 % while SF was kept constant as the 10 % of the binder. The mix proportion is as shown in Table 3. The superplasticizer used was Glenium® of 0.63wt % by cement mass to achieve the required consistency.

Table 3. Paste material compositions.

Sample ID	OPC (kg/m ³)	Iron filing (kg/m ³)	Water (kg/m ³)	SF (kg/m ³)	SP (kg/m ³)	Unit weight (kg/m ³)
M_{0.35}F₀S₀	1716.0	0.0	600.6	0.0	12.0	2328.6
M_{0.35}F₀S₁₀	1561.6	0.0	600.6	154.4	12.0	2328.6
M _{0.35} F ₀₅ S ₁₀	1475.8	85.8	600.9	155.3	12.0	2329.8
M _{0.35} F ₁₀ S ₁₀	1390.0	171.6	600.9	155.3	12.0	2329.8
M_{0.35}F₁₅S₁₀	1304.2	257.4	600.9	155.3	12.0	2329.8

2.2.3. Mixing of the specimen

OPC was first placed in Hobart planetary mixer after which the SF was added and then mixed homogeneously. IF powder was then added, and mixed together for 3 mins. Water (70 %) together with superplasticizer was added and then further mixed for 2 mins. The whole mixture was mixed continuously for additional 3 mins before adding the remaining water (30 %) to ensure homogeneous mixture. The pastes were then cast into 50×50×50 mm for water absorption tests while 25×25×250 mm moulds was used for shrinkage testing. The samples were demoulded after 12 hrs and then lowered into curing tank at the room temperature of 25 ± 2 °C except for the shrinkage specimens that was kept in the oven immediately at 50 °C.

2.3. Evaluation methods

2.3.1 Workability

The workability of the specimen was determined by flow table in accordance with ASTM C 1437 [28]. The slump value was expressed as a percentage as shown in Equation (1):

$$\text{Workability or slump} = \frac{\text{Measured flow} - 100}{100} \times 100. \quad (1)$$

2.3.2. Water absorption

The cubic sample of size 50 mm of known original weight were fully immersed in water while the absorption is measured by sensitive weighing balance upon drying the surface water using dry towel to ensure surface dry condition. The results are recorded as shown in Equation (2):

$$\text{Absorption (\%)} = \frac{\text{Weight after immersion period} - \text{Original weight}}{\text{Original weight}} \times 100. \quad (2)$$

2.3.3. Drying shrinkage

To test the performance of IF in terms of drying shrinkage performance, the prismatic paste specimens of dimension 25×25×250 mm were used in triplicate while the average results were recorded by computing Equation (3).

$$\text{Shrinkage (\%)} = \frac{\text{Length measured} - 250}{250} \times 100. \quad (3)$$

3. Results and Discussions

3.1. Raw materials physical properties and material characterization

The physical properties of IF shown in Table 2 indicating that IF has a bulk density of 1932 kg/m³ which is about 62 % of that of OPC whereas SF (630 kg/m³) is almost twice that of OPC. The specific gravity of IF – the densest of the constituent materials – doubled that of cement, Therefore, concrete produced with IF based paste or mortar can be used for providing adequate thrust for underground buried pipes or stabilizing the pipelines. Average size D₅₀ of IF was around 250 μm which could be categorized into fine aggregates in accordance with ASTM C33 [29].

Besides, the surface area of SF was higher than that of cement and IF. It has the lowest average size diameter that is capable of enhancing adequate packing within the larger particle sizes of OPC particle and IF. This frictional effects increase with the increase in the quantity of IF thereby reducing the workability of the mixtures as shown in Figure 3. Therefore, the samples without the presence of SF had better consistency in comparison with SF-free mixture. The presence of IF and SF within the cement particle increases the interfacial transition zones (ITZ). This caused and increased the inter-particle frictional resistance thereby inducing the paste low consistency by 12.5 %. With the inclusion of 5 % -10wt. % of IF, the flowability further reduced by 24 % and 25 %, respectively. The workability of the specimens varied exponentially with the IF content as shown in Equation (4). The correlation between the experimental and predicted data is as shown in Figure 4 such that the regression coefficient is 0.9 for SF = 0.1 (10 %).

$$\text{Workability} = 27.1 - 26.7e^{SF*Fe} \quad (R^2 = 0.90) \quad (4)$$

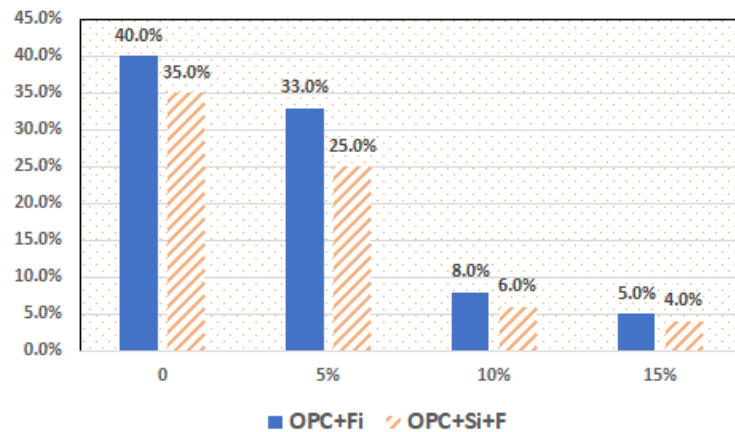


Figure 3. Workability of the paste with the presence of silica fume and iron-filing.

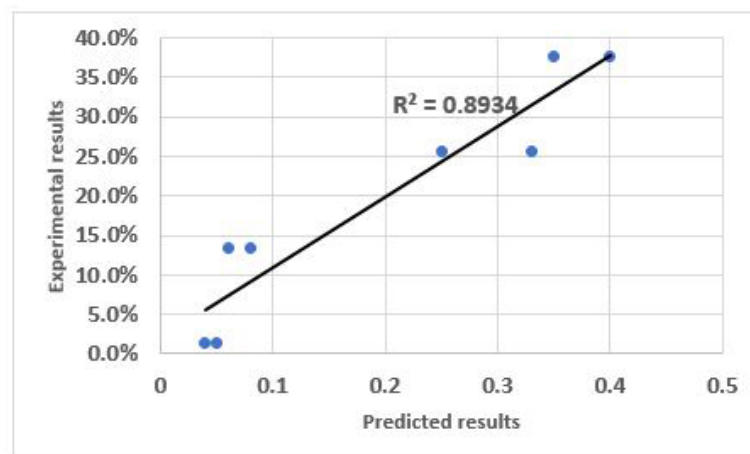


Figure 4. Workability of iron-filing and silica fume infused OPC paste.

3.2. Water absorption

Figure 5 shows percentage water absorption of paste containing iron-filing (IF). It is evident that the absorption increases with the content of IF due to its non-absorptive nature. The different between 0 and 5 % IF substitution in the absorption capacity of the sample is insignificant. However, as the increment increases

to 10 % IF, the percentage absorption increased by 36 %. The increment increases to 136.4 % as the substitution to 15 %. Presence of more IF create more ITZ thereby enhancing hydraulic permeability or conductivity of the matrix. Furthermore, the fineness of SF and its larger surface area enhance the filling of micropores thereby reducing the porosity of the matrix. This is evident in Figure 6 as the sample that contains SF within the OPC paste matrix with 5 % IF has the lower absorption in comparison with 15 % IF substitution. By comparing Figure 5 and 6, it is quite clear that SF influences the tortuosity of the microstructural pores. This is corroborated by the micrograph of SF infused sample as shown in Figure 7 and as indicated in the region 1 of the sample.

3.3. Drying shrinkage

3.3.1. Impact of iron-filing on paste shrinkage

From the specimens and their early exposure to higher temperature of 50 °C , the rate of shrinkage decreases – due to initial expansion – with increase in the content of IF in the mixture. Exposing the specimens to early heat treatment caused an abrupt reduction in the relative humidity within the matrix thereby aggravating the pore shrinkage due to surface energy change that existed between the interfaces of air/pore wall on one hand and water/pore wall on the other [30]. Further, addition of 5, 10 and 15 %wt. IF brought down the drying shrinkage value to 5.5.5, 21.1 and 23.8 %, respectively when compare to the control after 6 weeks as shown in Figure 8.

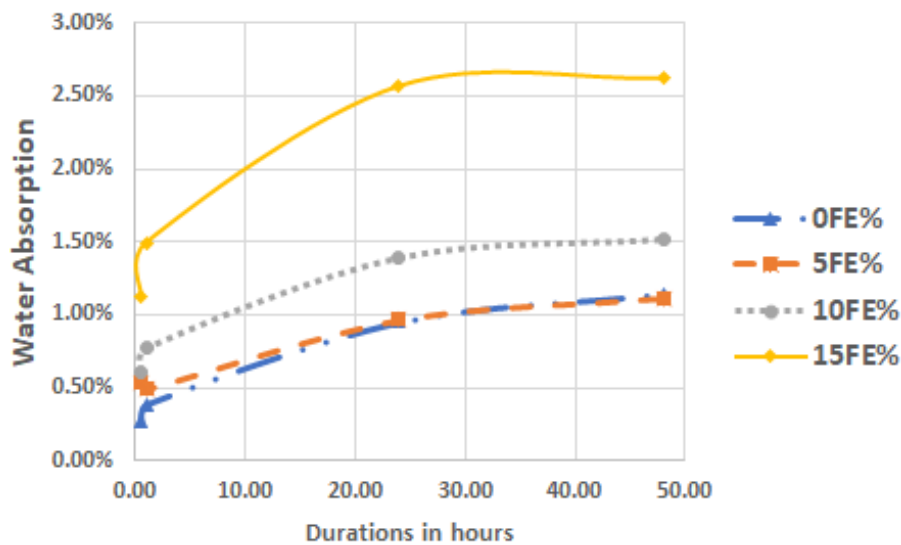


Figure 5. Water absorption based on the composition of iron-filing in paste.

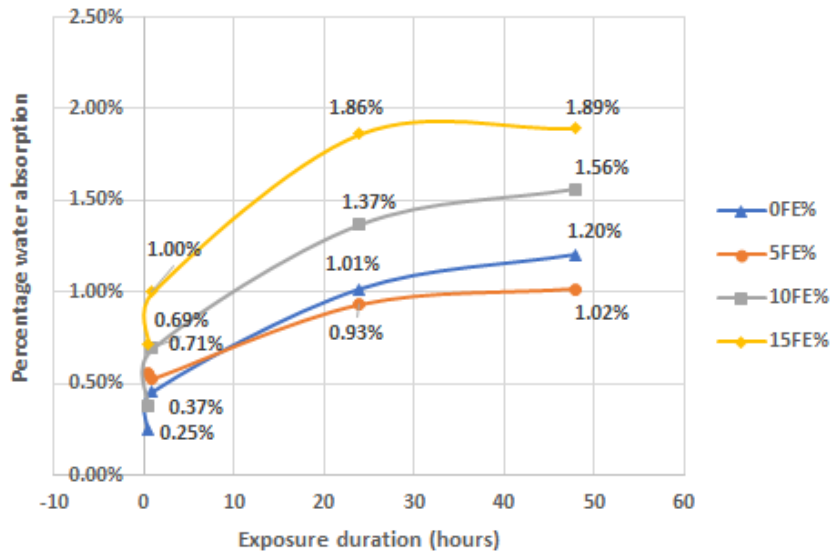


Figure 6. Effect of varied composition of iron-filing and silica fume (10 %) on the paste water absorption.

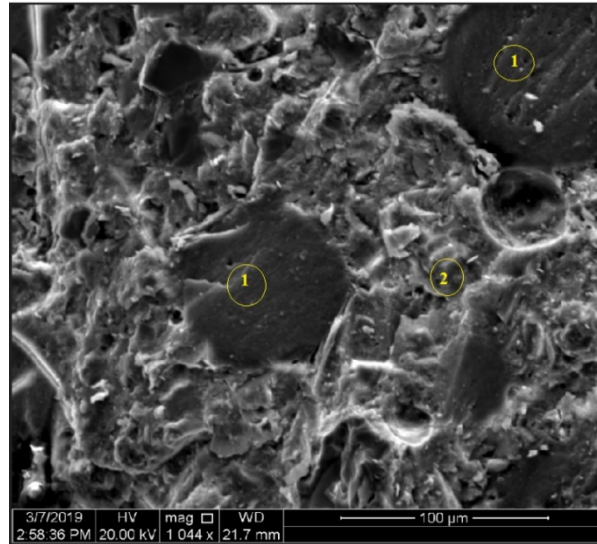


Figure 7. Micrographs of OPC paste and silica fume.

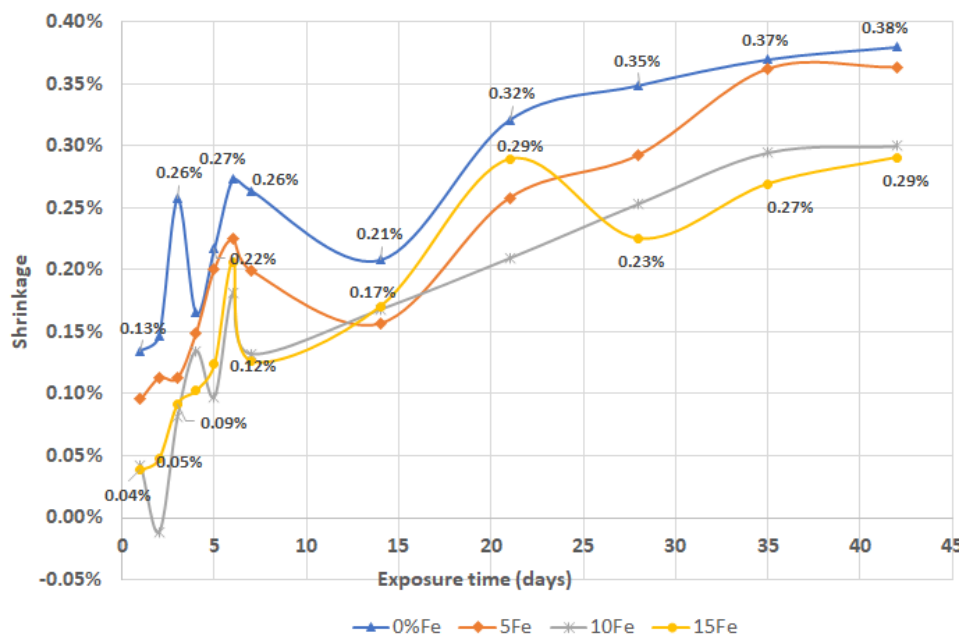


Figure 8. Shrinkage performance of iron-filing infused paste.

For the saturated pores, higher surface tension is developed due to the prolonged reduction in the menisci radii that accompanied dryness by ambient temperature in the oven. The aftermath of the developed surface tension due to reduction in pore relative humidity led to the development of tensile stresses within the pores and this increased with the increase in temperature in accordance with Scherer's model [31] and Kelvin's Equation (5) as reported by Adamson and Gast [32].

$$\sigma = \frac{RT}{V_m} \ln \left(\frac{RH}{X_w} \right), \quad (5)$$

where V_m corresponds to the pore volume;

R is the universal gas constant;

T is the temperature, RH is the relative humidity;

x_w is the mole of water per mole of pore solution that could possibly contains a solute (salts).

The developed tensile stresses had opposing effects (compression) on the pore walls thereby causing high shrinkage strains [33]. The reverse process happened during room temperature due to contraction. This induced compressive stresses caused concomitant contraction within the matrix of the microstructure. This is similar to what Sagoe-Crenstil [34] described as negative pressure within the capillary pores of the paste. The

strain curve of the control (OPC only) sample was found to be more critically wavy in the first 7 days compared to others due to absence of IF that partly absorbed the expansion and contraction by virtue of its higher conductivity (Figure 8). However, despite the alternating stresses, no visible cracks were noted on all the samples.

Moreover, the presence of IF caused restraint in internal deformation thereby leading to localized cracks or crack propagation arrest within the microstructure as shown in Figure 9. This is unlike interconnected crack in the microstructure of IF-free samples. This could be of great importance to promote utilization of IF for hot weather concreting with a view to improving the infrastructural durability challenge like shrinkage. From the FTIR spectra shown in Figure 10, it is quite evident that IF contributes to carbonation of the products by observing the deep trough of $-O=C=O$ vibration at wavenumber 1417 cm^{-1} . It also contributes to the retention of water molecule within the matrix. This assertion stems from the observation of asymmetric stretching of H-O-H at the wavenumber 2985 cm^{-1} which was absent in the control sample (OPC only).

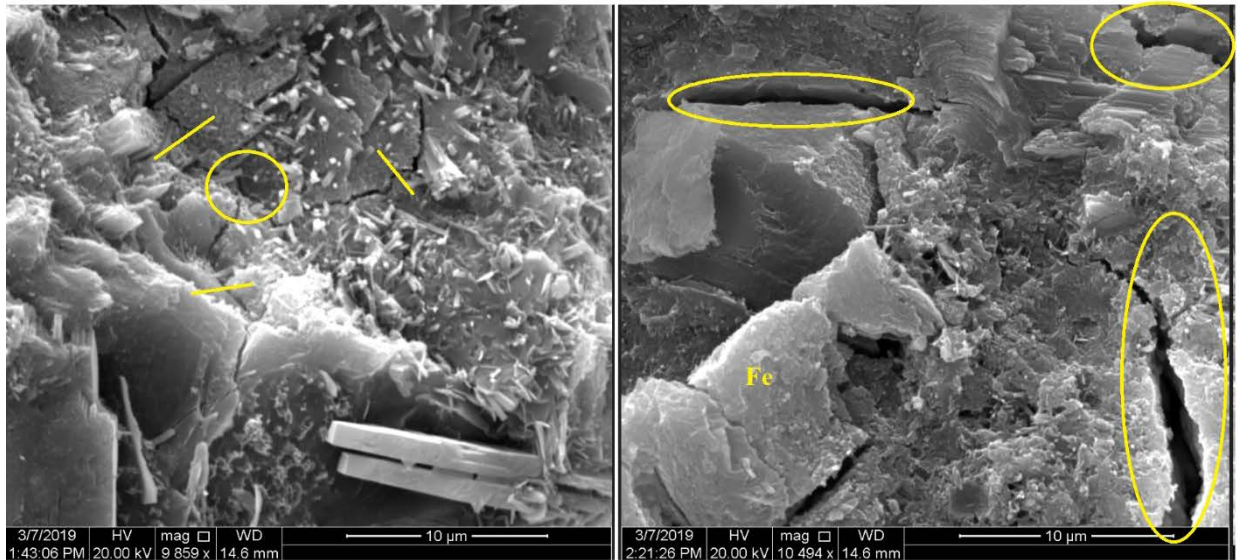


Figure 9. Micrographs of OPC paste (left) and OPC-Iron filing paste (right).

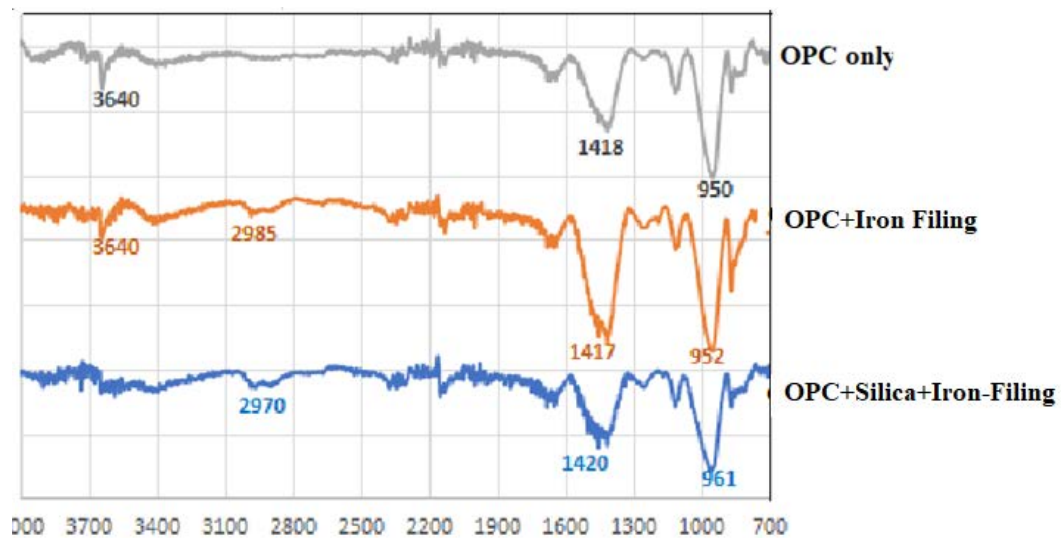


Figure 10. FTIR spectra (a) OPC only (b) OPC+10 %Fe (c) OPC+15 %Fe+10 %Si.

3.3.2. Impact of silica fume and iron-filing on shrinkage characteristics

Upon adding the silica fume (SF) into the mixture, the micro-filing effect is observed as shown in Figure 9. Figure 11 shows that the shrinkage values further reduced upon the addition of SF. For instance, the control sample is reduced by 21.1 % when comparing Figure 9 to Figure 11.

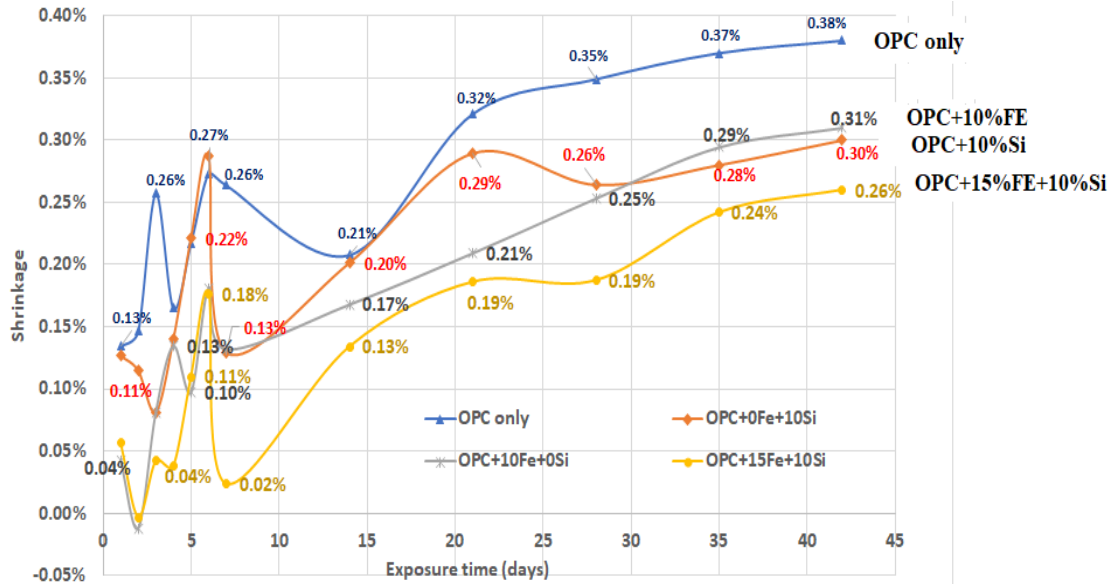
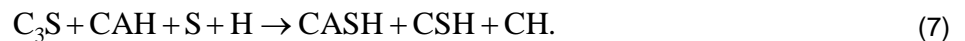


Figure 11. Impact of silica and iron-filing on the shrinkage of OPC paste.

The synergistic-effect of 15 % IF and 10 % SF reduced shrinkage further by 31.6 %. SEM+EDS shown in Figure 12 reflects the heterogeneous formations of different products within the microstructure as indicated in the regions 3, 4, 5. This suggests that the presence of the two materials enhanced pore filling and improved microstructural density as shown in regions 1 (Figures 7 and 9). Region 3 consists of Fe such that Fe/Si ratio was 0.21, while region 2 comprises more silica compare to other regions 4 and 5 (Table 4 and Figure 12). This implies that iron-filing is not uniformly distributed within the microstructure. It can be argued further that Fe present in the IF participated in the hydration process to form CA(F)SH as shown in Equation (6). This is further supported by the presence of Fe within the elements which is indicated by elemental diffractive spectroscopy (EDS) results as shown in Table 4.



The formation of calcium aluminosilicate hydrate (CASH) is also possible as shown in region 2, 4 and 5 as a result of secondary hydration or pozzolanic reactivity of SF. Further, region 5 has a low composition of alumina (Al), which implies that CSH could have probably dominated the region with traces of CASH as shown in Equation (7).



Furthermore, due to the lower water/binder ($w/b=0.25$) ratio, there is possibility of self dessication that mainly controls autogenous shrinkage. This phenomenon reduces the volumetric degree of saturation (S) while larger bulk density of IF (K_s) could cause decrease in the deformation as shown in Equation (8).

$$\partial = \frac{S}{3} \sigma \left(\frac{1}{K} - \frac{1}{K_s} \right), \quad (8)$$

where S is the volumetric degree of saturation and K volumetric bulk modulus of the entire mass while K_s is the volumetric modulus of solid while σ is the developed tensile stress.

4. Conclusions

The study investigated the influence of iron filing (IF) and silica fume (SF) on the paste through water absorption, shrinkage and workability of the resultant paste. This study would be of great importance to promote utilization of IF for hot weather concreting with a view to improving the infrastructural durability challenge like shrinkage. The following are the summary of the conclusions:

- The presence of IF and SF within the cement particle in the paste formation increased the interfacial transition zones that could reduce the inter-particle mobility due to frictional effect. Thus, inclusion of IF together with silica at lower water-binder ratio, and further reduced the workability of the paste.
- Water absorption value increased with the content of IF and thus 5 % IF-OPC substitution gave the better performance. It is quite clear that SF influenced the tortuosity of the microstructural pores thereby decreasing the water absorption.

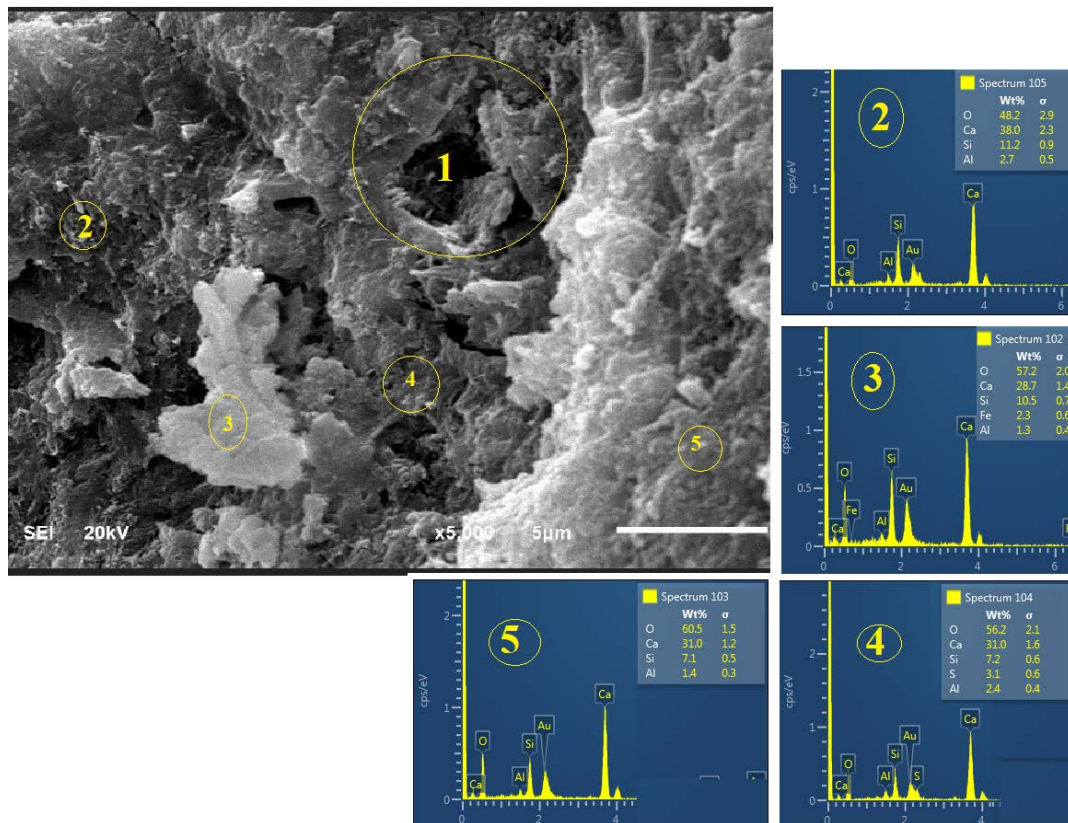


Figure 12. The micrograph of 10 %Si+OPC+15 %Fe.

Table 4. Elemental ratio from EDS obtained from the micrograph.

	Region 2	Region 3	Region 4	Region 5
Ca/Si	3.6	2.75	9.9	4.32
Si/Al	0.29	8.05	3.0	5.14
Si/S	0	0	2.3	0
Fe/Si	0	0.21	0	0

- Synergy of IF and SF reduced the drying shrinkage of OPC paste as 15 % IF and 10 % SF content gave the lowest shrinkage and the better performance.
- The presence of SF at low water/binder ratio caused self-desiccation which could potentially cause autogenous shrinkage whose effect could be counter-balanced by adding IF to maintain microstructural equilibrium with consequent reduction in the resultant shrinkage.
- IF favoured the formation of H-O-H bond vibration within the matrix as SF removed the precipitate of hydroxyl through secondary hydration process as indicated by the FTIR spectra.

5. Acknowledgement

The author appreciate the University of Hafr Al Batin for providing the opportunity to carry out this research.

References

1. Alserai, S.J., Alsaraj, W.K., Abass Z.W. Effect of Iron Filings on the Mechanical Properties of Different Types of Sustainable Concrete. The Open Civil Engineering Journal. 2018. 12. Pp. 441–457.
2. Alzaed, A.N. Effect of Iron Filings in Concrete Compression and Tensile Strength. International Journal of Recent Development in Engineering and Technology. 2014. Vol. 3. No. 4, October.
3. Familusi, A.O., Ogundare, D.A., Adewumi, B.E., Alao, M.O. Use of quarry dust and iron filings in concrete production. 5th National Conference on Engineering Technology Held at Federal Polytechnic Offa, February, 2018.
4. Kim, J., Heo, Y., Noguchi, T. Effect of Iron Powder on Inhibition of Carbonation Process in Cementitious Materials. ISIJ International. 2015. 55(7). Pp. 1522–1530.
5. Olutoge, F.A., Onugba, M.A.O., Ocholi, A. Strength Properties of Concrete Produced With Iron Filings as Sand Replacement. British Journal of Applied Science & Technology. 2016. 18(3).
6. Ghannam, S., Najim, H., Vasconez, R. Experimental study of concrete made with granite and iron powder as partial replacement of sand. Sustainable Materials and Technology. 2016. 9. Pp. 1–9.

7. Noori, K.M.G., Ibrahim, H.H. Mechanical Properties of Concrete Using Iron Waste as a Partial Replacement of Sand. 4th International Engineering Conference on Developments in Civil & Computer Engineering, 2018. Pp. 204–215.
8. Vasudevan, G. Performance on Used Iron Sand as Concrete Admixture, 3rd International Conference on Civil, Biological and Environmental Engineering (CBEE-2016) Feb. 4–5, 2016 Bali (Indonesia), 2016. Pp. 10–13.
9. Ahmad, S., Zubair, A., Maslehuddin, M. Effect of the keymixture parameters on shrinkage of reactive powder concrete. Hindawi Publishing Corporation: Scientific World Journal. 2014. Pp. 1–8.
10. Bagheri, A.R., Zanganeh, H., Moalemi, M.M. Mechanical and durability properties of ternary concretes containing silica fume and low reactivity blast furnace slag. Cement and Concrete Composites 2012. 34(5). Pp. 663–670.
11. Almusallam, A.A., Maslehuddin, M., Abdul-Waris, M., Khan, M.M. Effect of mix proportions on plastic shrinkage cracking of concrete in hot environments. Construction and Building Materials Ž. 1998. 12. Pp. 353–358.
12. Brooks, J.J., Megat Johari, M.A. Effect of metakaolin on creep and shrinkage of concrete. Cement & Concrete Composites. 2001. 23. Pp. 495–502.
13. Güneyisi, E., Gesoğlu, M., Mermerdaş, K. Improving strength, drying shrinkage, and pore structure of concrete using metakaolin. Materials and Structures. 2008. 41(5). Pp. 937–949.
14. Cartwright, C., Rajabipour, F., Radlińska, A. Shrinkage Characteristics of Alkali-Activated Slag Cements, Third International Conference on Sustainable Construction Materials and Technologies, August 18 – August 21 2013, Kyoto Research Park, Kyoto, Japan, 2013. Pp. 1–9.
15. Collins, F., Sanjayan, J.G. Effect of pore size distribution on drying shrinkage of alkali-activated slag concrete. Cement and Concrete Research. 2000. 30. Pp. 1401–1406.
16. Jankovic, D. Study of 'real' shrinkage by ESEM observations and digital image analysis, repository.tudelft.nl. 2007. Pp. 1–6..
17. Wang, K., Schlorholtz, S.M., Sriharan, S., Seneviratne, H., Wang X., Hou, Q. Investigation into shrinkage of high-performance concrete used for iowa bridge decks and overlays, Paper 22. Trans Project Reports. 2013. Pp. 1–141.
18. Jin, F., Gu, K., Al-Tabbaa, A. Strength and drying shrinkage of reactive MgO modified alkali-activated slag paste. Construction and Building Materials. 2014. 51. Pp. 395–404.
19. Kani, E.N., Allahverdi, A. Investigating shrinkage changes of natural pozzolan based geopolymer cement paste. Iranian Journal of Material Science. 2011. 8(3). Pp. 50–60.
20. Wallah, S.E. Drying shrinkage of heat-cured fly ash-based geopolymer concrete, World applied Science. 2009. 3(12). Pp. 12–21.
21. Kim, J.K., Lee C.-S. Prediction of differential drying shrinkage in concrete. Cement and Concrete Research. 1998. 28(7). Pp. 985–994
22. Slowik, V., Ju, J.W. Discrete modeling of plastic cement paste subjected to drying, in: e.a.e. B. H. Oh (Ed.) Fracture Mechanics of Concrete and Concrete Structures-Recent Advances in Fracture Mechanics of Concrete Korea Concrete Institute, 2010. Pp. 1–6.
23. Tam, C.M., Tam, V.W.Y., Ng, K.M. Assessing drying shrinkage and water permeability of reactive powder concrete produced in Hong Kong. Construction and Building Materials. 2012. 26(1). Pp. 79–89.
24. Tangchirapat, W., Jaturapitakkul, C. Strength, drying shrinkage, and water permeability of concrete incorporating ground palm oil fuel ash. Cement and Concrete Composites. 2010. 32(10). Pp. 767–774.
25. ASTM C150 / C150M-16e1, Standard Specification for Portland Cement, ASTM International, West Conshohocken, PA, 2016, www.astm.org
26. Yusuf, M.O., Megat, Johari, Ahmad, M.A., Arifin, Z.A., Maslehuddin M. Effects of addition of Al(OH)₃ on the strength of alkaline activated ground blast furnace slag-ultrafine palm oil fuel ash (AAGU) based binder. Construction and Building Materials. 2014. 50 (0). Pp. 361–367.
27. Yusuf, M.O., Megat, Johari, Ahmad, M.A., Arifin, Z.A., Maslehuddin M. Effects of H₂O/Na₂O molar ratio on the Strength of Alkaline Activated Ground Blast Furnace Slag-Ultrafine Palm Oil Fuel Ash Based Concrete. Materials & Design. 2014. 56(0). Pp. 158–164.
28. ASTM C-1437, Standard Test Method for Flow of Hydraulic Cement Mortar, American Society for Testing and Materials, ASTM International, West Conshohocken, PA, www.astm.org, 2013.
29. ASTM C-33, Standard specification for concrete aggregate, American Society for Testing and Materials, ASTM International, West Conshohocken, PA, www.astm.org, 2001.
30. Yusuf, M.O., Megat Johari, M.A., Ahmad, Z.A., Maslehuddin, M. Shrinkage and strength of alkaline activated ground steel slag/ultrafine palm oil fuel ash pastes and mortars. Materials & Design. 2014. 63. Pp. 710–718.
31. Scherer, G.W. Aging and drying of gels. Journal of Non-Crystalline Solids. 1988. 100. Pp. 77–92.
32. Adamson, A.W., Gast, A.P. Physical Chemistry of Surfaces, 6th Ed., Wiley-Interscience. New York, 1997.
33. Collins, F.G., Sanjayan, J.G. Workability and mechanical properties of alkali activated slag concrete. Cement and Concrete Research. 1999. 29. Pp 455–458.
34. Sagoe-Crenstil, K., Brown, T., Taylor A. Drying shrinkage and creep performance of geopolymer concrete. Journal of Sustainable Cement- A. Based Materials. 2013. 2(1). Pp. 35–42.

Contacts:

Moruf Yusuf, +966598373550; moruf@uhb.edu.sa



DOI: 10.18720/MCE.91.3

Heat transfer and thermal shock of recycled glass concrete

Y.S. Al Rjoub*, **M.F. Tamimi**

Jordan University of Science and Technology, Irbid, Jordan

*E-mail: ysalrjoub@just.edu.jo

Keywords: thermal shock, recycled glass concrete, heat transfer, residual strength, cracks

Abstract. In this paper, an experimental study is carried out to investigate the effect of thermal shock on the mechanical properties of recycled glass concrete exposed to temperatures between 150 °C to 600 °C due to rapid cooling regimes, namely, natural cooling, spraying water, using CO₂ fire extinguishers, and immersion in water. The amount of waste glass replacement of fine aggregate resulting in optimal compressive strength is studied and then used in all specimens. The heat transfer in recycled glass concrete exposed to 600 °C for one hour using an electric furnace is studied, with the results validated via a finite element model. It is found that recycled glass can enhance the residual strength and reduce the severity of cracks in concrete subjected to thermal shock caused by rapid cooling from temperatures up to 600 °C to room temperature. Using recycled glass in concrete decreases temperature rise with time when exposed to elevated temperatures. The results obtained show that replacing 25 % of fine aggregate with recycled glass gives the maximum value of compressive strength. Compared with natural cooling, thermal shock generated by fast cooling regimes causes more severe damage to concrete, in terms of greater losses in compressive and tensile splitting strength and crack severity. Among the eight cooling regimes used in this study, natural cooling in air maintained a relatively higher value of residual compressive strength, while the highest reduction in strength was observed when using CO₂ fire extinguishers. Tensile splitting strength shows the same trend.

1. Introduction

Millions of tons of waste glass are being generated annually all over the world. In the concrete industry, recycled glass has received remarkable attention because of it being one such by-product. The world is encouraging the use of recycled glass in concrete not only for its environmental benefits, such as reduction of landfill space and consumption of raw materials, but also to reduce industry costs. Glass provides several beneficial mechanical properties when used in concrete. Hitherto, its implementation as a substitute for fine aggregate has demonstrated equivalent concrete strength. Using recycled glass as a concrete component is new technology that needs more study and investigation to promote this application and confidently introduce recycled glass to the construction market as an alternative to primary material [1]. Recycled glass can be used in many engineering applications, such as water filtration, grit plastering, sand cover for sport turf, and sand replacement in concrete [2]. Many studies have shown that recycled glass crushed to different sizes can be used as fine aggregate without compromising concrete strength.

Concrete design used to rely heavily on assuring a load bearing capacity, sufficient to withstand ultimate loading conditions, both short and long-term [3, 4]. However, as the concrete industry advances, concrete standards and design codes are shifting towards safety assurance and risk control. From this perspective, concrete to be used in structural applications must satisfy various fire safety requirements [5–7]. Providentially, concrete is a multi-phase material, that is, when its main constituent materials (i.e., cement and aggregate) are chemically combined, it forms an inert material with a marginal thermal conductivity, high heat capacity and, thus, an inherent resilience against fire [8, 9]. This allows concrete to be unsurpassed in fire resistance as a bearing structural material.

Al Rjoub, Y.S., Tamimi, M.F. Heat transfer and thermal shock of recycled glass concrete. Magazine of Civil Engineering. 2019. 91(7). Pp. 27–38. DOI: 10.18720/MCE.91.3

Аль Раджаб Ю.С., Тамини М.Ф. Теплопередача и тепловой удар переработанного стеклобетона // Инженерно-строительный журнал. 2019. № 7(91). С. 27–38. DOI: 10.18720/MCE.91.3



This work is licensed under a CC BY-NC 4.0

Yet, owing to ever-imminent fire jeopardy as the most important risk for structures and their inhabitants, [10–12], and due to the ubiquitous use of concrete as a construction material, there is a growing demand to understand the effect of fire on concrete properties and behavior. Hitherto, several studies have shown that recycled glass can be used as fine aggregate without compromising concrete strength, but very little research has been carried out on the thermal properties of recycled glass concrete.

A significant amount of investigation has been carried out worldwide focusing on the recycling of waste concrete. An experimental study evaluated different proportions of crushed glass replacing fine aggregate in concrete in [13]. The results show that a 40 % proportion of glass as fine aggregate gives the highest compressive and tensile strength. The effect of using glass as a pozzolanic material in concrete using waste glass powder as a partial replacement for cement is studied by [14]. It is found that 10 % of cement replaced by waste glass yields the highest 28-day compressive strength compared to plain concrete. This percentage increases to 15 % for tensile splitting strength.

Most researchers have studied concrete failure, the mix design process, and concrete mechanical properties [15]. Only a few researchers have investigated the mechanical properties of recycled concrete at high temperatures. The authors of [16] were some of the pioneers who studied the residual compressive strength of recycled aggregate concrete at high temperatures. Another investigation done by [17] studied the effects of using recycled glass as a partial replacement for fine and coarse aggregates on the properties of concrete at elevated temperatures. They concluded that the compressive strength of recycled glass concrete decreased up to 20 % from its original value with elevated temperatures up to 700 °C. Concrete made with 10 % of coarse aggregate replaced by glass, as compared to natural coarse aggregate replacement, had better properties in the fresh and hardened concrete states at ambient and high temperatures than those with larger replacement percentages [18].

Many investigations have shown that the cooling process of concrete after exposure to elevated temperatures, followed by severe moisture loss, results in extensive micro-crack formation and propagation, which further decreases the residual strength. Therefore, it is evident that the residual strength of concrete is much lower than what appears in a hot-strength test [11]. For assessing post-exposure residual properties, the unstressed, residual-strength tests are considered more appropriate for simulating post-fire-extinguishment concrete properties [11, 19, 20]. It has since become customary to perform concrete strength experimentation subsequent to a sample's slow-cooling process. Hence, most of the extant research refers to experimental results of such residual-strength tests. The mechanical properties of engineered, cementitious composites subjected to elevated temperatures up to 800 °C using two cooling methods, quenching in water and cooling in air, are studied by [21–23]. The results show that the compressive and ultimate strengths increase up to a temperature of 200 °C and decrease beyond that temperature. The cooling regime of quenching in water aided the strength and stiffness recovery. The mechanical properties of concrete subjected to high temperatures and air-cooled are studied by [24]. The effect of cooling on high-strength/high-performance concrete (HSC/HPC) for a temperature range greater than 800 °C is studied by [25]. It was found that there is no effect at temperatures above 800 °C. The effect of thermal shock due to rapid cooling on the mechanical properties of fiber-reinforced concrete exposed to elevated temperatures is discussed in [20]. Natural cooling and quenching in water methods were used. The results from this experimental work show that thermal shock induced by water quenching causes more severe damage to concrete, compared to natural cooling. The difference in effect on the compressive strength of HPC between quick cooling (quenching) and slow cooling in air is done in [26]. Concrete was subjected to temperatures of 100 °C, 200 °C, 400 °C, and 600 °C. It was clear that the loss in compressive strength was more pronounced under quick cooling than slow cooling. The effect of quick cooling is dependent on a certain porosity of calcium-silicate-hydrate (C-S-H) gel. The degree of micro-cracking that exists after a certain temperature exposure is owing to the magnitude, duration, and rate of heating. Application of recycled glass as aggregate in concrete materials can offer significant economic and environmental benefits, provided that the alkali-silica reaction (ASR) of glass in concrete is properly controlled. Many papers discuss the use of glass sand in concrete and show that the reactivity of glass is influenced by its particle size. The use of waste glass in concrete has been avoided on the grounds that it is known to undergo a harmful ASR, but using glass as fine aggregate with particles smaller than 0.6 mm, passing the #30 sieve, does not produce deleterious ASR expansion within the time frame of the measurements [27]. In this study, most of the glass is very fine: 84 % of the glass used passes sieve #30 (0.595 mm).

To the authors' knowledge, there is no previous research showing the effects of thermal shock due to fast cooling, such as quenching in water, CO₂ fire extinguishers, and spraying water for different durations, on the residual mechanical properties of recycled glass concrete. In this paper, the effect of using recycled glass in concrete as a partial replacement for fine aggregate on heat transfer (through measuring the maximum temperature developed at different locations inside the concrete specimen) is investigated experimentally and validated using ABAQUS finite element modeling software. The FE model was also used to study heat flow inside the concrete specimens.

2. Methods

2.1. Experimental details

2.1.1 Raw materials

In this study, the concrete mixture used consisted of cement, fine aggregate, coarse aggregate, recycled glass as partial replacement for fine aggregate, and super plasticizer, to obtain the required workability. These materials were mixed at specific ratios to get a consistent mixture. The cement used in the production of all specimens was ordinary Type 1 Portland cement, manufactured in Jordan. The coarse aggregates used were brought from local suppliers. The coarse aggregate was of angular nature, with a 19 mm nominal maximum aggregate size. The fine aggregate was in the form of river sand. Super plasticizer with 1 %-2.5 % cement content was used as a water-reducing agent to maintain slump between 70 to 100mm. The specific gravity, absorption, and unit weight were obtained according to the ASTM C128-88 test method, as shown in Table 1. Glass in this experiment was collected from waste glass in Irbid, Jordan. The glass underwent crushing and milling in order to create a fine aggregate. The chemical composition of the waste glass aggregate can be seen in Table 2. The gradation of glass and fine aggregate is presented in Table 3.

Table 1. Physical properties of aggregate.

Properties	Type of aggregate		
	Coarse	Fine	Waste glass
Bulk Specific Gravity (BSG, Dry)	2.46	2.56	2.11
Fineness Modulus (FM)	-	2.99	2.42
Absorption (%)	0.58	0.45	0.4
Unit Weight (UW)	1455	1650	1320

Table 2. Chemical composition of waste glass.

Chemical composition of waste glass (%)								
SiO ₂	Al ₂ O ₃	Fe ₂ O ₂	CaO	MgO	SO ₃	Na ₂ O	K ₂ O	Cr ₂ O ₃
68.5	1.66	0.52	13.15	2.45	0.43	11.99	0.8	0.5

Table 3. Sieving analysis of fine aggregate and recycled glass.

Sieve size	Accumulated passing %	
	Waste glass	Fine aggregate
4.75 mm	100	100
2.36 mm	94	97.25
1.18 mm	89	92.12
600 μm	53	45.25
425 μm	32	34.22
300 μm	22	25.25
150 μm	1.25	2.25
75 μm	0.35	0.78

2.1.2. Experimental procedures

The experimental procedures were divided into three main parts. The first part determined the optimum waste glass content as a partial replacement for fine aggregate based on 28-day compressive strength. This optimum value was then used for all specimens. The second part included the heating process and various cooling methods. The third part was testing, encompassing compressive and tensile strength measurement, and crack formation observation. Table 4 shows the mix proportions used in this study: the control concrete mixture (containing 100 % fine aggregate without any recycled glass) and the concrete mixture containing waste glass content of 5 %, 10 %, 15 %, 20 %, 25 %, 30 %, 35 %, and 40 % (by weight of fine aggregate) as partial replacement for fine aggregate. The waste glass content that exhibited the highest compressive strength was then used to investigate its resistance to thermal shock and compare its efficiency to the control mixture. The specimens were exposed to temperatures of 150 °C, 200 °C, 400 °C, and 600 °C in an electric furnace, as shown in Figure 1. The specimens remained in the furnace at the target temperature for 2 hours, to ensure that the centers of the samples reached the target temperature. This duration was chosen based on many experimental trials. All specimens were subjected to various cooling regimes, as given in Table 5, until reaching room temperature again. For each cooling method, three cubes, with dimensions of 150x150x150 mm, were tested for each compressive strength and recycled glass concrete content, and three cylinders with dimensions of 100 mm in diameter and 200 mm in height were used for tensile splitting strength determinations. After the specimens cooled to room temperature, compressive strength, tensile splitting strength, and crack dimensions were measured, respectively. It should be mentioned here that the value of strength obtained in this study is an average value of the three specimens. In order to analyze the visible cracks in the cube specimens, the face that had the highest severity of cracking was selected. Then, those surfaces were washed with water and dried in an

oven at 50 °C for 8 hours. This temperature is used to avoid generating any new cracks or damage. A digital camera was used to take photographs of each of the selected faces. The last step aimed to calculate the distribution of cracks in each image by retouching the cracks in Adobe Photoshop using a pencil tool with a 4-pixel width to make crack recognition and detection easier.

Table 4. Mix proportions of concrete mixture containing waste glass.

Contents	Glass replacement percentage								
	0	5	10	15	20	25	30	35	40
Water (kg)	190	190	190	190	190	190	190	190	190
Cement (kg)	458	458	458	458	458	458	458	458	458
Coarse aggregate (kg)	952	952	952	952	952	952	952	952	952
Fine aggregate (kg)	750	712.5	675	637.5	600	562.5	525	487.5	450
Waste Glass (kg)	0	37.5	75	112.5	150	187.5	225	262.5	300

2.2. Temperature profile inside the specimens

The main objective of this work is to develop a model based on the finite element method using ABAQUS software in order to demonstrate the accuracy with which this model can predict the effect of using different percentages of recycled glass as a partial replacement for fine aggregate on the maximum temperature developed at different locations inside the specimen. The concrete specimens have dimensions of 150×150×150 mm. These specimens were exposed to a temperature of 600 °C for one hour. The temperature developed at the surface and at the centroid of the cube (7.5 cm in depth) were then measured. The geometry of the model and temperature measurement locations are shown in Figure 2.



Figure 1. Electric furnace.

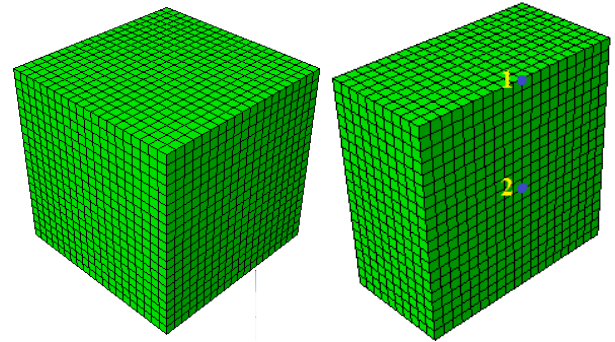


Figure 2. Finite element model and temperature measurement locations.

Table 5. Cooling regimes for heated concrete.

Cooling Regime	First stage	Second stage
CO ₂ Fire Extinguisher	5 seconds	Natural cooling
	10 seconds	
	20 seconds	
Water Spraying	5 minute	Natural cooling
	10 minutes	
	20 minutes	
Water Quenching	24 hours	-
Natural Cooling at Room Temperature	Natural cooling	Natural cooling

The models were built using ABAQUS, version 6.14. The software offers a wide range of solvers: standard, coupled temperature-displacement, risk analysis, implicit, explicit, among others. In this work, the appropriate solver was the coupled temperature-displacement solver. The ABAQUS modeling space can be 2D or 3D, depending on the complexity of the case. Additionally, the software provides a wide range of shapes, such as, solid, shell, wire, and point. In this paper, the modeling space for all parts is 3D. The element type is C3D8R, which indicates a 3D solid element with 8 nodes per element.

This part presents experimental work and finite element modeling of concrete cubes that have the same properties as the specimens used in the thermal shock experiment, namely, normal concrete, and recycled glass concrete. The difference between the two types of concrete is based on the material properties. Table 6 shows the properties of both normal and recycled glass concrete.

The results of the analyses will be compared to the experimental results. The typical cube specimen with thermocouples is shown in Figure 3. Thermocouples were cast at the centroid of the cubes, i.e., at a depth of 7.5 cm. These results were compared to the finite element results.

Table 6. Properties of plain and recycled glass concrete.

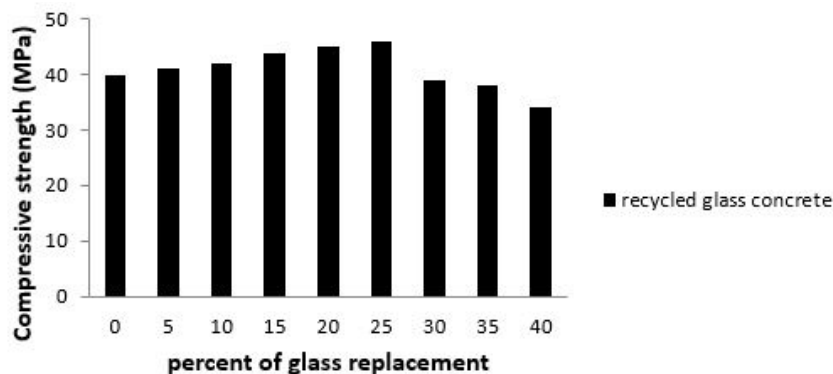
Material	Recycled glass replacement percentage of Fine-Agg., %(By mass)	Compressive strength, N/mm ² (Ksi)	Tensile strength, N/mm ² (Ksi)	Thermal conductivity, W/mK (BTU/hr-ft. ² °F)	Coefficient of thermal expansion	Modules of elasticity, KN/mm ² (Ksi)	Density, Kg/m ³ (pcf)
Plain Concrete, [28]	0	40 (6.1)	4.1	1.3 (0.75)	12*10-6	39.3 (5.7)	2450 (153)
Recycled glass Concrete, [29]	25	46 (6.5)	3.9	1.05 (0.61)	1.2*10-6	39.3 (5.7)	2385 (149)

**Figure 3. Photograph of a typical cube specimen with thermocouple used at the surface and centroid of the cubes.**

3. Results and Discussion

3.1. The optimum content of recycled glass

The optimum content of recycled glass as a partial replacement for fine aggregate was selected based on the maximum compressive strength after 28 days of curing in water. Different percentages of glass by weight of fine aggregate (5, % 10 %, 15 %, 20 %, 25 %, 30 %, 35 %, and 40 %) were used and tested. It can be seen from Figure 4 that the optimum value of recycled glass was 25 %, which gives a compressive strength of 46 MPa, compared to 40 MPa for plain concrete. This can be explained due to the angular nature of glass aggregate, which gives it a greater surface area than fine aggregate. When the glass percentage exceeded 25 %, the compressive strength decreased. This is because higher proportions of glass mean insufficient cement paste in the mix to facilitate bonding between particles, which creates microscopic voids, which adversely affect concrete strength [29]. This optimal percentage does not match that in the literature, [13], because 10 % crushed glass was used in the literature as a partial replacement for coarse aggregate. This percent was based on [14], who studied the effect of using recycled glass as a partial replacement for cement, while this study examines the effect of using recycled glass as a partial replacement for fine aggregate.

**Figure 4. Compressive strength development of concrete containing recycled glass.**

3.2. The effect of thermal shock on residual compressive strength

The compressive strength and reduction in compressive strength of recycled glass concrete and plain concrete exposed to temperatures between 150 °C and 600 °C for two hours, followed by different cooling regimes, fast and air cooling, is shown in Figures 5 and 6. For both types of concrete, the residual compressive strength of concrete was significantly influenced by the cooling regimen when the temperature exceeded 150 °C. Also, for all exposures, as the temperature increased from room temperature, the compressive strength

increased up to 150 °C for all cooling regimes. It can be seen that at a temperature of 150 °C, the compressive strength of recycled glass and plain concrete are higher than those at room temperature, since additional hydration of residual cement is activated. The percent increase of the compressive strength of recycled glass concrete is more than that of plain concrete. As the temperature surpasses 150 °C, the strength decreases. This is due to a decrease in calcium hydroxide content, as well as the shrinking of an unhydrated area function, which is detrimental to the microstructure. At 200 °C, the compressive strength of plain concrete decreased for all cooling methods, except using natural cooling and spraying water for 5 minutes. The compressive strength was 46 and 42 MPa, respectively. The compressive strength of the recycled glass concrete decreased when the specimens were cooled using a CO₂ fire extinguisher for 10 seconds or more and by immersion in water, while the rest of the cooling regimes increased the compressive strength by percentages ranging from 3.5 to 20 %. From 400 °C to 600 °C, the residual compressive strength of the plain and recycled glass concrete specimens decreased for all cooling regimes. The highest reductions in compressive strength were caused by the use of a CO₂ fire extinguisher for 20 seconds, immersion in water, and a CO₂ fire extinguisher for 10 seconds, respectively. The results show that the reduction increases with an increase in the time of use of the CO₂ fire extinguisher. Also, it can be seen that the reduction in strength due to air cooling (natural cooling) for the two types of concrete is always lower than that due to fast cooling. It should be noted here that all the cooling methods can be classified as fast cooling methods, except air cooling (natural cooling). The reduction in compressive strength of recycled glass concrete was less than the reduction for plain concrete for all temperatures and for all cooling methods, since glass has a lower thermal conductivity than fine aggregate and absorbs less heat, due to its low specific heat. Also, the thermal incompatibility of the various components, initial moisture content, and permeability index of recycled glass concrete are higher than those of plain concrete. Using CO₂ fire extinguishers causes the largest reduction in compressive strength because the CO₂ is compressed at a very low temperature, generally -76 °C, which leads the thermal gradient to be very high, causing the concrete sample to undergo increased expansion.

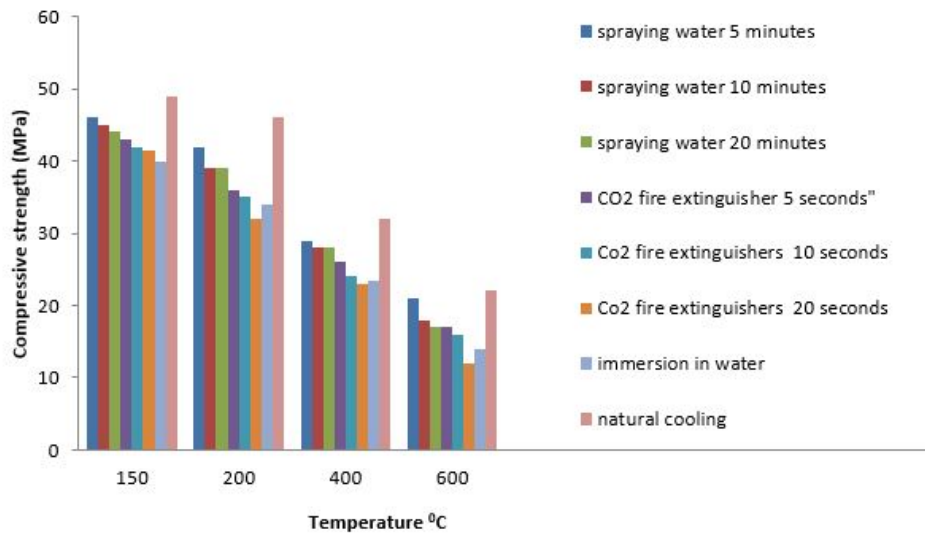


Figure 5. Bar chart for the residual compressive strength of plain concrete.

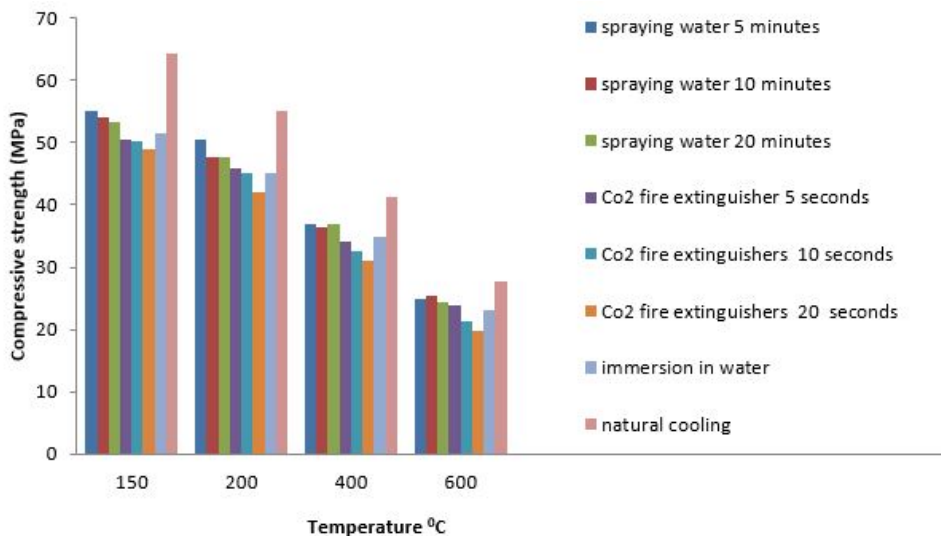


Figure 6. Bar chart for the residual compressive strength of recycled glass concrete.

3.3. The effect of thermal shock on residual tensile splitting strength

The residual tensile splitting results for the two types of concrete - plain and recycled glass concrete - subjected to elevated temperatures under various cooling regimes are presented in Figures 7 and 8. As previously observed, the residual tensile splitting strength due to natural cooling is higher than the other cooling methods for all temperatures for both types of concrete. Also, it is shown that, for all exposures, as the temperature increases from room temperature, the tensile splitting strength increases up to 150 °C, for all cooling regimes. At 200 °C, the tensile splitting strength of plain concrete for all cooling methods increased or remained constant by percentages ranging from 0 to 31 %, except when the specimens were cooled with a CO₂ fire extinguisher for 10 or 20 seconds. The tensile splitting strengths of those two cases were 3.2 and 3.1MPa, respectively, a decrease from the control sample of 8.5 % and 11.4 %, respectively. The tensile splitting strength of the recycled glass concrete decreased at 200 °C when the specimens were cooled with a CO₂ fire extinguisher for 20 seconds. The tensile splitting strength for this case was 4.11 MPa, a reduction of 2 %, while the rest of cooling regimes increased the tensile splitting strength from 0 to 36 %. For temperatures from 400 °C to 600 °C, the same conclusions can be made as in the compressive strength section. The reduction in tensile splitting due to fast cooling was more than natural cooling. This can be explained as in [30]: fast cooling produces residual stress between the outer and inner core of the concrete that creates micro-cracks in the core. It can also be seen that concrete containing recycled glass experienced less of a reduction in tensile splitting strength than plain concrete. This is because glass has a lower thermal conductivity than fine aggregate and sand.

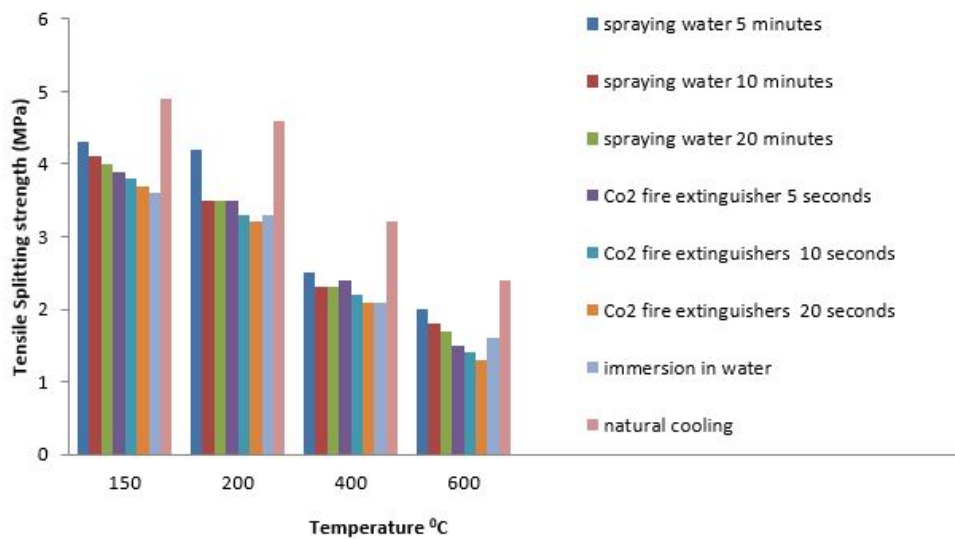


Figure 7. Bar chart for the residual tensile splitting strength of plain concrete.

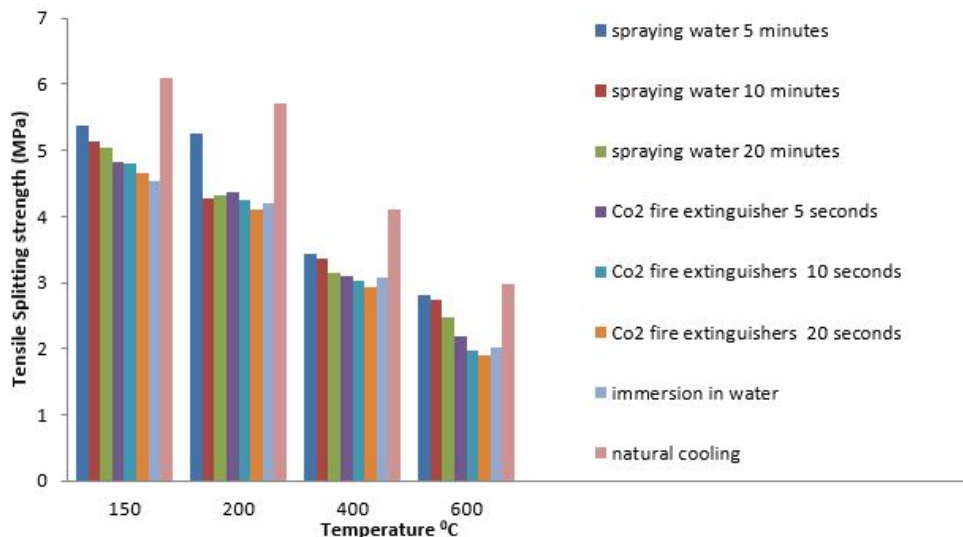


Figure 8. Bar chart for the residual tensile splitting strength of recycled glass concrete.

3.4. Crack formation

Figures 9, 10, and 11 show visible cracks in plain concrete and recycled glass concrete caused by heating and cooling processes for temperatures of 200 °C, 400 °C, and 600 °C, respectively. It is observed that there are noticeable effects on the crack length and density depending on the mixture. The cracks that were formed in the recycled glass concrete cube are less severe than those in the plain concrete for all

exposure temperatures. Crack depth was not considered in this experiment. The severity of the cracks depends on the exposure to heat, with the effect of the cooling regime becoming obvious above 400 °C. The severity of the cracks at 200 °C for all cooling regimes is very low and increases with an increase in temperature, until reaching maximum severity at 600 °C. In terms of the effect of cooling methods on crack development, it can be seen that immersing the samples in water, spraying water for 20 minutes, and using a CO₂ fire extinguisher for 20 seconds cause more severe cracking than the other cooling methods. Natural cooling, spraying water for 5 minutes, and using a CO₂ fire extinguisher for 5 seconds cause less severe cracking. Cracks developed in the recycled glass concrete specimens are less severe than those in plain concrete for the same temperature exposure and same cooling regime.

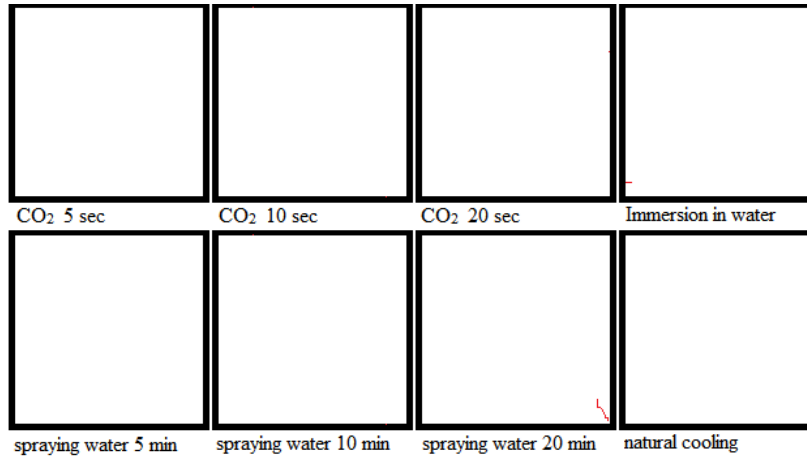


Figure 9(a). Retouched images of cracks developed at the surface of plain concrete specimens at 200 °C.

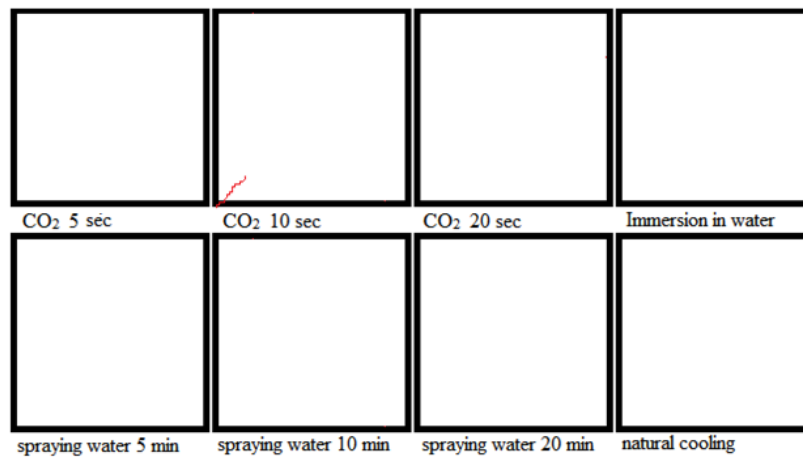


Figure 9(b). Retouched images of cracks developed at the surface of recycled glass concrete specimens at 200 °C.

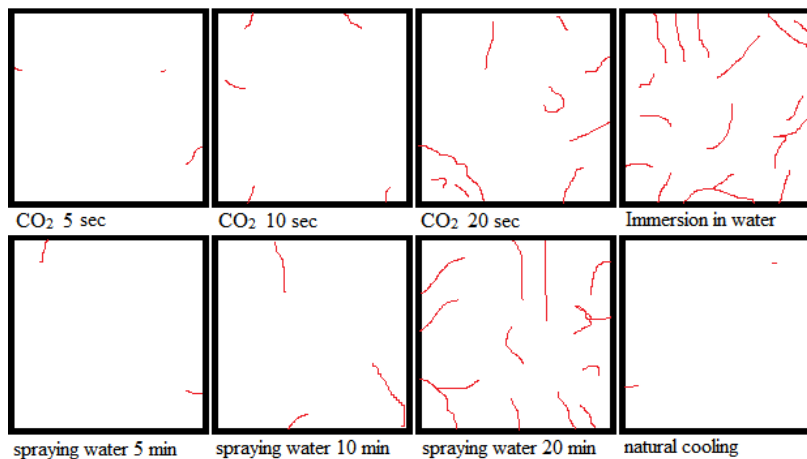


Figure 10(a). Retouched images of cracks developed at the surface of plain concrete specimens at 400 °C.

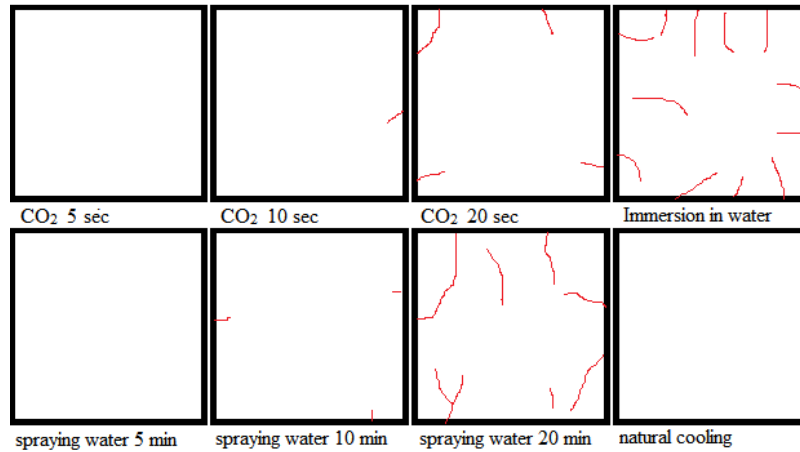


Figure 10(b). Retouched images of cracks developed at the surface of recycled glass concrete specimens at 400 °C.

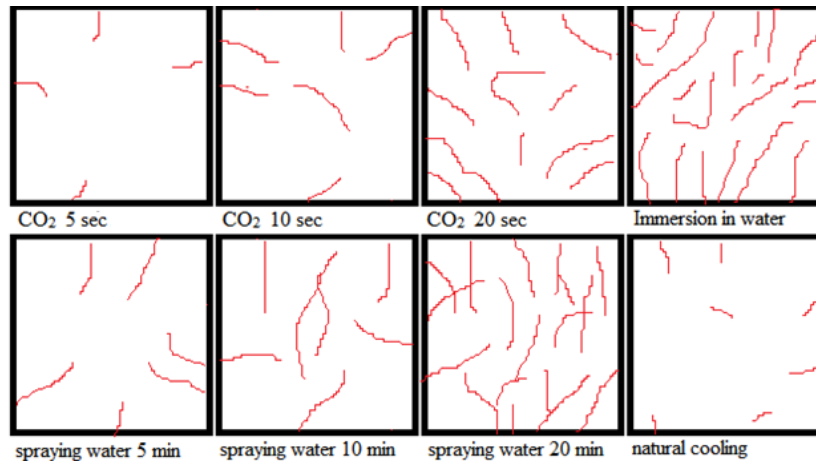


Figure 11(a). Retouched images of cracks developed at the surface of plain concrete specimens at 600 °C.

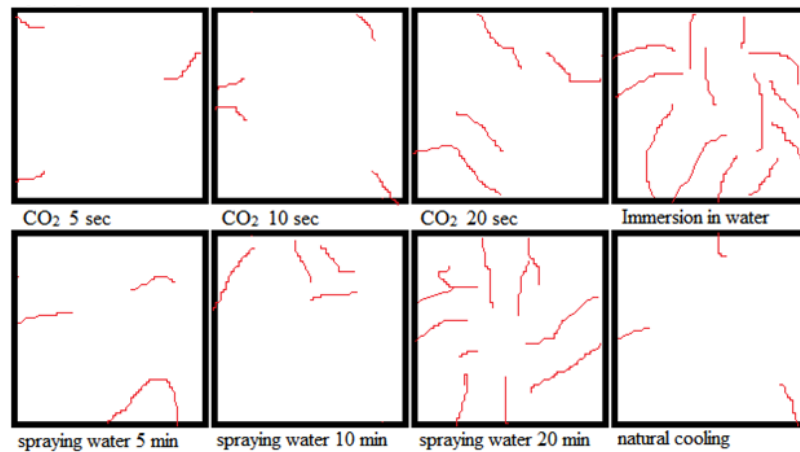


Figure 11(b). Retouched images of cracks developed at the surface of recycled glass concrete specimens at 600 °C.

3.5. Temperature profile over time

The temperature profile at the surface and at the centroid of the plain concrete specimen and recycled glass concrete are shown in Figures 12 and 13, respectively. It can be seen that the temperature rises more slowly at the surface and centroid of the recycled glass concrete specimens than plain concrete. This is because glass as aggregate exhibits better temperature stability, owing to a lower specific heat than sand and due to the pozzolanic activity of glass. In addition, the fine recycled glass concrete mixes have lower thermal conductivity coefficients when compared to normal concrete. The lower thermal conductivity of recycled aggregate concrete is due to the lower density and thermal conductivity of these aggregates.

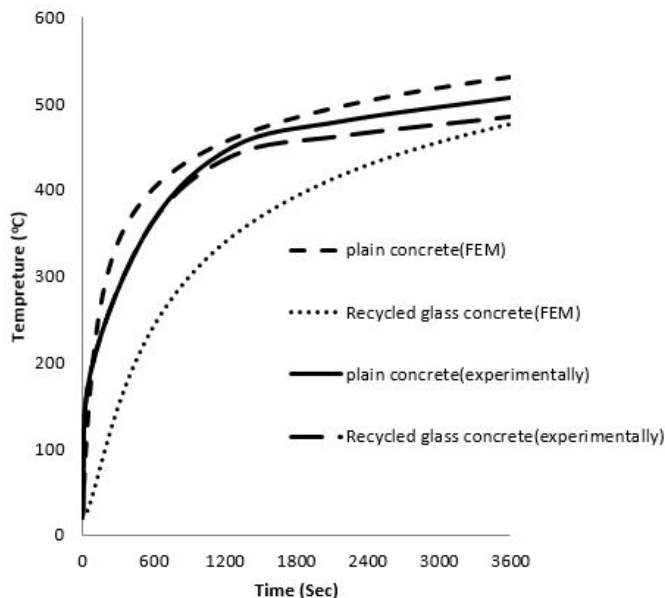


Figure 12. Temperature profiles over time at the specimen surface.

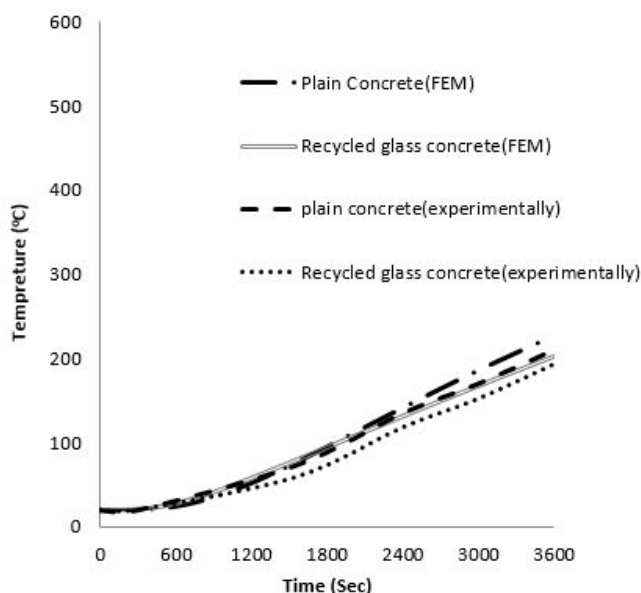


Figure 13. Temperatures profiles over time at the specimen centroid.

The maximum temperatures developed at the surface and centroid of plain concrete and recycled glass concrete after one hour were 515 °C, 226 °C, and 476 °C, 202 °C, respectively. The FE model predicted temperatures of 507 °C, 210 °C and 485 °C, 193 °C. The FEM curve and the experimental results for the two types of concrete generally agree.

4. Conclusions

This study was conducted in order to investigate the effectiveness of recycled glass as a partial replacement for fine aggregate on enhancing the resistance of concrete to thermal shock, as well as its effect on the thermal conductivity of concrete. To achieve this, a series of cubes and cylinders were cast and cured and exposed to high temperatures in an electric furnace, 150 °C, 200 °C, 400 °C, and 600 °C. The specimens remain in the furnace at the target temperature for two hours. After exposure to high temperatures, the specimens were subjected to various cooling regimes: CO₂ fire extinguishers, water spraying, water quenching, and natural cooling in room temperature, which is the control specimen. For each cooling method, six cubes were tested for compressive strength - three normal concrete and three recycled glass concrete. Six cylinders (three of normal concrete and three of recycled glass concrete) were tested for tensile splitting strength. In addition, the effect of using recycled glass as a partial replacement for fine aggregate on the maximum temperature developed at different locations inside a cube specimen heated in an electric furnace for one hour at 600 °C was investigated. The following conclusions are drawn based on the test results obtained:

1. The optimum replacement percentage of fine aggregate with crushed recycled glass aggregate was determined to be 25 %. For proportions exceeding 25 %, recycled glass negatively impacts compressive strength development.

2. The residual compressive strength increases with increasing temperature, up to 150 °C for all cooling regimes. Above this temperature, there was a reduction in strength and the effect of thermal shock becomes clear. The fast cooling methods lead to more damage in concrete specimens than the slow cooling method (natural cooling), with the highest reduction in residual strength being caused by CO₂ fire extinguishers.

3. In terms of cracking, the severity of cracks at 200 °C for all cooling regimes is very low, but worsens with increased temperature, with maximum severity occurring at 600 °C. The highest severity of cracking is caused by immersing samples in water, spraying water for 20 minutes, and using a CO₂ fire extinguisher for 20 seconds, while specimens subjected to natural cooling, spraying water for 5 minutes, and a CO₂ fire extinguisher for 5 seconds experience the lowest severity.

4. A finite element model was created with ABAQUS software to study the heat transfer inside the concrete specimens. This model was validated with the experimental results. The FEM results show reasonable agreement with the experimental values. The temperature developed on the recycled glass concrete specimens is slightly less than that on plain concrete. Recycled glass as a replacement for 25 % of fine aggregate in the concrete mix showed good results by reducing the maximum temperature developed after one hour by 4.3 % and 22.2 % at the surface and the centroid of the specimens, respectively.

5. Acknowledgments

The authors wish to acknowledge the assistance of the technicians at the civil engineering laboratories at JUST.

References

1. Taha, B., Nounu, G. Properties of concrete contains mixed colour waste recycled glass as sand and cement replacement. *Constr. Build. Mater.* 2008. 22. Pp. 713–720.
2. Carpenter, A., Cramer, S. Mitigation of Alkali-Silica Reaction in Pavement Patch Concrete That Incorporates Highly Reactive Fine Aggregate. *Transp. Res. Rec. J. Transp. Res.* 1999. Board 1668. Pp. 60–67. DOI: 10.3141/1668-09.
3. Kennedy, R.P. A review of procedures for the analysis and design of concrete structures to resist missile impact effects. *Nucl. Eng.* 1976. 37. Pp. 183–203.
4. Nilson, A.H., Darwin, D., Dolan, C.W. *Design of concrete structures.* 2010.
5. BS EN, 2004. Eurocode 2 : Design of concrete structures, British Standards Institution.
6. International Code Council, 2011. 2012 International Building Code, 2012th ed. ICC, Country Club Hills, IL
7. Japan Society of Civil Engineers. *Standard Specifications for Concrete Structures, Concrete.* 2007.
8. Gu, X., Jin, X., Zhou, Y. *Basic Principles of Concrete Structures.* 2016. Springer Berlin Heidelberg, Berlin, Heidelberg.
9. Mehta, P.K., Monteiro, P.J.M. *Concrete: microstructure, properties, and materials,* Concrete. 2006.
10. Chan, Y.N., Luo, X., Sun, W. Compressive strength and pore structure of high-performance concrete after exposure to high temperature up to 800 °C. *Cem. Concr. Res.* 2000. 30. Pp. 247–251.
11. Hertz, K.D. Limits of spalling of fire-exposed concrete. *Fire Saf. J.* 2003. 38. Pp. 103–116.
12. Netinger, I., Kesegic, I., Guljas, I. The effect of high temperatures on the mechanical properties of concrete made with different types of aggregates. *Fire Saf. J.* 2011. 46. Pp. 425–430.
13. Dinesh, S., Preetha, R., Subhi, M. Investigation on recycled glass as a replacement for fine aggregate in concrete. *Int. J. Eng. Res. Mod. Educ.* 2017. Pp. 105–108. DOI: 10.5281/zenodo.570519.
14. Anwar, A. The Influence of Waste Glass Powder as a Pozzolanic Material in Concrete. *Int. J. Civ. Eng. Technol.* 2016. 7. Pp. 131–148. ISSN: 2319-4847.
15. Xiao, J., Li, J., Zhang, C. Mechanical properties of recycled aggregate concrete under uniaxial loading. *Cem. Concr. Res.* 2005. 35. Pp. 1187–1194.
16. Teranishi, K., Doshio, Y., Narikawa, M., Kikuchi, M. Application on recycled aggregate concrete for structural concrete, Part 3 – Production of recycled aggregate by real-scale plant and quality of recycled aggregate concrete, *Sustainable Construction: Use of Recycled Concrete Aggregate.* London, UK. 1998.
17. Terro, M.J. Properties of concrete made with recycled crushed glass at elevated temperatures. *Build. Environ.* 2006. 41. Pp. 633–639.
18. Shi, C., Zheng, K. A review on the use of waste glasses in the production of cement and concrete. *Resour. Conserv. Recycl.* 2007. 52. Pp. 234–247.
19. Georgali, B., Tsakiridis, P.E. Microstructure of fire-damaged concrete. A case study. *Cem. Concr. Compos.* 2005. 27. Pp. 255–259.
20. Peng, G.-F., Bian, S.-H., Guo, Z.-Q., Zhao, J., Peng, X.-L., Jiang, Y.-C. Effect of thermal shock due to rapid cooling on residual mechanical properties of fiber concrete exposed to high temperatures. *Constr. Build. Mater.* 2008. 22. Pp. 948–955.
21. Bazant, Z.P., Kaplan, M.F., Bazant, Z.P. *Concrete at High Temperatures: Material Properties and Mathematical Models.* 1996. Addison-Wesley, London.
22. Phan, L.T. *Fire performance of high-strength concrete: State-of-the Art-Report.* Gaithersburg. 1996. P. 105. Gaithersburg, MD.
23. Yu, J., Weng, W., Yu, K. Effect of Different Cooling Regimes on the Mechanical Properties of Cementitious Composites Subjected to High Temperatures. *Sci. World J.* 2014. Pp. 1–7.
24. Sidhu, S.H., Kumar, R.A., S.H., S., Sidhu, R.U. Effect of Thermal Shocks on Compressive Strength of Heated Concrete Cooled In Air. *Int. J. Eng. Technol. Manag. Appl. Sci.* 2014. 2. Pp. 37–40.
25. Luo, X., Sun, W., Chan, S.Y.N. Effect of heating and cooling regimes on residual strength and microstructure of normal strength and high-performance concrete. *Cem. Concr. Res.* 2000. 30. Pp. 379–383.

26. Balendran, R.V., Tang, W.C., Nadeem, A., Kamineni, P.R., Maqsood, T. Effect of cooling methods on residual compressive strength of high performance concrete (HPC) subjected to elevated temperatures. In: 28th Conference on Our World in Concrete & Structures: 28–29. Singapore, 2003. Pp. 23–24.
27. Rajabipour, F., Maraghechi, H. and Fischer Investigating the Alkali-Silica Reaction of Recycled Glass Aggregates in Concrete Materials. Journal of Materials in Civil Engineering. 2010. 22(12). Pp. 1201–1208.
28. Ali F., Nadjai A., Abu-tair A. Experimental and Numerical Study on Performance of Concrete Slabs Subjected to Severe Fire, Fire Saf. Sci. 2008. 9. Pp. 1255–1266. DOI: 10.3801/IAFSS.FSS.9-1255.
29. Adaway, M., Wang, Y. Recycled glass as a partial replacement for fine aggregate in structural concrete -Effects on compressive strength. Electron. J. Struct. Eng. 2015. 14. Pp. 116–122. ISSN: 1443-9255.
30. Nadeem, A., Memon, S.A., Lo, T.Y. The performance of Fly ash and Metakaolin concrete at elevated temperatures. Constr. Build. Mater. 2014. 62. Pp. 67–76.

Contacts:

Yousef Al Rjoub, +962795204911; ysalrjoub@just.edu.jo

Mohammad Tamimi, +962795204911; mft.tamimi3@hotmail.com

© Al Rjoub, Y.S., Tamimi, M.F., 2019



DOI: 10.18720/MCE.91.4

Dynamics of a physically nonlinear viscoelastic cylindrical shell with a concentrated mass

D.A. Khodzhaev^a, R.A. Abdikarimov^b, M.M. Mirsaidov^a

^a Tashkent Institute of Irrigation and Agricultural Mechanization Engineers, Tashkent, Uzbekistan

^b Tashkent Financial Institute, Tashkent, Uzbekistan

* E-mail: rabdikarimov@mail.ru

Keywords: thin-walled structures, cylindrical shell, viscoelasticity, physical nonlinearity, concentrated mass, axisymmetric oscillations, nonlinear integro-differential equation, relaxation kernel, Bubnov-Galerkin method, numerical method

Abstract. It is known that the theory of linear and nonlinear elastic plates and shells is the most developed part of the theory of elasticity. In this area, the necessary equations are obtained and the methods to solve them are developed. At the same time, there are gaps in considering the viscoelastic properties of a material in the problems of thin-walled structures dynamic calculations. It should be noted that in some publications the viscoelastic properties of the material (i.e. the deviation of material test diagram from Hooke's law) were taken into account according to the Voigt model, not confirmed by experiments. Ignoring viscoelastic properties of the material significantly limits practical applicability of results. The first part of the paper presents the statement and method of solution to the problem of axisymmetric vibrations of a physically nonlinear viscoelastic cylindrical shell with concentrated masses. The function characterizing the deviation of stress intensity curve from the Hooke straight line is taken in the form of cubic nonlinearity. A mathematical model, solution method and computational algorithm were developed for the problem of axisymmetric oscillations of a cylindrical shell with a concentrated mass, taking into account physically nonlinear strain of the material under different boundary conditions in the frame of the Kirchhoff-Love hypothesis. For the study of the effect of a concentrated mass the Dirac delta function was introduced. With the Bubnov-Galerkin method, based on a polynomial approximation of deflections, the problem in question is reduced to the solution, in the general case, of non-decay systems of nonlinear integro-differential equations of Volterra type. To solve the resulting system with the Koltunov-Rzhanitsyn weakly singular kernel, a numerical method was applied based on the use of quadrature formulas. A unified computational algorithm has been developed to determine the deflection of a viscoelastic cylindrical shell with concentrated masses.

1. Introduction

In modern technology, construction and other fields of industry, the structures of more and more complex patterns are being used; to ensure their strength, reliability and high efficiency is a problem of great importance. It is impossible to optimally design them without constructing mathematical models that account for the maximum possible number of factors affecting the efficiency of such structures.

In literature there are a number of publications in which linear and nonlinear problems of thin-walled structures dynamics are considered with and without a concentrated mass. An analysis of these publications shows that little attention has been paid to the features of viscoelastic inhomogeneous systems inertial behavior. In these papers, the problems were considered either using the Voigt's differential model or the Boltzmann-Volterra integral model, where the exponential kernels that could not describe the actual processes occurring in shells and plates at initial point of time were taken in calculations as the relaxation

Khodzhaev, D.A., Abdikarimov, R.A., Mirsaidov, M.M. Dynamics of a physically nonlinear viscoelastic cylindrical shell with a concentrated mass. Magazine of Civil Engineering. 2019. 91(7). Pp. 39–48. DOI: 10.18720/MCE.91.4

Ходжаев Д.А., Абдикаримов Р.А., Мирсаидов М.М. Динамика физически нелинейной вязкоупругой цилиндрической оболочки с сосредоточенными массами // Инженерно-строительный журнал. 2019. № 7(91). С. 39–48. DOI: 10.18720/MCE.91.4



This work is licensed under a [CC BY-NC 4.0](https://creativecommons.org/licenses/by-nc/4.0/)

kernels [1]. The choice of the exponential kernel in calculations was not accidental. The systems of integro-differential equations obtained in calculations were reduced by differentiation to the solution of ordinary differential equations, which, in most cases, were solved by the well-known Runge–Kutta numerical method.

Static studies of viscoelastic materials for creep and relaxation indicate an extremely high intensity of relaxation processes at the initial stage of testing. The process velocity is so high that its direct measurement at the initial moment turns out to be impossible. The processes are considered as dynamic ones and their velocities are conditionally considered equal to infinity [1]. This fact can be described by weakly singular functions, which provide finite strains and stresses, in contrast to strongly singular functions. Such weakly singular functions describe well the velocities of relaxation processes if they contain a sufficient number of parameters. Such kernels include the Koltunov-Rzhanitsyn three-parameter kernel [2].

In practice, the materials are found in which stress σ and strain ε relation is nonlinear at increasing stress in the region of small strains, [3], i.e. the material has a physical nonlinearity. Physical nonlinearity can be with a soft or hard characteristic.

The monograph [4] provides the fundamentals of a physically nonlinear theory of elasticity, in construction of which Hooke's law is replaced by the nonlinear law of elasticity; geometrical linear relations of the classical theory of elasticity are preserved. Along with this, nonlinear static problems of the theory of elasticity under static load and the problems of nonlinear theory of oscillations are described in [4].

As shown by experimental studies, in most materials, namely, in soils, in polymeric materials, etc., physical nonlinearity manifests itself even at low stresses. Recently, the materials with nonlinear viscoelastic properties, have been widely used in practice. To describe such processes, it is desirable that the physically nonlinear viscoelasticity law has a simpler form and more accurately reflects physical properties of the material.

For a wide class of nonlinear problems in the theory of viscoelasticity, an account for real physical properties of a material allows revealing additional reserves of its strength and studying the effect of material properties, size and type of loads on the stress-strain state. Despite the complexity of solving the problem of nonlinear viscoelasticity, an account for the material features in the theory of viscoelasticity allows us to refine the strength calculation and to choose reliable optimal parameters of structures [3, 4]. Physically nonlinear problems relate to the complex problems of the theory of viscoelasticity and structural mechanics.

Various nonlinear viscoelasticity models were proposed by Yu.N. Rabotnov [1], A.A. Ilyushin [5]. However, some materials, depending on size and acting stresses duration, could not be described by one model only.

In mechanical engineering, construction and aviation industries, thin-walled structures such as plates and shells often play the role of a bearing surface, to which longitudinal and transverse ribs, linings and machine units are attached. In theoretical consideration of such problems, the attached elements are interpreted as an additional mass rigidly fixed to the systems and concentrated in points.

There is a number of papers in which linear and nonlinear problems of oscillations and dynamic stability of thin-walled structures such as plates and shells with a concentrated mass are considered. The problems were considered with and without account for inhomogeneous and viscoelastic properties of the material.

Analytical and experimental studies of dynamic instability of hinge-supported plates with an arbitrarily located concentrated mass are considered in [6]. Differential equations obtained with the Karman theory are solved by the Galerkin method. It is shown that a concentrated mass has a significant effect on dynamic instability of a plate.

In [7], nonlinear forced oscillations of rectangular plates carrying a concentrated mass in the center were investigated. It was assumed that the plate had rigidly fixed edges. The Karman non-linear theory of plates is used. The problem is discretized into a system with a multitude of degrees of freedom using the power approach and the Lagrange equations.

The eigenmodes of a rectangular plate, with two adjacent edges fixed, and the other two free (CCFF-plate) are investigated in [8]. The sought for deflection function is selected as the sum of two hyperbolic-trigonometric series. An analysis of the accuracy of calculations and comparison with known results are given.

In [9], orthotropic shallow shells with a double curvature are considered, as well as cylindrical panels reinforced from the side of the concavity by an orthogonal grid of ribbed stiffeners. External transverse load acting on the shell structure is uniformly distributed and linearly dependent on time. Calculations have shown a significant increase in critical load of instability, when the shell is reinforced with ribbed stiffeners.

To study free and forced axisymmetric oscillations of a cylindrical shell, two approaches were proposed in [10], based on three-dimensional theory of elasticity and division of initial cylindrical shell by concentric transverse circles.

A method for calculating natural oscillations of a cylindrical shell of an orthotropic material was proposed in [11]. The shell is reinforced by a set of rather densely arranged transverse-longitudinal ribs. The problem is reduced to a system of homogeneous algebraic equations, the number of which is equal to twice the number of discrete ribs. Comparison of calculated and experimental data is given.

The effect of a small added mass on the frequency and mode of free oscillations of a thin shell is studied in [12] using the theory of shallow shells. In proposed mathematical model it is assumed that the mass asymmetry, even in a linear statement, leads to coupled radial bending oscillations.

The most recent advances in the mechanics of soft and composite shells and their nonlinear vibrations and stability are presented in [13].

In [14], resolving equations were obtained and a calculation procedure was developed with account for nonlinear creep of three-layer plates and shallow shells with lightweight aggregate. The problem was reduced to a system of three differential equations for the stress function, displacement function and deflection.

Stability of rods, plates, and shells was investigated in [15], taking into account physical nonlinearity. Critical state of thin-walled structures is determined using some limit dependencies.

Wide use of personal computers in calculations made it possible to develop and implement numerical analysis methods for solving the problems of the hereditary theory of viscoelasticity and, thus, significantly expand the class of solved problems of the hereditary theory of viscoelasticity [16–21].

Based on the above, the aim of the first part of this study is to build a mathematical model, to develop a solution method and a unified computational algorithm for finding the deflection of the problem of axisymmetric oscillations of a physically nonlinear viscoelastic cylindrical shell with a concentrated mass.

2. Methods

Consider a viscoelastic cylindrical shell carrying concentrated masses M_p at points with coordinates (x_p) , $p = 1, 2, \dots, l$, obeying the Kirchhoff-Love hypothesis. The cylindrical shell of radius R_1 is under axisymmetric external pressure q . It is believed that there is no tensile force T_1 along the generatrix of cylindrical shell [5].

Figure 1 shows the shell element and the forces acting on it. The x -axis is directed along the generatrix of the middle surface, the y axis along the circumference and z -axis along the radius of the cylinder. The strain of cylindrical shell is characterized by radial displacement w , which is considered positive if it is directed towards positive direction of the z -axis and axial strain of the element of middle surface ε_1 . Shell material is taken as equally working in tension and compression. The directing stress and strain tensors coincide.

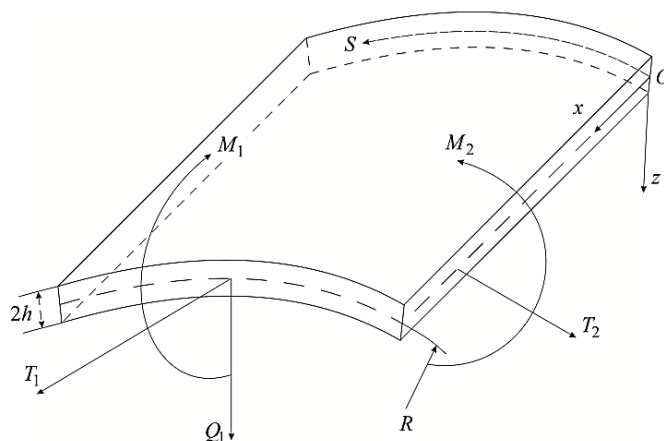


Figure 1. Element of cylindrical shell and the forces acting on it.

In accordance with the accepted assumptions and the axisymmetric nature of strain for any elementary layer located at a distance z from the middle surface, we get [5]:

$$\varepsilon_x = \varepsilon_1 - z \frac{\partial^2 w}{\partial x^2}, \quad \varepsilon_s = \varepsilon_2, \quad \varepsilon_z = -(\varepsilon_x + \varepsilon_s), \quad \varepsilon_2 = -\frac{w}{R_1}, \quad \varepsilon_{xs} = \varepsilon_{sz} = \varepsilon_{zx} = 0. \quad (1)$$

Here, relative elongations of the element of the middle surface as a result of shell strain are indicated by: $\varepsilon_1 = (\varepsilon_x)_{z=0}$, $\varepsilon_2 = (\varepsilon_s)_{z=0}$.

The condition for the absence of axial force $T_1 = 0$ is satisfied if and only if

$$\varepsilon_1 + \frac{1}{2}\varepsilon_2 = 0, \quad \varepsilon_1 = \frac{w}{2R_1}. \quad (2)$$

According to [17], the initial physical equations are taken as

$$\sigma_x - \frac{1}{2}\sigma_s = \frac{3}{2}(1-R^*)\varphi(\varepsilon_i)\varepsilon_x, \quad \sigma_s - \frac{1}{2}\sigma_x = \frac{3}{2}(1-R^*)\varphi(\varepsilon_i)\varepsilon_s, \quad (3)$$

here $R^* f(t) = \int_0^t R(t-\tau) f(\tau) d\tau$, where $R(t-\tau)$ is the relaxation kernel.

It is assumed that the shell strain is small; a nonlinear relationship is assumed between the intensity of stresses σ_i and the intensity of strains ε_i . The nonlinearity function $\varphi(\varepsilon_i)$ is taken as

$$\varphi(\varepsilon_i) = c + d\varepsilon_i^2, \quad (4)$$

here c, d are the constants, depending on the properties of shell material.

Calculate the strain rate [5, 16], taking into account (1) and (2)

$$\varepsilon_i = \frac{2}{\sqrt{3}} \left[\frac{3}{4}\varepsilon_2^2 + z^2 \left(\frac{\partial^2 w}{\partial x^2} \right)^2 \right]^{\frac{1}{2}}. \quad (5)$$

Solving (3) relative to stresses, and using (1) and (2), we get

$$\sigma_x = -2z(1-R^*)\varphi(\varepsilon_i)\frac{\partial^2 w}{\partial x^2}, \quad \sigma_s = -(1-R^*)\varphi(\varepsilon_i)\left(\frac{3}{2}\frac{w}{R_1} + z\frac{\partial^2 w}{\partial x^2}\right). \quad (6)$$

Using the last formula for stresses (6), calculate the force and moment acting on shell element using formulas [16]

$$M_1 = \int_{-h}^h \sigma_x z dz, \quad T_2 = \int_{-h}^h \sigma_s dz. \quad (7)$$

Substituting expressions (4)–(6) in (7) we get

$$M_1 = -D(1-R^*)\frac{\partial^2 w}{\partial x^2} - \frac{4bh^3}{3R_1^2}(1-R^*) \left[w^2 \frac{\partial^2 w}{\partial x^2} + \frac{4}{5}R_1^2 h^2 \left(\frac{\partial^2 w}{\partial x^2} \right)^3 \right]; \quad (8)$$

$$T_2 = -\frac{B}{R_1}(1-R^*)w - \frac{3bh}{R_1^3}(1-R^*) \left[w^3 + \frac{4}{9}R_1^2 h^2 w \left(\frac{\partial^2 w}{\partial x^2} \right)^2 \right], \quad (9)$$

where $D = \frac{4ah^3}{3}$; $B = 3ha$; h is the shell half thickness.

Differential equation of element equilibrium (Figure 1) has the form

$$\frac{\partial^2 M_1}{\partial x^2} + \frac{T_2}{R_1} + q = 0. \quad (10)$$

Adding inertial forces to the load q , according to the d'Alembert principle, and substituting (8) and (9) in (10) we get

$$\begin{aligned}
 D(1-R^*)\frac{\partial^4 w}{\partial x^4} + \frac{B}{R_1^2}(1-R^*)w + \frac{4bh^3}{3R_1^2}(1-R^*) \left\{ 2 \left[\left(\frac{\partial w}{\partial x} \right)^2 \frac{\partial^2 w}{\partial x^2} + w \left(\frac{\partial^2 w}{\partial x^2} \right)^2 + 2w \frac{\partial w}{\partial x} \frac{\partial^3 w}{\partial x^3} \right] + \right. \\
 \left. + \frac{12}{5} R_1^2 h^2 \left[2 \frac{\partial^2 w}{\partial x^2} \left(\frac{\partial^3 w}{\partial x^3} \right)^2 + \left(\frac{\partial^2 w}{\partial x^2} \right)^2 \frac{\partial^4 w}{\partial x^4} \right] + w^2 \frac{\partial^4 w}{\partial x^4} \right\} + \\
 + \frac{3bh}{R_1^4}(1-R^*) \left[w^3 + \frac{4}{9} R_1^2 h^2 w \left(\frac{\partial^2 w}{\partial x^2} \right)^2 \right] + m \frac{\partial^2 w}{\partial t^2} = q(x, t).
 \end{aligned} \quad (11)$$

The effect of a concentrated mass on viscoelastic shell is inertial in nature and is accounted in the equation of motion (11) with the Dirac δ -function [22]:

$$m(x) = \rho h + \sum_{p=1}^I M_p \delta(x - x_p)$$

where ρ is the density of the shell material.

Thus, the problem of axisymmetric oscillations of viscoelastic cylindrical shells in a physically nonlinear statement is reduced to a system of partial integro-differential equations of the form (11) with appropriate initial and boundary conditions.

Most of dynamic problems of viscoelastic thin-walled structures [17] after applying the Bubnov-Galerkin method are reduced to solving non-decay systems of integro-differential equations of the following form:

$$\begin{aligned}
 \sum_{n=1}^N (c_{kn} \ddot{w}_n + \omega_{kn}^2 w_n) = Z_k(t, w_1, \dots, w_N, \int_0^t \psi_k(t, \tau, w_1, \dots, w_N) d\tau), \\
 w_n(0) = w_{0n}, \dot{w}_n(0) = \dot{w}_{0n}, \quad n = 1, 2, \dots, N,
 \end{aligned} \quad (12)$$

where $w_n = w_n(t)$ are the unknown time functions;

Z_k, ψ_k are the continuous functions in the domain of change of arguments;

c_{kn}, ω_{kn}^2 are the given constant numbers.

Many nonlinear dynamic problems of viscoelasticity are reduced to system (12), in particular, problems of oscillations and dynamic stability of viscoelastic structures such as rods, beams and cylindrical shells bearing a concentrated mass.

Integrating system (12) twice over t , it is reduced to integral form. Assuming then that $t = t_i, t_i = i\Delta t, i = 1, 2, \dots$ ($\Delta t = \text{const}$ is the interpolation step) and replacing the integrals with quadrature formulas to calculate $w_{in} = w_n(t_i)$, we obtain the following system:

$$\begin{aligned}
 \sum_{n=1}^N c_{kn} w_{in} = \sum_{n=1}^N c_{kn} (w_{0n} + \dot{w}_{0n} t_i) + \sum_{j=0}^{p-1} A_j (t_p - t_j) \times \\
 \times \left\{ Z_k \left(t_j, w_{j1}, \dots, w_{jN}, B_s \psi_{1k} \sum_{s=0}^j (t_j, t_s, w_{s1}, \dots, w_{sN}) \right) - \sum_{n=1}^N \omega_{kn}^2 w_{jn} \right\}.
 \end{aligned} \quad (13)$$

The next step in numerical method is the regularization of a system of nonlinear integro-differential equations (13) with the singular Koltunov-Rzhanitsyn kernel [2]

$$\Gamma(t) = A e^{-\beta t} \cdot t^{\alpha-1}, \quad A > 0, \quad \beta > 0, \quad 0 < \alpha < 1.$$

Using change of variables

$$\frac{t}{\omega} - \frac{\tau}{\omega} = z^{\frac{1}{\alpha}}, \quad 0 \leq z \leq \left(\frac{t}{\omega}\right)^{\alpha}, \quad (0 < \alpha < 1)$$

the integral at the Koltunov-Rzhanitsyn kernel with a singularity of the following form

$$A \int_0^{\frac{t}{\omega}} \left(\frac{t}{\omega} - \frac{\tau}{\omega}\right)^{\alpha-1} e^{-\beta\left(\frac{t-\tau}{\omega}\right)} w(\tau) d\tau$$

has the form

$$\frac{A}{\alpha} \int_0^{\left(\frac{t}{\omega}\right)^{\alpha}} e^{-\beta z^{\frac{1}{\alpha}}} w\left(\frac{t}{\omega} - z^{\frac{1}{\alpha}}\right) dz.$$

Note that after the change of variables, the integrand with respect to z becomes regular. To numerically solve the system (13), we apply the method of direct replacement of integrals entering the system with a certain sum using some quadrature formula, in particular, using the trapezium formula

$$\frac{A}{\alpha} \sum_{k=0}^i B_k e^{-\beta t_k} w_{i-k},$$

where the coefficients are:

$$B_0 = \frac{1}{2} \left(\frac{\Delta t}{\omega}\right)^{\alpha}; \quad B_i = \frac{1}{2} \left(\frac{\Delta t}{\omega}\right)^{\alpha} (i^{\alpha} - (i-1)^{\alpha});$$

$$B_k = \frac{1}{2} \left(\frac{\Delta t}{\omega}\right)^{\alpha} ((k+1)^{\alpha} - (k-1)^{\alpha}), \quad k = \overline{1, i-1}.$$

Thus, due to twice integration of initial system (12) over time t and the use of the quadrature formula, system (13) is obtained to find the deflections $w_{in} = w_{in}(t_i)$. Solution (13) is found by the Gauss method.

3. Results and Discussion

Solution of equation (11) at initial conditions

$$w = \gamma(x), \quad \frac{\partial w(x,0)}{\partial t} = 0 \quad (14)$$

is sought in the following form [23, 24]

$$w(x,t) = \sum_{n=1}^N w_n(t) \psi_n(x), \quad (15)$$

where $\psi_n(x)$ are the known coordinate functions that satisfy all the boundary conditions of the shell.

Substituting (15) into (11) and performing the procedure of the Bubnov-Galerkin method, we obtain

$$\sum_{n=1}^N a_{kn} \ddot{w}_n + D(1-R^*) \sum_{n=1}^N b_{kn} w_n + 2B(1-R^*) \sum_{n,i,r=1}^N c_{knir} w_n w_i w_r = q_k, \quad (16)$$

$$w_n(0) = w_{0n}, \quad \dot{w}_n(0) = \dot{w}_{0n},$$

$$\text{where } a_{kn} = \int_0^a \left(\rho h + \sum_{p=1}^I M_p \delta(x-x_p) \right) \psi_n \psi_k dx, \quad b_{kn} = \int_0^a \left(\psi_{n,xxxx}^{IV} + 2\psi_{n,xyxy}^{IV} + \psi_{n,yyyy}^{IV} \right) \psi_k dx.$$

$$c_{knir} = \int_0^a \left(6\psi''_{n,xx}\psi'''_{i,xxx}\psi'''_{r,xxx} + 3\psi''_{n,xx}\psi''_{i,xx}\psi^{IV}_{r,xxx} + 3\psi'''_{n,xxx}\psi'''_{i,xxx}\psi''_{r,xx} + \right. \\ \left. + \psi'''_{n,xy}\psi'''_{i,xy}\psi''_{r,yy} + \psi''_{n,xx}\psi'''_{i,yyy}\psi'''_{r,xy} + \psi''_{n,xx}\psi''_{i,yy}\psi^{IV}_{r,xy} + 6\psi''_{n,xy}\psi'''_{i,xy}\psi'''_{r,xy} + \right. \\ \left. + 3\psi''_{n,xy}\psi''_{i,xy}\psi^{IV}_{r,xy} \right) \psi_k dx, \quad q_k = \int_0^a q \psi_k dx.$$

Integrating the system of resolving equations (16) twice over t , we can write it in integral form. Then, assuming that $t = t_i$, $t_i = i\Delta t$, $i = 1, 2, \dots$ (Δt is the integration step) and replacing the integrals with the quadrature formulas of the trapezium to compute the unknowns $w_{in} = w_{in}(t_i)$, we obtain the following recurrence formula

$$\sum_{n=1}^N a_{kn} w_{pn} = \sum_{n=1}^N a_{kn} (w_{0n} + \dot{w}_{pn} t_p) - \sum_{q=0}^{p-1} A_q (t_p - t_q) \left\{ D \sum_{n=1}^N b_{kn} \left(w_{qn} - \frac{A}{\alpha} \sum_{z=0}^q B_z e^{-\beta t_z} w_{q-z,n} \right) + \right. \\ \left. + 2B \sum_{n,i,r=1}^N c_{knir} \left(w_{qn} w_{qi} w_{qr} - \frac{A}{\alpha} \sum_{z=0}^q B_z e^{-\beta t_z} w_{q-z,n} w_{q-z,i} w_{q-z,r} \right) - q_k \right\}; \quad (17) \\ w_n(0) = w_{0n}, \quad \dot{w}_n(0) = \dot{w}_{0n},$$

where A_q, B_z are the numerical coefficients that do not depend on the choice of integrands and take on different values depending on the quadrature formulas used.

The dependence obtained makes it possible to study the axisymmetric oscillations of viscoelastic cylindrical shells carrying a concentrated mass with account for physical nonlinearity.

4. Conclusions

In the first part of this study in physically nonlinear and geometrically linear statements the following aspects were stated:

1. A boundary-value problem was formulated for the dynamic calculation of a cylindrical shell carrying concentrated masses based on the cubic theory of viscoelasticity.
2. Using the Bubnov-Galerkin method, the main resolving equations were obtained in the form of a system of non-decay integro-differential equations of the problem for dynamic calculation of a cylindrical shell carrying concentrated masses.
3. A method for solving the obtained systems of non-decay integro-differential equations based on the quadrature formula was proposed.

In the second part of the study, numerical results of the stress-strain state of a cylindrical shell with concentrated masses will be presented in physically nonlinear and geometrically linear statements.

References

1. Rabotnov, Yu. N. Elements of hereditary solid mechanics. Moscow: Mir Publishers, 1980. 387 p.
2. Mal'tsev, L.E. The analytical determination of the Rzhantsyn-Koltunov nucleus. Mechanics of Composite Materials. 1979. No. 1(15). Pp. 131–133.
3. Lurie, A.I. Nonlinear Theory of Elasticity. United Kingdom: Elsevier Science & Technology, 1990. 632 p.
4. Kauderer, H. Nichtlineare Mechanik. Springer-Verlag. Berlin, 1958. 684 p.
5. Ilyushin, A.A. Plastichnost. Osnovy obshchey matematicheskoy teorii [Plasticity. Foundations of general mathematical theory]. Moscow: Lenand, 2016. 272 p. (rus)
6. Zhong, Z., Liu, A., Pi, Y.L., Deng, J., Lu, H., Li, S. Analytical and experimental studies on dynamic instability of simply supported rectangular plates with arbitrary concentrated masses. Engineering Structures. 2019. Vol. 196. 109288. DOI: 10.1016/j.engstruct.2019.109288.
7. Amabili, M. Geometrically nonlinear vibrations of rectangular plates carrying a concentrated mass. Journal of Sound and Vibration. 2010. Vol. 329. Is. 21. Pp. 4501–4514. DOI: 10.1016/j.jsv.2010.04.024.
8. Sukhoterin, M.V., Baryshnikov, S.O., Knysh, T.P., Abdikarimov, R.A. Natural oscillations of a rectangular plates with two adjacent edges clamped. Magazine of Civil Engineering. 2018. 82(6). Pp. 81–94. DOI: 10.18720/MCE.82.8.
9. Semenov, A.A. Dynamic buckling of stiffened orthotropic shell structures. Magazine of Civil Engineering. 2018. 82(6). Pp. 3–11. DOI: 10.18720/MCE.82.1.
10. Marchuk, A.V., Gnedash, S.V., Levkovskii, S.A. Free and forced oscillations of thick-walled anisotropic cylindrical shells. International Applied Mechanics. 2017. 53(20). Pp. 181–195. DOI: 10.1007/s10778-017-0804-8.

11. Solomonov, Yu.S., Bagdasar'yan, A.A., Georgievskii, V.P. Free oscillations of a composite structurally orthotropic cylindrical shell stiffened by discretely positioned ring ribs. *Journal of Machinery Manufacture and Reliability*. 2018. Vol. 47. Is. 2. Pp. 137–141. DOI: 10.3103/S1052618818020127.
12. Leizerovich, G.S., Seregin, S.V. Free oscillations of circular cylindrical shells with a small added concentrated mass. *Journal of Applied Mechanics and Technical Physics*. 2016. Vol. 57. Is. 5. Pp. 841–846. DOI: 10.1134/S0021894416050102.
13. Amabili, M. *Nonlinear Mechanics of Shells and Plates in Composite, Soft and Biological Materials*. United Kingdom: Cambridge University Press, 2018. 586 p.
14. Chepurnenko, A.S. Calculation of three-layer shallow shells taking into account nonlinear creep. *Magazine of Civil Engineering*. 2017. 76(8). Pp. 156–168. DOI: 10.18720/MCE.76.14.
15. Rutman, J., Ulitin, V. Limit Dependences in Stability Calculations with Account for Physical Nonlinearity. *Journal of Mechanics*. 2017. 33(2). Pp. 157–160. DOI: 10.1017/jmech.2016.72.
16. Badalov, F., Eshmatov, Kh., Yusupov, M. On certain methods of solving systems of integrodifferential equations encountered in viscoelasticity problems. *Journal Applied Mathematics and Mechanics*. 51(5). Pp. 683–686. DOI: 10.1016/0021-8928(87)90025-6.
17. Abdikarimov, R.A., Khodzhaev, D.A. Computer modeling of tasks in dynamics of viscoelastic thin-walled elements in structures of variable thickness. *Magazine of Civil Engineering*. 2014. 49(5). Pp. 83–94. DOI: 10.5862/MCE.49.9. (rus)
18. Mirsaidov, M.M., Abdikarimov, R.A., Vatin, N.I., Zhgutov, V.M., Khodzhaev, D.A., Normuminov, B.A. Nonlinear parametric oscillations of viscoelastic plate of variable thickness. *Magazine of Civil Engineering*. 2018. 82(6). Pp. 112–126. DOI: 10.18720/MCE.82.11
19. Abdikarimov, R., Khodzhaev, D., Vatin, N. To Calculation of Rectangular Plates on Periodic Oscillations. *MATEC Web of Conferences*. 2018. 245. 01003. DOI: 10.1051/mateconf/201824501003
20. Khodzhaev, D.A., Abdikarimov, R.A., Vatin, N.I. Nonlinear oscillations of a viscoelastic cylindrical panel with a concentrated mass. *MATEC Web of Conferences*. 2018. 245. 01001. DOI: 10.1051/mateconf/201824501001
21. Abdikarimov, R.A., Zhgoutov, V.M. Mathematic models of nonlinear dynamics problems of viscoelastic orthotropic plates and shells of variable thickness. *Magazine of Civil Engineering*. 2010. 16(6). Pp. 38–47. DOI: 10.18720/MCE.16.3. (rus).
22. Amba-Rao, C.L. On the vibration of a rectangular plate carrying a concentrated mass. *Journal Applied Mechanics*. 1964. 31(3). Pp. 550–551. DOI: 10.1115/1.3629680.
23. Koltunov, M.A., Mirsaidov, M., Troyanovsky, I.E. Transient vibrations of axissymmetric viscoelastic shells. *Polymer Mechanics*. 1978. 14(2). Pp. 233–238. DOI: 10.1007/BF00857468
24. Mirsaidov, M., Troyanovsky, I.E. Forced axisymmetric oscillations of a viscoelastic cylindrical shell. *Polymer Mechanics*. 1975. 11(6). Pp. 953–955. DOI: 10.1007/BF00857626

Contacts:

Dadakhan Khodzhaev, +7(99871)2370981; dhodjaev@mail.ru
Rustamkhan Abdikarimov, +7(99890)9284554; rabdikarimov@mail.ru
Mirziyod Mirsaidov, +7(987)2370981; theormir@mail.ru

© Khodzhaev, D.A., Abdikarimov, R.A., Mirsaidov, M.M., 2019



DOI: 10.18720/MCE.91.4

Динамика физически нелинейной вязкоупругой цилиндрической оболочки с сосредоточенными массами

Д.А. Ходжаев^а, Р.А. Абдикаримов^{б*}, М.М. Мирсаидов^а

^а Ташкентский институт инженеров ирригации и механизации сельского хозяйства, г.Ташкент, Узбекистан

^б Ташкентский финансовый институт, г.Ташкент, Узбекистан

* E-mail: rabdikarimov@mail.ru

Ключевые слова: тонкостенные конструкции, цилиндрическая оболочка, вязкоупругость, физическая нелинейность, сосредоточенные массы, осесимметричные колебания, нелинейное интегро-дифференциальное уравнение, ядро релаксации, метод Бубнова-Галёркина, численный метод

Аннотация. Известно, что наиболее разработанной частью теории упругости является теория линейных и нелинейных упругих пластин и оболочек. В этой области получены все необходимые уравнения и разработаны методы их решения. В то же время, в области учета вязкоупругих свойств материала в задачах по динамическим расчетам тонкостенных конструкций имеются пробелы. Отметим, что в некоторых работах вязкоупругие свойства материала, т.е. отклонение диаграммы испытаний материала от закона Гука учитывались по модели Фойхта, не подтверждающиеся экспериментами. Не учет вязкоупругих свойств материала существенно ограничивает практическую применимость результатов. В первой части работы рассматриваются постановка и метод решения задачи об осесимметричных колебаниях физически нелинейной вязкоупругой цилиндрической оболочки с сосредоточенными массами. Функция, характеризующая меру отклонения кривой интенсивности напряжений от прямой Гука, принята в виде кубической нелинейности. Построена математическая модель, предложен метод решения и разработан вычислительный алгоритм задачи об осесимметричных колебаниях цилиндрической оболочки, несущей сосредоточенные массы, с учетом физически нелинейного деформирования материала при различных граничных условиях в рамках гипотезы Кирхгофа-Лява. Эффект действия сосредоточенных масс вводится с использованием дельта-функции Дирака. С помощью метода Бубнова-Галёркина, основанного на многочленной аппроксимации прогибов, рассматриваемая задача сводится к решению, в общем случае, не распадающихся систем нелинейных интегро-дифференциальных уравнений типа Вольтерры. Для решения полученной системы, при слабо-сингулярном ядре Колтунова-Ржаницына, применен численный метод, основанный на использовании квадратурных формул. Разработан единый вычислительный алгоритм для нахождения прогиба вязкоупругой цилиндрической оболочки с сосредоточенными массами.

Литература

1. Работнов Ю. Н. Элементы наследственной механики твёрдых тел. М.: Наука, 1977. 384 с.
2. Mal'tsev L.E. The analytical determination of the Rzhansyn-Koltunov nucleus // Mechanics of Composite Materials. 1979. № 1(15). Pp. 131–133.
3. Лурье А.И. Нелинейная теория упругости. М.: Наука, 1980. 512 с.
4. Kauderer H. Nichtlineare Mechanik. Springer-Verlag. Berlin, 1958. 684 p.
5. Ильюшин А.А. Пластичность. Основы общей математической теории. М.: Ленанд, 2016. 272 с.
6. Zhong Z., Liu A., Pi Y.L., Deng J., Lu H., Li S. Analytical and experimental studies on dynamic instability of simply supported rectangular plates with arbitrary concentrated masses // Engineering Structures. 2019. № 196. 109288. doi: 10.1016/j.engstruct.2019.109288
7. Amabili M. Geometrically nonlinear vibrations of rectangular plates carrying a concentrated mass // Journal of Sound and Vibration. 2010. № 21(329). Pp.4501–4514. doi: 10.1016/j.jsv.2010.04.024
8. Сухотерин М.В., Барышников С.О., Кныш Т.П., Абдикаримов Р.А. Собственные колебания прямоугольной пластины, защемленной по двум смежным краям // Инженерно-строительный журнал. 2018. № 6(82). С.81–94. doi: 10.18720/MCE.82.8
9. Семенов А.А. Динамическая устойчивость подкрепленных ортотропных оболочечных конструкций // Инженерно-строительный журнал. 2018. № 6(82). С. 3–11. doi: 10.18720/MCE.82.1
10. Marchuk A.V., Gnedash S.V., Levkovskii S.A. Free and forced vibrations of thick-walled anisotropic cylindrical shells // International Applied Mechanics. 2017. № 2(53). Pp. 181–195. doi: 10.1007/s10778-017-0804-8

11. Solomonov Yu.S., Bagdasar'yan A.A., Georgievskii V.P. Free oscillations of a composite structurally orthotropic cylindrical shell stiffened by discretely positioned ring ribs // Journal of Machinery Manufacture and Reliability. 2018. № 2(47). Pp. 137–141. doi: 10.3103/S1052618818020127
12. Leizerovich G.S., Seregin S.V. Free vibrations of circular cylindrical shells with a small added concentrated mass // Journal of Applied Mechanics and Technical Physics. 2016. № 5(57). Pp. 841–846. doi: 10.1134/S0021894416050102
13. Amabili M. Nonlinear Mechanics of Shells and Plates in Composite, Soft and Biological Materials. United Kingdom: Cambridge University Press, 2018. 586 p.
14. Чепурненко А.С. Расчет трехслойных пологих оболочек с учетом нелинейной ползучести // Инженерно-строительный журнал. 2017. № 8(76). С. 156–168. doi: 10.18720/MCE.76.14.
15. Rutman J., Ulitin V. Limit Dependences in Stability Calculations with Account for Physical Nonlinearity // Journal of Mechanics. 2017. № 2(33). Pp. 157–160. doi: 10.1017/jmech.2016.72
16. Бадалов Ф.Б., Эшматов Х., Юсупов М. О некоторых методах решения систем интегро-дифференциальных уравнений, встречающихся в задачах вязкоупругости // Прикладная математика и механика. 1987. № 5(51). С. 867–871.
17. Абдикаримов Р.А., Ходжаев Д.А. Компьютерное моделирование задач динамики вязкоупругих тонкостенных элементов конструкций переменной толщины // Инженерно-строительный журнал. 2014. № 5(49). С. 83–94. doi: 10.5862/MCE.49.9.
18. Мирсаидов М.М., Абдикаримов Р.А., Ватин Н.И., Жгутов В.М., Ходжаев Д.А., Нормуминов Б.А. Нелинейные параметрические колебания вязкоупругой пластинки переменной толщины // Инженерно-строительный журнал. 2018. № 6(82). С. 112–126. doi: 10.18720/MCE.82.11
19. Abdikarimov R., Khodzhaev D., Vatin N. To Calculation of Rectangular Plates on Periodic Oscillations // MATEC Web of Conferences. 2018. № 245. 01003. doi: 10.1051/mateconf/201824501003
20. Khodzhaev D.A., Abdikarimov R.A., Vatin N.I. Nonlinear oscillations of a viscoelastic cylindrical panel with a concentrated mass. MATEC Web of Conferences. 2018. № 245. 01001. doi: 10.1051/mateconf/201824501001
21. Абдикаримов Р.А., Жгутов В.М. Математические модели задач нелинейной динамики вязкоупругих ортотропных пластин и оболочек переменной толщины // Инженерно-строительный журнал. 2010. № 6(16). С. 38–47. doi: 10.18720/MCE.16.3.
22. Amba-Rao C.L. On the vibration of a rectangular plate carrying a concentrated mass // J. Appl. Mech. 1964. № 3(31). Pp. 550–551. doi: 10.1115/1.3629680.
23. Koltunov M.A., Mirsaidov M., Troyanovskii I.E. Transient vibrations of axisymmetric viscoelastic shells // Polymer Mechanics. 1978. № 2(14). Pp. 233–238. doi: 10.1007/BF00857468
24. Mirsaidov M., Troyanovskii I.E. Forced axisymmetric oscillations of a viscoelastic cylindrical shell // Polymer Mechanics. 1975. № 6(11). Pp. 953–955. doi: 10.1007/BF00857626

Контактные данные:

Дадахан Акмарханович Ходжаев, +7(99871)2370981; dhodjaev@mail.ru

Рустамхан Алимханович Абдикаримов, +7(99890)9284554; rabdikarimov@mail.ru

Мирзиед Мирсаидович Мирсаидов, +7(987)2370981; theormir@mail.ru

© Ходжаев Д.А., Абдикаримов Р.А., Мирсаидов М.М., 2019



DOI: 10.18720/MCE.91.5

The impact of cable spacing on the behavior of cable-stayed bridges

R. Al-Rousan*

Jordan University of Science and Technology, Irbid, Jordan

* E-mail: rzalrousan@just.edu.jo

Keywords: engineering, cable-stayed bridge, technology, civil engineering, structural concrete deck

Abstract. This paper aims to find the optimum cable spacing in terms of vertical deformation and cable stress for static and dynamic analysis. To achieve the objective of this study six models are developed using ABAQUS with six different cable spacing ((8.04 m, 30 cables), (9.42, 25), (11.11, 22), (13.72, 18), (15.56, 16), and (16.67, 15)). Firstly, a non linear static finite-element analysis is performed on the models; then pre-tensioning forces are applied to cables, after that the shape modes for each model are presented. Secondly, a nonlinear dynamic analysis is performed on the models; the results obtained from the finite-element analysis are used in the optimization. The results show that the maximum vertical deflection decreased and the cable stress increased with the increasing of cable spacing for both static and dynamic analysis. As a result, the unsupported length increased with the cable spacing increasing; this will lead to larger deflection and greater stresses in the cables. Finally, the optimum cable spacing is 11.2 m based on static and dynamic deflection and cable stress.

1. Introduction

Many types of bridges are used these days. The simplest bridge, the beam bridge, consists of two piers and one beam. However, the need for spans with long distances proposed new alternatives such as suspension bridges and cable-stayed bridges. The cost of the suspension bridges is relatively higher than the cost of the cable-stayed bridges. The elastically supported girder is the main tool in the simulation of the behavior of a cable-stayed girder. The square of the spacing is proportional to the local bending moment between the cables. The newly proposed design necessity that all cables be independently expendable makes closely spaced cables more attractive. It is generally essential that one cable can be dismantled, detensioned, and replaced under reduced traffic loading. The small cable spacing will not increase extremely the additional bending moment in the girder. Accessibility of ever best computer tools helps the engineer to simulate and analysis of the complexity of structure [1–11].

Cable-stayed bridges have been constructed all over the world, are mainly used for medium-to-long spans and are part of important transportation networks. Besides their structural efficiency, they owe their popularity due to an elegant and transparent appearance. The bridges constructed in earthquake-prone areas must be designed to withstand the seismic action. Cable-stayed bridges present long vibration periods, due to the long spans and their flexibility, which theoretically makes them not sensitive to dynamic excitation [10]. However, they feature inherent low damping, and their dynamic behavior is highly dependent on the stiffness and mass distribution. Therefore, any attempt to minimize the inertia forces and to maximize the resistance leads to an undesired decrease in the vibration periods and consequently to higher seismic forces. Furthermore, although concrete bridges feature higher damping than steel or composite bridges, they are also heavier, which implies higher inertia forces.

The dynamic behavior of cable-stayed bridges has been extensively studied by several authors. Abdel-Ghaffar and Nazmy [12] considered a three-dimensional model, including the geometrical nonlinearities, to

Al-Rousan, R. The impact of cable spacing on the behavior of cable-stayed bridges. Magazine of Civil Engineering. 2019. 91(7). Pp. 49–59. DOI: 10.18720/MCE.91.5

Аль-Рушан Р. Влияние расстояния между тросами на поведение вантовых мостов // Инженерно-строительный журнал. 2019. № 7(91). С. 49–59. DOI: 10.18720/MCE.91.5



This work is licensed under a CC BY-NC 4.0

study the dynamic behavior of long-span cable-stayed bridges under seismic loading. The cases of synchronous and non-synchronous support excitations were considered, and the effects of the non-dispersive traveling seismic wave on the bridge response were studied. Abdel-Ghaffar and Khaliffa [13] studied the dynamic behavior of cable-stayed bridges focusing on the importance of the cables' vibrations in the overall dynamic response of these bridges. Soneji and Jangid [14] studied the influence of dynamic soil-structure interaction on the behavior of seismically isolated cable-stayed bridges. Caetano et al. [15] focused on modeling the dynamic behavior of cable-stayed bridges. The authors developed a three-dimensional finite element model that includes the cable transversal motion and were tuned based on repeated campaigns of vibration data acquisitions of a cable-stayed bridge. Camara and Efthymiou [16] studied the deck-tower interaction in the transverse seismic response of cable-stayed bridges. The authors considered the contribution of different vibration modes and the influence of the main span length, the tower shape, the cable-system arrangement, the width and height of the deck, and the soil conditions. Concerning the optimization of cable-stayed bridges under seismic action only a few studies have been reported. Negrão and Simões [17] optimized steel cable-stayed bridges under seismic action considering both modal/spectral and time-history approaches. The cable areas and the cross-sectional dimensions of the deck and towers were considered as design variables. Ferreira and Simões [18] presented an algorithm for the optimum design of steel cable-stayed bridges considering active devices to control the response of the structure subjected to earthquakes.

Cable-stayed bridge design involves some complex problems, such as: defining the structural system, finding the members' cross-sections, the calculation of the cable forces distribution, the construction stages, and geometrical nonlinear effects. For concrete bridges, the time-dependent effects must also be considered. The seismic action adds more complexity to find an adequate mass and stiffness distribution that optimizes the dynamic bridge response. Therefore, optimization algorithms are particularly used to handle a large amount of information involved and thus, obtaining economical and structurally efficient solutions under both static and dynamic loading. Previous works concerning the optimization of cable-stayed bridges studied the cable forces calculation in steel [19, 20], composite [21, 22] and concrete bridges [23, 24]. The use of geometric and cross-sectional design variables was also reported in the optimization of steel and composite steel-concrete bridges [25] subjected to static loading. The main objective was to minimize the structural cost while ensuring that the stresses and displacements throughout the structure remain within allowable limits.

We are faced with a large optimization problem given the number of design variables and objectives representing several load cases, the consideration of geometrical nonlinearities and the dynamic analysis to access the structural response under seismic action. A cable-stayed bridge needs, including the time-dependent effects and poses additional difficulties to the optimization problem when formulating the sensitivities of the design objectives. This is due to the fact that the resistance of each cable-stayed bridge depends on the correspondent cross-sectional design variables.

2. Methods

The goal of this analysis is to determine the spacing of the optimum cable; the different models will be studied using ABAQUS. Eighteen models will be created and analyzed which have the same parameters except the cable spacing and the deck stiffness (three-deck stiffness and six cables spacing). The eighteen models are created based on design constants will be described later in this chapter, computer analyses will be conducted, then the optimum cable spacing and optimum deck stiffness will be calculated based on the results.

2.1. Design constants

A doubly symmetrical cable-stayed bridge about the two major axes with one middle span (500 meters long) and two side spans (250 meters each span) will be used; the bridge will have four towers (two at each side of the deck) as shown in Figure 1. The typical ratio which offers an economical solution for the design for the height to the main span ratio is 5, according to this ratio, the height of the towers is 100 m. The typical design range for the pylons to the towers' ratio is 2, so the height of piers is 50 m. The cross-section of the towers is (3.5 m × 5.5 m) of conventional concrete C30; this cross-section needs about 1.2 m² longitudinal reinforcement. The cable's material is a seven-wired strand T15S 1770 which has a diameter of 20 cm, modulus of elasticity equal to 165 GPa and the Poisson's ratio of 0.3. Based on the history of the cable-stayed bridges, the most preferred layout of the cable's arrangement is the double-plane semi-fan system, which provides better support to the deck. A reinforced concrete (RC) deck is used, the deck consists of 0.25 m thick. The steel used for the girders has an elastic modulus of 200 GPa, and Poisson's ratio of 0.3 and the mechanical prosperities of the RC slab are $f'c$ of 50 MPa, Poisson's ratio of 0.15 and normal weight density of 2400 kg/m³. The deck has four traffic lanes, two lanes at each side and a pedestrian walkway at each side too, the width of the deck will be taken is 25 m. For the boundary, the towers are fixed at their ends, and the deck is pinned at its ends, the intersection between the towers and the deck are pinned too.

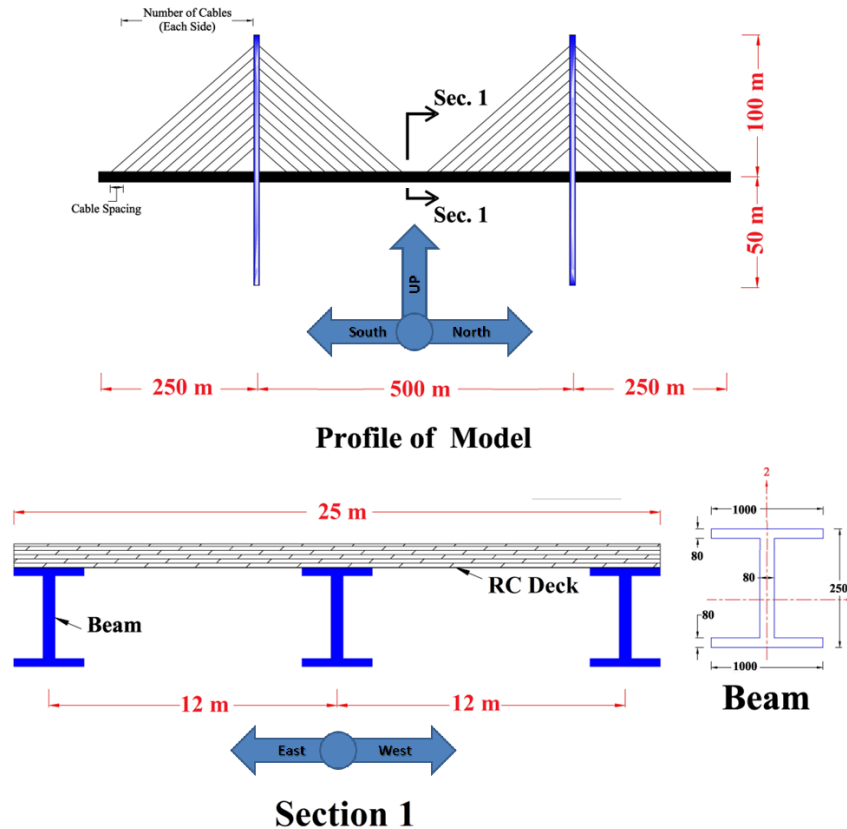


Figure 1. Bridge details and loading directions.

2.2. Finite elements

Thick shell element is suitable for the analysis of RC and sandwich shells (RC decks). Irregular meshes of S8R elements converge very poorly because of severe transverse shear locking; therefore, this element is recommended for use in usual mesh geometries for thick shell applications. As a conclusion, a S8R thick shell element with typical mesh geometries will be used for meshing the RC deck. The 3-node quadratic beam element (B32) will be used for meshing the Girders, the Cross-Beams, and the towers. Finally, the 2-node linear interpolation truss element (T3D2) will be used for meshing the cables. Truss elements (T3D2) are one-dimensional bars or rods that are assumed to deform by axial stretching. These elements pin jointed at their nodes, and so only translationally displacements and the initial position vector at each node are used in the discrimination. When the strains are large, the formulation is simplified by assuming that the trusses are made of incompressible material. There are two truss elements in Bequest: a 2-node linear interpolation truss and a 3-node quadratic interpolation truss. The quadratic interpolation version is in the library, mainly for compatibility with the quadratic interpolation elements of other types, such as a shell element S8R5. The same interpolation functions are used for both the Cartesian displacement components and for the Cartesian components of the initial position vector, so these elements are the simplest form of nonparametric elements.

2.3. Models

Table 1 shows the simulated models to be analyzed; every model has different spacing for the cables as results of six different models. It is common knowledge that the cables work more effectively when they form angles between (25–65°) with the deck, and it is very common for cable-stayed bridges to have been spacing between 8.04 m to 16.67 m between cables. The deck supported on three I-steel beams, as shown in Figure 1. All models arrangement leads to minimum and maximum angles of 22.7° and 66.12° respectively. The cable spacing and the number of cables in each side for the first, second, third, fourth, fifth, and sixth model will be taken (8.04 m, 30 cables), (9.42, 25), (11.11, 22), (13.72, 18), (15.56, 16), and (16.67, 15), respectively. The total number of cables for the model equals eight times the number of cables on each side. Shell elements were used to represent the RC slab; tie connections were used to connect the slab with the steel frame; the steel frame consists of the steel girders and cross beams. The cross beams have the same dimensions as the steel girders for simplification. Beam elements were used to represent the steel frame. The cables and girders are connected using MPC constraint's pin type, and the towers and cables are connected using MPC constraint's tie type. The cables are represented using truss elements, and beam elements were used for representing the towers.

Table 1. Details of simulated models and static results.

Model Number	Cable Spacing (m)	Number of cables (Each Side)	$\Delta_{Max,B}$, m	$\Delta_{Max,A}$, m	$\sigma_{Max,B}$, MPa	$\sigma_{Max,B}/\sigma_u$, %	$\sigma_{Max,A}$, MPa	$\sigma_{Max,A}/\sigma_u$, %
B1CS8.04	8.04	30	6.16	0.05029	641	40	173	9.8
B1CS9.42	9.42	25	9.68	0.06195	723	64	191	10.8
B1CS11.11	11.11	22	9.34	0.06155	829	62	190	10.7
B1CS13.72	13.72	18	10.71	0.06135	1001	76	264	14.9
B1CS15.56	15.56	16	7.08	0.0488	1365	52	457	25.8
B1CS16.67	16.67	15	8.61	0.04419	1049	65	248	14.0

Note: $\Delta_{Max,B}$: Maximum deflection before pre-tensioning; $\Delta_{Max,A}$: Maximum deflection after pre-tensioning; $\sigma_{Max,B}$: Maximum stress in cables before pre-tensioning; $\sigma_{Max,A}$: Maximum stress in cables after pre-tensioning; σ_u : Ultimate stress of cable.

2.3.1. Static Loading

In accordance to AASHTO, the load combination has been taken into account for the static case is "STRENGTH I", which is equal to:

$$T.L = 1.25 \times D.L + 1.5 \times S.D.L + 1.75 \times L.L, \quad (1)$$

where $T.L$ is the factored total load;

$D.L$ is the dead load;

$S.D.L$ is the superimposed dead load,

$L.L$ is the live load. The static load applied as pressure on the deck surface in the gravity direction. Nonlinear analysis was performed to account for the nonlinear performance of the cables.

2.3.2. Pre-tensioning

The conventional «Zero-Displacement» method proposed by Wang et al. [21] was used to achieve the pre-tensioning forces in the cables. Firstly, the towers were restricted from the vertical and horizontal movements, and then prestressing forces were applied to the cables until a zero vertical displacement at the center of the mid-span is achieved. After that, the towers were allowed to move in the vertical and horizontal directions. Finally, the prestressing forces were adjusted until we had zero vertical displacements at the span center.

2.3.3. Earthquake Loading

The earthquake – time history that has been used is the AQABA earthquake, as shown in Figure 2. AQABA earthquake happened on 22/11/1995 and the station that record the time history is "Eilat" station; the earthquake had peak ground acceleration (PGA) = 0.109g (Figure 2) in the vertical direction (UP) (Figure 1), 0.086g (Figure 2) in the horizontal direction (North-South) (Figure 1) and 0.097g (Figure 2) in the horizontal direction (East-West) (Figure 1) and its lasted for sixty seconds. In accordance to AASHTO, the "EXTREME EVENT I" load combination has been taken into account for the dynamic case:

$$T.L = 1.25 \times D.L + 1.5 \times S.D.L + 0.5 \times L.L + 1.0 \times EQ, \quad (2)$$

where EQ is the earthquake loading. The earthquake loading was applied at the ends of the towers and the dead load, superimposed dead load, and the live load was applied as pressure on the surface of the deck.

3. Results and Discussion

3.1. Static analysis

Table 1 shows the summary of static analysis results, and Figure 3 shows the deflection due to static loading along the bridge before and after pre-tensioning. Inspection of Table 1 reveals that the maximum deflections were more than the AASHTO allowable deflection of 0.625 m ($L/800$) in the middle of the mid-span. In addition, the maximum cable stresses were less than the ultimate strength of the cables of 1770 MPa. After applying the pre-tensioning forces in the cables using the Zero-Deflection method, the maximum deflection was reduced to be less than the AASHTO allowable deflection of 0.625 m, as shown in Figure 3. Finally, the maximum stress in cables after pre-tensioning was less than the AASHTO allowable strength of 708 MPa (40 % of the ultimate strength of the cable).

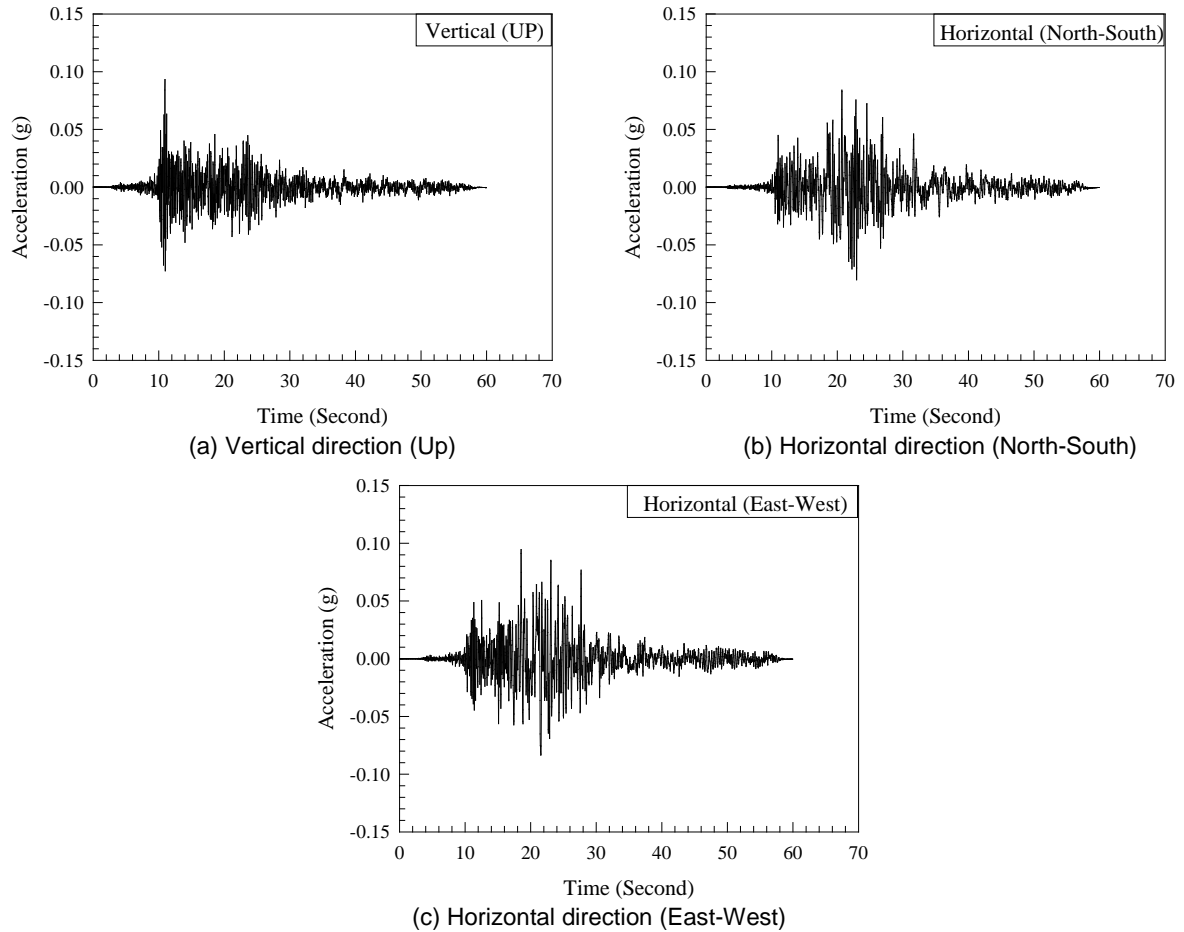


Figure 2. AQABA earthquake acceleration – time history.

3.2. Modes of the bridge with the corresponding natural frequencies

Figure 4 shows the typical ten modes of the bridge with the corresponding natural frequencies for the bridge. Mode one represents the symmetrical lateral movement of the towers; mode two represents an anti-symmetrical lateral movement of the towers; mode three represents the cross movement of the towers; mode four represents symmetrical lateral movement of the towers – adjacent towers move in opposite direction; mode five represents the symmetrical torsion of the deck; mode six represents the symmetrical bending of the deck, mode seven represents the anti-symmetrical bending of the deck; mode eight represents the symmetrical torsion of the deck opposite of Mode five, mode nine represents the anti-symmetrical torsion of the deck, and finally mode ten represents the lateral planer bending of the deck. Inspection of Figure 4 reflected that all-natural frequencies are below 0.70 cycles/s. Moreover, mode ten had the highest natural frequency of 0.69564 cycles/s; while mode one had the lowest natural frequency of 1.1124 cycles/s. Finally, mode eight, which is the opposite of mode five, had a natural frequency of 1.55 times the natural frequency of mode five. Therefore, the sequence of natural frequency for the ten modes is classified as following from the strongest to the weakness: the lateral planer bending, the symmetrical bending, symmetrical torsion, and symmetrical lateral movement.

Table 2. Summary of dynamic analysis results.

Model Number	$\Delta_{Max,S}$, m	$\sigma_{Max,S}$, MPa	$\sigma_{Max,S}/\sigma_u$, %	$\Delta_{Max,D}$, m	$\sigma_{Max,D}$, MPa	$\sigma_{Max,D}/\sigma_u$, %	$\frac{\Delta_{Max,D}}{\Delta_{Max,S}}$, %	$\frac{\sigma_{Max,D}}{\sigma_{Max,S}}$, %
B1CS8.04	0.05029	173	9.8	0.1437	214	12.1	35.0	123.7
B1CS9.42	0.06195	191	10.8	0.2187	250	14.1	28.3	130.9
B1CS11.11	0.06155	190	10.7	0.1727	246	13.9	35.6	129.5
B1CS13.72	0.06135	264	14.9	0.2091	341	19.3	29.3	129.2
B1CS15.56	0.0488	457	25.8	0.1935	357	20.2	25.2	78.1
B1CS16.67	0.04419	248	14.0	0.2151	383	21.6	20.5	154.4

Note: $\Delta_{Max,S}$: Maximum deflection due to static loading; $\Delta_{Max,D}$: deflection due to dynamic loading; $\sigma_{Max,S}$: Maximum stress in cables due to static loading; $\sigma_{Max,A}$: Maximum stress in cables due to dynamic loading; σ_u : Ultimate stress of cable.

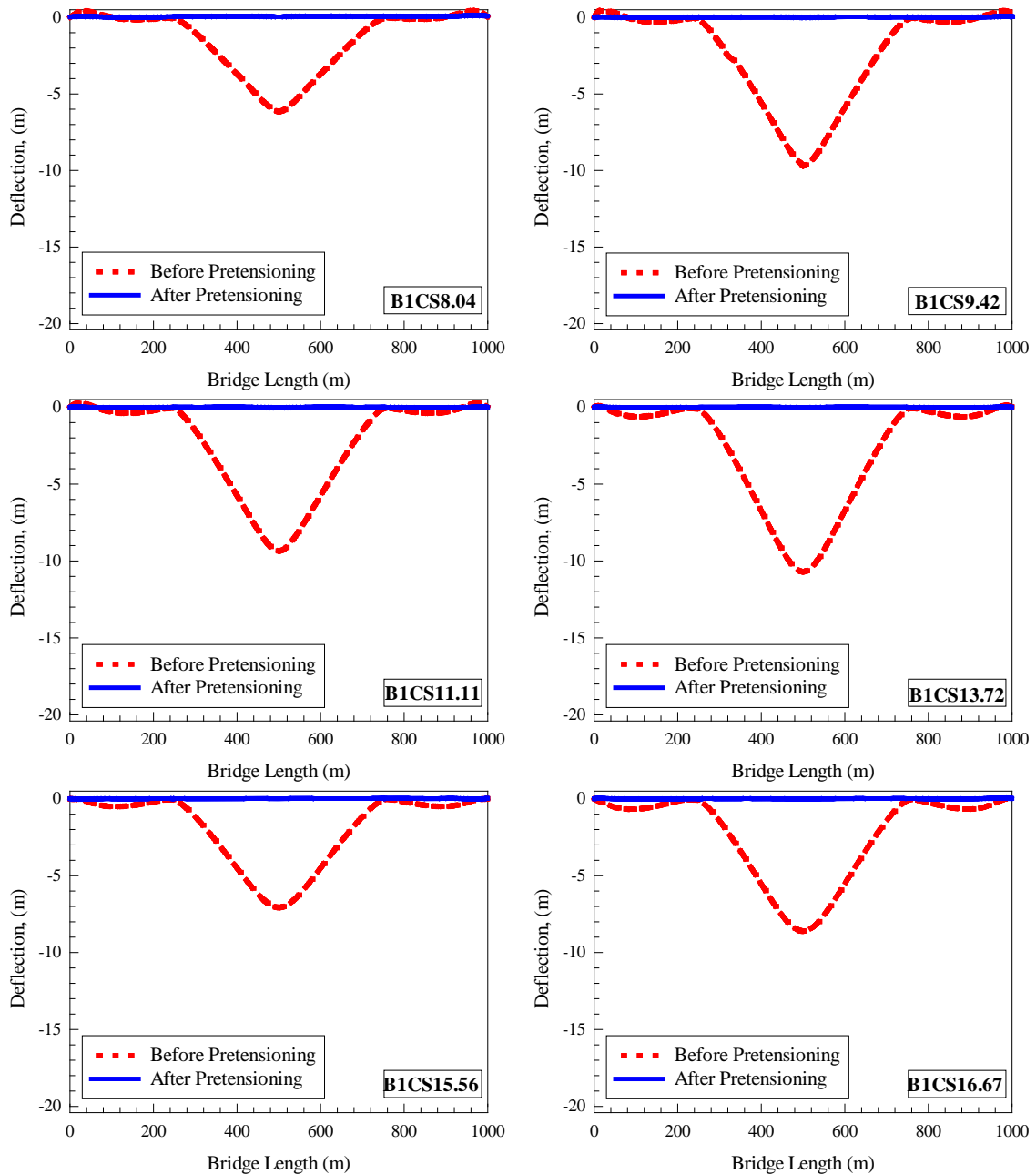


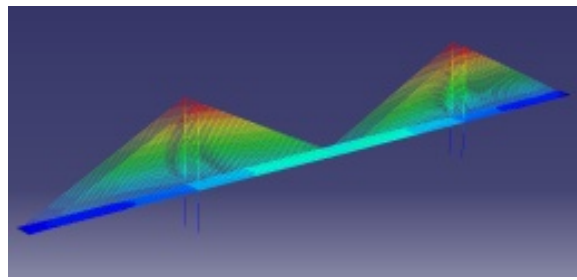
Figure 3. Typical deflection along the bridge before and after pre-tensioning.

3.3. Dynamic analysis

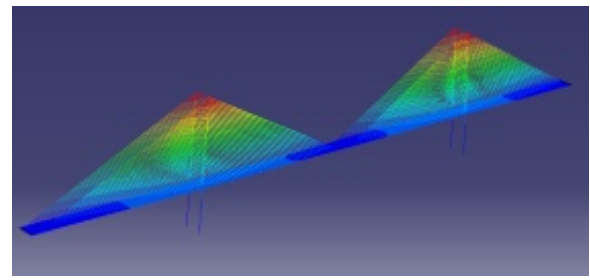
AQABA 1995 earthquake was applied on the bridge in three directions (UP, North-South, and East-West) as shown in Figure 2. Each direction had an acceleration-time history; the earthquake was applied to the supports. Table 2 shows the summary of dynamic analysis results, and Figure 5 shows the deflection along the bridge due to static and dynamic loading. Inspection of Figure 5 and Table 2 reveal that the maximum deflections due to static and dynamic loading were less than the AASHTO allowable deflection of 0.625 m. Also, the maximum cable stresses behave the same as maximum deflection, which is less than the AASHTO allowable strength of 708 MPa. In addition, Table 2 shows that the deflection and stress in the cable due to dynamic loading is more than static ranged from 20-35% and 78-154%, respectively. Therefore, the effect of dynamic loading had a higher impact on the maximum vertical deflection than maximum stress in the cables.

3.4. Optimum cable spacing

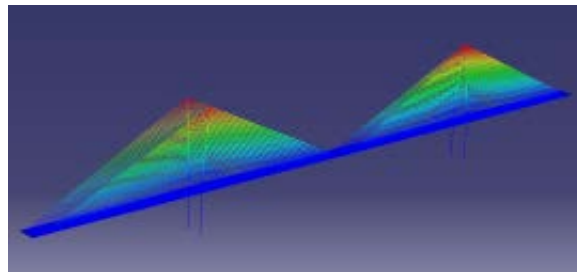
Figure 6 shows the maximum deflection due to static loading ($\Delta_{Max,S}$), maximum deflection due to dynamic loading ($\Delta_{Max,D}$); maximum stress in cables due to static loading ($\sigma_{Max,S}$); maximum stress in cables due to dynamic loading ($\sigma_{Max,A}$) were normalized with respect to value of bridge at cable spacing of 8.04 m. The inspection of Figure 6 reveals that the optimum cable spacing is 11.2 m. Figure 6 shows that the vertical deflection increased with the increasing of the cable spacing. Therefore, the maximum vertical deflection decreased, and the cable stress increased as the cable spacing increasing. As a result, the unsupported length increased with the cable spacing increasing; this will lead to larger deflection and greater stresses in the cables.



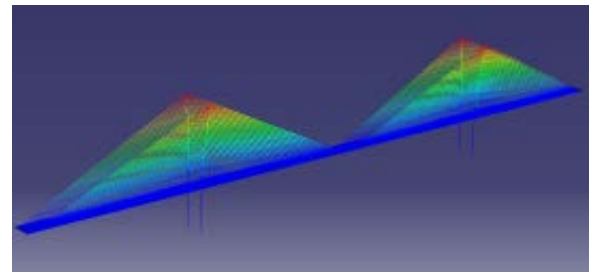
Mode One: Frequency = 1.1124 cycles/s



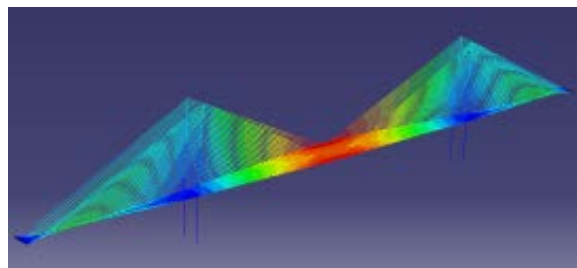
Mode Two: Frequency = 0.12012 cycles/s



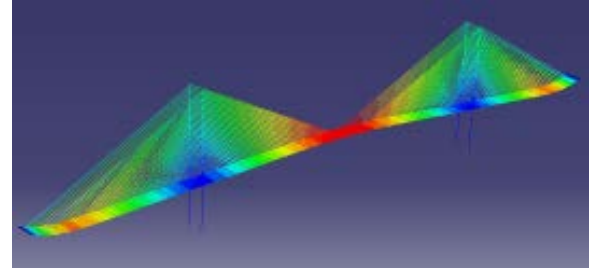
Mode Three: Frequency = 0.1677 cycles/s



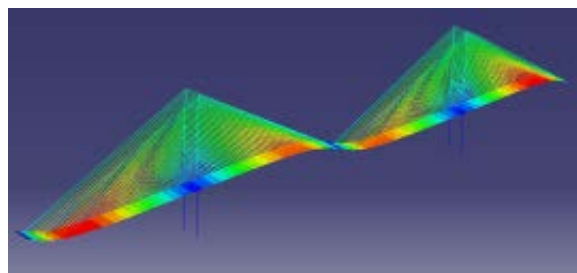
Mode Four: Frequency = 0.20124 cycles/s



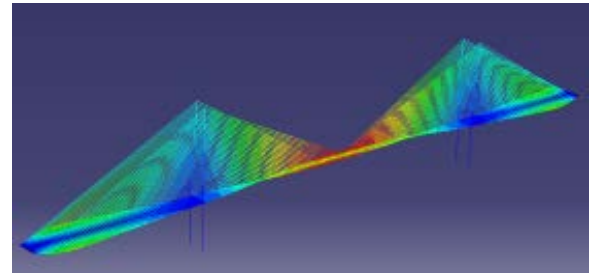
Mode Five: Frequency = 0.32775 cycles/s



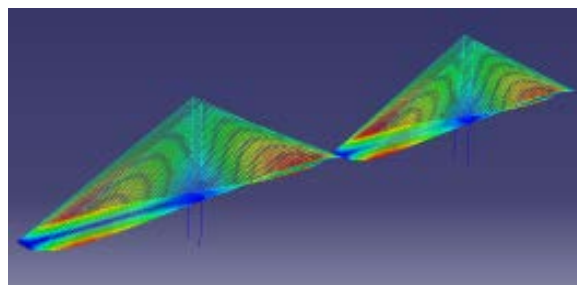
Mode Six: Frequency = 0.36096cycles/s



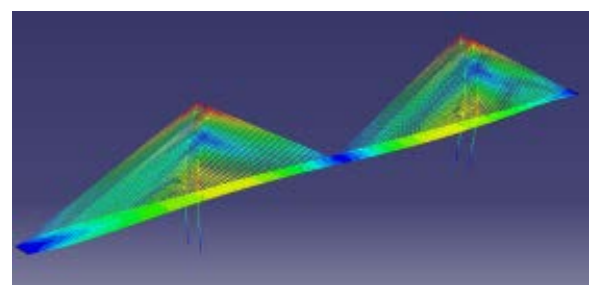
Mode Seven: Frequency = 0.46584 cycles/s



Mode Eight: Frequency = 0.49956cycles/s



Mode Nine: Frequency = 0.56496 cycles/s



Mode Ten: Frequency = 0.69564 cycles/s

Figure 4. Typical mode shape obtained from B1CS8.04.

3.5. Optimization

The relation between cable spacing and deformation of the bridge will be formed for each deck, and then the optimum cable spacing will be found from these equations. Secondly, the optimum deck stiffness for each cable spacing was found. The approximate equation that can be used to represent the deformation and the cable spacing is:

$$u_i(x) = \alpha_0 + \alpha_1 x_i + \alpha_2 x_i^2 + \alpha_3 x_i^3 + \alpha_4 x_i^4 + \alpha_5 x_i^5; \quad i = 1, 2, 3, 4, 5, 6; \quad (3)$$

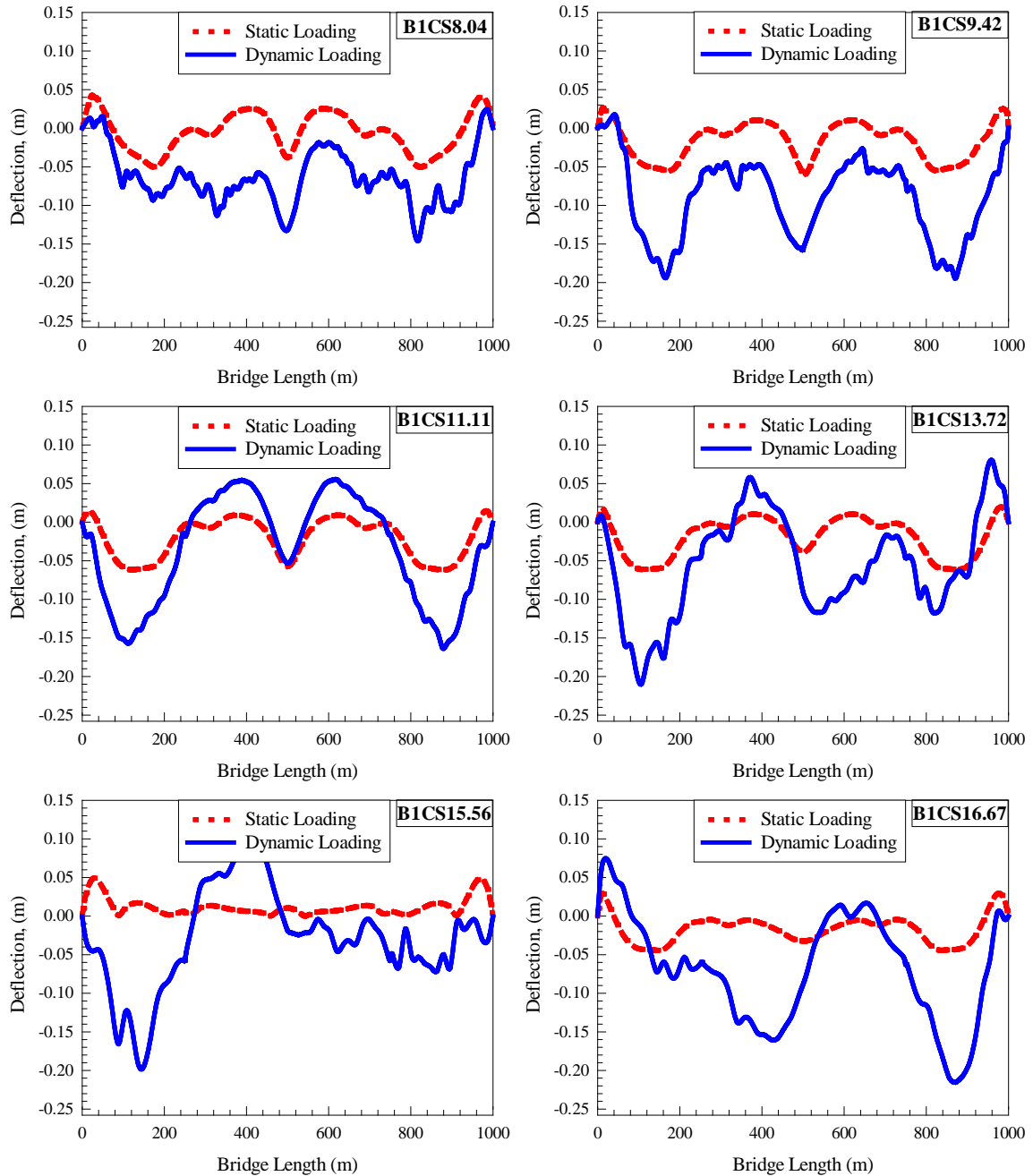


Figure 5. Typical deflection along the bridge due to static and dynamic loading.

$$\begin{Bmatrix} u_1(x) \\ u_2(x) \\ u_3(x) \\ u_4(x) \\ u_5(x) \\ u_6(x) \end{Bmatrix} = \begin{Bmatrix} 1 & x_1 & x_1^2 & x_1^3 & x_1^4 & x_1^5 \\ 1 & x_2 & x_2^2 & x_2^3 & x_2^4 & x_2^5 \\ 1 & x_3 & x_3^2 & x_3^3 & x_3^4 & x_3^5 \\ 1 & x_4 & x_4^2 & x_4^3 & x_4^4 & x_4^5 \\ 1 & x_5 & x_5^2 & x_5^3 & x_5^4 & x_5^5 \\ 1 & x_6 & x_6^2 & x_6^3 & x_6^4 & x_6^5 \end{Bmatrix} \times \begin{Bmatrix} \alpha_0 \\ \alpha_1 \\ \alpha_2 \\ \alpha_3 \\ \alpha_4 \\ \alpha_5 \end{Bmatrix}; \quad (4)$$

$$\{\alpha\} = [x]^{-1} \{u\}, \quad (5)$$

where $u(x)$ is the maximum deformation in meters and x is the cable spacing in meters. The constants $\alpha_0, \alpha_1, \alpha_2, \alpha_3,$ and α_4 can be solved using the values of Table 2. Using MATLAB for solving the previous matrices, the constants were calculated and the derived function becomes:

$$u(x) = 0.0002x^5 - 0.0136x^4 + 0.3386x^3 - 4.1599x^2 + 25.148x - 59.607. \quad (6)$$

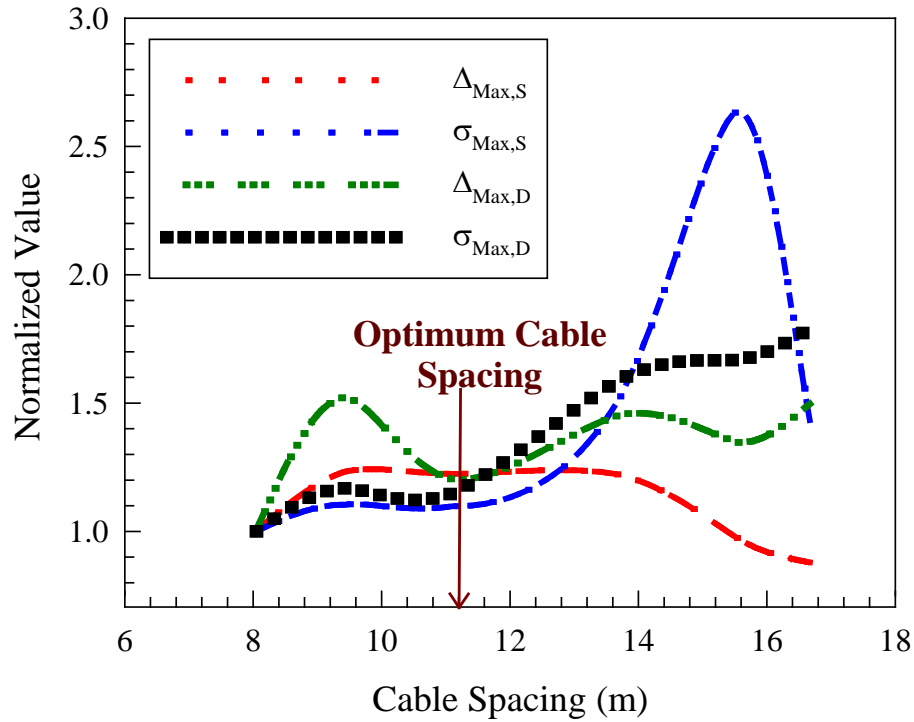


Figure 6. The normalized value of studied parameters with cable spacing ($\Delta_{Max,S}$: Maximum deflection due to static loading; $\Delta_{Max,D}$: deflection due to dynamic loading; $\Delta_{Max,S}$: Maximum stress in cables due to static loading; $\Delta_{Max,A}$: Maximum stress in cables due to dynamic loading).

Equation (6) is plotted in Figure 7, which reflected that a cable spacing greater than 15 m is not possible and less than 8.5 m is too dense. After differentiation once, at cable spacing of 11.2 m, the function has a local minimum, $u = 0.11$ m. In terms of bridge design, 22 cables with cable spacing of 11.11 m are needed on each side of each tower, by using Equation (6) the deformation equal to 0.1717 m.

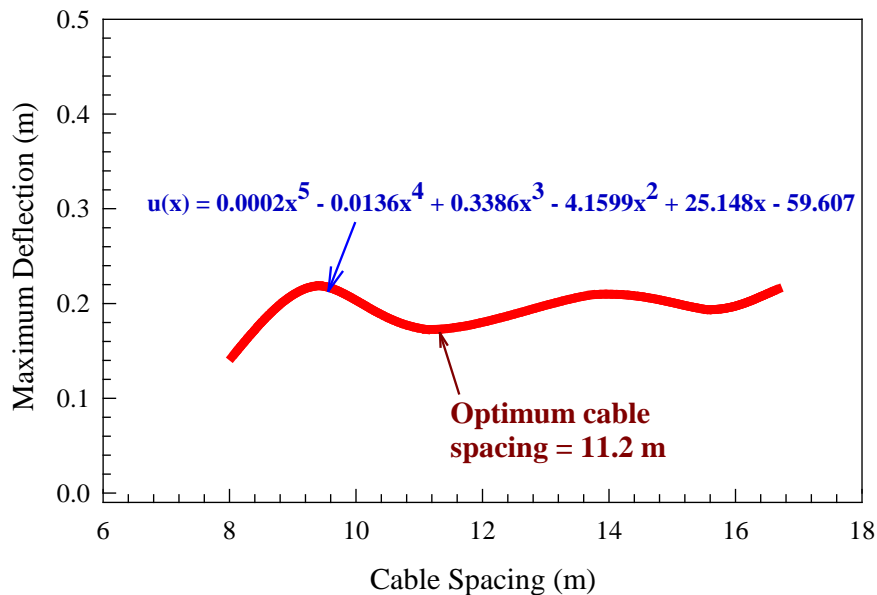


Figure 7. Maximum deformation with cable spacing.

3.6. Materials consumption and total cost

Al-Rousan et al. [10] show that the initial cost of the FRP decks is significantly higher than the reinforced concrete decks; however, the life cycle cost of FRP decks is comparable to the cost of RC decks. Al-Rousan et al. [10] also indicated that the use of the FRP deck instead of the concrete deck would lead to fewer deformations and fewer stresses in the bridge because of the lightweight of the FRP material and the cost of FRP deck is acceptable than the concrete deck for long term stage. Also, the initial cost of the steel bridge

deck is significantly higher than the reinforced concrete bridge deck. However, the use of concrete in the bridge deck is probable to decrease the maintenance cost and increase the service life because the concrete does not exhibit corrosion problems than steel materials.

4. Conclusions

This paper aims to find the optimum cable spacing in terms of vertical deformation and cable stress for static and dynamic analysis. To achieve the objective of this study six models are developed using ABAQUS with six different cable spacing ((8.04 m, 30 cables), (9.42, 25), (11.11, 22), (13.72, 18), (15.56, 16), and (16.67, 15)). The following conclusions are drawn based on the findings of this study:

1. For static loading, the maximum vertical deflection decreased, and the cable stress increased with the increasing of cable spacing.

2. The dynamic loading had more inverse effect on the vertical deflection and direct effect on the cable stress than static loading

3. The cable stresses and the maximum deck deflection increased as the spacing between cables increased. As a result, the unsupported length increased with the cable spacing increasing; this will lead to more significant deflection and higher stresses in the cables.

4. The cable stresses, and the maximum deck deflection increased as the spacing between cables increased. As a result, the unsupported length increased with the cable spacing increasing; this will lead to more significant deflection and more significant stresses in the cables.

5. The cable spacing of 11.2 m is considered as optimum cable spacing in terms of static and dynamic deflection as well as cable stress.

5. Acknowledgments

The authors acknowledge the technical support provided by the Jordan University of Science and Technology.

References

- Negrão, J., Simões, L. Optimization of cable-stayed bridges with three-dimensional modeling. *Computer & Structures*. 1997. 64(1-4). Pp. 741–758. DOI: 10.1016/S0045-7949(96)00166-6
- Simões, L., Negrão, J. Sizing and geometry optimization of cable-stayed bridges. *Computer & Structures*. 1994. 52(2). Pp. 309–321. DOI: 10.1016/0045-7949(94)90283-6
- Simões, L., Negrão, J. Optimization of cable-stayed bridges with box-girder decks. *Advances in Engineering Software*. 2000. 31. Pp. 417–423. DOI: 10.1016/S0965-9978(00)00003-X
- Ferreira, L., Simoes, L. Optimum design of controlled cable stayed bridge subject to earthquakes. *Structure Multidisc Optimization*. 2011. 44. Pp. 517–528. DOI: 10.1007/s00158-011-0628-9
- Baldomir, A., Hernandez, S., Nieto, F., Jurado, J. Cable optimization of a long span cable stayed bridge in La Coruña (Spain). *Advances in Engineering Software*. 2010. 41. Pp. 931–938. DOI: 10.2495/OP090101
- Lute, V., Upadhyay, A., Singh, K. Genetic Algorithms-Based Optimization of Cable Stayed Bridges. *Journal Software Engineering and Applications*. 2011. 4. Pp. 571–578. DOI: 10.4236/jsea.2011.410066.
- Wilson, E.L., Kiureghian, A., Bayo, E.P. A replacement for the SRSS method in seismic analysis. *Earthquake Engineering and Structural Dynamics*. 1981. 9. Pp. 187–192. DOI: 10.1002/eqe.4290090207
- Ito, M. Cable-supported steel bridges: design problems and solutions. *Journal of Construction Steel Research*. 1996. 39. Pp. 69–84. DOI: 10.1016/0143-974X(96)00026-0
- Freire, A.M.S., Negrão, J.H.O., Lopes, A.V. Geometrical nonlinearities on the static analysis of highly flexible steel cable-stayed bridges. *Computer Structures*. 2006. 84(31-32). Pp. 2128–2140. DOI: 10.1016/j.compstruc.2006.08.047
- Al-Rousan, R., Haddad, R.H., Al Hijaj, M.A. Optimization of the economic practicability of fiber-reinforced polymer (FRP) cable-stayed bridge decks. *Bridge Structures*. 2014. 10(4). Pp. 129–143. DOI: 10.3233/BRS-150082
- Wang, P.H., Tseng, T.C., Yang, C.G. Initial shape of cable-stayed bridges. *Journal of Computers Structures*. 1993. 46. Pp. 1095–1106. DOI: 10.1016/0045-7949(93)90095-U
- Abdel-Ghaffar, A.M., Nazmy, A.S. 3-D nonlinear seismic behavior of cable-stayed bridges. *J Struct Eng*. 1991. 117(11). Pp. 3456–3476. DOI: 10.1061/(ASCE)0733-9445(1991)117:11(3456)
- Abdel-Ghaffar, A.M., Khalifa, M.A. Importance of cable vibration in dynamics of cable-stayed bridges. *J Eng Mech*. 1991. 117(11). Pp. 2571–2589. DOI: 10.1061/(ASCE)0733-9399(1991)117:11(2571)
- Soneji, B.B., Jangid, R.S. Influence of soil–structure interaction on the response of seismically isolated cable-stayed bridge. *Soil Dyn Earthq Eng*. 2008. 28(4). Pp. 245–257. DOI: 10.1016/j.soildyn.2007.06.005
- Caetano, E., Cunha, A., Gattulli, V., Lepidi, M. Cable–deck dynamic interactions at the International Gadiana Bridge: on-site measurements and finite element modelling. *Struct. Contr. Health Monit*. 2008. 15(3). Pp. 237–264. DOI: 10.1002/stc.241
- Camara, A., Efthymiou, E. Deck–tower interaction in the transverse seismic response of cable-stayed bridges and optimum configurations. *Eng Struct*. 2016. 124. Pp. 494–506. DOI: 10.1016/j.engstruct.2016.06.017
- Simões, L.M.C., Negrão, J.H.J.O. Optimization of cable-stayed bridges subjected to earthquakes with non-linear behaviour. *Eng Optim*. 1999. 31(4). Pp. 457–478. DOI: 0.1080/03052159908941382
- Ferreira, F.L.S., Simoes, L.M.C. Optimum design of a controlled cable stayed bridge subject to earthquakes. *Struct Multidiscip Optim*. 2011. 44(4). Pp. 517–528. DOI: 0.1007/s00158-011-0628-9

19. Baldomir, A., Hernandez, S., Nieto, F., Jurado, J.A. Cable optimization of a long span cable stayed bridge in La Coruña (Spain). *Adv Eng Softw.* 2010. 41(7-8). Pp. 931–938. DOI: 10.2495/OP090101
20. Sung, Y.-C., Chang, D.-W., Teo, E.-H. Optimum post-tensioning cable forces of Mau- Lo Hsi cable-stayed bridge. *Eng Struct.* 2006. 28(10). Pp. 1407–1417. DOI: 10.1016/j.engstruct.2006.01.009
21. Hassan, M.M. Optimization of stay cables in cable-stayed bridges using finite element, genetic algorithm, and B-spline combined technique. *Eng Struct.* 2013. 49. Pp. 643–654. DOI: 10.1016/j.engstruct.2012.11.036
22. Hassan, M.M., Nassef, A.O., El Damatty, A.A. Determination of optimum post-tensioning cable forces of cable-stayed bridges. *Eng Struct.* 2012. 44. Pp. 248–259. DOI: 10.1016/j.engstruct.2012.06.009
23. Martins, A.M.B., Simões, L.M.C., Negrão, J.H.J.O. Optimization of cable forces on concrete cable-stayed bridges including geometrical nonlinearities. *Comput Struct.* 2015. 155. Pp. 18–27. DOI: 10.1016/j.compstruc.2015.02.032.
24. Martins, A.M.B., Simões, L.M.C., Negrão, J.H.J.O. Cable stretching force optimization of concrete cable-stayed bridges including construction stages and time-dependent effects. *Struct Multidiscip Optim.* 2015. 51(3). Pp. 757–772. DOI: 10.1007/s00158-014-1153-4
25. Hassan, M.M., Nassef, A.O., El Damatty, A.A. Optimal design of semi-fan cable-stayed bridges. *Can J Civ Eng.* 2013. 40(3). Pp. 285–97. DOI: 10.1139/cjce-2012-0032

Contacts:

Rajai Al-Rousan, +962799887574; rzalrousan@just.edu.jo

© Al-Rousan, Rajai, 2019



DOI: 10.18720/MCE.91.6

The fine high-calcium fly ash as the basis of composite cementing material

O.M. Sharonova*, V.V. Yumashev, L.A. Solovyov, A.G. Anshits

Federal Research Center «Krasnoyarsk Science Center of the Siberian Branch of the Russian Academy of Sciences», Krasnoyarsk, Russia

** E-mail: sharon05@yandex.ru*

Keywords: high-calcium fly ash, cementitious materials, superplasticizer, hydration, compressive strength, calcium compounds, X-ray diffraction

Abstract. The high-calcium fly ashes (HCFA) of Krasnoyarsk TPP-2, Russia were studied. The HCFA were selected from each of the 4 fields of the electrostatic precipitator. It was determined that the size distribution, chemical and quantitative phase composition vary significantly from 1st to 4th EF field. The fine high-calcium fly ash ($d_{90} < 10$ microns) selected from the fourth field of electrostatic precipitator was the source for high strength specimens. In the composition with a superplasticizer at a water:binder ratio of $W/B = 0.25$ the specimens were made and then cured from 1 to 120 days, with their compressive strength increasing from 17 to 72 MPa. The strength of these specimens is comparable to the strength of specimens based on Portland cement PC 42.5 N without superplasticizer. The methods of simultaneous thermal analysis (STA) and quantitative X-ray phase analysis (XRD) were used to study phase transformations of high-calcium fly ash in the process of hydration curing. The major newly formed phases are ettringite $3CaO \cdot Al_2O_3 \cdot 3CaSO_4 \cdot 32H_2O$, as well as calcium carboaluminate hydrates $Ca_4Al_2(OH)_{13}(CO_3)0.5 \cdot 4H_2O$ and $Ca_4Al_2(OH)_{12}CO_3 \cdot 5H_2O$ with low crystallinity. The new phases can form a wide range of solid solutions by replacing Al^{3+} with Fe^{3+} . The more the curing age was, the more transformations of calcium silicate amorphous substance contribute to form cryptocrystalline calcium hydrosilicates that increased the initial and long-term strength of the material. The phase transformations and strength indicators allow to use fine high-calcium fly ash of coal-fired power plants as an independent cementing material in modern technologies for producing building materials, in particular, in the technology of self-compacting composite concrete (SCC). The proposed alternative to cement contributes to the solution of a complex environmental problem: (1) in the heat power engineering the accumulation of fine ash particles can be lowered with consequent reduction of the pollution of water, soil and atmosphere with thin dust particles, and (2) in the construction materials industry a part of the cement can be replaced by the fine HCFA, that will save energy and natural resources.

1. Introduction

Although the share of alternative energy sources is growing, the contribution of coal-fired power plants to electricity production remains quite high and is about 40 % in the world [1]. Coal fly ashes, a by-product of coal combustion, have a complex composition, and therefore differ in the properties and methods of utilization [2]. Recycling of coal fly ashes is constantly increasing, they are used in cement and concrete production, road base and pavement construction, soil amendment, zeolite synthesis, ceramic industry; as filler in polymer, but the current average utilization rate is don't exceed 25 % in the world [1–4]. High calcium fly ashes have a smaller contribution to ash wastes compared with aluminosilicate fly ashes, but they are more toxic when stored in ash dumps, since they form alkaline solutions with pH 11–13 [3].

The use of coal ash in the construction industry as a substitute for cement and as an active mineral additive to concrete is the most promising trend of their large-scale use [1–7]. The HCFA are composed of crystalline phases with hydraulic activity (lime, aluminates, sulfates, sulfoaluminates, aluminoferrites of calcium), as well as active glass-crystal microspheres, due to the high content of Ca^{2+} cations in the glass [8–12]. For those reasons, in addition to pozzolanic activity, they have independent cementing properties. Usually 25–40 % of Portland cement (PC) is replaced with such ashes [13]. The use of high-calcium fly ash from the combustion of Kansk-Achinsk coal in the production of autoclaved and non-autoclaved aerated concrete, in addition to saving cement, leads to a decrease in shrinkage and an increase in the strength of products [12]. The high-volume fly ash concretes where 50–70 % PC was substituted, are of great interest because they bring ecological, economical and technological benefits [2]. It was shown that it is possible to produce the concrete with the strength of 28–32 MPa by 28 days of hardening, with 100 % replacement of PC with HCFA, in composition with recycled glass [14].

The current trend in the energy industry is the modernization of thermal power plants, in order to increase the degree of exhaust gas purification to 99–99.7 %, including ash particles. This aim was achieved at a number of foreign and Russian thermal power plants by improving the operation of electrostatic precipitators or their combination with bag filters [15]. As a result, the capture of the smallest ash particles less than 10 microns in size and, especially, less than 2.5 microns was increased. Micro- and submicron ash particles can be effectively used in modern technologies to produce new materials, in particular, self-compacting concrete (SCC) with the compressive strength from 50 to 100 MPa [16]. The key element of the SCC technology is the use of polymer superplasticizer, which ensures the effective dispersion of fine cementing components in the liquid phase and the formation of a dense and durable microstructure due to close contact and interaction of the newly formed phases with each other and with unreacted components [16, 17].

High calcium fly ashes trapped in different fields of electrostatic precipitators vary dramatically in fractional composition and, to a considerable extent, in chemical and phase composition [9, 18–20]. It was found [9], that the dispersity increases significantly along the gas-dust flow, for example, 90 % of the fly ash particles from the 1st field are less than 40 microns in size; from the 2nd and 3rd fields are less than 12 microns; from the 4th field are less than 8 microns. It was noticed that the content of CaO , SiO_2 , and Fe_2O_3 phases decreases from the 1st to the 4th fields of the electrostatic precipitator, while the contents of CaSO_4 and glass increase. Thus, HCFA obtained in different fields of the electrostatic precipitator are ash separation products significantly various in composition and, especially, particle size distribution, and, consequently, in their cementing properties. The main regularities to form the composition and properties of HCFA in the fields of electrostatic precipitators are described by the authors [19, 20]. Based on these data, it was proposed to use finely dispersed fly ashes of the last fields of electrostatic precipitators containing a smaller amount of free CaO , as a binder material.

The aim of this work is to study the dispersity and chemical and phase composition of high-calcium fly ashes, selected from each of the 4 fields of the electrostatic precipitator and to determine their cementing properties, which are promising for obtaining high-strength composite materials.

2. Materials and Methods

2.1. Materials

The objects of the study were high-calcium fly ashes (HCFA) from burning of pulverized low-ash (11 %) brown coal grade B2 of the Kansk-Achinsk basin, Russia. The coal was burned at the Krasnoyarsk TPP-2 (Krasnoyarsk, Russia) in boiler units of the BKZ-420 type with liquid slag removal at a temperature of 1400–1500 °C. High-calcium fly ashes (1–4) were selected from each of the 4 fields of electrostatic precipitator in a facility with an ash collection efficiency of ≥ 98 %. Portland cement PC 42.5N of the Krasnoyarsk cement plant was taken for comparison.

2.2. Methods

The macro component composition (components SiO_2 , Al_2O_3 , Fe_2O_3 , CaO , MgO , SO_3 , Na_2O , K_2O , and TiO_2) and the loss on ignition (LOI) were determined by chemical analysis methods according to National standard GOST 5382–91. The particle size distribution was measured with a Fritsch Analysette 22 MicroTec laser particle analyzer (Germany) using a dry cell. The SEM images for fly ashes were taken with a Hitachi TM-1000 electron microscope (Japan).

X-ray powder diffraction quantitative phase analysis was carried out using the full-profile Rietveld method and the derivative difference minimization approach [21]. The diffractograms were recorded in the reflection geometry on a PANalytical X'Pert PRO diffractometer (Co $K\alpha$ radiation, graphite monochromator, scan range $2\theta = 7$ – 100°) equipped with a PIXcel detector. The weight fraction of crystalline and amorphous components was determined by the external standard method with corundum used as the standard. The overall absorption coefficients of the samples were calculated from the total elemental composition according

to the chemical analysis data. This method was successfully applied to determine the quantitative phase composition of high-calcium fly ash middlings [9] and narrow fractions of ferrospheres recovered from fly ashes [22].

The specimens shaped as 20×20×20 mm cubes were manufactured from 100 % of fly ash selected from each of the 3rd and 4th fields of electrostatic precipitator at a water/binder ratio $W/B = 0.4$. For comparison, the same specimens were made from 100 % Portland cement PC 42.5N taken from the Krasnoyarsk cement plant. For the finest fly ash of the 4th field of the electrostatic precipitator, the specimens were made at $W/B = 0.25$ with addition of the Melflux 5581F superplasticizer (0.12 wt %).

The concentration of superplasticizer was chosen according to the results of tests for fluidity. The fluidity was measured at 20 °C from the diameter of a spot of binder paste flowing from a tube with an internal diameter of 50 mm and a height of 51 mm according to JASS 15 M103 [23]. The spot diameter (F) was used to calculate the relative flow surface area (G) characterizing the deformability of a mixture by the equation $G = F^2/50^2 - 1$. At $W/B = 0.25$, acceptable $G = 8$ was attained at a Melflux concentration of 0.12 %. The specimens were stored above the water layer in the desiccators for 1, 3, 7, 28, 60, 80, and 120 days. The strength tests of specimens were performed on an Instron 3360 tabletop dual-column testing machine (United States) at a return speed of 5 mm/min.

The simultaneous thermal analysis (STA) of hydrated specimens after drying for 2 h at 60 °C was performed on a Netzsch Jupiter STA 449C analyzer (Germany) with a Netzsch Aeolos QMS 403C mass spectrometer (Germany) in lidded Pt–Rh crucibles using a sample portion of 20.0 ± 0.1 mg. The measurement of the mass change (TG, DTG), the heat flux (DSC), and the composition of gaseous products (by Ar^+ , O_2^+ , CO_2^+ , CO^+ , H_2O^+ , and SO_2^+ molecular ions) was performed in the mode of linear temperature increase at a speed of 10 °C / min within a temperature range of 40–1000 °C, supplying the 20 % O_2 + 80 % Ar gas mixture (total flow rate, 50 cm³(NTP)/min).

3. Results and Discussions

3.1. Initial fly ashes

The studied high-calcium fly ashes of 1–4 fields of electrostatic precipitator significantly differ from each other by their fineness (Figure 1). About 90 % of particles (d_{90}) of the fly ashes selected from the 1st and 2nd fields of the electrostatic precipitator are less than 40 microns, and 50 % of particles (d_{50}) are less than 13 microns. The fly ashes of the 3rd and, especially, the 4th field of electrostatic precipitator have a higher dispersity, the value d_{90} of which is about 30 and 10 microns, and d_{50} is about 9 and 4 microns, respectively. The particle size distribution for the PC 42.5 N (Figure 1) is somewhat shifted towards larger particles, the values of d_{90} and d_{50} are 55 and 20 microns, respectively. At the same time, the content of particles less than 10 microns in cement is close to the fly ashes of the 1st and 2nd fields of the electrostatic precipitator.

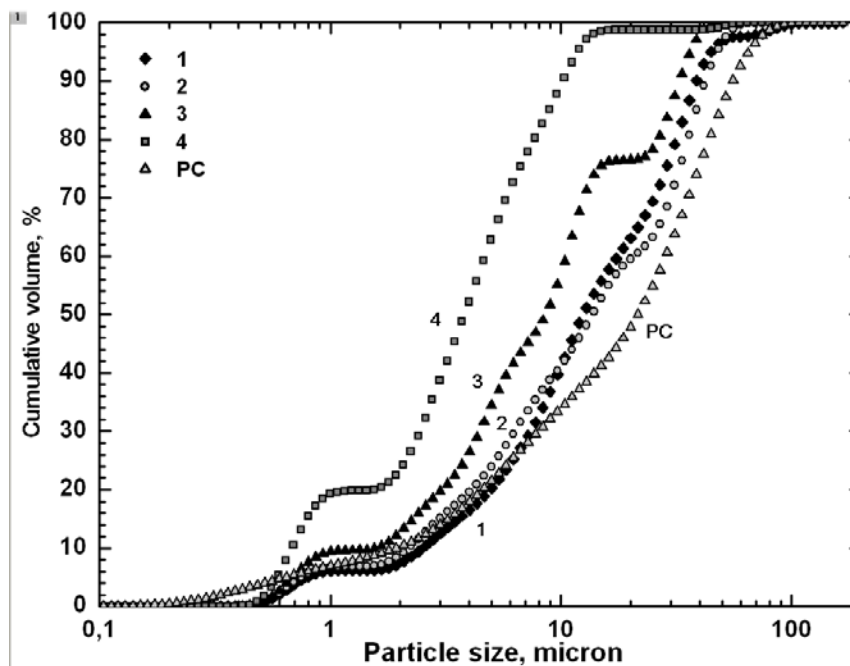


Figure 1. Particle size distribution for HCFA selected from 1–4 fields of the electrostatic precipitator (1–4), and for Portland cement 42.5 N (PC).

The general view of the fly ashes taken from the 1st and 4th fields of the electrostatic precipitator is shown in Figure 2, from which it follows that the fly ashes consist of mainly microspheres with the different size and morphology. The studied high-calcium fly ashes were formed in a boiler with liquid slag removal at a temperature of 1400–1500 °C, which led to the melting of the ash substance and the formation of melt drops in the gas-air flow, and during cooling, microspherical particles [11].

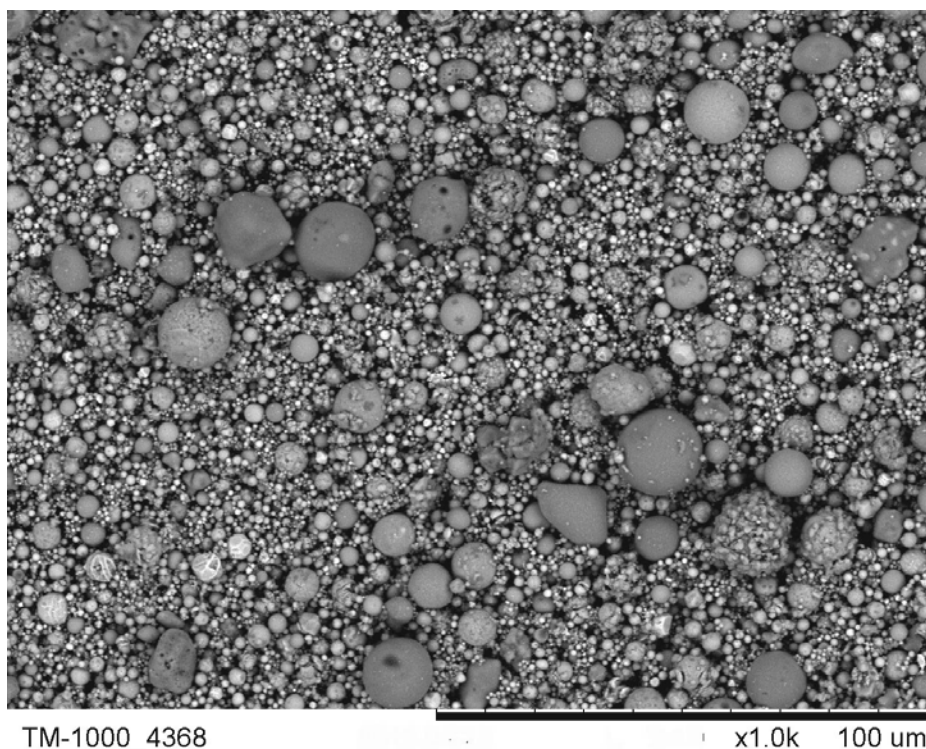
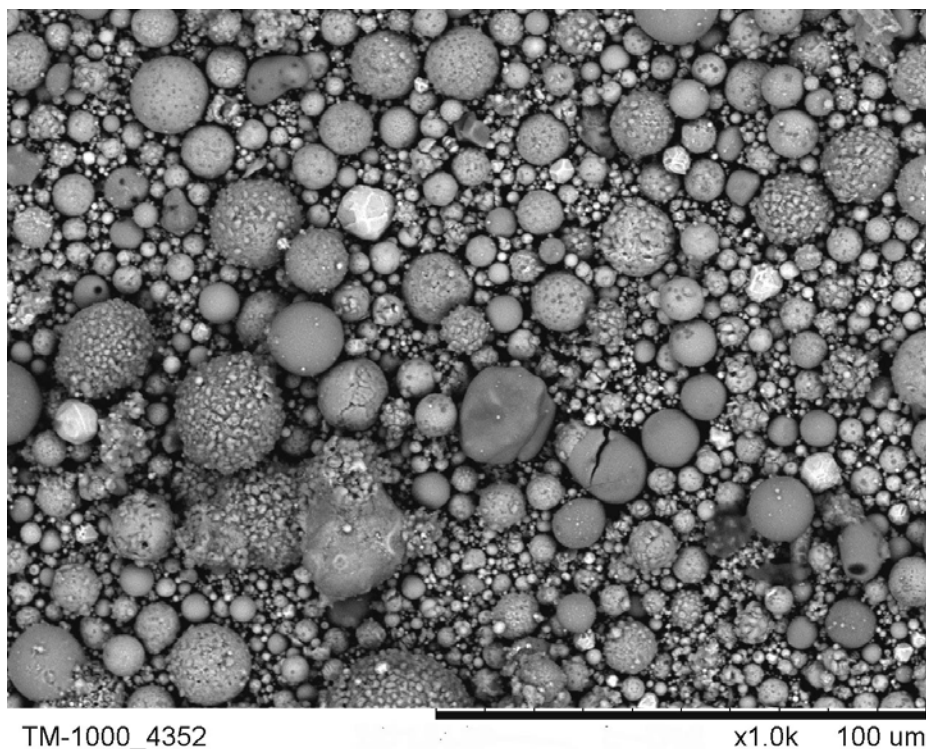


Figure 2. SEM images for HCFA selected from 1st (top) and 4th (bottom) fields of the electrostatic precipitator.

The chemical composition of fly ashes 1–4 (Table 1) is presented by predominant CaO (40–46 wt %), rather plentiful SiO₂ (21–28 wt %), and a much lower content of other macro components (wt %): Al₂O₃ (4–7); Fe₂O₃ (12–14); MgO (8–10) and SO₃ (2–4). The composition of fly ashes 1–4 is close to PC [22, 23] by the content of SiO₂ and Al₂O₃ (Table 1), but differs from it by a lower content of CaO and a higher content of Fe₂O₃, MgO, and SO₃.

Table 1. Chemical composition (wt. %) of the HCFA selected from 1–4 fields of the electrostatic precipitator and Portland cement (PC).

HCFA	Components									
	CaO	SiO ₂	Al ₂ O ₃	Fe ₂ O ₃	MgO	$\frac{SO_3}{SO_3}$	Na ₂ O	K ₂ O	TiO ₂	LOI
1	46.15	20.89	4.53	12.65	9.92	3.60	0.75	0.20	0.25	0.60
2	40.6	27.60	4.43	12.06	9.28	3.83	0.80	0.23	0.27	0.60
3	40.0	24.26	6.71	13.45	9.60	3.94	0.72	0.18	0.20	1.0
4	39.69	24.60	7.30	14.29	8.24	2.29	0.71	0.20	0.25	1.96
PC 42.5N	63.99	20.41	4.87	4.18	–	2.46	–	–	–	–
PC [24]	66.4	21.9	5.7	3.2	1.2	0.4	0.7	–	0.3	–
PC [25]	67.17	22.14	3.12	2.51	–	2.13	–	–	–	1.68

The major component in the phase composition of fly ashes 1–4 (Table 2) is a predominantly (Ca,Fe)-silicate amorphous phase (19–42 wt %). The clinker phases, such as tricalcium aluminate 3CaO•Al₂O₃ (9.9–16 wt %) and calcium aluminoferrite Ca₂Fe_xAl_yO₅ (13.4–18.7 wt %) are in amounts comparable with the PC clinker. At the same time, the fly ashes do not contain the Ca₃SiO₅ and Ca₂SiO₄ calcium silicate phases, which attain 75–80 wt % in conventional PCs (Table 2) and cause their binding properties. Moreover, the fly ashes contain a considerable amount of free oxides CaO, MgO, SiO₂ as well as the phases of CaCO₃ and CaSO₄. It should be noted that the content of amorphous phase grows from 19 to 42 wt %, while the content of free CaO decreases from 23.5 to 4.2 wt % in the series of fly ashes from 1 to 4 (Table 2). From a comparison of the chemical and phase composition of the HCFA, it follows that the predominant components of the amorphous phase are (in decreasing order) SiO₂, CaO and Fe₂O₃. It should be noted also that the ratio of SiO₂/CaO in its composition is significantly reduced (from 4.7 to 1.3) in a row of fly ash from 1 to 4. In the calculations of glass composition for the phase of calcium aluminoferrite Ca₂Fe_xAl_yO₅, x = y = 0.5 was used.

Table 2. Phase composition (wt %) of HCFA selected from 1–4 fields of the electrostatic precipitator and Portland cement (PC).

HCFA	Phases													
	Ca ₃ Al ₂ O ₆	Ca ₂ Fe _x Al _y O ₅	CaO	MgO	α - SiO ₂	CaCO ₃	CaSO ₄	Ca(OH) ₂	Ca ₃ SiO ₅	Ca ₂ SiO ₄	Ferrosphenel	CaSO ₄ *0.5H ₂ O	CaSO ₄ *2H ₂ O	Amorphous phase
1	12.7	18.7	23.5	9.3	6.2	–	7.4	–	–	–	3.2	–	–	19.0
2	16.0	13.4	14.6	7.5	9.1	3.9	4.8	–	–	–	2.1	–	–	28.6
3	14.7	13.8	14.0	6.9	6.7	3.0	5.8	–	–	–	2.6	–	–	32.6
4	9.9	16.9	4.2	5.7	5.3	4.9	6.5	2.1	–	–	2.4	–	–	42.1
PC 42.5N	5.8	13.2	–	–	0.5	2.4	–	–	64.5	9.2	–	3.9	0.5	–
PC [24]	7.9	10.1	0.6	0.2	–	–	–	–	66.9	13.2	–	–	–	–
PC [25]	1.2	7.0	–	–	–	1.8	1.4	–	71.1	15.0	–	–	1.2	–

3.2. Compressive Strength of Cured Specimens

As follows from the data presented in Figure 3, the compressive strength (σ_{comp}) of specimens made from 100 % fly ash of the 3rd field at $W/T = 0.4$ (curve 1) is almost 2 times lower compared to specimens based on fly ash of the 4th field (curve 2). For curve 2, it can be seen that the σ_{comp} value increases from 11 to 22 MPa and then to 30 MPa with the curing age 3, 28 and 80 days, respectively. The fly ashes 3 and 4 (Table 1) have a very similar chemical composition, but significantly differ in particle size (Figure 1). It follows that the higher strength of the samples based on fly ash of the 4th field is presumably due to their higher dispersion ($d_{90} < 10$ microns), which contributes to an accelerated and more complete interaction of the components of microspheres (especially free CaO and amorphous phase) with the liquid phase to obtain strong structures. Strength tests of samples based on 100 % fly ashes of the 1st and 2nd fields seem to be irrational, since they are characterized by even lower dispersion, higher content of free CaO and, as expected, will have lower strength. It should be noted that the specimens based on fly ash 4 are significantly inferior to the comparison the specimens prepared from PC 42.5N at $W/B = 0.4$ (Figure 3, curve 3), for which the σ_{comp} value is 25, 48 and 61 MPa at a curing age of 3, 28 and 80 days, respectively.

The high tendency to agglomeration of finely dispersed HCFA does not allow to fully implementing the possibilities of their hydration interaction. The use of high-polymer polycarboxylate superplasticizers prevents

agglomeration, changes the surface properties and promotes the dispersion of micron and submicron particles, leading to the interaction of each individual particle with the liquid phase [16, 17]. The use of 0.12 wt % superplasticizer Melflux 5581F additive allowed reducing the value of W/B to 0.25, while maintaining the necessary fluidity. As a result, high-strength specimens were obtained based on 100 % fly ash of the 4th field (Figure 3, curve 4), the σ_{comp} value of which increases from 24 to 45 and 72 MPa on days 3, 28, and 120, respectively. Thus, the use of finest HCFA in a composition with 0.12 % polycarboxylate superplasticizer Melflux 5581F made it possible to produce specimens with the σ_{comp} value comparable to the strength of specimens based on PC 42.5 N without the addition of superplasticizer. High strength specimens based on HCFA of 4-field of the electrostatic precipitator with the addition of superplasticizer were studied by the CTA and XRD methods in detail. Some of the results of these studies were published in [26].

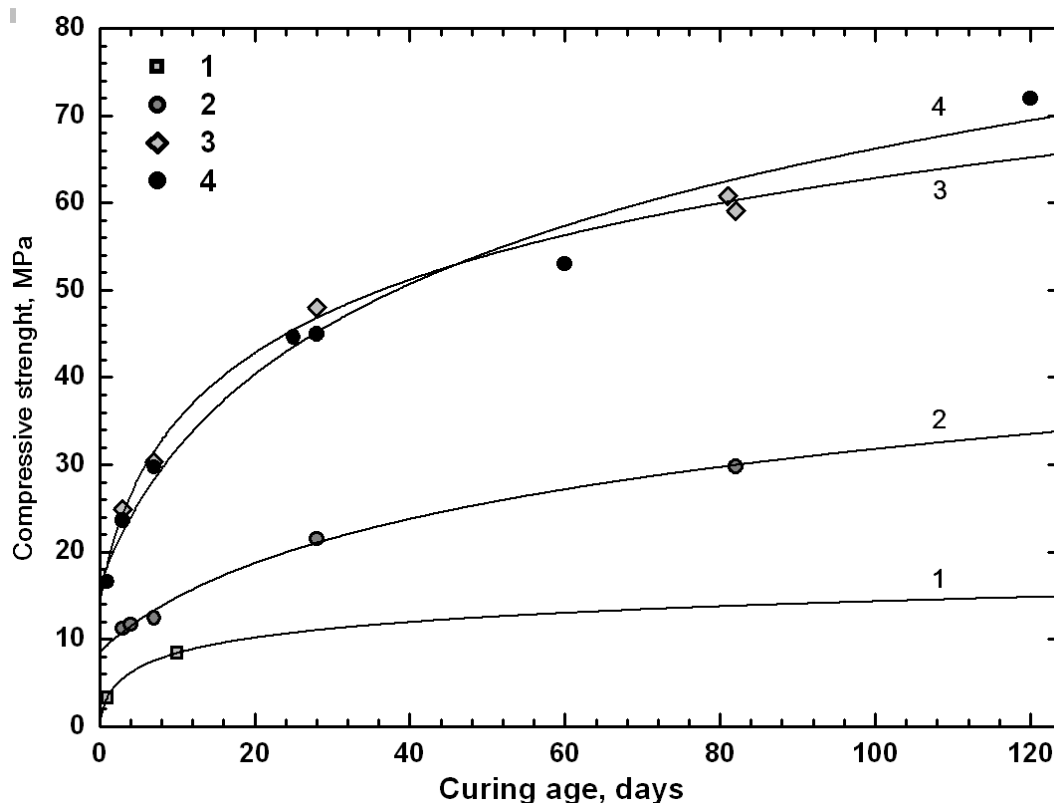
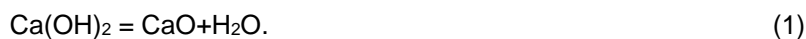


Figure 3. Dependence of the compressive strength on a curing age for the specimens, made at $W/B = 0.4$ (1 and 2 – from HCFA of 3rd and 4th fields; 3 – from Portland cement 42.5N) and 4 – from HCFA of 4th fields with Melflux 5581F superplasticizer at $W/B = 0.25$.

3.3. STA analysis of Cured Specimens

From the data in Figure 4a for the specimens after three days of hardening it follows that intensive removal of bound water occurs at temperatures of 60–200 °C, the significantly lower water losses are observed at 200–300 °C. At temperatures of 410–520 °C, characteristic peak of portlandite decomposition by reaction (1) is observed.



Weight loss at the temperature 520–750 °C is caused by the decomposition of calcium carbonate by the reaction (2):



With an increase in curing age up to 28 days (Figure 4b), water losses increase in all ranges, but to a greater extent at temperatures of 60–200 °C. The peak of water removal in the range of 320–410 °C also becomes more distinct.

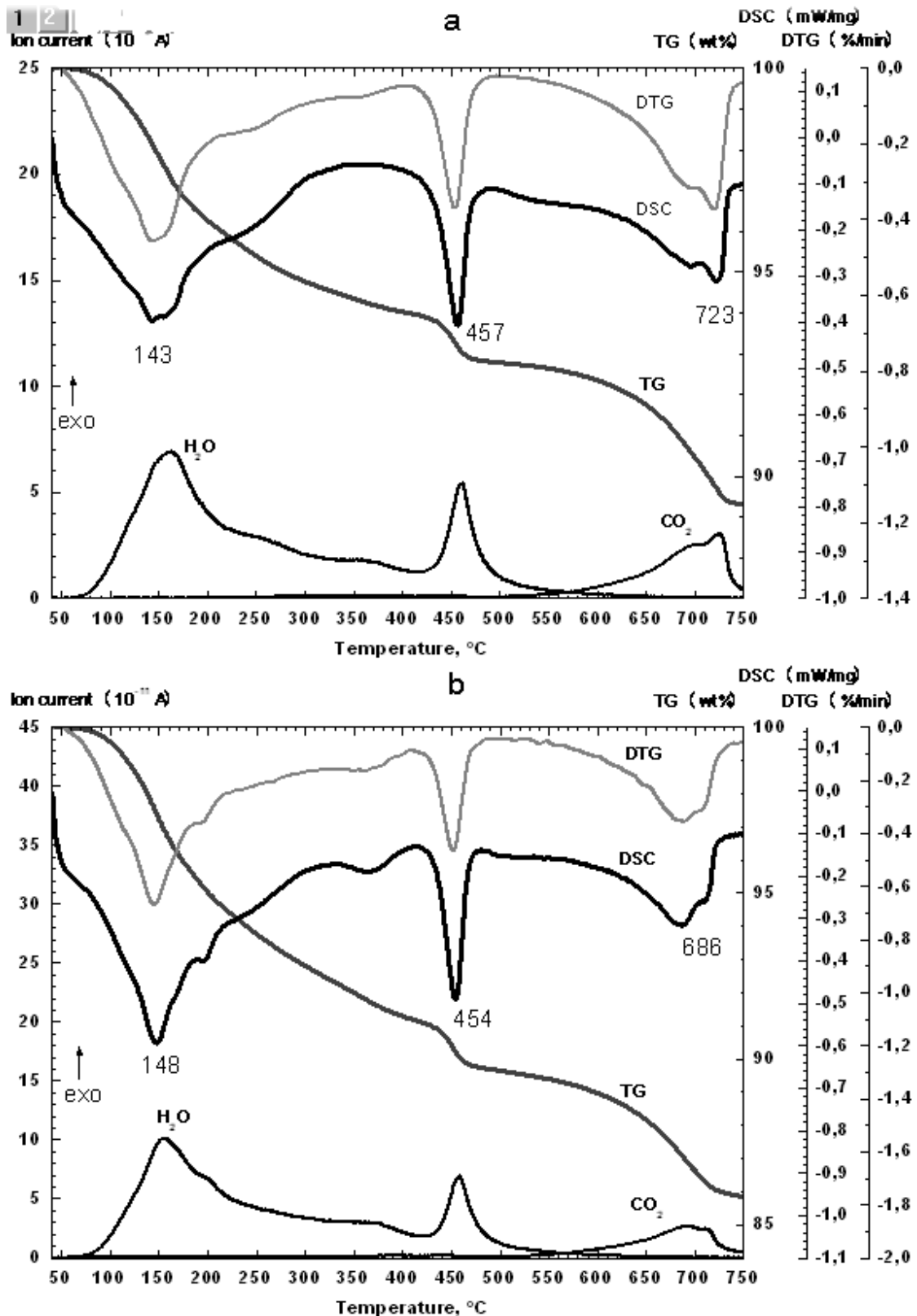


Figure 4. STA data (TG, DTG, DSC and MS of H₂O and CO₂) for the specimens made from HCFA of 4th fields with Meliflux 5581F superplasticizer at W/B = 0.25 at a curing age 3 days (a) and 28 days (b).

The data in Table 3 shows that the total loss of bound water Σ (60–410 °C) increases from 5.4 to 12.7 wt % with an increase in the curing age from 1 to 120 days. The greatest contribution to water desorption is observed in the temperature range of 60–200 °C (increasing from 3.6 to 8.1 wt %), and to less extent in the range of 200–320 °C (increasing from 1.35 to 2.9 wt %). In the ranges 320–410 °C and 410–520 °C, the water losses increase during curing age 1–60 days, and decrease at 120 days. The losses of weight due to decarbonization of CaCO₃ in the range of 520–750 °C increase for 28-days old specimens, and significantly decrease for the specimens of long-term curing (60 and 120 days).

Table 3. Weight loss (wt %) for the specimens produced from HCFA of 4th field of the electrostatic precipitator at different curing age.

Curing age, days	Temperature range (°C)						
	60–200	200–320	320–410	$\Sigma(60-410)$	410–520	520–750	$\Sigma(60-750)$
1	3.56	1.35	0.49	5.40	1.16	3.45	10.01
3	3.72	1.68	0.62	6.02	1.24	3.43	10.69
7	3.96	1.71	0.71	6.38	1.33	3.38	11.09
28	4.96	2.56	1.28	8.80	1.65	3.71	14.16
60	7.20	2.79	1.72	11.71	1.99	2.58	16.28
120	8.13	2.90	1.69	12.72	1.41	1.90	16.03

It is known for the systems of similar composition [24, 27], that endothermic peaks in the dehydration range below 200 °C are correlated with the removal of the main part of water from ettringite, as well as from weakly crystallized and amorphous phases of calcium hydrosilicates. According to [24], the maximum intensity at 135–140 °C corresponds to the dehydration of the ettringite, which is actively formed on the first day of Portland cement hydration, and the peak at 115–125 °C corresponds to the dehydration of amorphous (cryptocrystalline) calcium hydrosilicates. Much lower water losses occur in the range of 200–320 °C and correspond to the dehydration of AFm phases and more ordered structures of calcium hydrosilicates [27]. A weak endothermic peak with a water loss in the range of 320–410 °C attributes to the dehydration of poorly crystallized boehmite $\text{AlO}(\text{OH})$ or other decomposition products of ettringite, as well as $\text{CaO} \cdot \text{Al}_2\text{O}_3 \cdot 6\text{H}_2\text{O}$ hydrates [28, 29]. An increase in the amount of $\text{Ca}(\text{OH})_2$, which is an indicator of pozzolanic reactions [30, 31], means that its formation during hydration of CaO exceeds its consumption in pozzolanic reactions during 1–60 days of curing, although this trend changes for 120 days of curing.

Thus, the STA study of specimens cured within 1–120 days made it possible to establish the forms of bound water and the tendencies of their change in curing age. It is known that the strength of cement stone grows along with increasing quantity of the hydrated substance [22]. As follows from Table 3, the amount of bound water, which is removed from crystalline hydrates and their thermal decomposition products in the range of 60–410 °C, is increasing from 5.4 to 12.7 wt. % for 1–120 days old specimens and correlates with the strength of the samples changing from 17 to 72 MPa.

3.4. Quantitative Phase Composition of Cured Specimens

The essence of hydraulic binders is to form strong structures of hydrate compounds as a result of their chemical and physicochemical transformations when they interact with water.

As follows from Table 4, only calcium aluminoferrite $\text{Ca}_2\text{Fe}_x\text{Al}_y\text{O}_5$ and calcium sulfate CaSO_4 crystalline phases completely reacted on the 3rd day of hydration curing. The decrease in the content of CaO phase and the amorphous phase is observed. Ettringite (theoretical composition $3\text{CaO} \cdot \text{Al}_2\text{O}_3 \cdot 3\text{CaSO}_4 \cdot 32\text{H}_2\text{O}$), calcium carbonate CaCO_3 and portlandite $\text{Ca}(\text{OH})_2$ are actively formed.

On the 28th day of hardening, the main difference is a significant decrease in the amount of calcium carbonate and the formation of poorly crystallized hydrates of calcium carboaluminates $\text{Ca}_4\text{Al}_2(\text{OH})_{13}(\text{CO}_3)_{0.5} \cdot 4\text{H}_2\text{O}$ and $\text{Ca}_4\text{Al}_2(\text{OH})_{12}\text{CO}_3 \cdot 5\text{H}_2\text{O}$. In addition, the amount of portlandite significantly increases, but the content of the amorphous phase decreases. On the 120th day of curing, the content of portlandite decreases and the ratio for hydrates of calcium carboaluminates changes, the $\text{Ca}_4\text{Al}_2(\text{OH})_{12}\text{CO}_3 \cdot 5\text{H}_2\text{O}$ content increases with a simultaneous decrease in $\text{Ca}_4\text{Al}_2(\text{OH})_{13}(\text{CO}_3)_{0.5} \cdot 4\text{H}_2\text{O}$.

The hydration products of high-calcium fly ashes of Kansk-Achinsk coal [12, 32] contained tricalcium sulfoaluminate (ettringite $3\text{CaO} \cdot \text{Al}_2\text{O}_3 \cdot 3\text{CaSO}_4 \cdot 32\text{H}_2\text{O}$) and monocalcium sulfoaluminate $3\text{CaO} \cdot \text{Al}_2\text{O}_3 \cdot \text{CaSO}_4 \cdot 12\text{H}_2\text{O}$, as well as calcium hydrosilicate gel C-S-H and C-A-S-H. The formation of ettringite and monocalcium sulfoaluminate phases was accompanied by the disappearance of the anhydrite phase and a decrease of the line intensity for the phases CaO , aluminate and calcium aluminoferrite.

From the chemistry of hardening of Portland cements, it is known that ettringite is formed by the interaction of hydrated forms of calcium aluminate $\text{Ca}_3\text{Al}_2\text{O}_6$ and CaSO_4 [24]. However, taking into account a small decrease in the $\text{Ca}_3\text{Al}_2\text{O}_6$ content for the 28-days and 120-days old specimens comparing to the initial one, the formation of ettringite during hydration of the HCFA occurs mainly due to the participation of calcium aluminoferrite $\text{Ca}_2\text{Fe}_x\text{Al}_y\text{O}_5$. It was also established [24, 30] that the hydration products of calcium aluminoferrite are in many respects similar to the hydration products of $\text{Ca}_3\text{Al}_2\text{O}_6$ aluminate, forming a wide range of solid solutions of hydrates of the type $4\text{CaO}(\text{Al}_{1-x}, \text{Fe}_x)_2\text{O}_3 \cdot 19\text{H}_2\text{O}$ or $3\text{CaO}(\text{Al}_{1-x}, \text{Fe}_x)_2\text{O}_3 \cdot 6\text{H}_2\text{O}$. Interacting with CaSO_4 , they can form almost continuous series of solid solutions of Al, Fe-ettringites.

Table 4. Phase composition (wt %) of the initial HCFA selected from of 4th field of the electrostatic precipitator and the specimens produced from this HCFA at curing age 3, 28 and 120 days.

Phase	Initial HCFA	3 days	28 days [26]	120 days [26]
<i>Crystalline phases</i>				
Ca ₂ Fe _x Al _y O ₅	16.9	–	–	–
Ca ₃ Al ₂ O ₆	9.9	11.9	8.1	6.9
CaSO ₄	6.5	–	–	–
MgO	5.7	6.1	4.0	4.2
α-SiO ₂ (quartz)	5.3	5.6	5.7	6.3
CaCO ₃	4.9	12.6	2.1	3.0
CaO	4.2	3.3	2.3	1.4
Ferrosipinel	2.4	2.9	2.7	2.9
Ca(OH) ₂	2.1	4.0	9.6	8.1
Ca ₆ Al ₂ (SO ₄) ₃ (OH) ₁₂ ·26H ₂ O (ettringite)	–	8.6	12.4	15.5
Ca ₂ SiO ₄ (larnite)	–	5.7	3.4	4.0
Σ	57.9	60.7	50.3	52.3
<i>Poorly crystallized and amorphous phase</i>				
Ca ₄ Al ₂ (OH) ₁₃ (CO ₃) _{0.5} ·4H ₂ O	–	2.0	14.1	5.9
Ca ₄ Al ₂ (OH) ₁₂ CO ₃ ·5H ₂ O	–	–	5.3	12.7
<i>Amorphous phase</i>	42.1	37.3	30.3	29.1
Σ	42.1	39.3	49.7	47.7

About 21 % and 27 % of the Ca₂Fe_xAl_yO₅ phase is consumed on the formation of ettringite according to the data for 28 and 120 days. Under the conditions of sulfate ion deficiency, the significant part of Ca₂Fe_xAl_yO₅ is actively involved in the formation of calcium carboaluminate hydrates, which belong to the so-called AFm phases. It is known [24] that hydrates of calcium aluminoferrites in the presence of Ca(OH)₂ and CaSO₄ can form AFm phases of the general composition [Ca₂ (Al, Fe) (OH)₆] • X • xH₂O, where X is one singly charged anion or 0.5 doubly charged anion. The anions X can be OH⁻, SO₄²⁻ and CO₃²⁻. It should be noted that Al- and Fe-substituted AFm phases are isostructural analogues and, depending on temperature, they form solid solutions of various degrees of substitution. In the presence of Ca (OH)₂ these phases are weakly crystallized and closely mixed with each other and with other phases, in particular, with the calcium silicate hydrates [24]. Thus, the phases of ettringite and calcium carboaluminate hydrates are solid solutions due to the isomorphic substitution of Al³⁺ for Fe³⁺. It was not possible to assess the degree of substitution by XRD, mainly due to the low crystallinity of these phases.

The main source of silicates in the HCFA is the amorphous phase of microspheres, which reactivity, as known [8, 24], grows with increasing calcium content. In the initial period, the microspheres having the highest calcium content will participate in the dissolution. Later, as the pH of the solution and the reaction time will increase, the microspheres with lower calcium content and higher silicon content will interact. The result of long hydration time is an increasing amount of calcium hydrosilicates, which usually very weakly crystallize under ordinary conditions. It is also known [24] that during hardening of Portland cement, calcium silicate hydrates are cryptocrystalline substances that serve as a cementing material, linking unhydrated clinker particles and large crystals of Ca(OH)₂, ettringite, etc. In the 28-days and 120-days old composite specimens, the amount of the amorphous phase decreased from 42 % to 30 % and 29 % compared to the initial fly ash and, apparently, a significant part is newly formed calcium silicate hydrates, the proportion of which increases with a curing time.

Thus, the high-strength specimens were produced from the finest high-calcium fly ash of the 4th field of the electrostatic precipitator in the composition with the Melflux 5581F superplasticizer at $W/B = 0.25$. Their compressive strength increased from 17 to 72 MPa as the curing age increased from 1 to 120 days. The strength of these composite specimens is comparable to the strength of specimens based on PC 42.5 N without the addition of superplasticizer. The close mixture of newly formed hydrated phases (ettringite, hydrates of calcium carboaluminates, portlandite and amorphous calcium hydrosilicates) ensures high strength of the material.

4. Conclusion

1. The high-calcium fly ashes (HCFA) selected from each of the 4 fields of the electrostatic precipitator of Krasnoyarsk TPP-2 were studied. It was established that the dispersity and composition of the HCFA vary considerably.

2. Compressive strength tests of the specimens produced from 100 % of the HCFA of the 3rd and the 4th fields at a water/binder ratio of $W/B = 0.4$ were performed. It was established that the strength of the 4th field specimens is 2 times higher compared to the 3rd field specimens and 2 times lower than the strength PC 42.5N specimens.

3. High-strength specimens were manufactured from the fine high-calcium fly ash of the 4th field ($d_{90} < 10$ microns) in composition with a polycarboxylate superplasticizer (Melflux 5581F) at a ratio $W/B = 0.25$. The compressive strength of the specimens increased from 17 to 72 MPa at a curing age from 1 to 120 days. The strength of these specimens is comparable to the strength of specimens based on PC 42.5 without superplasticizer.

4. Synchronous thermal analysis (CTA) and quantitative X-ray phase analysis (XRD) were used to study the phase transformations of the HCFA components in the process of hydration curing, and also to establish the main newly formed hydrate phases providing early and long-term strength. The results on the quantitative phase composition of high-strength specimens create additional opportunities to control the hardening processes of HCFA based binding materials.

5. Acknowledgments

The study was carried out due to the basic research project of the SB RAS V.45.3.3 at Institute of Chemistry and Chemical Technology SB RAS, Federal Research Center «Krasnoyarsk Science Center of the Siberian Branch of the Russian Academy of Sciences».

References

1. Gollakota, A.R.K., Volli, V., Shu, C.M. Progressive utilisation prospects of coal fly ash [Online]: A review. *Science of the Total Environment*. 2019. 672. Pp. 951–989. DOI: 10.1016/j.scitotenv.2019.03.337. URL: <https://doi.org/10.1016/j.scitotenv.2019.03.337>
2. Blissett, R.S., Rowson, N.A. A review of the multi-component utilisation of coal fly ash [Online]. *Fuel*. 2012. 97. Pp. 1–23. DOI: 10.1016/j.fuel.2012.03.024. URL: <http://dx.doi.org/10.1016/j.fuel.2012.03.024>.
3. Yao, Z.T., Ji, X.S., Sarker, P.K., Tang, J.H., Ge, L.Q., Xia, M.S., Xi, Y.Q. A comprehensive review on the applications of coal fly ash [Online]. *Earth-Science Reviews*. 2015. 141. Pp. 105–121. DOI: 10.1016/J.EARSCIREV.2014.11.016. URL: <https://www.sciencedirect.com/science/article/pii/S0012825214002219?via%3Dihub>
4. Belviso, C. State-of-the-art applications of fly ash from coal and biomass: A focus on zeolite synthesis processes and issues [Online]. *Progress in Energy and Combustion Science*. 2018. 65. Pp. 109–135. DOI: 10.1016/j.pecs.2017.10.004. URL: <https://doi.org/10.1016/j.pecs.2017.10.004>
5. Sirotyuk, V.V., Lunev, A.A. Strength and deformation characteristics of ash and slag mixture [Online]. *Magazine of Civil Engineering*. 2017. 74(6). Pp. 1–14. DOI: 10.18720/MCE.74.1. URL: https://elibrary.ru/download/elibrary_30743038_30964333.pdf
6. Lunev, A.A., Sirotyuk, V.V. Stress distribution in ash and slag mixtures [Online]. *Magazine of Civil Engineering*. 2019. 86(2). Pp. 72–82. DOI: 10.18720/MCE.86.7. URL: https://elibrary.ru/download/elibrary_38582747_15498330.pdf
7. Ovcharenko, G.I., Fomichev, Y.Y. Tehnologiya pererabotki visokokalsievoy zoly i shlaka TES v silikatnii kirpich [Processing technology the high calcium ashes and slag from thermal power station in silicate brick]. *News of Higher Educational Institutions [Online]. Construction*. 2012. (11–12). Pp. 47–53. URL: <https://elibrary.ru/item.asp?id=18974275>. (rus)
8. Enders, M. Microanalytical characterization (AEM) of glassy spheres and anhydrite from a high-calcium lignite fly ash from Germany [Online]. *Cement and Concrete Research*. 1995. 25(6). Pp. 1369–1377. URL: [https://doi.org/10.1016/0008-8846\(95\)00129-Z](https://doi.org/10.1016/0008-8846(95)00129-Z)
9. Sharonova, O.M., Solovyov, L.A., Oreshkina, N.A., Yumashev, V. V., Anshits, A.G. Composition of high-calcium fly ash middlings selectively sampled from ash collection facility and prospect of their utilization as component of cementing materials [Online]. *Fuel Processing Technology*. 2010. 91(6). Pp. 573–581. DOI: 10.1016/j.fuproc.2010.01.003. URL: <http://dx.doi.org/10.1016/j.fuproc.2010.01.003>
10. Zhao, Y., Zhang, J., Tian, C., Li, H., Shao, X., Zheng, C. Mineralogy and chemical composition of high-calcium fly ashes and density fractions from a coal-fired power plant in China. *Energy and Fuels*. 2010. 24(2). Pp. 834–843. DOI: 10.1021/ef900947y.
11. Sharonova, O.M., Zhizhaev, A.M., Oreshkina, N.A. Composition and structure of calcium aluminosilicate microspheres [Online]. *Thermal Engineering*. 2017. 64(6). Pp. 415–421. DOI: 10.1134/S0040601517060064. URL: <https://elibrary.ru/item.asp?id=31029838>
12. Ovcharenko, G.I., Shchukina, Yu.V., Chernyh, K.P. Gazobeton na osnove visokokalsievykh zol TEZ [Gas concrete based on high-calcium ash from thermal power station]. Barnaul: Publishing House of Altai State Technical University, 2009 [Online]. URL: <https://elibrary.ru/item.asp?id=19629146> (rus)
13. Ahmaruzzaman, M. A review on the utilization of fly ash [Online]. *Progress in Energy and Combustion Science*. 2010. 36(3). Pp. 327–363. DOI: 10.1016/j.pecs.2009.11.003. URL: <http://dx.doi.org/10.1016/j.pecs.2009.11.003>.
14. Cross, D., Stephens, J., Vollmer, J. Structural Applications of 100 Percent Fly Ash Concrete. in *Proc. 2005 World of Coal Ash (WOCA) Conf.*, Lexington, KY, USA, Apr. 10–15, 2005 [Online]. URL: <http://www.flyash.info/2005/131cro.pdf>; 2005. P. 131. URL: <https://p2infohouse.org/ref/45/44859.pdf>
15. Tumanovskii, A.G. Prospects for the development of coal-steam plants in Russia. *Thermal Engineering*. 2017. 64(6). Pp. 399–407. DOI: 10.1134/S0040601517060088
16. Li, Z. *Advanced concrete technology* [Online]. John Wiley & Sons, Inc, New Jersey, USA, 2011. URL: <https://epdf.pub/advanced-concrete-technology.html>
17. Lange, A., Plank, J. Optimization of comb-shaped polycarboxylate cement dispersants to achieve fast-flowing mortar and concrete [Online]. *Journal of Applied Polymer Science*. 2015. 132(37). Pp. 1–9. DOI: 10.1002/app.42529
18. Lee, S.H., Kim, K.D., Sakai, E., Daimon, M. Mineralogical variability of fly ashes classified by electrostatic precipitator [Online]. *Journal of the Ceramic Society of Japan*. 2003. 111(1289). Pp. 11–15. URL: <https://doi.org/10.2109/jcersj.111.11>
19. Savinkina, M.A., Logvinenko, A.T. *Zoli kanskoachinskikh burih ugley. (Flu ashes of Kansko-Achinsk brown coals)*. Novosibirsk: Nauka, 1979.

20. Ovcharenko, G.I. Zoli ugley KATEKa v stroitel'nih materialah (KATEK coal ashes in building materials). Krasnoyarsk: Publishing House Krasnoyarsk. univ., 1992.
21. Solovyov, L.A. Full-profile refinement by derivative difference minimization research papers. Journal of Applied Crystallography. 2004. 37(5). Pp. 743–749. DOI: 10.1107/S0021889804015638.
22. Sharonova, O.M., Anshits, N.N., Solovyov, L.A., Salanov, A.N., Anshits, A.G. Relationship between composition and structure of globules in narrow fractions of ferrospheres [Online]. Fuel. 2013. 111. Pp. 332–343. DOI: 10.1016/j.fuel.2013.03.059. URL: <http://dx.doi.org/10.1016/j.fuel.2013.03.059>.
23. Yamada, K., Takahashi, T., Hanehara, S., Matsuhisa, M. Effects of the chemical structure on the properties of polycarboxylate-type superplasticizer [Online]. Cement and Concrete Research. 2000. 30(2). Pp. 197–207. URL: [http://doi.org/10.1016/S0008-8846\(99\)00230-6](http://doi.org/10.1016/S0008-8846(99)00230-6).
24. Taylor, H.F.W. Cement Chemistry. 2nd Ed Thomas Telford [Online]. London, 1997. 476 p. URL: <https://www.icvlibrary.com/doi/book/10.1680/cc.259>
25. Sorelli, L., Constantinides, G., Ulm, F.J., Toutlemonde, F. The nano-mechanical signature of Ultra High Performance Concrete by statistical nanoindentation techniques. Cement and Concrete Research. 2008. 38(12). Pp. 1447–1456. DOI: 10.1016/j.cemconres.2008.09.002.
26. Sharonova, O.M., Kirilets, V.M., Yumashev, V.V., Solovyov, L.A., Anshits, A.G. Phase composition of high strength binding material based on fine microspherical high-calcium fly ash [Online]. Construction and Building Materials. 2019. 216. Pp. 525–530. DOI: 10.1016/j.conbuildmat.2019.04.201. URL: <https://doi.org/10.1016/j.conbuildmat.2019.04.201>.
27. Deschner, F., Winnefeld, F., Lothenbach, B., Seufert, S., Schwesig, P., Dittich, S., Goetz-Neunhoffer, F., Neubauer, J. Hydration of Portland cement with high replacement by siliceous fly ash [Online]. Cement and Concrete Research. 2012. 42(10). Pp. 1389–1400. DOI: 10.1016/j.cemconres.2012.06.009. URL: <http://dx.doi.org/10.1016/j.cemconres.2012.06.009>
28. Panasyuk, G.P., Belan, V.N., Voroshilov, I.L., Kozerzhets, I.V. Hydrargillite → boehmite transformation. Inorganic Materials. 2010. 46(7). Pp. 747–753. DOI: 10.1134/S0020168510070113.
29. Torréns-Martín, D., Fernández-Carrasco, L., Blanco-Varela, M.T. Thermal analysis of blended cements. Journal of Thermal Analysis and Calorimetry. 2015. 121(3). Pp. 1197–1204. DOI: 10.1007/s10973-015-4569-1.
30. Giergiczy, Z. The hydraulic activity of high calcium fly ash. Journal of Thermal Analysis and Calorimetry. 2006. 83(1). Pp. 227–232. DOI: 10.1007/s10973-005-6970-7.
31. Roszczynialski, W. Determination of pozzolanic activity of materials by thermal analysis. Journal of Thermal Analysis and Calorimetry. 2002. 70(2). Pp. 387–392. DOI: 10.1023/A:1021660020674.
32. Ovcharenko, G.I., Shchukina, Yu.V., Khizhinkova, E.Yu. Analiz productov gidratazii zol uglei KATEKa metodami DTA i DSK [Analysis of hydration products for coal ashes of KATEK coals by DTA and DSC methods] [Online]. Polzunovsky vestnik. 2006. 2. Pp. 210–212. URL: <https://elibrary.ru/item.asp?id=13027758>

Contacts:

Olga Sharonova, +7(923)3697036; sharon05@yandex.ru

Vladimir Yumashev, +7(962)0780323; yumashev_vlad@mail.ru

Leonid Solovyov, +7(906)9732912; leosol@icct.ru

Alexander Anshits, +7(950)4370735; anshits@icct.ru

© Sharonova, O.M., Yumashev, V.V., Solovyov, L.A., Anshits, A.G., 2019



DOI: 10.18720/MCE.91.6

Тонкодисперсная высококальциевая летучая зола как основа композитного цементирующего материала

О.М. Шаронова*, **В.В. Юмашев**, **Л.А. Соловьев**, **А.Г. Аншиц**

Федеральное государственное бюджетное научное учреждение «Федеральный исследовательский центр «Красноярский научный центр Сибирского отделения Российской академии наук», г. Красноярск, Россия

* E-mail: sharon05@yandex.ru

Ключевые слова: высококальциевая летучая зола, цементирующие материалы, суперпластификатор, гидратация, прочность на сжатие, соединения кальция, рентгенофазовый анализ

Аннотация. Исследованы высококальциевые летучие золы (ВКЛЗ), отобранные с каждого из 4-х полей электрофильтров (ЭФ) Красноярской ТЭЦ-2. Определено, что распределение по размерам, химический и количественный фазовый состав значительно изменяются от 1 к 4 полю ЭФ. Образцы высокой прочности были получены на основе тонкодисперсной ВКЛЗ с 4 поля ЭФ ($d_{90} < 10$ микрон) в композиции с суперпластификатором при соотношении вода:связующее $B/C = 0.25$, их прочность на сжатие возрастала от 17 до 72 МПа при отверждении от 1 до 120 суток. Прочность этих образцов сопоставима с прочностью образцов на основе портландцемента ПЦ 42.5Н без добавки суперпластификатора. Образцы высокой прочности исследованы методами синхронного термического анализа (СТА) и количественного рентгенофазового анализа (РФА). Установлено, что главными новообразованными фазами являются этtringит $3CaO \cdot Al_2O_3 \cdot 3CaSO_4 \cdot 32H_2O$, а также гидраты карбоалюминатов кальция $Ca_4Al_2(OH)_{13}(CO_3)0,5 \cdot 4H_2O$ и $Ca_4Al_2(OH)_{12}CO_3 \cdot 5H_2O$ с низкой окристаллизованностью. За счет замещения Al^{3+} на Fe^{3+} новые фазы могут образовывать широкие ряды твердых растворов. Из совокупности данных методов СТА и РФА можно утверждать, что при увеличении сроков твердения возрастает вклад превращений кальцийсиликатного аморфного вещества с образованием скрытокристаллических гидросиликатов кальция, повышающих начальную и долговременную прочность материала. Фазовые превращения и показатели прочности позволяют использовать тонкодисперсные высококальциевые летучие золы угольных ТЭЦ как самостоятельный цементирующий материал в современных технологиях получения строительных материалов, в частности, в технологии самоуплотняющихся композитных бетонов (СУБ). Предложенная альтернатива цементу способствует решению комплексной экологической проблемы: (1) в области теплоэнергетики уменьшается накопление тонкодисперсных частиц золы, а, следовательно, уменьшается загрязнение вод, почв и атмосферы тонкими пылевидными частицами и (2) часть цемента в промышленности строительных материалов замещается на ВКЛЗ, что позволит сэкономить энерго- и природные ресурсы.

Литература

1. Gollakota A.R.K., Volli V., Shu C.M. Progressive utilisation prospects of coal fly ash: A review // Science of the Total Environment. 2019. (672). Pp. 951–989. DOI: 10.1016/j.scitotenv.2019.03.337.
2. Blissett R.S., Rowson N.A. A review of the multi-component utilisation of coal fly ash // Fuel. 2012. (97). Pp. 1–23. DOI: 10.1016/j.fuel.2012.03.024.
3. Yao Z.T., Ji X.S., Sarker P.K., Tang J.H., Ge L.Q., Xia M.S., Xi Y.Q. A comprehensive review on the applications of coal fly ash // Earth-Science Reviews. 2015. (141). Pp. 105–121. DOI: 10.1016/J.EARSCIREV.2014.11.016.
4. Belviso C. State-of-the-art applications of fly ash from coal and biomass: A focus on zeolite synthesis processes and issues // Progress in Energy and Combustion Science. 2018. (65). Pp. 109–135. DOI: 10.1016/j.peccs.2017.10.004.
5. Sirotyuk V.V., Lunev A.A. Strength and deformation characteristics of ash and slag mixture // Magazine of Civil Engineering. 2017. 6(74). Pp. 1–14. DOI: 10.18720/MCE.74.1.
6. Lunev A.A., Sirotyuk V.V. Stress distribution in ash and slag mixtures // Magazine of Civil Engineering. 2019. 2(86). Pp. 72–82. DOI: 10.18720/MCE.86.7.
7. Овчаренко Г.И. Фомичев Ю.Ю. Технология переработки высококальциевой золы и шлака тэц в силикатный кирпич [Электронный ресурс] // Известия высших учебных заведений. Строительство. 2012. № 11–12. С. 47–53. URL: <https://elibrary.ru/item.asp?id=18974275>

8. Enders M. Microanalytical characterization (AEM) of glassy spheres and anhydrite from a high-calcium lignite fly ash from Germany [Электронный ресурс] // Cement and Concrete Researc. 1995. 6(25). Pp. 1369–1377. URL: [https://doi.org/10.1016/0008-8846\(95\)00129-Z](https://doi.org/10.1016/0008-8846(95)00129-Z)
9. Sharonova O.M., Solovyov L.A., Oreshkina N.A., Yumashev V. V., Anshits A.G. Composition of high-calcium fly ash middlings selectively sampled from ash collection facility and prospect of their utilization as component of cementing materials // Fuel Processing Technology. 2010. 6(91). Pp. 573–581. DOI: 10.1016/j.fuproc.2010.01.003.
10. Zhao Y., Zhang J., Tian C., Li H., Shao X., Zheng C. Mineralogy and chemical composition of high-calcium fly ashes and density fractions from a coal-fired power plant in China // Energy and Fuels. 2010. 2(24). Pp. 834–843. DOI: 10.1021/ef900947y.
11. Шаронова О.М., Орешкина Н.А. Жижаев А.М. Состав и строение кальцийалюмосиликатных микросфер // Теплоэнергетика. 2017. 6(64). С. 22–29. DOI: 10.1134/S0040363617060066.
12. Овчаренко Г.И., Щукина Ю.В., Черных К.П. Газобетоны на основе высококальциевых зол ТЭЦ [Электронный ресурс]. Барнаул: Изд-во АлтГТУ, 2009. 233 с. URL: <https://elibrary.ru/item.asp?id=19629146>
13. Ahmaruzzaman M. A review on the utilization of fly ash // Progress in Energy and Combustion Science. 2010. 3(36). Pp. 327–363. DOI: 10.1016/j.pecs.2009.11.003.
14. Cross D., Stephens J., Vollmer J. Structural Applications of 100 Percent Fly Ash Concrete [Электронный ресурс] // in Proc. 2005 World of Coal Ash (WOCA) Conf., Lexington, KY, USA, Apr. 10–15, 2005. P 131. URL: <http://www.flyash.info/2005/131cro.pdf>
15. Тумановский А.Г. Перспективы развития угольных ТЭС России // Теплоэнергетика. 2017. 6(64). С. 3–13. DOI: 10.1134/S004036361706008X.
16. Li. Z. Advanced concrete technology [Электронный ресурс]. John Wiley & Sons, Inc, New Jersey, USA, 2011. 506 p. URL: <https://epdf.pub/advanced-concrete-technology.html>
17. Lange A., Plank J. Optimization of comb-shaped polycarboxylate cement dispersants to achieve fast-flowing mortar and concrete // Journal of Applied Polymer Science. 2015. 37(132). Pp. 1–9. DOI: 10.1002/app.42529.
18. Lee S.H., Kim K.D., Sakai E., Daimon M. Mineralogical variability of fly ashes classified by electrostatic precipitator [Электронный ресурс] // Journal of the Ceramic Society of Japan. 2003. 1289(111). Pp. 11–15. URL: <https://doi.org/10.2109/jcersj.111.11>
19. Савинкина М.А., Логвиненко А.Т. Золой канско-ачинских бурых углей. Новосибирск: Наука, 1979. 168 с.
20. Овчаренко Г.И. Золой углей КАТЭКа в строительных материалах. Краснодар: Изд-во Краснояр. ун-та, 1992. 216 с.
21. Solovyov L.A. Full-profile refinement by derivative difference minimization research papers // Journal of Applied Crystallography. 2004. 5(37). Pp. 743–749. DOI: 10.1107/S0021889804015638.
22. Sharonova O.M., Anshits N.N., Solovyov L.A., Salanov A.N., Anshits A.G. Relationship between composition and structure of globules in narrow fractions of ferrospheres // Fuel. 2013. (111). Pp. 332–343. DOI: 10.1016/j.fuel.2013.03.059.
23. Yamada K., Takahashi T., Hanehara S., Matsuhisa M. Effects of the chemical structure on the properties of polycarboxylate-type superplasticizer [Электронный ресурс] // Cement and Concrete Research. 2000. 2(30). Pp. 197–207. URL: [http://doi.org/10.1016/S0008-8846\(99\)00230-6](http://doi.org/10.1016/S0008-8846(99)00230-6)
24. Taylor H.F.W. Cement Chemistry. 2nd Ed. Thomas Telford [Электронный ресурс]. London, 1997. 476 p. URL: <https://www.icevirtuallibrary.com/doi/book/10.1680/cc.259>
25. Sorelli L., Constantinides G., Ulm F.J., Toutlemonde F. The nano-mechanical signature of ultra high performance concrete by statistical nanoindentation techniques // Cement and Concrete Research. 2008. 12(38). Pp. 1447–1456. DOI: 10.1016/j.cemconres.2008.09.002.
26. Sharonova O.M., Kirilets V.M., Yumashev V. V., Solovyov L.A., Anshits A.G. Phase composition of high strength binding material based on fine microspherical high-calcium fly ash // Construction and Building Materials. 2019. (216). Pp. 525–530. DOI: 10.1016/j.conbuildmat.2019.04.201.
27. Deschner F., Winnefeld F., Lothenbach B., Seufert S., Schwesig P., Dittrich S., Goetz-Neunhoeffler F., Neubauer J. Hydration of Portland cement with high replacement by siliceous fly ash // Cement and Concrete Research. 2012. 10(42). Pp. 1389–1400. DOI: 10.1016/j.cemconres.2012.06.009.
28. Панасюк Г.П., Белан В.Н., Ворошилов И.Л., Козерожец И.В. Превращение гидрагиллит → бемит [Электронный ресурс] // Неорганические материалы. 2010. № 7(46). С. 831–837. URL: https://elibrary.ru/download/elibrary_15108829_49939095.pdf
29. Torrrens-Martín D., Fernández-Carrasco L., Blanco-Varela M.T. Thermal analysis of blended cements // Journal of Thermal Analysis and Calorimetry. 2015. 3(121). Pp. 1197–1204. DOI: 10.1007/s10973-015-4569-1.
30. Giergiczny Z. Effect of some additives on the reactions in fly ash-Ca(OH)₂ system // Journal of Thermal Analysis and Calorimetry. 2004. 3(76). Pp. 747–754. DOI: 10.1023/B:JTAN.0000032259.80031.b2.
31. Roszczynialski W. Determination of pozzolanic activity of materials by thermal analysis // Journal of Thermal Analysis and Calorimetry. 2002. 2(70). Pp. 387–392. DOI: 10.1023/A:1021660020674.
32. Овчаренко Г.И., Щукина Ю.В., Хижинкова Е.Ю. Анализ продуктов гидратации зол углей катака методами ДТА и ДСК [Электронный ресурс] // Позуновский вестник. 2006. № 2. С. 210–212. URL: <https://elibrary.ru/item.asp?id=13027758>

Контактные данные:

Ольга Михайловна Шаронова, +7(923)3697036; эл. почта: sharon05@yandex.ru

Владимир Витальевич Юмашев, +7(962)0780323; эл. почта: yumashev_vlad@mail.ru

Леонид Александрович Соловьев, +7(906)9732912; эл. почта: leosol@icct.ru

Александр Георгиевич Аншиц, +7(950)4370735; эл. почта: anshits@icct.ru



DOI: 10.18720/MCE.91.7

Structural performance of reinforced concrete beams containing plastic waste caps

J. Khatib^{a*}, A. Jaham^b, A. Elkordi^b, O. Baalbaki^b

^a University of Wolverhampton, Wolverhampton, United Kingdom

^b Beirut Arab University, Beirut, Lebanon

* E-mail: ahjahamy@hotmail.com

Keywords: load deflection, reinforced concrete beam, plastic waste, strain distribution, ductility

Abstract. Municipal solid waste contains large amounts of plastic and their utilization has environmental benefits including the reduction of raw materials used and landfill spaces. One of the possible uses of waste plastic is in construction applications such as partial replacement of coarse aggregate in concrete materials. In this paper, the structural capacity of reinforced concrete beams containing waste plastic was investigated. The waste plastic was the cap of a plastic bottle. Four concrete mixes were prepared. The coarse aggregate was replaced with 0, 10 %, 15 %, and 20 % (by volume) waste plastic. All mixes had constant mix proportions and water to cement ratio. All beams were cured for 28 days at 20 °C. The structural performance was assessed by examining the central deflection of the beam at different load increments until failure. In addition, the mode of failure was examined visually. The results indicated that it is possible to use a certain amount of waste plastic in structural applications without affecting the flexural characteristics of reinforced concrete beams.

1. Introduction

Concrete is the second most widely used material in the world after water. Large volumes of virgin materials are required to produce concrete. Any attempts to replace these materials with waste will be greatly advantageous as this will reduce the amounts of quarried materials and reduce the need for landfill spaces [1–5]. Waste materials include solid waste generated from the industry and households including plastic waste. Plastic is one of the most significant innovations of 20th-century material and the amount of plastic waste generated annually has been growing steadily and becoming a serious environmental problem. The estimated annual generation of plastic waste is 4.9 billion tons (reference). For solving the disposal of a large amount of plastic material, the use of recycled plastic in concrete industry may be considered a feasible option. The bulk of the concrete volume consists mainly of aggregates and it plays a substantial role in concrete properties such as workability, strength, dimensional stability, and durability. Using waste materials such as waste plastic in concrete as partial aggregates replacement will affect the structural performance of concrete. Plastic bottle caps are one type of plastic waste that has a designated cylindrical shape that is expected to have an effect on the properties of concrete produced and structural performance of reinforced concrete beams if used as partial replacement of coarse aggregates.

The workability of concrete was found to reduce when Plastic Fibre Reinforced Concrete (PFRC) is incorporated [6]. This was attributed to resistance caused by the fibre, which would hinder the movement of aggregates. The dry density is also reduced in PFRC, which results in the reduction of the self-weight of concrete. This preliminary study has thus shown that the relationships between compressive strength, as used in European standard for plain concrete, can be applied to concrete containing PET-fibres. It was observed during experimentations that normal concrete specimens were suddenly broken into two pieces either cubes or cylinders but PFRC specimens did not suddenly break and failure was ductile.

Khatib, J., Jahami, A., Elkordi, A., Baalbaki, O. Structural performance of reinforced concrete beams containing plastic waste caps. Magazine of Civil Engineering. 2019. 91(7). Pp. 73–79. DOI: 10.18720/MCE.91.7

Хатиб Дж., Джахами А., Элкорди А., Баалбаки О. Конструктивные характеристики железобетонных балок, содержащих отходы пластика // Инженерно-строительный журнал. 2019. № 7(91). С. 73–79. DOI: 10.18720/MCE.91.7



Plastic waste can be used in concrete as a replacement of coarse aggregate instead of its disposal. Replacing up to 20 % of coarse aggregate with waste plastic gives an adequate concrete strength specified in the Indian Standard [7]. The density of concrete reduces beyond 20 % replacement of coarse aggregates. Similar findings were reported elsewhere [8]. The compressive strength and splitting tensile strength of concrete containing plastic aggregate are not much different from the reference concrete specimens (i.e. 0 % waste plastic) [8]. However, and beyond 20 % waste plastic replacement, the strength is noticeably decreased. It has been concluded that 20 % of plastic waste aggregate can be incorporated as coarse aggregate replacement in concrete without any long term detrimental effects on the performance of concrete properties [6,7]. In another investigation, the bulk density of cement mortar prepared by replacing 0–100 % (by volume) of sand with two different sizes of polyethylene Terephthalate (PET) aggregates. The results showed that the reduction of bulk density remained small when the volume occupied by aggregates varies between 0 % and 30 %, regardless of their size. However, when this volume exceeded 50 %, the composite bulk densities started to decrease until reaching a value of 1000 kg/m³. They also found that for the same volumetric percentage of substitution the bulk density decreased with decreasing particle size.

Replacing the fine aggregate with plastic waste containing 80 % polyethylene and 20 % polystyrene was found to cause a reduction in compressive strength [9]. The concrete with 10 % of plastic waste displayed the lowest compressive strength at 28 days of curing, which is about 30 % lower than that of the reference concrete. In addition, the study found a reduction in density of 5 %, 7 %, and 8.7 % for concretes containing 10 %, 15 %, and 20 % plastic aggregates respectively. This is in agreement with results obtained on concretes incorporating lightweight aggregate made with Polyethylene Terephthalate (PET) bottles [10]. The splitting tensile strength of concrete decreased with the increase in plastic waste made from bottles. This decrease was 19 %, 31 %, and 54 % for concrete containing 25 %, 50 %, and 75 % waste plastic respectively. The trend was similar for the modulus of elasticity. Frigione et al [11] replaced the fine aggregate in the concrete with 5 % PET aggregate and concretes had varying w/c ratios were prepared. The splitting tensile strength was reduced in concrete containing PET aggregate and this reduction is more at higher w/c ratio. Moreover, Kou et al [12] reported a decrease in splitting tensile strength when fine aggregate is partially replaced with scraped PVC pipes. The splitting tensile strength at 28 days was 3.06, 2.89, 2.82, 2.58 and 1.83 MPa for concrete incorporating 0 %, 5 %, 15 %, 30 % and 45 % (by volume) respectively PET aggregate. The flexural strength, which is directly related to the splitting tensile strength, was found to increase at 5 % PET replacement at different water to cement ratios [13]. However, at a 15 % replacement, there was a drop in flexural strength compared with the control [13].

The behaviour of reinforced concrete beams containing PET waste [14]. PET particles were shredded and replaced fine aggregate by 5, 10, and 15 %. The beams were lightly reinforced with steel rebar and designed to fail in flexure. The presence of PET waste caused a reduction in compressive strength between 12 and 21 %. The stiffness and mode of failure for recycled PET waste reinforced concrete are almost identical to those of normal beams. There are small reductions in the ultimate load capacity and a slight change in the load-deflection response when using up to 15 % of PET waste. In another investigation, PET waste was used as fibers in reinforced concrete beams [15]. Four different shapes of PET were used in the concrete mixes; ring-shaped, irregularly shaped, synthetic waste wire, and manufactured synthetic macro-fibers. A total of eighteen beams were cast and subjected to four points bending test to study their flexural behaviour. The experiments confirmed that adding ringed shape PET fibers to the reinforced concrete beams did not reduce the deflection. The ductility for reinforced concrete beams was improved with the presence of ring-shaped PET fibers compared with other shapes of fibers.

There has been limited research on the structural assessment of reinforced concrete beams containing waste plastic. Therefore, this paper is concerned with the behaviour of reinforced concrete beams containing waste plastic obtained from bottle caps. This research is part of an ongoing investigation on the use of waste plastic in construction. The specific objectives are to determine the compressive strength and elastic modulus of plain concrete containing plastic bottle caps. In addition, the flexural behaviour and the strain distribution along the depth of the reinforced concrete beams containing waste plastic have been examined. Future work will include the effect of impact and dynamic loads on the behaviours of reinforced concrete beams containing waste plastic [16, 17].

2. Methods

2.1. Mix design

Four concrete mixes were used to examine the structural behavior of reinforced concrete beam containing plastic waste. The control mix (PBC 0) had a proportion of 1 (cement): 3 (fine aggregate): 3 (coarse aggregate) by weight and no waste plastic was used. In mixes PCB10, PCB15 and PBC 20, the coarse aggregate was replaced with 10 %, 15 % and 20 % (by volume) waste plastic bottle caps (PBC) respectively. These caps have a diameter of 25mm and a depth of 12mm. The free water to cement (W/C) ratio for all concrete mixes was kept constant at 0.6. These proportions of materials were selected based on initial trial mixes to achieve adequate workability. The details for all mixes are presented in Table 1.

Table 1. Details of concrete mixes.

Sample	R* %	Quantities per cubic meter (Kg/m ³)				
		Cement	Water	Sand	Gravel	PBC**
PBC 0	0	314	188.5	942.7	942.7	0.0
PBC10	10	314	188.5	942.7	848.4	30.5
PBC15	15	314	188.5	942.7	801.3	45.7
PBC20	20	314	188.5	942.7	745.1	60.9

* % replacement by volume of coarse aggregate with PBC

** Plastic bottle caps

2.2. Reinforced Concrete Beam Details

Reinforced concrete beams of dimensions 200×300×1200 mm were used. The main reinforcement consists of 3 bars mild steel with 8 mm diameter and this remained the same for all four beams used. Only the content of PBC varied from 0–20 % (by volume of coarse aggregates). The links had a diameter of 6 mm and they were spaced at 200 mm. Figure 1 shows the cross-sectional area of the beam and the reinforcing bars while Figure 2 shows the longitudinal section of the beam with the spaces between stirrups. Three pairs of demec points were located in the upper half of the beam and three in the lower half in order to examine the strain distribution along the cross-section at different loading points as shown in Figure 3.

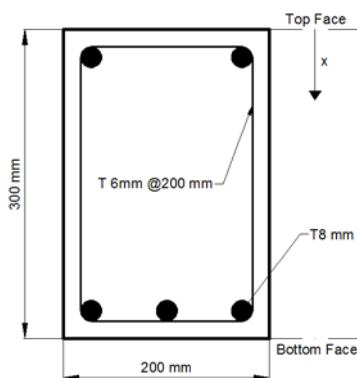


Figure 1. Cross-section of the beam and reinforcement.

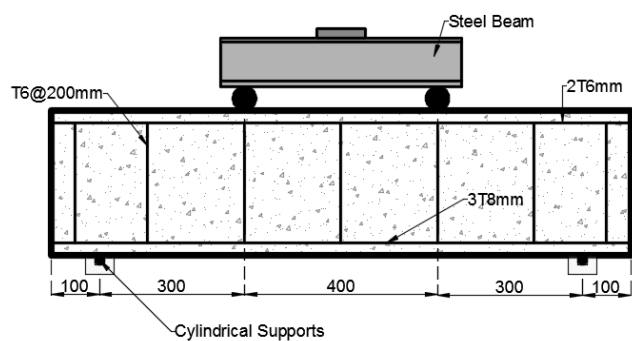


Figure 2. Longitudinal section of the beam with supports and loads (dimensions in mm).

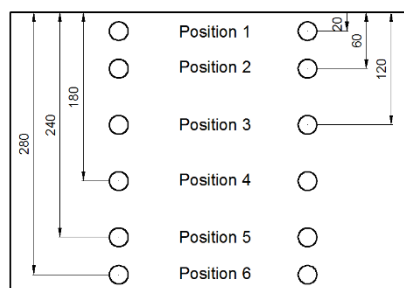


Figure 3. Position of strain measurements (dimensions in mm).

2.3. Casting

After calculating the quantity of materials required for the mix (i.e. cement, aggregate, sand, bottle caps, and water), the materials were weighed. Timber molds were used to cast the concrete specimens (i.e. cubes and beams). The molds were cleaned and oiled before casting. For the compressive strength test, cubes of 100 mm in size were used. These cubes were also used to measure the ultrasonic pulse velocity and to determine the density of concrete. For the Modulus of Elasticity (E) cylinders of 100 mm diameter and 200 mm length were cast. For the structural performance, beams of 200×300×1200 mm were used. The coarse aggregates were placed first in the mixer, followed by the fine aggregate and cement. The dry materials were mixed for two minutes, then water was added slowly and mixing continued until a homogenous mix was obtained as shown in Figure 4. This usually took between 3–4 minutes. Before casting the slump for each mix was measured as shown in Figure 5. The casting of cubes and beams was carried out in two and three layers respectively. Each layer is compacted in order to remove entrapped air as shown in Figure 6. Then specimens of the mixes underwent a slump test. The slump for the control mix was 12.5 mm and 0 mm for those with PBC replacements due to the bond between PBC and fresh concrete. For each mix, 8 cubes, two cylinders, and one beam were cast. After casting the cubes and cylinders were placed in a water tank, while the beam is covered with wet burlap and remained in the lab until testing.



Figure 4. Mixing of concrete.



Figure 5. Control mix slump.



Figure 6. Casting and compaction.

2.4. Testing

The compressive strength and the modulus of elasticity tests were conducted according to BS EN 12350-1:2000 [18] and BS EN 12390-13:2013 [19] respectively. The four-point test was used to determine the flexure behaviour of reinforced concrete beams. Figure 2 shows the location of the supports and point loads. The beam was tested at 5kN increment until yielding started. At each load, the machine was stopped in order to measure the central deflection and the strain at different levels as shown in Figure 3. The load at first crack was recorded. Then, the loading continued until failure and the central deflection was measured. The propagation of cracks was observed throughout the duration of the test.

3. Results and Discussion

Figure 7 shows the average density of each concrete sample. The density of the reference sample (PBC0) was 2.49 t/m³, whereas when PBC was used, a noticeable reduction in density occurred. The reduction was about 9 % for concrete with 20 % PBC. This is partly due to the low-density PBC and the voids created by the empty space of PBC.

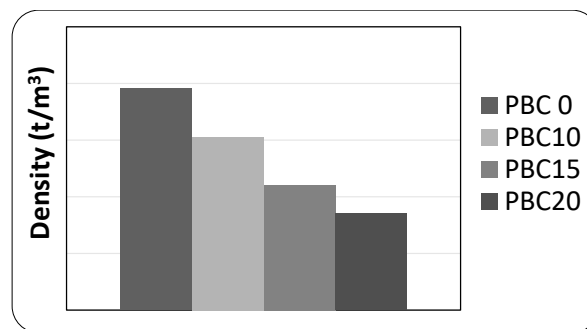


Figure 7. Average Density for concrete samples.

Figures 8 and 9 show the compressive strength and modulus of elasticity at 28 days for all concrete mixtures respectively. The compressive strength for the control mix is slightly less than concretes with PBC. The same trend was observed for the modulus of elasticity. This could be due to the better bond between plastic caps and the mortar, and the geometrical shape of bottle caps. This may be due partly to the rough surface of the curved side and the empty space of the PBC.

Figure 10 shows the load-deflection curve for all concrete beams. In general, the control beam shows more ductility than beams with PBC. The ductility factor that relates the yield displacement (Δy) to the maximum displacement just before failure (Δm) was calculated and presented in Table 2. It can be clearly noticed that the ductility factor for the control beam (0 % PCB) is more than twice that of the beam with 20 % PCB. However, the maximum load for PBC beams is slightly higher than that of the control. This may be due to the higher compressive strength and modulus of elasticity (E) obtained in the mix with 20 % PCB. Khatib et al 2017 [20] reported similar results.

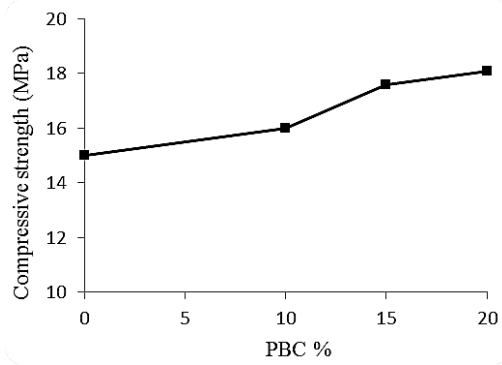


Figure 8. Compressive Strength (28 days).

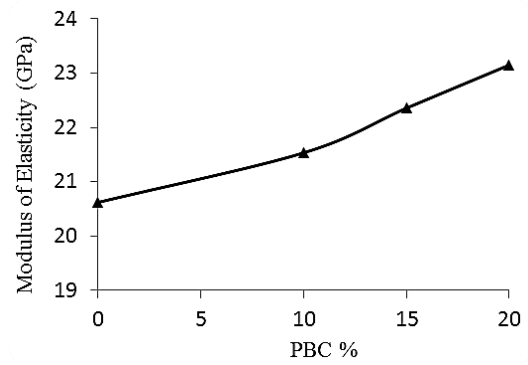


Figure 9. Modulus of Elasticity.

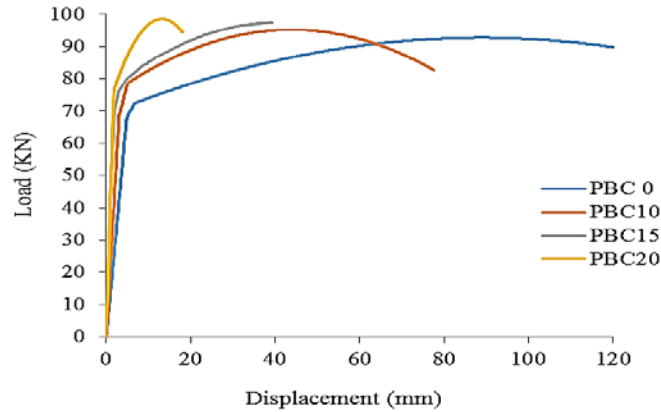


Figure 10. Load-Displacement Curve for all samples.

Table 2. Load-Displacement results.

Sample	Δ_y (mm)	Δ_m (mm)	Δ_m / Δ_y	P_{max} (KN)	P_{max} / P_{ref}
PBC 0	5	120	24	92	—
PBC10	3.4	77.5	22.8	96	1.04
PBC15	2	39.2	19.6	97	1.05
PBC20	1.7	18.1	10.6	98	1.07

The mode of failure for beams with and without PBC is illustrated in Figures 11 and 12. The crack pattern and the mode of failure are similar, and both reflect the flexural failure mode. The cracks started from the bottom face of beams and then propagated vertically through the sides till forming U-shape cracks covering both sides. As for the first crack appearance, Table 3 presents the first crack load and ultimate load reached by each sample. It can be noticed that the reference beam (PBC0) start cracking at a lower load than the samples with PBC. The maximum load for the beams is higher for those with PCB. However, the maximum load was similar to all beams containing PCB.



Figure 11. Flexural cracks for 0 % PBC beam.



Figure 12. Flexural cracks for 10 % PBC beam.

Table 3 Load at first and final crack.

Sample	First Crack Load (KN)	Ultimate Load (KN)
PBC 0	56	92
PBC10	58	96
PBC15	63	97
PBC20	66	98

The strain distribution along the depth of the beam at different load increments is shown in Figure 13 to 16 for mixes with 0, 10, 15 and 20 % PBC respectively. The strain values for the control beams are larger than those for beams with PCB for the same load. This correlates with the larger central displacement for the control beam as compared with the beam consisting of PBC for the same load. This does not seem to agree with the results on the lightweight aggregate reported by Khatib [20]. This can be due to the amount of recycled aggregate used in each case and the type of lightweight aggregates used. The neutral axis shifts upwards as the load increases. This is better illustrated in Table 4, where the distance (x) of the neutral axis (Figure 1) from the top face is presented. The depth of neutral axis in beams with PBC is higher than that for control (PBC0) at the same loading condition.

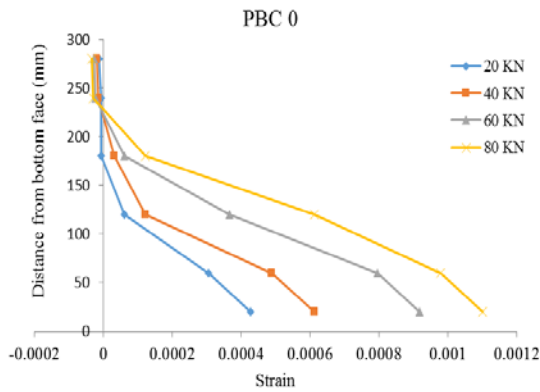


Figure 13. Strain Distribution for PBC0.

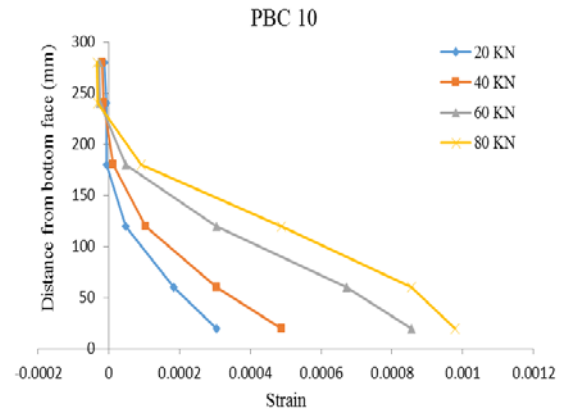


Figure 14. Strain Distribution for PBC10.

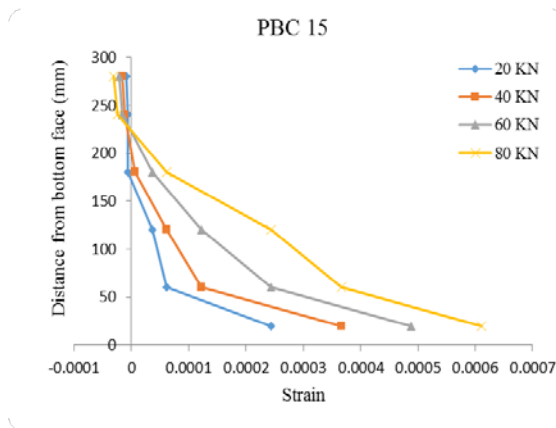


Figure 15. Strain Distribution for PBC15.

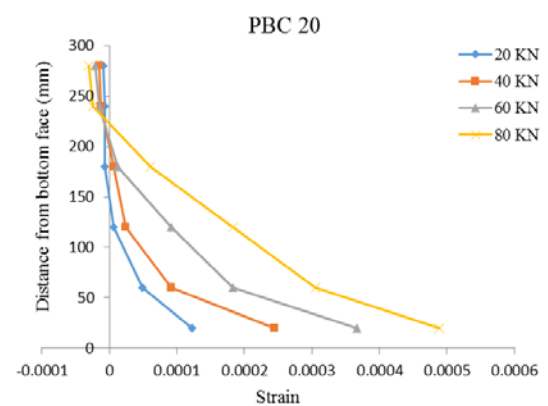


Figure 16. Strain Distribution for PBC20.

Table 4. Neutral axis depth (x) at different loads.

PBC0		PBC10		PBC15		PBC20	
Load (kN)	x (mm)						
20	45	20	46.3	20	51.3	20	53.6
40	41.5	40	43.2	40	49.3	40	52
60	36.2	60	37.6	60	42.3	60	45.1
80	32.8	80	34.3	80	39.4	80	39.9

4. Conclusion

The following conclusions are based on the results of this study:

- Replacing coarse aggregates with PBC reduces the concrete density. At 20 % PCB replacement, the concrete density is reduced by about 10. The workability of concrete is reduced when PCB is present in the mix.
- There was an increase in compressive strength and modulus of elasticity when PBC is incorporated in the concrete mix. The load at failure was also higher when PBC is present. This could be due to the better bond between plastic caps and the mortar, and the geometrical shape of bottle caps.
- The ductility of concrete containing PBC is reduced. For example, the control mix had a ductility factor of 24 while the mix with 20 % PBC the ductility factor was 10.

• The failure mode for both beams was flexural mode. That occurred as expected since all samples were designed to fail in flexural. The first crack appeared on the control beam (PBC0) was at a load of 56KN, and it gradually increased with the increase in PBC content reaching 66KN at 20 % PBC replacement. This is a good indication of delaying crack appearance when using PBC in concrete.

• As for strain distribution, it was found that for the same load the tensile strain in the control beam was higher than those with PBC. This can be justified by the larger central deflection for the control beam. The depth of the neutral axis decreased as the load increased for all beams. The presence of PBC increased the depth of the neutral axis at similar loads.

References

1. Casanova-del-Angel, F., Vázquez-Ruiz, J.L. Manufacturing Light Concrete with PET Aggregate. ISRN Civil Engineering. 2012. 2012. Pp. 1–10. DOI: 10.5402/2012/287323.
2. Skominas, R., Zvinakevičius, L., Gurskis, V., Šadzevičius, R. Evaluation of suitability to use plastic waste in concrete production. Aleksandras Stulginskis University, 2018.
3. Tiwari, A.V., Rao, Y.R.M. Study on compressive strength of plastic waste bituminous concrete for road construction. Nauchno-tehnicheskiy vestnik Bryanskogo gosudarstvennogo universiteta. 2018. 4(3). Pp. 328–337. DOI: 10.22281/2413-9920-2018-04-03-328-337.
4. Jahami, A., Khatib, J., Baalbaki, O., Sonebi, M. PREDICTION OF DEFLECTION IN REINFORCED CONCRETE BEAMS CONTAINING PLASTIC WASTE [Online]. URL: https://www.researchgate.net/publication/334151577_PREDICTION_OF_DEFLECTION_IN_REINFORCED_CONCRETE_BEAMS_CONTAINING_PLASTIC_WASTE (reference date: 31.08.2019).
5. Khatib, J., Jahami, A., Baalbaki, O., FLEXURAL CHARACTERISTICS OF REINFORCED CONCRETE BEAMS CONTAINING LIGHTWEIGHT AGGREGATE IN THE TENSILE ZONE [Online]. URL: https://www.researchgate.net/publication/334611596_FLEXURAL_CHARACTERISTICS_OF_REINFORCED_CONCRETE_BEAMS_CONTAINING_LIGHTWEIGHT_AGGRGATE_IN_THE_TENSILE_ZONE (reference date: 31.08.2019).
6. Nibudey, R., Nagarnaik, P., Parbat, D., Pande, A. Cube and cylinder compressive strengths of waste plastic fiber reinforced concrete. International Journal of Civil and Structural Engineering. 2013. 4(2). Pp. 174–182.
7. Patil, P., Mali, J., Tapkire, G., Kumavat, H. Innovative Techniques of waste plastic used in concrete mixture. International Journal of Research in Engineering and Technology. 2014. 3(9). Pp. 25–28.
8. Subramani, T., Pugal, V. Experimental study of plastic waste as a coarse aggregate for structural concrete. International Journal of Application or Innovation in Engineering & Management (IJAEM). 2015. 4(5). Pp. 144–152.
9. Ismail, Z.Z., AL-Hashmi, E.A. Use of waste plastic in concrete mixture as aggregate replacement. Waste Management. 2008. 28(11). Pp. 2041–2047. DOI: 10.1016/j.wasman.2007.08.023.
10. Choi, Y.W., Moon, D.J., Chung, J.S., Cho, S.K. Effects of waste PET bottles aggregate on the properties of concrete. Cement and Concrete Research. 2005. 35(4). Pp. 776–781. DOI: 10.1016/j.cemconres.2004.05.014.
11. Frigione, M. Recycling of PET bottles as fine aggregate in concrete. Waste Management. 2010. 30(6). Pp. 1101–1106. DOI: 10.1016/j.wasman.2010.01.030.
12. Kou, S.C., Lee, G., Poon, C.S., Lai, W.L. Properties of lightweight aggregate concrete prepared with PVC granules derived from scraped PVC pipes. Waste Management. 2009. 29(2). Pp. 621–628. DOI: 10.1016/j.wasman.2008.06.014.
13. Rahmani, E., Dehestani, M., Beygi, M.H.A., Allahyari, H., Nikbin, I.M. On the mechanical properties of concrete containing waste PET particles. Construction and Building Materials. 2013. 47. Pp. 1302–1308. DOI: 10.1016/j.conbuildmat.2013.06.041.
14. Mohammed, A.A. Flexural behavior and analysis of reinforced concrete beams made of recycled PET waste concrete. Construction and Building Materials. 2017. 155. Pp. 593–604. DOI: 10.1016/j.conbuildmat.2017.08.096.
15. Khalid, F.S., Irwan, J.M., Ibrahim, M.H.W., Othman, N., Shahidan, S. Performance of plastic wastes in fiber-reinforced concrete beams. Construction and Building Materials. 2018. 183. Pp. 451–464. DOI: 10.1016/j.conbuildmat.2018.06.122.
16. Temsah, Y., Jahami, A., Khatib, J., Sonebi, M. Numerical analysis of a reinforced concrete beam under blast loading. MATEC Web of Conferences. 2018. 149. Pp. 1–5. DOI: 10.1051/mateconf/201714902063.
17. Temsah, Y., Jahami, A., Khatib, J., Sonebi, M. Numerical Derivation of Iso-Damaged Curve for a Reinforced Concrete Beam Subjected to Blast Loading. MATEC Web of Conferences. 2018. 149. Pp. 1–5. DOI: 10.1051/mateconf/201714902016.
18. BS EN 12350-1:2000, British Standards Institution. Testing fresh concrete. Part 1. Sampling. British Standards Institution, 2000.
19. BS EN 12390-13:2013 Testing hardened concrete. Determination of secant modulus of elasticity in compression, British Standards Institution – Publication Index | NBS [Online]. URL: <https://www.thenbs.com/PublicationIndex/documents/details?Pub=BSI&DocID=311778> (reference date: 31.08.2019).
20. Khatib, J., Jefimiuk, A., Khatib, S. Flexural Behaviour Of Reinforced Concrete Beams Containing Expanded Glass As Lightweight Aggregates. Slovak Journal of Civil Engineering. 2016. 23(4). Pp. 1–7. DOI: 10.1515/sjce-2015-0017.

Contacts:

Jamal Khatib, +96170382861; j.m.khatib@wlv.ac.uk
 Ali Jahami, +96171859962; ahjahamy@hotmail.com
 Adel Elkordi, +9617985080; a.elkordi@bau.edu.lb
 Ossama Baalbaki, 009613348851; obaalbaki@bau.edu.lb



DOI: 10.18720/MCE.91.8

Equilibrium finite elements for plane problems of the elasticity theory

Yu. Ya. Tyukalov

Vyatka State University, Kirov, Russia

* E-mail: yutvgu@mail.ru

Keywords: stress approximations, additional energy, finite element method, plane problem

Abstract. The work is devoted to the finite elements construction, based on the stresses approximation, for solving plane problems of the elasticity theory. Such elements are alternative to existing finite elements obtained using displacements approximation. Alternative solutions allow more accurate assessment of the structure stress-strain state. The proposed method for constructing finite elements is based on the principles of minimum additional energy and possible displacements. Various stress approximation variants are considered. All approximations variants satisfy the differential equilibrium equations for the case of no distributed load. A comparison is made of the solutions which are obtained by the proposed method with analytical solutions for the ring and the bent beam. The considered stress approximation variants show for test problems good accuracy and convergence, when we grind finite elements grid. It is shown that the best accuracy in calculating stresses and displacements is provided by the finite element with piecewise constant approximations of stresses. In addition, such finite element ensures the displacements convergence to exact values from above. Other finite element variants may be convenient for calculating branched and combined structures. The proposed equilibrium finite elements can be used to more accurately determine the stresses in the calculated structures. The proposed technique can be used to build volumetric finite elements.

1. Introduction

To the basics of the finite element method large number of fundamental studies are devoted, for example papers [1, 2]. These present various variational principles, based on which, finite element solutions can be constructed for the wide range of structural design problems. Alternative principles of minimum potential energy and additional energy are considered. In addition, various variants of hybrid and mixed variational principles are studied. It is noted that the solutions based on the principle of minimum potential energy make it possible to obtain, under certain conditions, the lower limit of displacements, and those obtained using the principle of additional energy can provide the upper limit of displacements. It is obvious that by applying various approximations for displacements in the area of finite element, we thereby forcefully reduce the number of system freedom degrees, which leads to an increase its rigidity [3]. Therefore, the values of displacements determined by the finite element method in displacements will always be less of accurate values. In addition, as rule, the approximations used for displacements do not ensure the deformations continuity, and hence the stresses continuity, along the finite element boundaries. This leads to the appearance of stress field discontinuities along the finite element boundaries.

The finite element method is successfully used to solve various geometrically and physically nonlinear problems. It successfully used for calculating rods, plates, shells and volume problems of the elasticity theory [4, 5]. The finite element method is widely used to solve problems with geometric nonlinearity, shear deformations and for calculation thin-walled structures. The finite element method in displacements is the universal method for solving various problems of the construction's stability and dynamics [6, 7].

The papers [8, 9] are devoted to mixed variants of the finite element method. In mixed methods, approximations of both displacements and stresses (forces) are used. In [9], to approximate displacements and stresses, low-order functions are used. Then two numerical examples are given to demonstrate the

Tyukalov, Yu.Ya. Equilibrium finite elements for plane problems of the elasticity theory. Magazine of Civil Engineering. 2019. 91(7). Pp. 80–97. DOI: 10.18720/MCE.91.8

Тюкалов Ю.Я. Равновесные конечные элементы для плоских задач теории упругости // Инженерно-строительный журнал. 2019. № 7(91). С. 80–97. DOI: 10.18720/MCE.91.8



This work is licensed under a [CC BY-NC 4.0](https://creativecommons.org/licenses/by-nc/4.0/)

stability and efficiency of the proposed approach. The solution obtained by the mixed method, when crushing the finite element's grid, can approach the exact solution both from the bottom and from the top and does not give any lower or upper boundaries of displacements [10, 11].

As an alternative to the finite element method in displacements, for certain structure's types, numerical methods are used, which based on the decomposition of the displacement function into trigonometric series [12,13]. Such methods allow obtaining high-precision solutions for the certain class of problems and can use to testing of other numerical methods.

Also, the boundary element method which use boundary displacement approximations is applied to calculate various constructions [14, 15]. In [16], solutions of three-dimensional problems of the elasticity theory near the border are investigated using modern computational technologies. In [17] for the analysis of axisymmetric elastic problems, the new hybrid finite element method was proposed. This technique uses fundamental solutions in combination with boundary integration method. The formulation uses two independent displacement fields. One field is used within the region of the element and the second is used on the element border, that combines the advantages of the traditional methods of finite and boundary elements. In [18], the Galerkin's method in the weak form is used to reduce the approximating function orders.

In [19, 20], finite element solutions were developed based on stress (force) approximations. At the same time, to build the solution the combination of principles of the minimum additional energy and the possible displacements was used. Such approach makes it possible to find solutions that are alternative of solutions obtained by the finite element method in displacements. It is known, the finite element method in displacements gives an approximate and one-sided solution of the problem. Therefore, despite the great success in using the finite element method in displacements, the search and development of additional, and alternative solutions are relevant. Alternative solutions make it possible to obtain the necessary assessment of the solutions accuracy, which obtained by the finite element method in displacements, and thus ensure the adoption of more reliable design solutions. In [21, 22], this approach is used to solve stability problems and free oscillations of rod systems.

This work aim is to develop the method to solve the flat elasticity problems, which is based on various variants of stress approximations at finite element region. In this case, it is supposed to use various options for approximating stresses that satisfy homogeneous differential equilibrium equations in the finite element region. The method using stress approximations is an alternative to the standard, widely used, finite element method, which is based on the displacement approximations. The flat elasticity theory problems are encountered at the calculations of wide range of the modern building structures. Therefore, the improvement of their solution methods remains the urgent task.

2. Methods

The solution of the theory elasticity problems in stresses can be obtained based on the additional energy functional [1, 2]:

$$\Pi^c = \frac{1}{2} \iint \{\sigma\}^T [E]^{-1} \{\sigma\} d\Omega - \int \{T\}^T \{\bar{\Delta}\} dS \rightarrow \min. \quad (1)$$

$\{\bar{\Delta}\}$ is the vector given displacements of nodes;

$\{T\}$ is the vector boundary forces;

S is the boundary surface, on which the displacement nodes are given;

Ω is the subject area;

$\{\sigma\}^T = (\sigma_x \quad \sigma_y \quad \tau_{xy})$ is the stresses vector;

$[E]$ is the material stiffness matrix.

We shall obtain the necessary relations for an arbitrary quadrangular finite element (Figure 1). In Figure 1, points A, B, C, D are located on the middles of corresponding sides.

To approximate stresses over the finite element region, we shall use functions that satisfy homogeneous differential equilibrium equations for the plane elasticity theory problem:

$$\frac{\partial \sigma_x}{\partial x} + \frac{\partial \tau_{xy}}{\partial y} = 0, \quad \frac{\partial \sigma_y}{\partial y} + \frac{\partial \tau_{xy}}{\partial x} = 0. \quad (2)$$

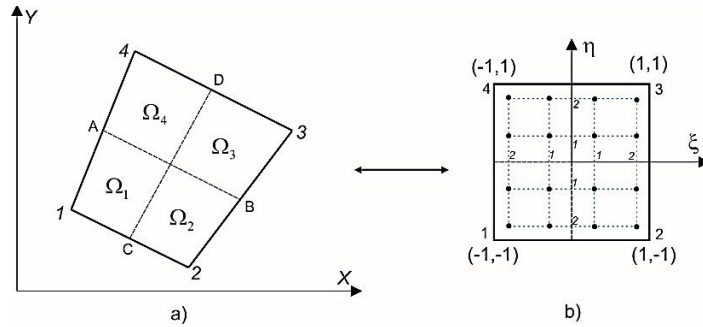


Figure 1. Converting an arbitrary quadrangular finite element into the square.
a) areas with constant stresses for variant 4;
b) points 1, 2 on the axes are the points for numerical integration on Gauss.

To compare the solutions, we shall use four variants of approximating functions, which are presented in Table 1.

Table 1. Variants of the approximating functions for the stresses.

Variant	σ_x	σ_y	τ_{xy}
1	$a_1 + a_4 y + a_6 x$	$a_2 + a_5 x + a_7 y$	$a_3 - a_6 y - a_7 x$
2	$a_1 + a_4 y$	$a_2 + a_5 x$	a_3
3	$a_1 + a_6 x$	$a_2 + a_7 y$	$a_3 - a_6 y - a_7 x$
4	$\sigma_{x,i}, (x, y) \in \Omega_i$	$\sigma_{y,i}, (x, y) \in \Omega_i$	$\tau_{xy,i}, (x, y) \in \Omega_i$

Variants 2 and 3 are obtained from variant 1 by eliminating some unknown parameters. All the approximation functions satisfy equations (2). In variants 1–3, the unknown parameters $a_1 \div a_7$ are independent for each finite element; therefore, the stress fields will have discontinuities along the finite elements' boundaries. Variant 4 uses piecewise constant functions $\sigma_{x,i}, \sigma_{y,i}, \tau_{xy,i}$ that are nodal stress values. Thus, stresses are approximated by constant functions in each region $\Omega_1 \div \Omega_4$ of the finite element (Figure 1a). Such stress fields are continuous at nodes and along the finite elements boundaries but have discontinuities inside the elements. Such approximations for rectangular and triangular finite elements are used in [19–22].

For the stress fields to satisfy the equilibrium equations for the entire subject area under the given load action, we construct the equilibrium equations for finite element grid nodes. For that we shall use the possible displacements principle. The unit displacements along the coordinate axes (Figure 2) are taken as possible displacements. In this case, only finite elements that are adjacent to the node are will deformed.

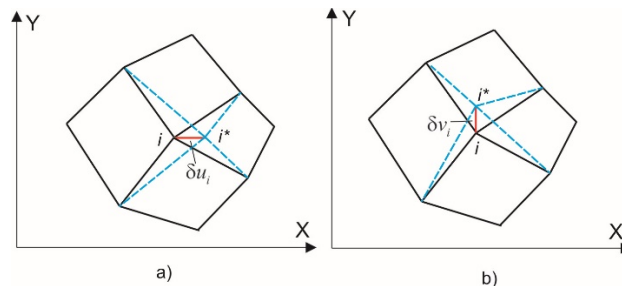


Figure 2. Possible displacements of node i .

Such equilibrium equations can be written as follows:

$$\begin{aligned} \{C_{i,x}\}^T \{\sigma_i\} + \bar{P}_{i,x} &= 0, \quad i \in \Xi_x, \\ \{C_{i,y}\}^T \{\sigma_i\} + \bar{P}_{i,y} &= 0, \quad i \in \Xi_y. \end{aligned} \quad (3)$$

$\{\sigma_i\}$ is the unknown parameters vector of stresses for finite elements that are adjacent to node i ;

Ξ_x, Ξ_y are the sets of nodes that have loose displacements along the X and Y axes, respectively;

$\bar{P}_{i,x}, \bar{P}_{i,y}$ are the generalized forces corresponding to the external loads potential on single possible displacements of the node i , which are directed along the axes X, Y ;

$\{C_{i,x}\}, \{C_{i,y}\}$ are the vectors containing coefficients for unknown nodal stress parameters in the equilibrium equations of node i .

Using any variant of the approximating functions (Table 1), the expression of the functional (1), when the given displacements are absent, can be written in the following matrix form:

$$\Pi^c = \frac{1}{2} \{\sigma\}^T [D] \{\sigma\} \rightarrow \min. \quad (4)$$

The matrix $[D]$ is the flexibility matrix of the entire system. Thus, we have obtained the problem of the quadratic function minimizing (4) with constraints, which are represented as the system of linear algebraic equations (3). Using for solving the Lagrange's multipliers method, we shall get the following extended functional:

$$\Pi^c = \frac{1}{2} \{\sigma\}^T [D] \{\sigma\} + \sum_{j=x,y} \sum_{i \in \Xi_j} u_{i,j} \left(\{C_{i,j}\}^T \{\sigma_i\} + \bar{P}_{i,j} \right) \rightarrow \min, \quad (5)$$

$u_{i,j}$ is the displacement of node i in direction j . With this solution, additional unknowns appear in the form of nodes displacements. But we must accent, that displacements fields approximations in the finite element region are not used.

Expression (5) can be represented in the more convenient to solve form:

$$\Pi^c = \frac{1}{2} \{\sigma\}^T [D] \{\sigma\} + \{u\}^T (\{F\} - [L] \{\sigma\}) \rightarrow \min, \quad (6)$$

$\{u\}$ is the global vector of unknown nodal displacements;

$\{F\}$ is the vector whose elements are equal to the works of external forces on the corresponding single displacements;

$[L]$ is the "equilibrium" matrix, the rows of which are formed from the corresponding vectors $\{C_{i,j}\}$.

If we equate to zero the derivatives with respect to the vectors $\{\sigma\}$ and $\{u\}$, we obtain the following algebraic equations system:

$$\begin{bmatrix} [D] & -[L]^T \\ -[L] & [0] \end{bmatrix} \begin{Bmatrix} \{\sigma\} \\ \{u\} \end{Bmatrix} = \begin{Bmatrix} 0 \\ -[F] \end{Bmatrix}. \quad (7)$$

The first matrix equation in (7) is the strain compatibility equations, which are written in stresses. The second matrix equation is the equilibrium equations of nodes. The matrix is block-diagonal form for any approximation variant from Table 1 and is easily reversible. Therefore, the system of equations (7) is conveniently solved in the following sequence:

$$[K] = [L][D]^{-1}[L]^T, \quad (8)$$

$$[K]\{u\} = \{F\}, \quad (9)$$

$$\{\sigma\} = [D]^{-1}[L]^T \{u\}. \quad (10)$$

Thus, solving the algebraic equations system (9), we obtain the nodal displacements values $\{u\}$, and then we shall calculate the stresses parameters vector $\{\sigma\}$ from (10).

Next, we shall obtain the necessary expressions for $[D]$, $[L]$, $[F]$. For this we shall use variants stresses approximations, which are presented in Table 1.

2.1. Variant of approximation of stresses 1.

Let us introduce the notation for the unknown parameters vector of the finite element k $\{\sigma_k\}^T = (a_1 \ a_2 \ a_3 \ a_4 \ a_5 \ a_6 \ a_7)$ and for the stress approximations matrix

$$[H] = \begin{bmatrix} 1 & 0 & 0 & y & 0 & x & 0 \\ 0 & 1 & 0 & 0 & x & 0 & y \\ 0 & 0 & 1 & 0 & 0 & -y & -x \end{bmatrix}. \quad (11)$$

Then, the stresses vector of finite element k

$$\{\sigma\} = \begin{Bmatrix} \sigma_x \\ \sigma_y \\ \tau_{xy} \end{Bmatrix} = [H]\{\sigma_k\} \quad (12)$$

Material stiffness matrix

$$[E]^{-1} = \frac{t}{E} \begin{bmatrix} 1 & -\mu & 0 \\ -\mu & 1 & 0 \\ 0 & 0 & 2(1+\mu) \end{bmatrix}. \quad (13)$$

E is the material elasticity modulus;

t is the plate thickness;

μ is the Poisson's coefficient.

The finite element flexibility matrix is defined by the following expression:

$$[D^k] = \iint [H]^T [E]^{-1} [H] d\Omega. \quad (14)$$

To obtain the solution and calculate the integral (14), we shall use the well-known transformation of the arbitrary quadrilateral element (Figure 1a) to the square element (Figure 1b). Such coordinate transformation can be written in the following form:

$$x = \sum_{i=1}^4 N_i(\xi, \eta) \cdot x_{i,k}, \quad y = \sum_{i=1}^4 N_i(\xi, \eta) \cdot y_{i,k}, \quad N_i(\xi, \eta) = \frac{1}{4}(1 + \xi_i \xi)(1 + \eta_i \eta). \quad (15)$$

$x_{i,k}$, $y_{i,k}$ are the finite element nodes coordinates in the global coordinate system. The functions $N_i(\xi, \eta)$ will later be used to specify the possible displacements over the finite element region (Figure 2). Therefore it is necessary to calculate the derivatives $N_i(\xi, \eta)$ with respect to the coordinates x and y .

For partial derivatives of the function $N_i(\xi, \eta)$ the following expressions can be written:

$$\frac{\partial N_i}{\partial \xi} = \frac{\partial N_i}{\partial x} \frac{\partial x}{\partial \xi} + \frac{\partial N_i}{\partial y} \frac{\partial y}{\partial \xi}, \quad \frac{\partial N_i}{\partial \eta} = \frac{\partial N_i}{\partial x} \frac{\partial x}{\partial \eta} + \frac{\partial N_i}{\partial y} \frac{\partial y}{\partial \eta}. \quad (16)$$

Index i denotes the local number node of the finite element (Figure 1a). The equations (16) may be written in the following matrix form:

$$\begin{Bmatrix} \frac{\partial N_i}{\partial \xi} \\ \frac{\partial N_i}{\partial \eta} \end{Bmatrix} = \begin{bmatrix} \frac{\partial x}{\partial \xi} & \frac{\partial y}{\partial \xi} \\ \frac{\partial x}{\partial \eta} & \frac{\partial y}{\partial \eta} \end{bmatrix} \begin{Bmatrix} \frac{\partial N_i}{\partial x} \\ \frac{\partial N_i}{\partial y} \end{Bmatrix}, \quad [J] = \begin{bmatrix} \frac{\partial x}{\partial \xi} & \frac{\partial y}{\partial \xi} \\ \frac{\partial x}{\partial \eta} & \frac{\partial y}{\partial \eta} \end{bmatrix}. \quad (17)$$

Using relations (15), we shall obtain the expressions of the matrix $[J]$ elements:

$$\begin{aligned} J_{11} &= \frac{\partial x}{\partial \xi} = \sum_{i=1}^4 \frac{\xi_i(1+\eta\eta_i)}{4} x_{i,k} = \frac{1}{4} [(1-\eta)(x_{2,k} - x_{1,k}) + (1+\eta)(x_{3,k} - x_{4,k})], \\ J_{12} &= \frac{\partial y}{\partial \xi} = \sum_{i=1}^4 \frac{\xi_i(1+\eta\eta_i)}{4} y_{i,k} = \frac{1}{4} [(1-\eta)(y_{2,k} - y_{1,k}) + (1+\eta)(y_{3,k} - y_{4,k})], \\ J_{21} &= \frac{\partial x}{\partial \eta} = \sum_{i=1}^4 \frac{\eta_i(1+\xi\xi_i)}{4} x_{i,k} = \frac{1}{4} [(1-\xi)(x_{4,k} - x_{1,k}) + (1+\xi)(x_{3,k} - x_{2,k})], \\ J_{22} &= \frac{\partial y}{\partial \eta} = \sum_{i=1}^4 \frac{\eta_i(1+\xi\xi_i)}{4} y_{i,k} = \frac{1}{4} [(1-\xi)(y_{4,k} - y_{1,k}) + (1+\xi)(y_{3,k} - y_{2,k})]. \end{aligned} \quad (18)$$

From relation (17), we obtain the expressions of the necessary derivatives:

$$\begin{Bmatrix} \frac{\partial N_i}{\partial x} \\ \frac{\partial N_i}{\partial y} \end{Bmatrix} = [J]^{-1} \begin{Bmatrix} \frac{\partial N_i}{\partial \xi} \\ \frac{\partial N_i}{\partial \eta} \end{Bmatrix}, \quad [J]^{-1} = \begin{bmatrix} b_{11} & b_{12} \\ b_{21} & b_{22} \end{bmatrix}. \quad (19)$$

Matrix elements have the following expressions:

$$\det J = J_{11}J_{22} - J_{12}J_{21}, \quad b_{11} = \frac{J_{22}}{\det J}, \quad b_{12} = \frac{-J_{12}}{\det J}, \quad b_{21} = \frac{-J_{21}}{\det J}, \quad b_{22} = \frac{J_{11}}{\det J}. \quad (20)$$

Using the expression (19) and (15), we get

$$\begin{aligned} \frac{\partial N_i}{\partial x} &= b_{11} \frac{\xi_i(1+\eta\eta_i)}{4} + b_{12} \frac{\eta_i(1+\xi\xi_i)}{4}, \\ \frac{\partial N_i}{\partial y} &= b_{21} \frac{\xi_i(1+\eta\eta_i)}{4} + b_{22} \frac{\eta_i(1+\xi\xi_i)}{4}. \end{aligned} \quad (21)$$

Using the introduced coordinate transformation, the integral (14) can be written as follows:

$$[D^k] = \iint [H]^T [E]^{-1} [H] d\Omega = \int_{-1}^1 \int_{-1}^1 [H]^T [E]^{-1} [H] \cdot \det J d\eta d\xi. \quad (22)$$

To determine the matrix (22) elements, it is convenient to precompute the following integrals:

$$\begin{aligned} i_1 &= \int_{-1}^1 \int_{-1}^1 \det J d\eta d\xi = A, & i_2 &= \int_{-1}^1 \int_{-1}^1 x \cdot \det J d\eta d\xi, \\ i_3 &= \int_{-1}^1 \int_{-1}^1 y \cdot \det J d\eta d\xi, & i_4 &= \int_{-1}^1 \int_{-1}^1 x^2 \cdot \det J d\eta d\xi, \\ i_5 &= \int_{-1}^1 \int_{-1}^1 xy \cdot \det J d\eta d\xi, & i_6 &= \int_{-1}^1 \int_{-1}^1 y^2 \cdot \det J d\eta d\xi. \end{aligned} \quad (23)$$

Integrals (23) are calculated numerically using the four-point Gauss' formula. The following integration points and weight coefficients were taken in the calculations:

$$\begin{aligned} \xi_{g,1} = \eta_{g,1} &= \pm 0.339981, & W_1 &= 0.652145, \\ \xi_{g,2} = \eta_{g,2} &= \pm 0.861136, & W_2 &= 0.347855. \end{aligned} \quad (24)$$

Using expressions (22) and (23), we get:

$$[D^k] = \frac{t}{E} \begin{bmatrix} A & -\mu \cdot A & 0 & i_3 & -\mu \cdot i_2 & i_2 & -\mu \cdot i_3 \\ & A & 0 & -\mu \cdot i_3 & i_2 & -\mu \cdot i_2 & i_3 \\ & & 2(1+\mu)A & 0 & 0 & -2(1+\mu) \cdot i_3 & -2(1+\mu) \cdot i_2 \\ & & & i_6 & -\mu \cdot i_5 & i_5 & -\mu \cdot i_6 \\ & & & & i_4 & -\mu \cdot i_4 & i_5 \\ & & & & & i_4 + 2(1+\mu) \cdot i_6 & (2+\mu) \cdot i_5 \\ & & & & & & i_6 + 2(1+\mu) \cdot i_4 \end{bmatrix}. \quad (25)$$

The global flexibility matrix for the entire system $[D]$ is formed from matrices flexibility $[D^k]$ of finite elements.

To calculate matrix $[L]$ elements we use the possible node displacement δu_i of the finite element (Figure 2) along the X axis:

$$\delta u_i = N_i(\xi, \eta) = \frac{1}{4}(1 + \xi_i \xi) \cdot (1 + \eta_i \eta). \quad (26)$$

Possible deformations that occur in the finite element are determined using expressions (21).

$$\begin{aligned}\delta\varepsilon_x &= \frac{\partial N_i}{\partial x} = b_{11} \frac{\xi_i(1+\eta\eta_i)}{4} + b_{12} \frac{\eta_i(1+\xi\xi_i)}{4}, \\ \delta\gamma_{xy} &= \frac{\partial N_i}{\partial y} = b_{21} \frac{\xi_i(1+\eta\eta_i)}{4} + b_{22} \frac{\eta_i(1+\xi\xi_i)}{4}.\end{aligned}\quad (27)$$

We introduce the notation of the possible deformations vector of the finite element k

$$\{\delta\varepsilon_k\} = \begin{Bmatrix} \delta\varepsilon_x \\ \delta\varepsilon_y \\ \delta\gamma_{xy} \end{Bmatrix} = \begin{Bmatrix} b_{11} \frac{\xi_i(1+\eta\eta_i)}{4} + b_{12} \frac{\eta_i(1+\xi\xi_i)}{4} \\ 0 \\ b_{21} \frac{\xi_i(1+\eta\eta_i)}{4} + b_{22} \frac{\eta_i(1+\xi\xi_i)}{4} \end{Bmatrix}.\quad (28)$$

The work of internal forces is

$$\delta U_{i,x}^k = t \iint_{\Omega_k} \{\delta\varepsilon_k\} \{\sigma\}^T d\Omega = t \int_{-1}^1 \int_{-1}^{-1} \{\delta\varepsilon_k\}^T [H] \{\sigma_k\} \det J d\eta d\xi = \{C_{i,x}^k\}^T \{\sigma_k\}.\quad (29)$$

In (29) the notation is entered:

$$\{C_{i,x}^k\}^T = t \int_{-1}^1 \int_{-1}^{-1} \{\delta\varepsilon_k\}^T [H] \det J d\eta d\xi.\quad (30)$$

To calculate the vector $\{C_{i,x}^k\}$ elements it is convenient to pre-compute numerically. For that we use the four-point Gauss' formula, the following integrals:

$$\begin{aligned}\alpha_{1,i} &= t \int_{-1}^1 \int_{-1}^{-1} \frac{\partial N_i}{\partial x} \det J d\eta d\xi, & \alpha_{1x,i} &= t \int_{-1}^1 \int_{-1}^{-1} \frac{\partial N_i}{\partial x} x \cdot \det J d\eta d\xi, & \alpha_{1y,i} &= t \int_{-1}^1 \int_{-1}^{-1} \frac{\partial N_i}{\partial x} y \cdot \det J d\eta d\xi, \\ \alpha_{2,i} &= t \int_{-1}^1 \int_{-1}^{-1} \frac{\partial N_i}{\partial y} \det J d\eta d\xi, & \alpha_{1y,i} &= t \int_{-1}^1 \int_{-1}^{-1} \frac{\partial N_i}{\partial y} x \cdot \det J d\eta d\xi, & \alpha_{2y,i} &= t \int_{-1}^1 \int_{-1}^{-1} \frac{\partial N_i}{\partial y} y \cdot \det J d\eta d\xi.\end{aligned}\quad (31)$$

Using (11), (28), (30) and (31) we get

$$\{C_{i,x}^k\}^T = (\alpha_{1,i} \quad 0 \quad \alpha_{2,i} \quad \alpha_{1y,i} \quad 0 \quad (\alpha_{1x,i} - \alpha_{2y,i}) \quad -\alpha_{2x,i}).\quad (32)$$

Next, we consider the possible displacement of finite element node along the Y axis

$$\delta v_i = N_i(\xi, \eta) = \frac{1}{4}(1 + \xi_i \xi)(1 + \eta_i \eta).\quad (33)$$

The possible deformations that occur in the finite element are determined using expressions (21).

$$\begin{aligned}\delta\varepsilon_y &= \frac{\partial N_i}{\partial y} = b_{21} \frac{\xi_i(1+\eta\eta_i)}{4} + b_{22} \frac{\eta_i(1+\xi\xi_i)}{4}, \\ \delta\gamma_{xy} &= \frac{\partial N_i}{\partial x} = b_{11} \frac{\xi_i(1+\eta\eta_i)}{4} + b_{12} \frac{\eta_i(1+\xi\xi_i)}{4}.\end{aligned}\quad (34)$$

Performing similar transformations, which are given above, we shall get:

$$\delta U_{i,y}^k = \{C_{i,y}^k\}^T \{\sigma_k\},\quad (35)$$

$$\{C_{i,y}^k\}^T = (0 \quad \alpha_{2,i} \quad \alpha_{1,i} \quad 0 \quad \alpha_{2x,i} \quad -\alpha_{1y,i} \quad (-\alpha_{1x,i} + \alpha_{2y,i})).\quad (36)$$

We combine the internal force works at the possible displacements for all finite element nodes into the vector

$$\{\delta U^k\}^T = (\delta U_{1,x}^k \quad \delta U_{1,y}^k \quad \delta U_{2,x}^k \quad \delta U_{2,y}^k \quad \delta U_{3,x}^k \quad \delta U_{2,y}^k \quad \delta U_{4,x}^k \quad \delta U_{4,y}^k). \quad (37)$$

Rows (32) and (36) are combined into the matrix

$$[L^k] = \begin{bmatrix} \alpha_{1,1} & 0 & \alpha_{2,1} & \alpha_{1,y,1} & 0 & (\alpha_{1,x,1} - \alpha_{2,y,1}) & -\alpha_{2,x,1} \\ 0 & \alpha_{2,1} & \alpha_{1,1} & 0 & \alpha_{2,x,1} & -\alpha_{1,y,1} & (-\alpha_{1,x,1} + \alpha_{2,y,1}) \\ \alpha_{1,2} & 0 & \alpha_{2,2} & \alpha_{1,y,2} & 0 & (\alpha_{1,x,2} - \alpha_{2,y,2}) & -\alpha_{2,x,2} \\ 0 & \alpha_{2,2} & \alpha_{1,2} & 0 & \alpha_{2,x,2} & -\alpha_{1,y,2} & (-\alpha_{1,x,2} + \alpha_{2,y,2}) \\ \alpha_{1,3} & 0 & \alpha_{2,3} & \alpha_{1,y,3} & 0 & (\alpha_{1,x,3} - \alpha_{2,y,3}) & -\alpha_{2,x,3} \\ 0 & \alpha_{2,3} & \alpha_{1,3} & 0 & \alpha_{2,x,3} & -\alpha_{1,y,3} & (-\alpha_{1,x,3} + \alpha_{2,y,3}) \\ \alpha_{1,4} & 0 & \alpha_{2,4} & \alpha_{1,y,4} & 0 & (\alpha_{1,x,4} - \alpha_{2,y,4}) & -\alpha_{2,x,4} \\ 0 & \alpha_{2,4} & \alpha_{1,4} & 0 & \alpha_{2,x,4} & -\alpha_{1,y,4} & (-\alpha_{1,x,4} + \alpha_{2,y,4}) \end{bmatrix}. \quad (38)$$

Using (37) and (38) we can write

$$\{\delta U^k\} = [L^k] \{\sigma^k\}. \quad (39)$$

The matrix $[L]$ is formed from the finite element matrices $[L^k]$.

Since unknown stresses parameters $\{\sigma_k\}^T = (a_1 \ a_2 \ a_3 \ a_4 \ a_5 \ a_6 \ a_7)$ are independent for finite elements, the formation of the resolving equations system can be performed in the same way as it is done for the finite element method in displacements. In this case, for each finite element we can form the matrix

$$[B^k] = [L^k][D^k][L^k]^T. \quad (40)$$

Then, from the matrices $[B^k]$, in accordance with the node numbering, the matrix $[K]$ is formed for the equations system (9). The matrix $[B^k]$ is an analogue of the finite element stiffness matrix.

To form vector $\{F\}$, it is necessary to calculate the work of loads distributed over the finite element at possible node displacements:

$$\delta V_{i,x}^k = \int_{\Omega_k} q_x^k \delta u_i d\Omega = \int_{-1}^1 \int_{-1}^1 q_x^k N_i(\xi, \eta) \cdot \det J d\eta d\xi = P_{x,i}^k, \quad (41)$$

$$\delta V_{i,y}^k = \int_{\Omega_k} q_y^k \delta v_i d\Omega = \int_{-1}^1 \int_{-1}^1 q_y^k N_i(\xi, \eta) \cdot \det J d\eta d\xi = P_{y,i}^k. \quad (42)$$

To calculate (41), (42) for each finite element node ($i = 1, 2, 3, 4$), the Gauss' numerical integration procedure is used. In accordance with the nodes numbering forces $P_{x,i}^k$ and $P_{y,i}^k$ are summed with the corresponding elements of the vector $\{F\}$. The concentrated in the nodes forces P_x, P_y are also added to the elements of the vector $\{F\}$.

2.2. Variants of approximation of stresses 2 and 3

All solving equations for these variants coincide with the equations for variant 1. It is necessary to simply exclude some columns of the matrices $[L^k]$, which is corresponding of the excluded parameters, and the same rows and columns of the matrices $[D^k]$ (see Table 1).

2.3. Variant of approximation of stresses 4

As unknown parameters the stresses values in the nodes of the finite element grid $\sigma_{x,i}, \sigma_{y,i}, \tau_{xy,i}$ are used directly. In this case the stresses are constant values in each of the finite element regions $\Omega_1 \div \Omega_4$ and

The matrix $[L^k]$ consists of lines (48):

$$[L^k] = \begin{bmatrix} \beta_{1,1}^x & 0 & \beta_{1,1}^y & \beta_{1,2}^x & 0 & \beta_{1,2}^y & \beta_{1,3}^x & 0 & \beta_{1,3}^y & \beta_{1,4}^x & 0 & \beta_{1,4}^y \\ 0 & \beta_{1,1}^y & \beta_{1,1}^x & 0 & \beta_{1,2}^y & \beta_{1,2}^x & 0 & \beta_{1,3}^y & \beta_{1,3}^x & 0 & \beta_{1,4}^y & \beta_{1,4}^x \\ \beta_{2,1}^x & 0 & \beta_{2,1}^y & \beta_{2,2}^x & 0 & \beta_{2,2}^y & \beta_{2,3}^x & 0 & \beta_{2,3}^y & \beta_{2,4}^x & 0 & \beta_{2,4}^y \\ 0 & \beta_{2,1}^y & \beta_{2,1}^x & 0 & \beta_{2,2}^y & \beta_{2,2}^x & 0 & \beta_{2,3}^y & \beta_{2,3}^x & 0 & \beta_{2,4}^y & \beta_{2,4}^x \\ \beta_{3,1}^x & 0 & \beta_{3,1}^y & \beta_{3,2}^x & 0 & \beta_{3,2}^y & \beta_{3,3}^x & 0 & \beta_{3,3}^y & \beta_{3,4}^x & 0 & \beta_{3,4}^y \\ 0 & \beta_{3,1}^y & \beta_{3,1}^x & 0 & \beta_{3,2}^y & \beta_{3,2}^x & 0 & \beta_{3,3}^y & \beta_{3,3}^x & 0 & \beta_{3,4}^y & \beta_{3,4}^x \\ \beta_{4,1}^x & 0 & \beta_{4,1}^y & \beta_{4,2}^x & 0 & \beta_{4,2}^y & \beta_{4,3}^x & 0 & \beta_{4,3}^y & \beta_{4,4}^x & 0 & \beta_{4,4}^y \\ 0 & \beta_{4,1}^y & \beta_{4,1}^x & 0 & \beta_{4,2}^y & \beta_{4,2}^x & 0 & \beta_{4,3}^y & \beta_{4,3}^x & 0 & \beta_{4,4}^y & \beta_{4,4}^x \end{bmatrix}. \quad (49)$$

The global $[L]$ matrix is formed from the all finite elements matrices $[L^k]$. Note that in this case the direct matrix $[K]$ formation, by calculating the matrix $[B^k]$ (see (40)) for each finite element, is impossible. The expressions of the load's potential (41), (42) don't depend on the stresses approximations types.

Note that the width of the nonzero elements tape for the matrix $[K]$ is approximately two times the tape width of the equations system for the finite element method in displacements and the matrix $[K]$ tape width for variants of stresses approximations 1–3.

3. Results and Discussion

An analytical solution for ring loaded with concentrated forces is given in [23]. Due to symmetry, a quarter of the ring was calculated. That is shown in Figure 3a. The ring has an inner radius r and an outer radius $R = 2 \cdot r$. To solve the problem, the following ring parameters were taken: $E = 10\,000$ kN/m², $\mu = 0.3$, $r = 3$ m, $P = 20$ kN. In nodes are along the line AB , we excluded displacements which directed along the X axis, in nodes are along line CD , we excluded displacements which directed along the Y axis.

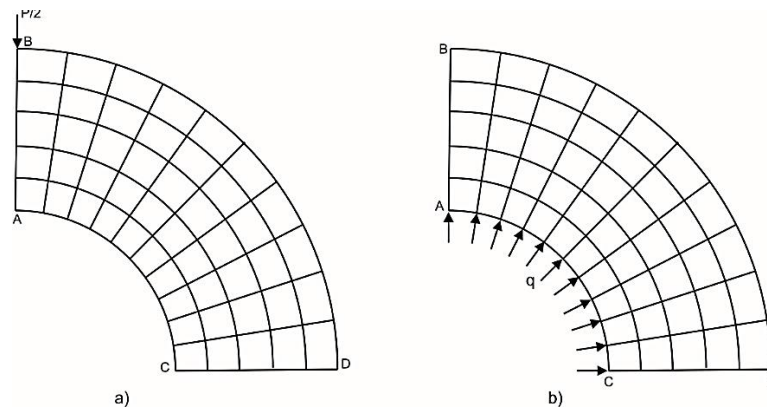


Figure 3. A quarter of the ring (the grid of 5x10 finite elements).
a) concentrated force P ; b) uniform internal pressure q .

Table 3 shows the displacements values of point C for different finite element grids. The values in the Table 3 show the displacements convergence rapid. For the case piecewise constant approximation of stresses (variant 4), there is strict displacements convergence to the exact value from above.

Table 3. Displacement $100u_c$, m (Figure 3a).

Grid	Variants of the stress approximations			
	1	2	3	4
5x10	0.60274	0.61341	0.62238	0.66561
10x20	0.61633	0.61902	0.62146	0.63407
20x40	0.61993	0.62061	0.62123	0.62461
30x60	0.62061	0.62091	0.62119	0.62272

In [23], the analytically calculate stresses values are given for nodes which lay at the lines AB and CD (Figure 3a). Stress values are given in dimensionless form:

$$\bar{\sigma}_{x(y)} = \frac{\pi R}{2P} \sigma_{x(y)}. \quad (50)$$

For the solutions comparison, the stresses values at the indicated points, which were obtained for the finite element mesh 10×20 , are given in Tables 4 and 5. Stresses were calculated for four stress approximations variants. For approximations 1–3, the stresses are discontinuous along the element boundaries. Therefore, in Table 4 for the grid internal nodes, two values are given. These values were calculated in the two finite elements which are adjoining at the node. In each finite element, stresses were calculated for the corresponding node point. To do this, node coordinates were substituted into the stress expressions (Table 1). For the variant 4, the stresses are calculated directly for the grid nodes, therefore one value was presented.

Table 4. Stresses $\bar{\sigma}_y$ at nodes along the CD line.

Node	Variant of approximations				Value of [23]
	1	2	3	4	
1-C	-8.833	-8.819	-7.690	-8.391	-8.942
2	-6.311	-6.210	-7.690	-6.412	-
	-6.342	-6.355	-5.518		
3	-4.561	-4.483	-5.518	-4.682	-4.610
	-4.519	-4.538	-3.892		
4	-3.183	-3.116	-3.892	-3.163	-
	-3.105	-3.121	-2.559		
5	-2.043	-1.980	-2.559	-2.052	-2.012
	-1.948	-1.958	-1.518		
6	-1.059	-0.998	-1.518	-0.999	-
	-0.956	-0.961	-0.574		
7	-0.179	-0.118	-0.574	-0.133	-0.113
	-0.073	-0.073	0.280		
8	0.632	0.694	0.280	0.715	-
	0.738	0.742	1.076		
9	1.396	1.459	1.076	1.478	1.477
	1.501	1.508	1.832		
10	2.129	2.192	1.832	2.233	-
	2.234	2.242	2.563		
11-D	2.842	2.903	2.563	2.798	2.940

Table 5. Stresses $\bar{\sigma}_x$ at nodes along the CD line.

Node	Variant of approximations				Value of [23]
	1	2	3	4	
1-A	9.818	9.807	8.144	9.399	10.147
2	6.162	6.019	8.144	6.216	-
	6.050	6.075	5.086		
3	4.002	3.915	5.086	4.200	4.002
	3.778	3.797	3.173		
4	2.500	2.434	3.173	2.421	-
	2.231	2.234	1.804		
5	1.350	1.289	1.804	1.299	1.24
	1.055	1.037	0.749		
6	0.390	0.326	0.749	0.532	-
	0.065	0.020	-0.213		
7	-0.482	-0.567	-0.213	-0.546	-0.594
	-0.850	-0.949	-1.021		
8	-1.354	-1.452	-1.021	-0.433	-
	-1.785	-1.974	-1.971		
9	-2.423	-2.679	-1.971	-3.134	-2.185
	-2.893	-3.394	-3.370		
10	-4.164	-4.273	-3.370	-5.852	-
	-5.005	-5.757	-3.187		
11-B	-13.562	-15.832	-3.187	-19.300	-3.788

The results analysis, which is given in Tables 3–5, shows that less accurate stresses values were obtained for the third stress approximation variant. The stress values of the first and second variants are close, but the first variant gives closer stress values to the analytical solution at the extreme nodes. In intermediate nodes, the 1–3 approximation variants have discontinuities in the stresses, therefore, the deviations from the

analytical solution are more significant compared with the fourth variant. To improve the results accuracy for variants 1–3, it is necessary to calculate the average stresses values for intermediate grid nodes. The fourth variant of stresses approximations allows one to obtain stresses directly at the grid nodes and ensures the displacements convergence to exact values from above. It should be noted that point B is the point of singularity. At this node, the stresses tend to infinity, so it is impossible to compare values for this point. But it is obvious that the analytical solution [23] for this point does not provide the drastic change of the stress's values. Therefore, the value $\bar{\sigma}_{x,B} = -3.788$ can't serve as the reference of comparison with other solutions.

In addition, the stress value $\bar{\sigma}_{x,9} = -2.185$ in the neighboring node is also unreliable, that is due to the inaccuracy of the analytical solution in the singularity zone. Note that the solutions of the approximation's variants 1, 2 and 4 more accurately represent the stresses change at the singularity zone and allow us to obtain more accurate and consistent stress values.

When using the finite element method in displacements, usually, the stresses are determined not at the nodal points, but at the finite element centers. If we want to improve the accuracy of their values, the finite element grid should be grinding. Tables 6–8 show the stresses at the finite element centers, which is adjacent to points C , D and A , for the considered stresses approximations variants, as well as those obtained using the LIRA-SAPR program. For variant 4, the stress values are given directly for the nodes.

Table 6. Stress $\bar{\sigma}_y$ at the finite element closest to point C . Analytical value $\bar{\sigma}_y = -8.942$.

Grid	Variant of approximations				LIRA-SAPR
	1	2	3	4	
5x10	-6.431	-8.437	-6.629	-8.078	-6.120
10x20	-7.559	-8.819	-7.628	-8.391	-7.449
20x40	-8.199	-8.908	-8.219	-8.618	-8.167
30x60	-8.425	-8.917	-8.434	-8.698	-8.411

Table 7. Stress $\bar{\sigma}_y$ at the finite element closest to point D . Analytical value $\bar{\sigma}_y = 2.940$.

Grid	Variant of approximations				LIRA-SAPR
	1	2	3	4	
5x10	2.129	2.869	2.267	2.734	2.146
10x20	2.549	2.903	2.589	2.798	2.547
20x40	2.745	2.917	2.755	2.826	2.744
30x60	2.807	2.921	2.812	2.888	2.807

Table 8. Stress $\bar{\sigma}_x$ in the finite element closest to point A . Analytical value $\bar{\sigma}_x = 10.147$.

Grid	Variant of approximations				LIRA-SAPR
	1	2	3	4	
5x10	6.301	6.359	6.501	8.977	5.850
10x20	7.967	7.975	8.098	9.399	7.811
20x40	8.980	8.980	9.007	9.679	8.931
30x60	9.352	9.351	9.365	9.803	9.329

The values given in Tables 6–8 show that approximation variants 2 and 4 provide the greatest accuracy. At the smallest grid, for point A by 5 % more accurate stresses values are calculated by the fourth version of approximations, and for points C and D by 2–3 % the second variant is more accurate. The stresses values obtained by the LIRA-SAPR program are less accurate compared to variants 2 and 4, by about 5–6 %, and their values are smaller.

The analytical solution for ring loaded with uniform internal pressure (Figure 3b) is given in [15]. For the CD line, this solution can be written as follows:

$$\sigma_x = \frac{qr^2}{R^2 - r^2} \left(1 - \frac{R^2}{x^2} \right), \sigma_y = \frac{qr^2}{R^2 - r^2} \left(1 + \frac{R^2}{x^2} \right), \tau_{xy} = 0, u = \frac{qr^2 x (1 + \mu)}{E (R^2 - r^2)} \left(1 - 2\mu + \frac{R^2}{x^2} \right). \quad (51)$$

To estimate the proposed method accuracy, quarter-ring calculations were performed (Figure 3b) with different finite element meshes for the stress approximation variants 1–4, as well as using the LIRA-SAPR program. The following ring parameters were used for calculations: $E = 10\,000$ kN/m², $\mu = 0.3$, $r = 3$ m, $q = 10$ kN/m.

Table 9. Displacement $100u_c$, m (Figure 3b).

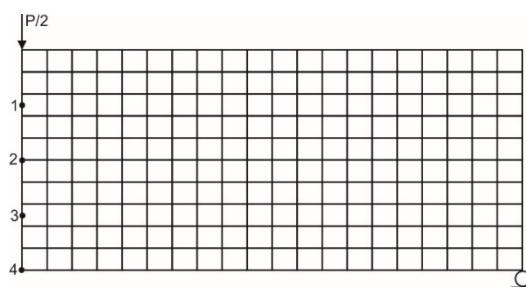
Grid	Variant of approximations				LIRA-SAPR
	1	2	3	4	
5×10	0.5893	0.5925	0.5891	0.5943	0.5859
10×20	0.5898	0.5907	0.5897	0.5913	0.5890
20×40	0.5900	0.5902	0.5899	0.5903	0.5897
30×60	0.5900	0.5901	0.5900	0.5902	0.5900
Exact value 0.5720					

The displacements of point C for the four stresses approximation variants are given in Table 9. All variants show good accuracy and fast convergence of the displacement value. With the grid of 30×60, the solutions practically coincide for all the considered variants. Variants 2 and 4 demonstrate convergence to the exact value from above.

Table 10. Stresses at points C and B (Figure 3b) for various approximation variants.

Grid	Variant	$\sigma_{x,C}$, kN/m ²		$\sigma_{y,C}$, kN/m ²		$\sigma_{y,B}$, kN/m ²	
		node	f. e.	node	f. e.	node	f. e.
5×10	1	-8.040	-7.598	16.919	14.383	6.580	7.004
10×20		-8.961	-8.737	16.887	15.440	6.629	6.834
20×40		-9.463	-9.352	16.804	16.028	6.650	6.750
30×60		-9.637	-9.354	16.765	16.235	6.656	6.722
5×10	2	-7.808	-7.668	16.572	14.252	6.559	7.091
10×20		-8.794	-8.754	16.819	15.391	6.616	6.859
20×40		-9.366	-9.355	16.802	16.013	6.642	6.757
30×60		-9.570	-9.565	16.771	16.228	6.650	6.725
5×10	3	-8.233	-7.605	14.739	14.480	7.030	6.948
10×20		-9.102	-8.743	15.546	15.478	6.837	6.818
20×40		-9.546	-9.354	16.058	16.040	6.750	6.746
30×60		-9.698	-9.565	16.233	16.241	6.722	6.720
5×10	4	-9.427		15.874		6.891	
10×20		-9.875		16.079		6.807	
20×40		-9.967		16.318		6.728	
30×60		-9.985		16.420		6.706	
5×10	LIRA-SAPR		-7.595		14.013		6.934
10×20			-8.739		15.325		6.817
20×40			-9.352		15.996		6.746
30×60			-9.569		16.224		6.722
Exact value			-10		16.6667		6.6667

The stresses at points B and C for different finite element meshes are given in Table 10. The stresses for approximations 1–3 were determined twice. The first value (title column is “f. e.”) is the stresses at the center of the finite element, which is adjacent to the corresponding point. The second value (title column is “node”) is the stresses were determined by substituting the node coordinates into the expression for the stress approximation functions (see Table 1). Comparison of the obtained results with exact values shows that the fourth variant has the best accuracy. The remaining variants have similar stresses values. With the greatest error, approximately 2.7 %, the stress values were calculated of third approximation variant and according to the LIRA-SCAD program. Of course, the stress values calculated for the nodes are more accurate.

**Figure 4. Half of hinged supported beam. Finite element grid 10×20.**

Also, calculations were carried out of hinged supported beam on the concentrated force action. Figure 4 shows half of the beam. The following parameters were adopted: span is 4 m, section height is $h = 1$ m, section width is $b = 1.0$ m, $E = 10\,000$ kN/m², $\mu = 0.3$, $P = 10$ kN. The book [23] provides analytical solutions for stresses in sections which is located near the concentrated force application point. The stresses values are presented in the following form:

$$\sigma_x = \sigma_{x,b} + \beta_x \left(\frac{2P}{h} \right), \sigma_y = \beta_y \left(\frac{2P}{h} \right). \tag{52}$$

$\sigma_{x,b}$ is the stress which was calculated by the beam theory in accordance with the Kirchhoff's hypothesis. The stresses values calculated in accordance with (52) for points 1–4 are given in Table 11.

Table 11. Analytical solution for the beam [23].

Point	β_x	σ_x , kN/m ²	β_y	σ_y , kN/m ²
1	0.428	-20.44	-1.230	-24.6
2	0.121	2.42	-0.456	-9.12
3	-0.136	27.28	-0.145	-2.90
4	-0.133	57.32	0	0

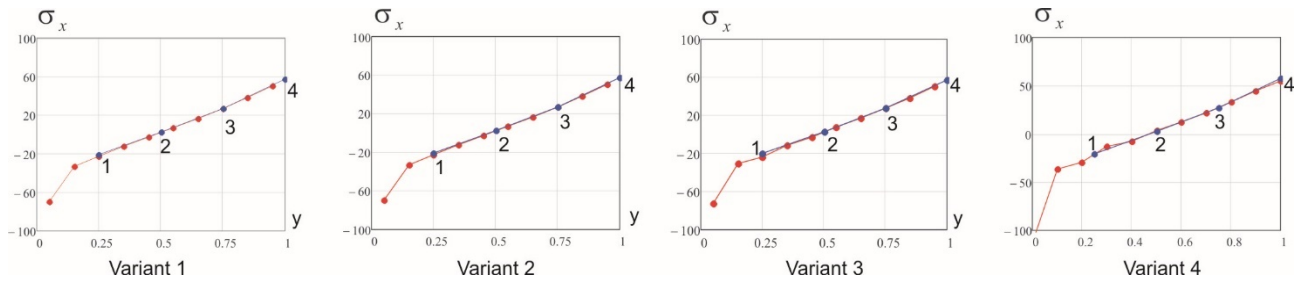


Figure 5. Stresses σ_x at the finite element centers, which lay on line 1–4, in the beam middle section (Figure 4). The blue line is the analytical solution.

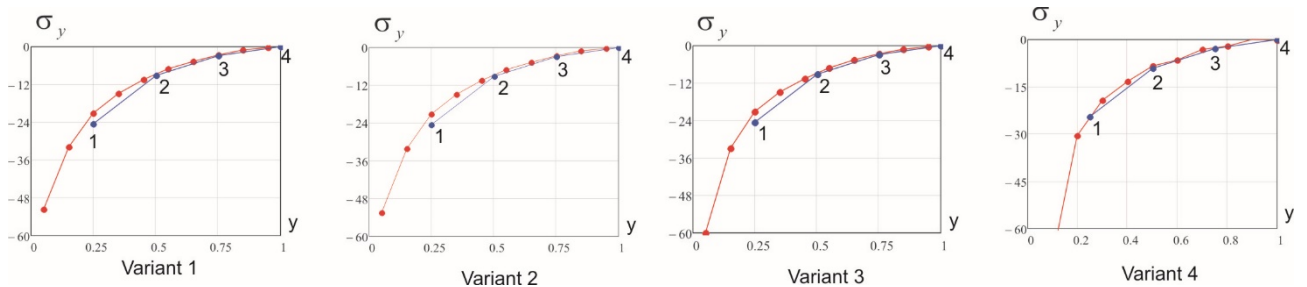


Figure 6. Stresses σ_y at the finite element centers, which lay on line 1–4, in the beam middle section (Figure 4). The blue line is the analytical solution.

The Figures 5–6 present the solutions for the considered stresses approximations variants, when was using the rather coarse 10×20 grid. The obtained solutions are in good agreement with the analytical solution. The fourth stresses approximations variant which use the piecewise constant functions allows to obtain the most accurate solutions for stresses. For variants 1–3, the greatest difference from the analytical solution is observed at point 1 which is closest to the point of concentrated force application and is the singularity point. Table 12 shows the obtained by the proposed methods stresses values.

Table 12. Stresses at point 1 (Figures 5–6).

Stress	Variant of approximations			Exact value
	1	2	3	
σ_x , kN/m ²	-22.58	-22.67	-23.91	-20.44
σ_y , kN/m ²	-21.09	-21.10	-21.03	-24.60

As in the previous examples, the approximation variants 1 and 2 provide closer to exact stresses values (Table 12). The stresses σ_x differ from the exact ones by about 11 %, and the stresses σ_y – by 14 %. Note that the solution of variant 4 practically coincides with the analytical solution at all points which lay along the height of the section.

In [1], algorithm the stiffness matrix constructing of rectangular finite element, which was based on the second stresses approximations variant, is considered. To build the stiffness matrix at first the strains are expressed through the stresses. Then the displacement functions are determined by integrating the deformations expressions. As a result, the displacements expressions turn out to be dependent on the transverse deformations coefficient. It is noted that for such element the inter-element displacements continuity is not provided. On the example of the cantilever beam calculation, it is shown that this element provides fast displacements convergence to the exact solution.

The approach proposed in this paper allows us to develop various equilibrium finite elements which are based on the fundamental principles of the additional energy minimum and possible displacements. These elements can be used for plane theory elasticity problems. The proposed method is based on stresses fields approximations. The considered stresses approximations variants showed good accuracy and convergence for test problems, when we grind the finite element grid. The best accuracy is demonstrated by stresses approximations variants 4, 1 and 2.

4. Conclusion

1. The method is proposed for constructing equilibrium arbitrary quadrangular finite elements for solving plane problems in the elasticity theory. The technique is based on the principles of additional energy minimum and possible displacements and it provides to use the necessary approximations of stresses.

2. Comparison of the solutions which were obtained by the proposed method with analytical solutions for the ring and the bent beam is performed. The best accuracy is provided by the variant which use piecewise constant approximations of stresses over finite element region. The deviation calculated values from exact solutions does not exceed 2 %. Such stresses approximations can provide the displacements convergence to exact values from above.

3. The stresses approximations which are based on variants 1 and 2 are discontinuous along the finite elements' boundaries, but also provide good accuracy in the stress' determination. Even we use coarse grids, the deviation calculated values from the exact solutions is 5–6 %. Such finite elements can be convenient when we must solve branched and combined structures.

4. The proposed method can be further used to build equilibrium triangular finite elements and to solve bulk problems of the elasticity theory.

References

- Zenkevich, O. Metod konechnykh elementov v tekhnike [The finite element method in technique]. Moscow: Mir, 1975. 541 p. (rus)
- Zenkevich, O., Morgan, K. Konechnyye elementy i approksimatsiya [Finite Elements and Approximations]. Moscow: Mir, 1986. 318 p. (rus)
- Gallager, R. Metod konechnykh elementov. Osnovy [Finite element method. The basics]. Moscow: Mir, 1984. 428 p. (rus)
- Artioli, E., de Miranda, S., Lovadina, C., Patruno, L. A stress/displacement Virtual Element method for plane elasticity problems. *Comput. Methods Appl. Mech. Eng.* 2017. Vol. 325. Pp. 155–174.
- Chernysheva, N.V., Kolosova, G.S., Rozin, L.A. Combined method of 3d analysis for underground structures in view of surrounding infinite homogeneous and inhomogeneous medium. *Magazine of Civil Engineering.* 2016. No. 2 (62). Pp. 83–91. DOI: 10.5862/MCE.62.8
- Tyukalov, Yu.Ya. Refined finite element of rods for stability calculation. *Magazine of Civil Engineering.* 2018. 79(3). Pp. 54–65. DOI: 10.18720/MCE.79.6
- Lalin, V.V., Rozin, L.A., Kushova, D.A. Variatsionnaya postanovka ploskoy zadachi geometricheski nelineynogo deformirovaniya i ustoychivosti uprugikh sterzhney [Variational statement of a plane problem geometrically nonlinear deformation and stability elastic rods]. *Magazine of Civil Engineering.* 2013. 36(1). Pp. 87–96. (rus) DOI: 10.5862/MCE.36.11.
- Artioli, E., Miranda, S., Lovadina, C., Patruno, L. A family of virtual element methods for plane elasticity problems based on the Hellinger–Reissner principle. *Computer Methods in Applied Mechanics and Engineering.* 2018. 340. Pp. 978–999.
- Li, Z., Chen, S., Qu, S., Li, M. Stabilization of low-order mixed finite elements for the plane elasticity equations // *Computers & Mathematics with Applications.* 2017. 73. Pp. 363–373.
- Leonetti, L., Garcea, G., Nguyen-Xuan, H. A mixed edge-based smoothed finite element method (MES-FEM) for elasticity. *Computers & Structures.* 2016. Vol. 173. Pp. 123–138.
- Elakkad, A., Bennani, M.A., Mekkaoui, J., Elkhalfi, A.A. Mixed Finite Element Method for Elasticity Problem. *International Journal of Advanced Computer Science and Applications.* 2013. Vol. 4. No. 2. Pp. 161–166.
- Mirsaidov, M.M., Abdikarimov, R.A., Vatin, N.I., Zhgutov, V.M., Khodzhayev, D.A., Normuminov, B.A. Nonlinear parametric oscillations of viscoelastic plate of variable thickness. *Magazine of Civil Engineering.* 2018. 82(6). Pp. 112–126. DOI: 10.18720/MCE.82.11
- Sukhoterlin, M.V., Baryshnikov, S.O., Knysh, T.P., Abdikarimov, R.A. Natural oscillations of a rectangular plates with two adjacent edges clamped. *Magazine of Civil Engineering.* 2018. No. 6(82). Pp. 81–94. DOI: 10.18720/MCE.82.8.
- Wang, Q., Zhou, W., Cheng, Y., Ma, G., Chang, X., Chen, E. NE-IIBEFM for problems with body forces: a seamless integration of the boundary type meshfree method and the NURBS boundary in CAD. *Adv. Eng. Softw.* 2018. Vol. 11. Pp. 1–17.
- Zhou, W., Yue, Q., Wang, Q., Feng, Y.T., Chang, X. The boundary element method for elasticity problems with concentrated loads based on displacement singular elements. *Engineering Analysis with Boundary Elements.* 2019. Vol. 99. Pp. 195–205.
- Gu, Y., Zhang, C., Qu, W., Ding, J. Investigation on near-boundary solutions for three-dimensional elasticity problems by an advanced BEM. *Int. J. Mech. Sci.* 2018. Vol. 142. Pp. 269–275.

17. Zhou, J., Wang, K., Li, P. A hybrid fundamental-solution-based 8-node element for axisymmetric elasticity problems. *Engineering Analysis with Boundary Elements*. 2019. Vol. 101. Pp. 297–309.
18. Lin, Mu, Junping, Wang, Xie, Ye. A hybridized formulation for the weak Galerkin mixed finite element method. *Journal of Computational and Applied Mathematics*. 2016. Vol. 307. Pp. 335–345.
19. Tyukalov, Yu.Ya. Finite element models in stresses for bending plates. *Magazine of Civil Engineering*. 2018. 82(6). Pp. 170–190. DOI: 10.18720/MCE.82.16
20. Tyukalov, Yu.Ya. Finite element models in stresses for plane elasticity problems. *Magazine of Civil Engineering*. 2018. 77(1). Pp. 23–37. DOI: 10.18720/MCE.77.3.
21. Tyukalov, Yu.Ya. Finite element model of Reisner's plates in stresses. *Magazine of Civil Engineering*. 2019. 89(5). Pp. 61–78. DOI: 10.18720/MCE.89.6
22. Tyukalov, Yu.Ya. Calculation method of bending plates with assuming shear deformations. *Magazine of Civil Engineering*. 2019. 85(1). Pp. 107–122. DOI: 10.18720/MCE.85.9.
23. Timoshenko, S.P., Gudyer, Dzh. *Teoriya uprugosti [Elasticity theory]*. Moskow: Nauka, 1979. 560 p. (rus)

Contacts:

Yury Tyukalov, +7(912)8218977; yutvgu@mail.ru

© Tyukalov, Yu.Ya., 2019



DOI: 10.18720/MCE.91.8

Равновесные конечные элементы для плоских задач теории упругости

Ю.Я. Тюкалов

Вятский государственный университет, г. Киров, Россия

* E-mail: yutvgu@mail.ru

Ключевые слова: аппроксимации напряжений, дополнительная энергия, метод конечных элементов, плоская задача

Аннотация. Работа посвящена построению конечных элементов на основе аппроксимации напряжений для решения плоских задач теории упругости. Такие элементы являются альтернативными существующим конечным элементам, полученным с использованием аппроксимации перемещений. Альтернативные решения позволяют более точно оценивать напряженно-деформированное состояние конструкции. Предлагаемая методика построения конечных элементов основывается на принципах минимума дополнительной энергии и возможных перемещений. Рассматриваются различные варианты аппроксимации напряжений, которые удовлетворяют дифференциальным уравнениям равновесия для случая отсутствия распределенной нагрузки. Выполнено сравнение решений, полученных по предлагаемой методике, с аналитическими решениями для кольца и изгибаемой балки. Рассмотренные варианты аппроксимации напряжений показывают для тестовых задач хорошую точность и сходимость при измельчении сетки конечных элементов. Показано, что лучшую точность вычисления напряжений и перемещений обеспечивает конечный элемент с кусочно-постоянными аппроксимациями напряжений. Кроме того, такой конечный элемент обеспечивает сходимость перемещений к точным значениям сверху. Другие варианты конечных элементов могут быть удобны для расчета разветвлённых и комбинированных конструкций. Предлагаемые равновесные конечные элементы могут быть использованы для более точного определения напряжений в рассчитываемых конструкциях. Предлагаемая методика может быть использована для построения объемных конечных элементов.

Литература

1. Зенкевич О. Метод конечных элементов в технике. М.: Мир, 1975. 541 с.
2. Зенкевич О., Морган К. Конечные элементы и аппроксимация. М.: Мир, 1986. 318 с.
3. Галлагер Р. Метод конечных элементов. Основы. М.: Мир, 1984. 428 с.
4. Artioli E., de Miranda S., Lovadina C., Patruno L. A stress/displacement Virtual Element method for plane elasticity problems // Comput. Methods Appl. Mech. Eng. 2017. Vol. 325. Pp. 155–174.
5. Чернышева Н.В., Колосова Г.С., Розин Л.А. Пространственные расчеты подземных сооружений с учетом работы окружающего бесконечного массива в однородных и неоднородных областях комбинированным способом // Инженерно-строительный журнал. 2016. № 2(62). С. 83–91.
6. Тюкалов Ю.Я. Улучшенный стержневой конечный элемент для решения задач устойчивости // Инженерно-строительный журнал. 2018. № 3(79). С. 54–65. DOI: 10.18720/MCE.79.6
7. Лалин В.В., Розин Л.А., Кушова Д.А. Вариационная постановка плоской задачи геометрически нелинейного деформирования и устойчивости упругих стержней // Инженерно-строительный журнал. 2013. № 1(36). С. 87–96. DOI: 10.5862/MCE.36.11
8. Artioli E., Miranda S., Lovadina C., Patruno L. A family of virtual element methods for plane elasticity problems based on the Hellinger–Reissner principle // Computer Methods in Applied Mechanics and Engineering. 2018. Vol. 340. Pp. 978–999.
9. Li Z., Chen S., Qu S., Li M. Stabilization of low-order mixed finite elements for the plane elasticity equations // Computers & Mathematics with Applications. 2017. Vol. 73. Pp. 363–373.
10. Leonetti L., Garcea G., Nguyen-Xuan H. A mixed edge-based smoothed finite element method (MES-FEM) for elasticity // Computers & Structures. 2016. Vol. 173. Pp. 123–138.
11. Elakkad A., Bennani M.A., Mekkaoui J., Elkhalfi A. A Mixed Finite Element Method for Elasticity Problem // International Journal of Advanced Computer Science and Applications. 2013. Vol. 4. No. 2. Pp. 161–166.
12. Мирсаидов М.М., Абдикаримов Р.А., Ватин Н.И., Жгуты В.М., Ходжаев Д.А., Нормуминов Б.А. Нелинейные параметрические колебания вязкоупругой пластинки переменной толщины // Инженерно-строительный журнал. 2018. № 6(82). С. 112–126. DOI: 10.18720/MCE.82.11
13. Сухотерин М.В., Барышников С.О., Кныш Т.П., Абдикаримов Р.А. Собственные колебания прямоугольной пластины, защемленной по двум смежным краям // Инженерно-строительный журнал. 2018. № 6(82). С. 81–94. DOI: 10.18720/MCE.82.8

14. Wang Q., Zhou W., Cheng Y., Ma G., Chang X., Chen E. NE-IIBEFM for problems with body forces: a seamless integration of the boundary type meshfree method and the NURBS boundary in CAD // *Adv. Eng. Softw.* 2018. Vol. 11. Pp. 1–17.
15. Zhou W., Yue Q., Wang Q., Feng Y.T., Chang X. The boundary element method for elasticity problems with concentrated loads based on displacement singular elements // *Engineering Analysis with Boundary Elements.* 2019. Vol. 99. Pp. 195–205.
16. Gu Y., Zhang C., Qu W., Ding J. Investigation on near-boundary solutions for three-dimensional elasticity problems by an advanced BEM // *Int. J. Mech. Sci.* 2018. Vol. 142. Pp. 269–275.
17. Zhou J., Wang K., Li P. A hybrid fundamental-solution-based 8-node element for axisymmetric elasticity problems // *Engineering Analysis with Boundary Elements.* 2019. Vol. 101. Pp. 297–309.
18. Lin Mu, Junping Wang, Xie Ye. A hybridized formulation for the weak Galerkin mixed finite element method // *Journal of Computational and Applied Mathematics.* 2016. Vol. 307. Pp. 335–345.
19. Тюкалов Ю.Я. Конечно элементные модели в напряжениях для изгибаемых пластин // *Инженерно-строительный журнал.* 2018. № 6(82). С. 170–190. DOI: 10.18720/MCE.82.16
20. Тюкалов Ю.Я. Конечно-элементные модели в напряжениях для задач плоской теории упругости // *Инженерно-строительный журнал.* 2018. № 1(77). С. 23–37. DOI: 10.18720/MCE.77.3.
21. Тюкалов Ю.Я. Конечно-элементная модель в напряжениях для пластин Рейснера // *Инженерно-строительный журнал.* 2019. № 5(89). С. 61–78. DOI: 10.18720/MCE.89.6
22. Тюкалов Ю.Я. Метод расчета изгибаемых плит с учетом деформаций сдвига // *Инженерно-строительный журнал.* 2019. № 1(85). С. 107–122. DOI: 10.18720/MCE.85.9
23. Тимошенко С.П., Гудьер Дж. Теория упругости. М.: Наука, 1979. 560 с.

Контактные данные:

Юрий Яковлевич Тюкалов, +7(912)8218977; эл. почта: yutvgu@mail.ru

© Тюкалов Ю.Я., 2019



DOI: 10.18720/MCE.91.9

Effects of polymer modified nanoclay on the performance of asphalt mixture

E. Siddig, P. Cheng*, Y. Li

Northeast Forestry University (NEFU), Harbin, China

* E-mail: chengpeifeng@nefu.edu.cn

Keywords: asphalt binder, asphalt mixtures, rheological properties, rutting parameters, nanoclay

Abstract. Recently, polymer-modified nanomaterial has received extensive attention as a key solution for improving the performance of asphalt binders. This study investigates the effect of polymer modified nanoclay (PMN) that made of ethylene vinyl acetate copolymer and nanoclay mixtures on the high-temperature performance of the asphalt binder and mixture. Moreover, the modified binder samples are prepared with PMN by using melt processing technique at concentrations of 1 %, 3 %, 5 % and 7 % with the weight of asphalt. Furthermore, the effect of the modifier on the binder properties is assessed using conventional tests like penetration and softening point, viscosity measurements, multiple stress creep recovery, and dynamic shear rheometry. Additionally, wheel tracking and moisture sensitivity tests are applied to investigate the high-temperature performance of the hot mix asphalt (HMA) mixture. The experimental results show that the rheological and physical properties are improved when PMN is used. The addition of PMN to HMA mixtures significantly improves the resistant to the rutting and moisture induced damages. Therefore, this study provides substantial technical support for improving the high-temperature performance of asphalt pavement in hot regions to reduce rutting concerns.

1. Introduction

The rapid economic growth increased number of vehicles per citizen and heavier traffic loads and speed. Thus, the asphalt pavement roads are required to increase its ability to carry the traffic loads under different conditions without causing distresses [1]. Rutting and moisture damage are among the most common problems of hot mix asphalt (HMA) asphalt pavement, and these defects increase further distress in the pavement. Therefore, the best performance is desired to encourage good adhesion and cohesion of the asphalt mixture to obey with the requirements of strong pavements that may enhance moisture susceptibility and rutting resistance of HMA mixture at high-temperature [2]. From this perspective, a significant amount of work has been done using various types of modifiers and additives. These includes carbon black, crumb rubber, sulfur, fly ash, bio oil, amine, and polymers, which improve the physical and rheological properties of asphalt binders [3–5]. Among them, the polymers which produce polymer modified asphalt (PMA) obtained the highest achievement.

Several polymers have been tested as modifiers, involving thermoplastic elastomers, plastomers, and reactive polymers. However, only thermoplastic block copolymers and ethylene-vinyl acetate (EVA) received an extensive application in practice [6, 7]. Some of these copolymers are acceptable in terms of performance and cost [8, 9]. Additionally, the EVA copolymer is known as one of the top modifiers that significantly enhances the rheological behavior, physical and mechanical properties of base asphalt [10]. That said, EVA are different from conventional asphalt in molecular weight, density, and chemical nature making the interphase of EVA modified asphalt inadequate, and it is easy to separate [11]. Furthermore, the interphase of EVA modified asphalt is reduced due to short-term aging of EVA binders through production, storage, and transportation, besides long-term aging during the service life of pavement [12]. Therefore, an EVA binder

Siddig, E., Cheng, P., Li, Y. Effects of polymer modified nanoclay on the performance of asphalt mixture. Magazine of Civil Engineering, 2019, 91(7), Pp. 98–111. DOI: 10.18720/MCE.91.9

Сиддиг Е., Ченг П., Ли Ю. Влияние модифицированной полимером наноглины на характеристики асфальтобетонной смеси // Инженерно-строительный журнал. 2019. № 7(91). С. 98–111. DOI: 10.18720/MCE.91.9



This work is licensed under a CC BY-NC 4.0

becomes hard and brittle resulting in pavement deterioration [13]. The EVA modified asphalt needs to be modified by another material to improve its performance.

Recently, nanomaterials have received considerable attention in the field of modified asphalt to produce more efficient materials. These materials can enhance the performance and strength of asphalt. Many types of nanomaterials have been applied to modify asphalt: e.g. nanotitanium, nanosilicon dioxide, nanoclay, and carbon nanofibers [14]. Recent studies demonstrated that the nanoclay can improve the characteristics of asphalt binders used in asphalt concrete mixtures. Polymeric nanocomposites are one of the common potential materials identified. The physical properties of the asphalt binder are effectively improved when a polymer is adjusted with small amounts of nanoclay, especially when the clay is dispersed at a nanoscopic level [8]. On the other hand, nanoclay (NC) have been utilized as a minor modifier to extra improve the performance of PMA [15–17]. However, limited work has been done to assess the asphalt modification using NC combined with EVA and the effect of NC on the interphase of EVA PMA. Comprehensive research is needed in this direction to understand the complex structure–property association in various nanocomposites. It is important to perform extensive rheological measurements and study the physical and mechanical properties of asphalt mixtures made from the various content of polymer-modified nanoclay (PMN) binder.

Therefore, this study aims to evaluate the effect of PMN on the high-temperature performance of asphalt binders and mixtures. The following binder properties were carried out i.e. penetration, softening point, viscosity measurement, multiple stress creep recovery and dynamic shear rheometry for unaged and rolling thin film oven test (RTFOT) aged binders. In addition, the HMA performance factors i.e. Marshall stability and flow, rutting resistance, and moisture sensitivity were examined.

2. Materials and Methods

2.1. Materials

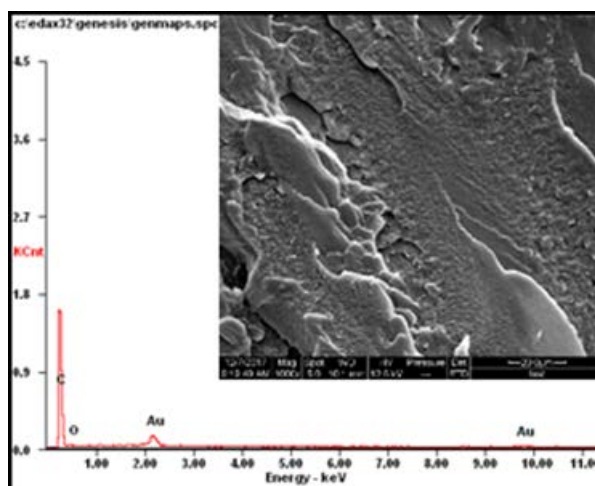
The paving asphalt AH-70#, according to the Chinese classification, was used to prepare a modified asphalt binder in this research. The physical properties of base asphalt are provided in Table 1. The EVA copolymer with a content of 28 % of vinyl acetate by weight was used as the polymer modifier (Figure 1). Properties of the EVA are presented in Table 2. The used NC modifier is delivered from montmorillonite clay mineral (see Figure 2) as provided by Fenhong Clay chemical factory, China. The properties of NC are given in Table 3. The aggregates (coarse and fine) used in this study are crushed basalt minerals with a maximal normal size of 16 mm delivered from Harbin, China. Figure 3 shows the aggregate gradation and further properties are presented in Table 4.

Table 1. Some properties of asphalt binder.

Test	Standard	Result
Penetration depth (100 g, 5 s, 25°C), 0.1 mm	ASTM D5	75.05
Ductility (25 °C, 5 cm/min), cm	ASTM D113	150+
Softening point (°C)	ASTM D36	48.7
Specific gravity at 25 °C (g/cm ³)	ASTM D70	1.03
Flash Point (°C)	ASTM D92	320
Retained penetration after RTFO (%)	ASTM D5	63.5
Softening point (°C) after RTFO	ASTM D36	51.4



(a)



(b)

Figure 1. The EVA copolymer (a) sample; (b) EDAX graph and corresponding SEM image.

Table 1. Physical and mechanical properties of EVA used in this study.

Property	Specification	Value
Molecular structure	–	Linear
Density (g/cm ³)	ASTM D792	0.9335
Physical form	–	pellet
Melt flow rate	ASTM D1238	7
Tensile strength (MPa)	ASTM D412	29
Flexural modulus (MPa)	ASTM D412	3100
Shore hardness (A)	ASTM D2240	70
Elongation at break (%)	ASTM D 412	800

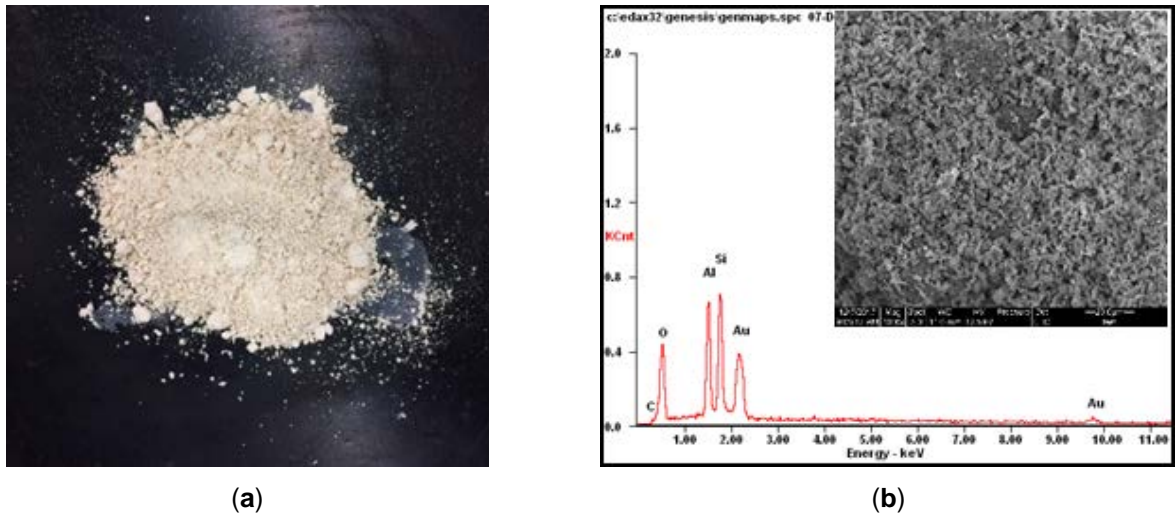


Figure 2. The Nanoclay (a) sample; (b) EDAX graph and corresponding SEM image.

Table 2. Properties of the NC sample used in this study.

Property	Value
Base	Montmorillonite
Concentration of modifier %	48
PH	7.1
Free space between particles (A°)	60
Specific surface (m ² /g)	80
Density (g/cm ³)	6

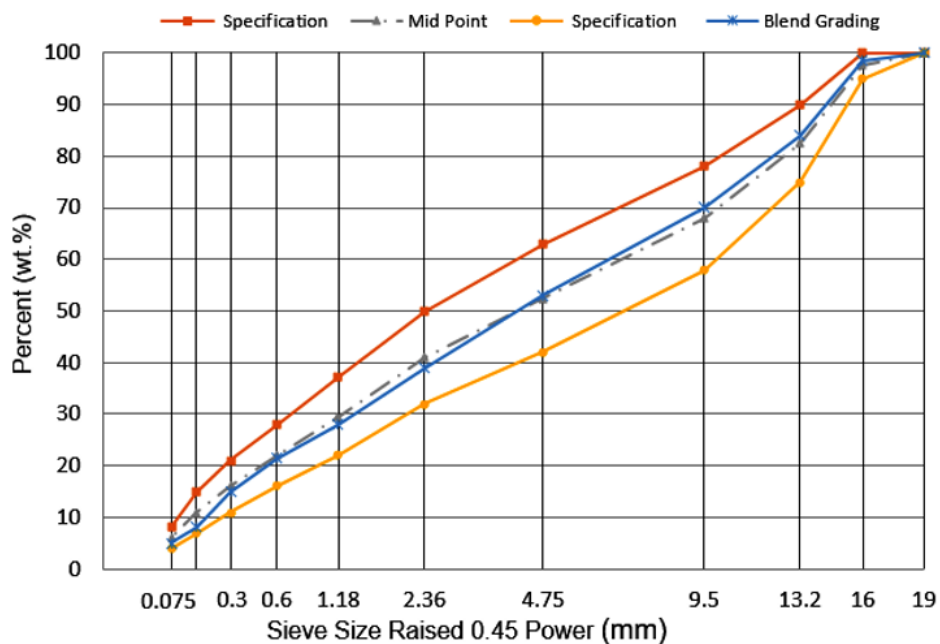


Figure 3. Aggregate gradation chart.

Table 3. Aggregates properties.

Aggregate Property	Value
Crushing value (coarse aggregate) (%)	13.1
Los Angeles abrasion value (%)	15.1
Apparent specific gravity	2.78
Water absorption (%)	0.39
Apparent specific gravity (fine aggregate)	2.69
Sand equivalent (%)	93.7

2.2. PMN Formulation

The PMN was produced by using a melt processing method because it is efficiently and simplicity. Firstly, a 60:40 mass ratio of EVA: NC are mixed under high shear at a rate of 60 rpm and for 15 minutes at 185 °C using a conventional twin-screw extruder mixer to produce sheets of about 2.0 mm thickness. Subsequently, the product was cooled for nearly three hours, followed by grinding to the required size by a sheet pelletizer. Finally, the PMN sample (see Figure 5) was characterized and utilized to prepare the modified asphalt binder samples with a different concentration.

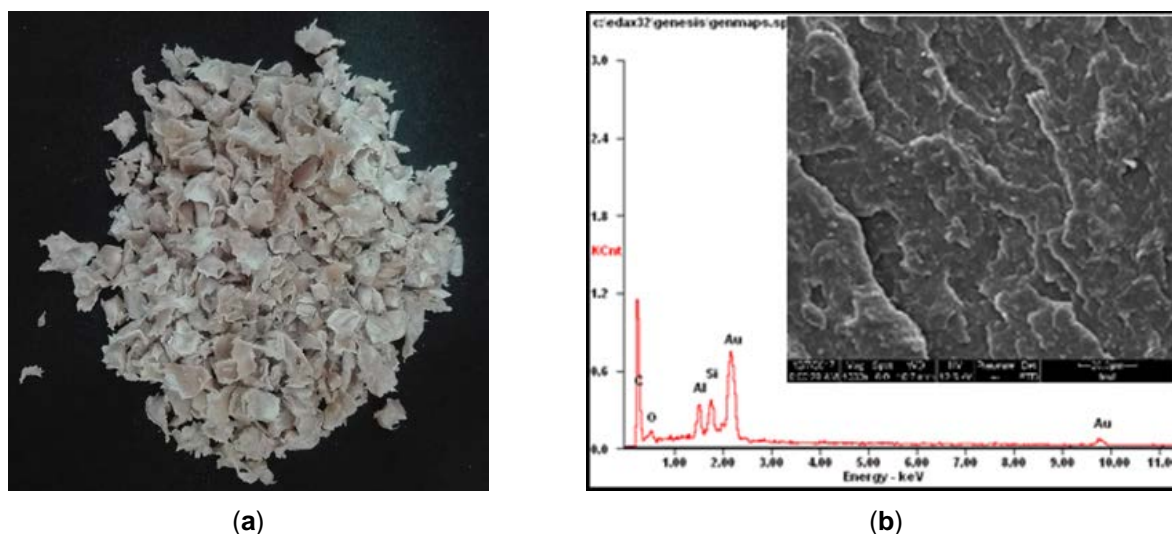


Figure 4. The PMN (a) sample; (b) EDAX graph and corresponding SEM image.

2.3. Preparation and Characterization of PMNs Binder

Energy Dispersive Analysis X-Ray (EDAX) is an analytical technique to complete the elemental and chemical analysis. The EDAX was used to analyse the elemental compositions of NC, EVA, and PMN during imaging in SEM. Figure 5 demonstrates the Field Emission Scanning Electron Microscope (FE-SEM) machine and Pelletizer machine used in this work. The EDAX results and its corresponding SEM images are displayed in Figures 1, 2 and 4. An electronic beam SEM and EDAX systems were used to inspect the chemical composition of PMN, NC, and EVA samples. The characterization was done at several locations of NC, EVA, and PMN samples. The SEM micrographs of EVA, NC, and produced PMN are shown in Figures 1, 2 and 4, respectively. Figure 4 shows the PMN of the melted EVA matrix mixed with NC and indicates the homogeneity of the mixture, good distribution, and dispersion of nanoclay layers in the polymer matrix. The segregations, inclusions and agglomeration of nanoclay particles did not occur. This confirmed that the processing and mixing techniques adopted to prepare PMN can create a homogeneous distribution.

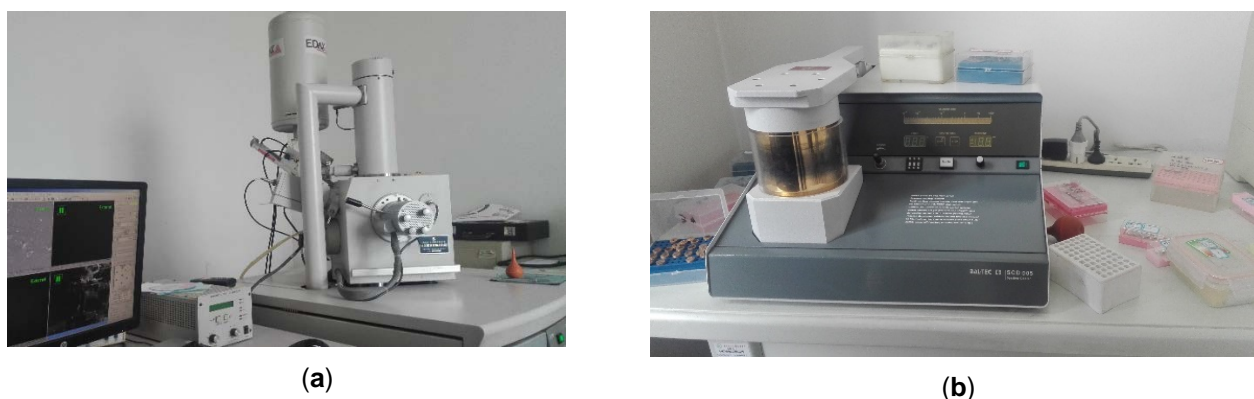


Figure 5. (a) Field Emission Scanning Electron Microscope; (b) Pelletizer machine.

The PMN binders were prepared by utilizing a mechanical mixer and a high-shear mixer. More specifically, 500 g of base asphalt was heated to reach 0.175 Pa.s of viscosity level. Later, different mass concentrations of PMN (1, 3, 5, and 7 %) by weight of base asphalt were gradually added to the base asphalt. The material was mixed at 500 rpm for 10 minutes in a mechanical mixer. Consequently, the samples were shifted to the high-speed mixer and mixed at a speed of 4500 rpm while maintaining a temperature of 150 ± 5 for 45 minutes. Finally, the mixtures were degassed for 5 minutes to remove air molecules trapped during mixing.

2.4. HMA Mixtures Preparations

Marshall's mix design method (ASTM D-1559) is used in China to optimize HMA mixtures. In this study, five asphalt percentages (3.5 %, 4.0 %, 4.5 %, 5.0 % and 5.5 %) were used for the HMA mixture's design. It has been detected that at 4.0 % air voids, the required asphalt content is 4.8 %, as the optimum asphalt content (OAC) used for preparing all HMA mixtures.

2.5. Testing Procedure

2.5.1. Binder Properties Testing

The rheological properties of PMN asphalt binders were assessed using conventional tests (softening point and penetration), as well as rotational viscosity, Multiple Stress Creep Recovery (MSCR) and Dynamic Shear oscillatory (DSR), according to the corresponding specifications ASTM D36, ASTM D5, ASTM D4402, ASTM D7405, and ASTM D4402.

The DSR test is applied to measure viscoelastic behaviour (rheological behaviour) of asphalt at intermediate to high temperatures. The complex shear modulus (G^*) and phase angle (δ) are measured to determine the rutting parameter ($G^*/\sin(\delta)$) of a binder. In this study the DSR tests were conducted for both unaged and RTFO-aged binders using a 25-mm-diameter plate and a 1 mm gap with a fixed oscillation frequency of 10 rad/sec (1.59 Hz to simulate the track run with a speed of nearly 55 mph) and a shear stress of 12.5 % applied to unaged and 10 % RTFO to aged binders, based on ASTM D4402.

The MSCR test was established to evaluate the high-temperature permanent deformation resistance of modified asphalt binder. It was adopted as a high-temperature rutting parameter for the Performance Grading (PG) of asphalt binders under the Superpave system in (FHA 2011) to replace the existing high-temperature binder test ($G^*/\sin \delta$). In this paper, The MSCR test was performed on by the DSR device to obtain non-recoverable creep compliance (Jnr) and percent recovery (R) of RTFO-aged asphalt binder at 52, 58, 64, 70 and 76 °C with 0.1 and 3.2 kPa creep stress according to ASTM D7405. A total of 10 cycles of creep and recovery 1 s of constant shear load and 9 s of recovery using a constant shear load of 0.1 kPa, followed by 10 cycles with a constant shear load of 3.2 kPa [18]. The compliance value at 0.1 and 3.2 kPa was denoted as Jnr0.1 and Jnr3.2.

2.5.2. Mixture Performance Testing

To evaluate the performance of PMN-modified asphalt mixture on the mechanical properties of HMA, the Marshall stability and flow, indirect tensile strength (ITS), and wheel tracking test (rutting test) were performed according to ASTM-D1559, ASTM D4867, and AASHTO T 324.

The Marshall stability and flow test were performed in line with ASTM D1559. Marshall specimens were stored in a water bath at a temperature of 60 °C for 35 minutes before starting the test. After 35 minutes, the specimens were placed in the Marshall apparatus and tested directly. The Marshall stability was applied at maximum load with a constant strain of 51mm per minute up to failure. During the test, a dial gauge was used to measure the vertical deformation of the specimen. The Marshall flow value was expressed as the vertical deformation that happens at the failure point of a specimen.

The wheel tracking test was used to evaluate the permanent deformation (rutting) performance of the HMA mixtures by recording the high-temperature stability of the asphalt mixture. In this test, the rut depth produced by the repeated wheel loading and pressure of 700 N and 0.7 MPa respectively was measured. The rutting test was executed according to the standard test method JTG E20-2011, T 0719 with the sample being kept at 60 ± 1 °C for six hours. The dimensions of test samples were 300 mm × 300 mm × 50 mm. Dynamic stability (DS) can be calculated as follow:

$$DS = \frac{(t_2 - t_1)NC_1C_2}{(d_2 - d_1)}, \quad (1)$$

where DS is the dynamic stability (cycle/mm);

d_1, d_2 are rut depth (mm) at time t_1 (45 minutes) and time t_2 (60 min), respectively (mm);

C_1, C_2 are machine and specimen factors (here both are 1.0);

N is the number of times the wheel passes per minute (here it is 42 cycles/minute).

The moisture susceptibility test was executed by comparing the ITS of 6 Marshall samples compacted to 7 % air void. The samples were divided into two groups, each containing 3 samples of HMA mixture. The first group was immersed in water at 60 ± 1 °C for 24 hours (conditional group) and the second group was set at 25 ± 1 °C (unconditional group). Next, the samples were placed in a loading machine with the load at a speed of 50 mm/min to reach the failure point. The ITS and tensile strength ratio (TSR) can be calculated by Equations (2) and (3) respectively.

$$ITS = \frac{2P_{max}}{\pi td}, \tag{2}$$

where ITS is the indirect tensile strength (Pa),

P_{max} is the maximum applied load (N);

t is the thickness of the specimen (mm);

d is the diameter of the specimen (mm).

$$TSR (\%) = \frac{\bar{R}_{T2}}{\bar{R}_{T1}} \times 100, \tag{3}$$

where \bar{R}_{T1} is the average ITS of an unconditional set (MPa),

\bar{R}_{T2} is the average ITS of conditional specimens (MPa) and TSR is the average tensile strength ratio (%).

3. Results and Discussion

3.1. Binder Properties Tests

The results obtained from the conventional test of PMN binder are displayed in Figure 6. From Figure 6(a) displays that the penetration depth of the asphalt binder is decreased while the softening point is increased with increasing PMN concentration. Obviously, the penetration values of asphalt were decreased by 21 %, 32 %, 36 % and 39 % for given concentrations i.e. 1 %, 3 %, 5 % and 7 % of PMN, respectively. The softening point increased from 48.5 to 60 with an increasing percentage of about 23 % of base asphalt. It is was greater than the maximum pavement temperature during the summer season. Importantly, this indicated that the PMN had a considerable enhancement on the consistency of the asphalt. Specifically, this enhancement made the PMNs modified asphalt binder more appropriate for pavement construction with a high bond strength and less susceptibility to permanent deformation at high-temperature.

Figure 6(b) illustrates the relationship between the rotational viscosity at a temperature of 135 °C and PMN content. It was observed that the viscosity values of asphalt binder have been increased linearly with PMN contents. The viscosity values of asphalt binder were increased by 29 %, 56 %, 83 %, and 101 % when the addition values of PMN content were 1 %, 3 %, 5 % and 7 % PMN. Clearly, the highest viscosity value is achieved at 7 % PMN modified binder. The increase in the value of viscosity was consistent with the specification limits (the SHRP specifications stated that the viscosity values at 135 °C should be ≤ 3.0 Pa s to avoid difficult workability induced by high viscosity). The viscosity within the prescribed range will increase the adhesion between aggregates and binder and improve the mixture's workability. Eventually, it will reduce the stripping rate and improve the stability of the asphalt concrete mixture.

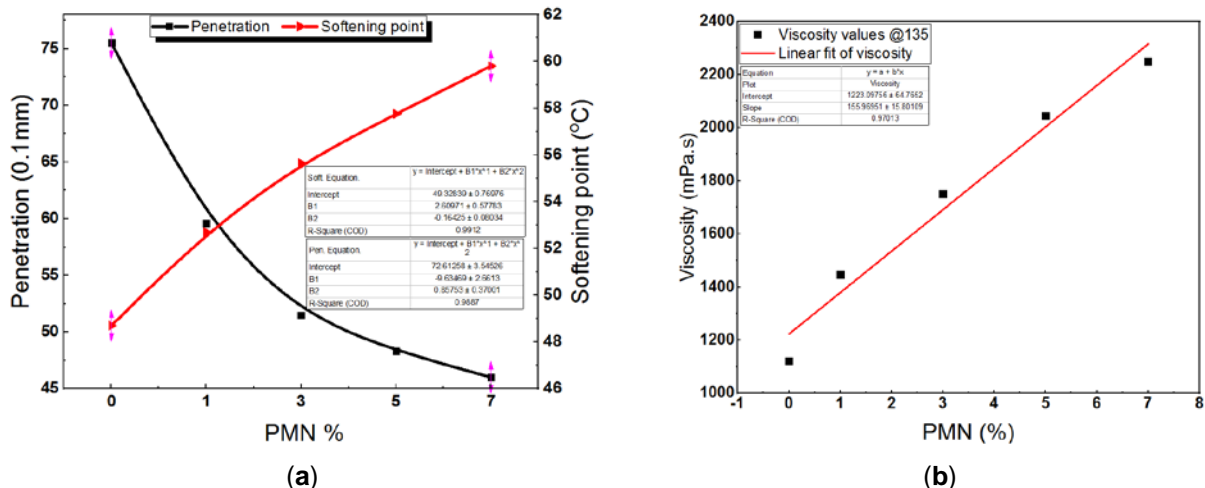


Figure 6. Effect of PMN content on the (a) penetration and softening point; (b) viscosity measurement.

3.1.1. Temperature Sensitivity

The effects of PMN as an additive on the temperature sensitivity were evaluated by penetration index (PI) and penetration viscosity number (PVN). The results of conventional tests (penetration, softening point and viscosity) were used to determine the PI and PVN. There are several models which define the consistency changes on asphalt with temperature. One of the famous models established by Pfeiffer and Van Doormaal [19] is stated as follows:

$$PI = \frac{1952 - 500 \log(\text{pen}) - 20SP}{50 \log(\text{pen}) - SP - 120}, \quad (4)$$

where Pen is the penetration depth in 0.1 mm @25 °C;

SP is the softening point temperature.

Equation (4) was applied to determine the PI from the measured penetrations depth and softening point temperatures.

The asphalt binder used in the highway pavement has a PI range from -3 to +7 for high-temperature sensitivity binder and highly blown low-temperature sensitivity binder, respectively [19, 20]. Moreover, the PI of base asphalt is -0.522 whereas the value of PMNs binder increases with the increase of the modifier content up to +0.781 for PMN7 as illustrated in Table 5. This indicates that the temperature sensitivity of the asphalt has been decreased with the increasing of PMN content.

The PVN can be determined according to the value of penetration at 25 °C and viscosity at 135 °C using Equation (5) [21]

$$PVN = 1.5 \frac{4.258 - 0.7967 \log(Pen_{25}) - \log(Vis_{135})}{0.795 - 0.1858 \log(Pen_{25})}, \quad (5)$$

where Pen_{25} is the penetration depth in 0.1 mm @25°;

Vis_{135} is viscosity value @135 °C.

Table 5 presents the PVN values and reflects that all PMN-binder samples are less susceptible to temperature variations than the base asphalt. Most significantly, the asphalt binder used for pavement construction has a PVN range from -2.0 to +0.5 pertaining to high-temperature sensitivity and low-temperature sensitivity, respectively [7, 22]. In this study, the PVN values varied between 0.097 and 0.145 for 0 and 7 % of PMN binder. These PVN values lie within the referenced range. Thus, base asphalt is considered as the maximum temperature sensitivity binder, and PMN is the minimum temperature sensitivity binder. Therefore, the temperature susceptibility was considerably reduced in the PI and PVN for PMN modified asphalt binders. This indicates that they are more disposed to permanent deformation at high temperatures and become rigid and brittle at low temperatures. The PI and PVN values propose that PMN binder is appropriate to use in road pavement.

Table 4. Penetration index (PI) and penetration viscosity number (PVN).

PMN %	PI	PVN
0	-0.522	0.097
1	-0.124	0.105
3	0.188	0.112
5	0.482	0.125
7	0.781	0.145

3.1.2. Dynamic Shear Oscillatory Test

The complex shear modulus (G^*) and phase angle (δ) are generally used to characterize viscoelastic properties of asphalt binders. Figure 7(a) and (b) show (G^*) and (δ) versus temperature, obtained from DSR test of base and PMNs modified asphalt binder before and after RTFO aging respectively. As can be seen from Figure 7 the values of G^* are significantly decreased. On the other hand, the values of δ were gradually increased with increasing temperature for all binders (base and modified asphalt). The results given in Figure 7 show that G^* values increased, while the δ magnitudes decrease with increasing of PMN %. This increase in G^* increases indicates that PMN binder is stiffer than unmodified asphalt which may increase the contribution of asphalt in permanent deformation resistance. Furthermore, a decrease in δ after adding PMNs indicates improves in the elastic response of asphalt binder, which can recover to its original shape after being

deformed by a load. Comparing the values of G^* and δ before and after RTFOT aging, it can be noticed that the G^* and δ values for the RTFO-aged binders are higher than the unaged binders. Indicates that PMN had stiffening effects on the asphalt binders. In contrast, the reduction in δ value gives an indication of more elasticity. Therefore, the hardness of asphalt was increased after adding PMNs led to improves the high-temperature performance of asphalt. Additionally, PMNs had a positive effect in enhancing the aging resistance of the asphalt binder.

The rutting parameter $G^*/\sin(\delta)$ is used to evaluate the resistance of asphalt binders to permanent deformation at high temperatures. $G^*/\sin(\delta)$ values of base and PMN- modified asphalt binders are presented in Figure 8. It is shown that the $G^*/\sin(\delta)$ increased with increasing PMN %, while significantly decreased with increasing temperature for both modified and unmodified asphalt binder. However, $G^*/\sin(\delta)$ of PMNs modified binder's is always higher than that of base asphalt at the same temperature before and after RTFO aging. Therefore, the PMNs enhances the high-temperature performance of the base asphalt binder by increasing resistance of asphalt binder to rutting.

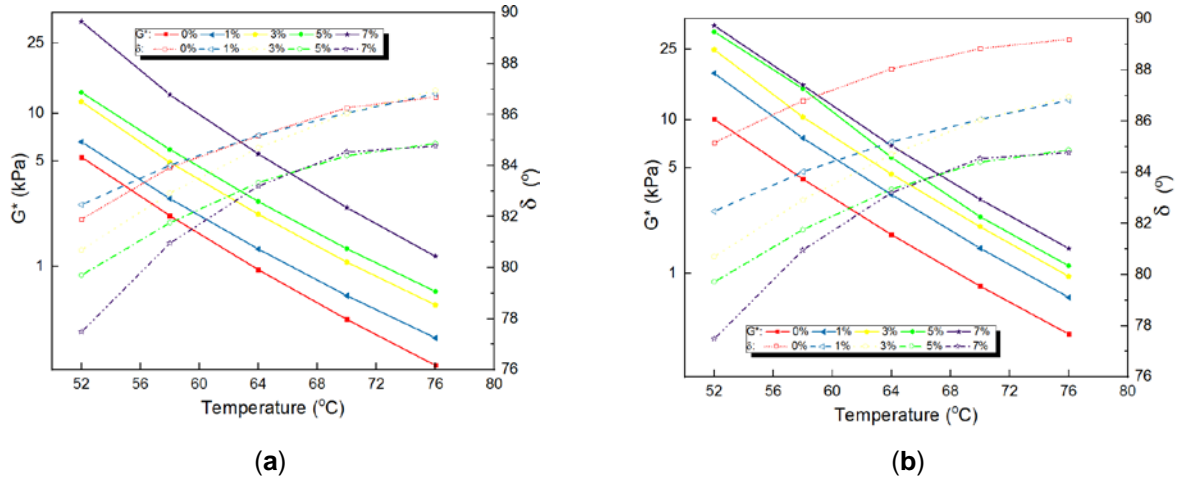


Figure 7. Complex shear modulus G^* (left) and phase angle δ (right) at different temperature (a) before and (b) after aging.

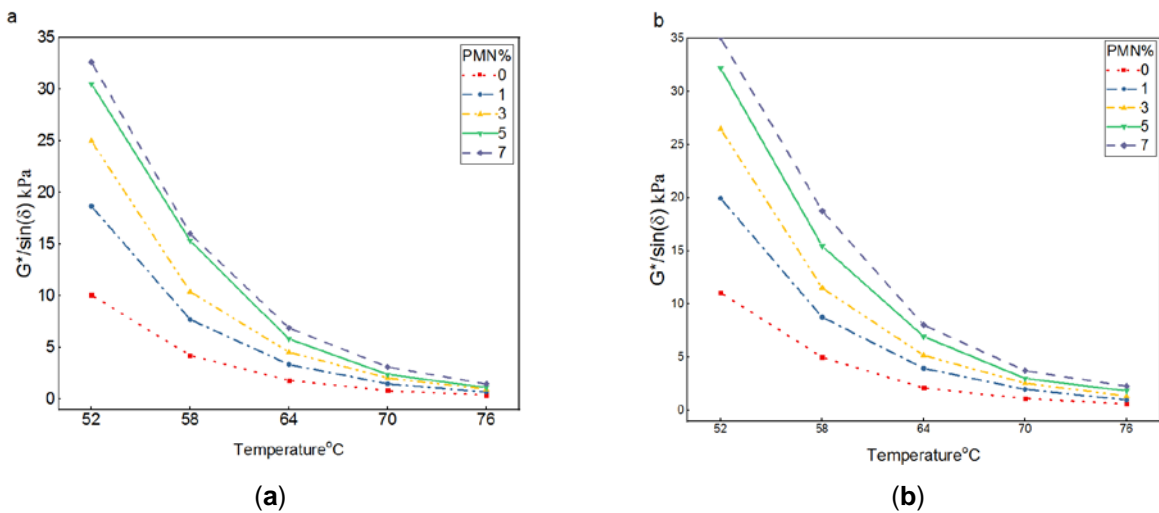


Figure 8. Rutting parameters ($G^*/\sin(\delta)$) based on DSR measurements at different temperatures (a) before and (b) after aging.

The critical temperature (T_c) conducted by performance grade (PG) is the temperature at which $[G^*/\sin(\delta) \leq 1 \text{ kPa}]$ at a frequency of 10 rad/s and strain value is 10 % for an un-aging binder, and that at which $[G^*/\sin(\delta) \leq 2.2 \text{ kPa}]$ at strain value is 12 % and a frequency of 10 rad/s for a RTFO aging binder. Consequentially, the T_c is determined from DSR software and presented in Table 6, T_c of PMN was higher than that of the base asphalt, proving that modified binders with higher PMN contents have higher critical temperatures leads to improve the PG-temperature grade. It also observes from Table 6, that the T_c of asphalt binders after RTFO aging is lower than that before aging. However, the true PG-temperature grade of base asphalt was shifted from PG58-xx to PG76-xx for PMN binders with concentrations of 7 % by weight. The PG76-xx binder can be successfully implemented into pavement construction in hot climates, owing to its good high-temperature performance.

Table 5. True Grade Temperature (PG Grade) for permanent deformation.

PMN %	True Temperature				PG Grade
	Before RTFOT		After RTFOT		
	T _c [°C]	G*/sin(δ)	T _c [°C]	G*/sin(δ)	
0	64	2.19	63	5.051	PG58-XX
1	67	1.31	68	3.961	PG64-XX
3	71	1.074	70	2.559	PG70-XX
5	73	1.317	71	2.999	PG70-XX
7	77	1.171	76	2.276	PG76-XX

3.1.3. Multiple Stress Creep Recovery

Figure 9 displays the accumulated strain of PMN modified asphalt samples at 0.1 kPa and 3.2 kPa stress level at a temperature of 64 °C as an example. Comparing Figure 9 (a) and (b), it can be realized that a higher creep stress level was associated with a higher accumulated creep strain levels; it means that the stress level has a serious effect on the accumulated strain and the growth rate of strain direct proportion with stress level. With the same stress level, the addition of PMN reduced the accumulated strain value, and the asphalt binder modified by PMN had the lowest value and indicates the better rutting resistance. In order to evaluate the strain response by asphalt binder to stress, the non-recoverable compliance (J_{nr}) is presented in Figure 10. The J_{nr} is generally used as indicating to resistance against deformation of the binder at high temperature and repeated loading [23–25]. From Figure 10 J_{nr} values at both stress level (0.1 kPa and 3.2 kPa) of unmodified asphalt are greater than that of PMN modified asphalt at all temperature range. The J_{nr} decreased from over 16 to less than 4 kPa-1 for as the dosage of PMN increased from 1 % to 7 %. For instance, in Figure 10 (a) the J_{nr} value of base asphalt being lower by 45 %, 49 %, 61 %, and 80 % at PMN content of 1 %, 3 %, 5 %, and 7 % respectively. Figure 10 (b) show that the J_{nr} value of base asphalt being lower by 51 %, 48 %, 57 %, and 69 % at and PMN content of 1 %, 3 %, 5 %, and 7 % respectively. It indicates, the addition of PMN decreased the non-recoverable deformation of binder and can contribute to the rutting resistance of associated asphalt mixtures. The effects of PMN dosage on elastic recovery (R) at two stress levels are displayed in Figure 11. It can be detected that the asphalt binder samples prepared using PMN had much better recoveries than base asphalt. For the same sample, the lower stress level compares with a higher elastic recovery. The sample prepared with 7 % PMN gained the highest recovery at both 0.1 kPa and 3.2 kPa stress. After increasing the PMN %, the R-value is increased from around 8 % to nearly 30 %. For example, in Figure 11 (a) the R-value of base asphalt is increased from 9 % to 21.1 %, 32.1 %, 41.6 % and 45.3 % when used 1 %, 3 %, 5 %, and 7 % PMN respectively. Figure 11 (b) show that the R-value of base asphalt increased from 5 % to 14.2 %, 24.6 %, 33.35 and 38.71 % when used 1 %, 3 %, 5 %, and 7 % PMN respectively. However, variations of PMN dosage have had further influence on recovery values, which suggests that PMN has the ability to improve the elastic recovery of asphalt binder. The MSCR test results demonstrate that the PMN dramatically increases the resistance of binder to permanent deformation.

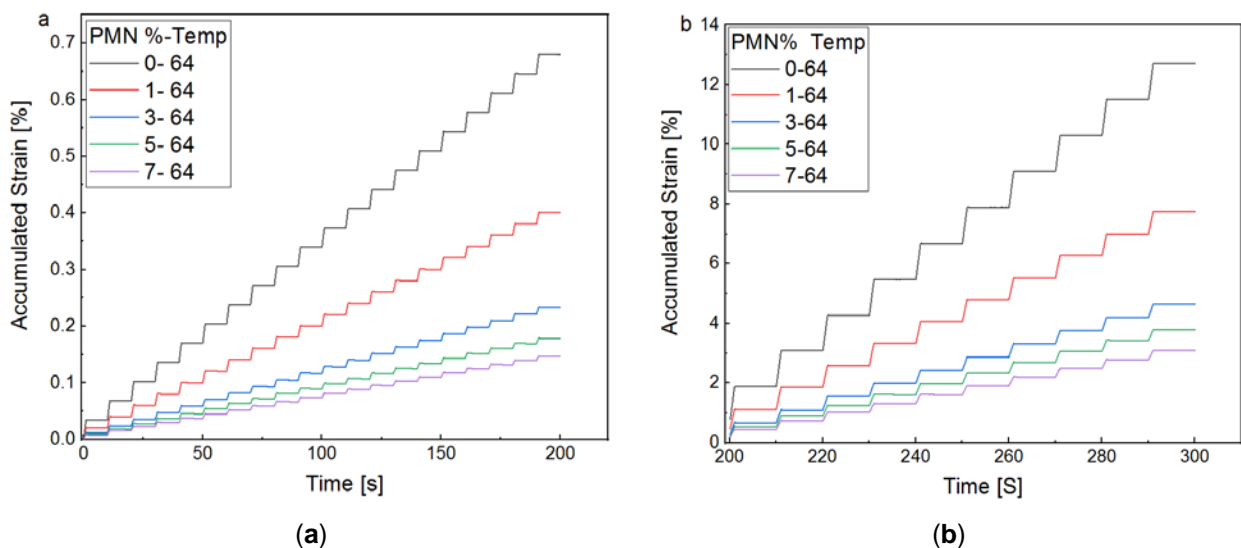


Figure 9. Accumulated strain on asphalt binder obtained from MSCR tests at 64 °C under different stress levels: (0–200 s) 0.1 kPa (a) and (200–300 s) 3.2 kPa (b).

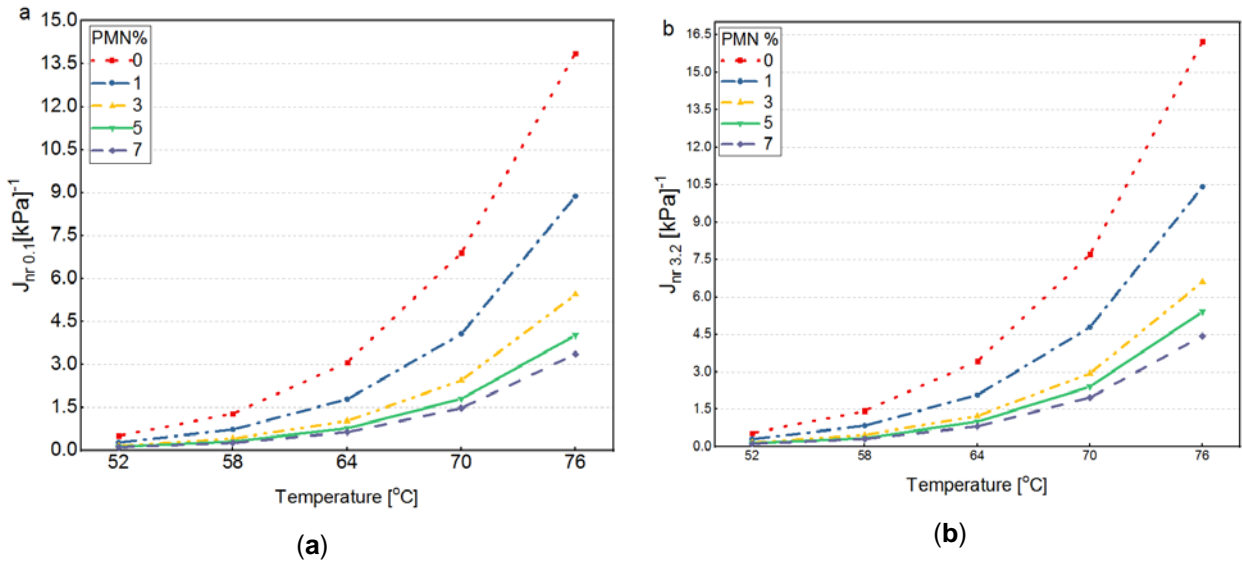


Figure 10. Non-recoverable creep compliance (J_{nr}) at different temperatures and stress levels; 0.1 kPa (a) and 3.2kPa (b).

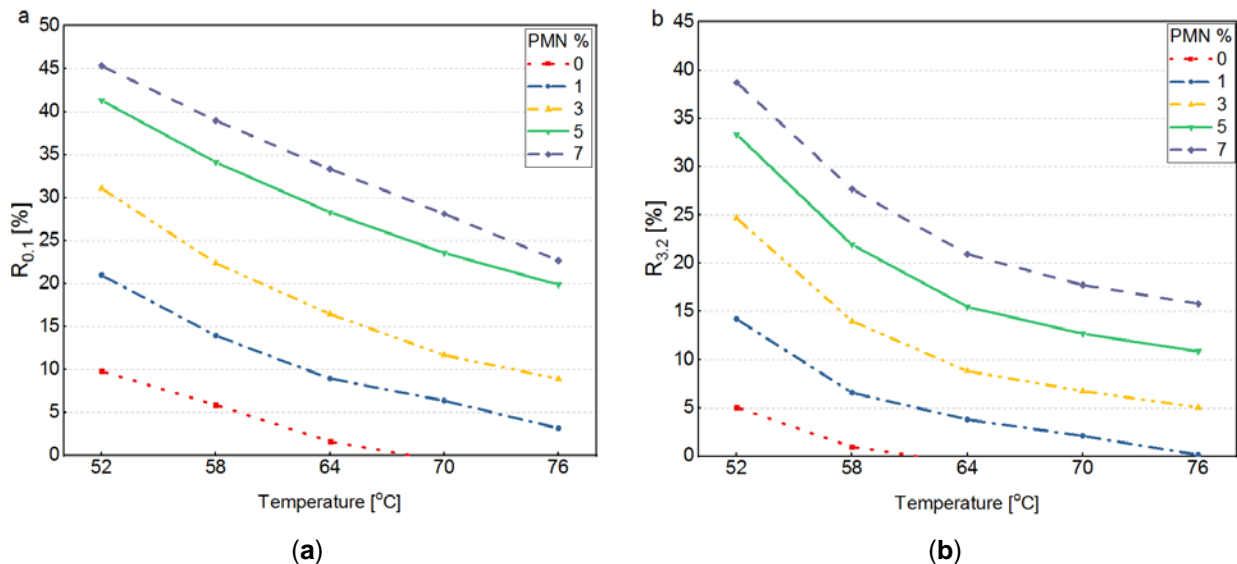


Figure 11. Elastic recovery (R) at different temperature and stress levels 0.1 kPa (a) and 3.2 kPa (b).

3.2. Mixture Performance Testing

3.2.1. Result of Marshall Tests

The relationships between average Marshall Stability (MS), Flow and Marshall Stiffness or Quotient (MQ) and PMN are presented in Figure 12. The MQ is the ratio of stability to flow and it indicates an estimate of the load to deformation ratio based on the specific conditions of the test, it can be used as a measure of the asphalt mixture's resistance to permanent deformation during service in life. In other words, MQ is described as the relationship between stability and flow. A higher MQ a stiffer mixture is which may indicate good permanent deformation resistance. Figure 12 shows that the addition of PMN increases the stability and decreases the flow value of the asphalt mixture. This implies that PMN has improved non-deformability of HMA mixture. Moreover, the mixture containing 7 % of PMN have greater stability and low flow compared with the control mixture. The acceptable Marshall Flow range is 2–4 mm corresponding to heavy traffic category. The Marshall Flow values present in Figure 12 were varied from 2.9 to 3.6 mm, which satisfy specifications criteria. Furthermore, the stability and MQ are both increased with increasing PMN content. The mixture with 7 % of PMN has stability approximately twice higher than that of the control mixture. Subsequently, maximum MQ was achieved by the mixture prepared using 7 % of PMN, while the base asphalt has a minimum value. These results indicate that PMN modified asphalt mixture may distribute the traffic loads to a larger area and superior resistance to permanent deformation, due to increase in mixture stiffness after adding PMN content.

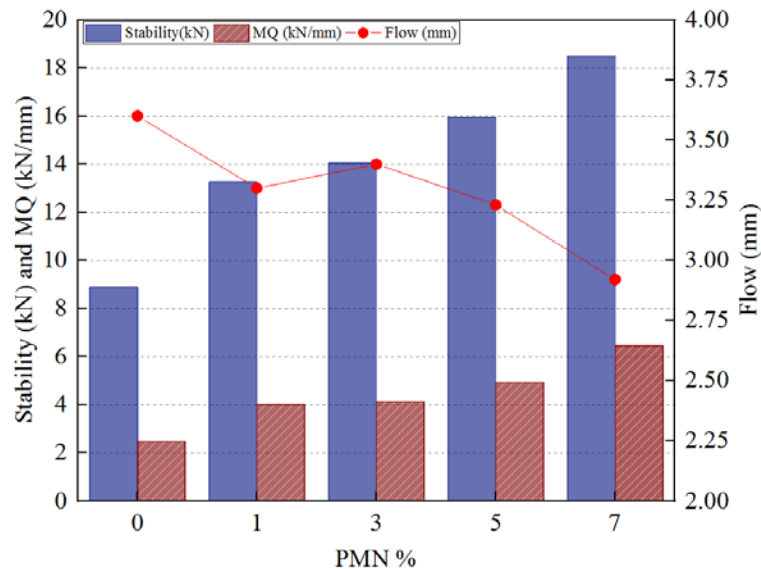


Figure 12. Effect of PMN % on Marshall stability (MS), quotient (MQ) and flow,

3.2.2. Results of Moisture Susceptibility Test

Moisture susceptibility of asphalt concrete mixtures usually concerned to like the potential of anti-stripping incident manifestation. Moreover, the stripping is considered one of the critical damage's occurrences in asphalt pavements [26]. Figure 13 presents the ITS test results for HMA mixtures, as the relationship between PMN % with the ITS (both dry and conditioned specimens) and TSR of control and PMN modified asphalt mixtures. Figure 13 shows that there are significant increases in both ITS and TSR due to the addition of PMN % as compared to the control mixture. From Figure 13, all mixtures prepared using PMN were exceeding the Superpave TSR criterion of 80 %, and the TSR values were increased from 77.5 % for the control mixture to 84.2 %, 88.1 %, 95.0 % 96.1 % corresponding to 1 %, 3 %, 5 % and 7 % of PMN modified asphalt mixture respectively. These results prove that ITS and TSR were significantly increased with increasing PMN %; this may increase the adhesion between aggregate and asphalt binder, which may reduce the stripping of HMA.

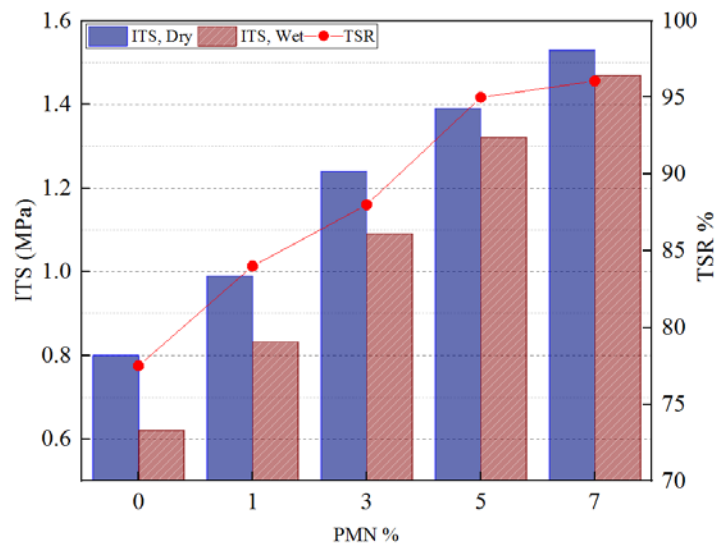


Figure 13. Effect of PMN % on indirect tensile strength (ITS) and tensile strength ratio (TSR).

In order to further investigate the influence of PMNs on moisture-induced damage of asphalt mixtures, the Marshall conditioning (24 at 60 °C) was carried out and the results were compared to unconditioned Marshall specimens (35 min at 60 °C). The Marshall stability ratio (MSR) was determined as stability a ratio of conditioned to unconditioned specimens. The percent of MSR and Marshall stability values of conditioned and unconditioned specimens are presented in Figure 14. The PMNs mixtures have the highest MSR than that of control mixture. The stability ratio value of more than 75 % is suggested as a criterion for a mixture to be resistant to moisture induced damages. These results give great evidence, that the PMN-modified asphalt has the potential to improve the anti-stripping property and decrease the moisture susceptibility of asphalt mixtures. Therefore, the PMN modifier is considered a useful alternative to decrease the risk of moisture-induced damage in asphalt pavement.

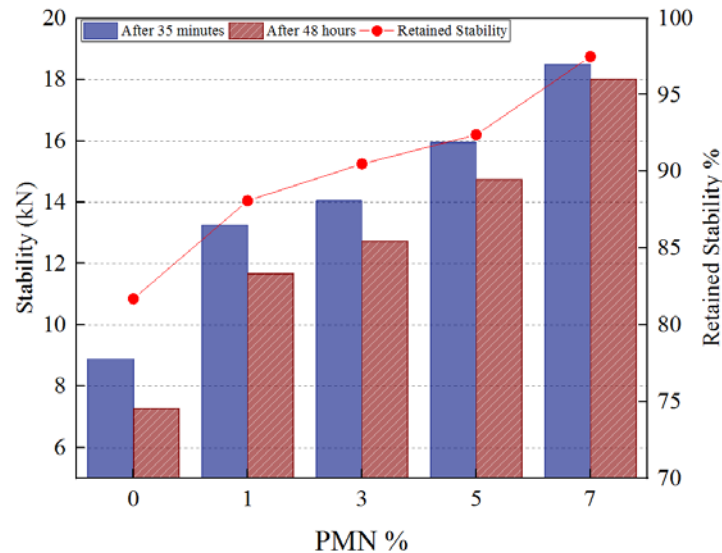


Figure 14. Effect of PMN % on marshal stability (MS) and marshal stability ratio (MSR).

3.2.3. Results of Wheel Tracking Test

The wheel tracking test (WTT) is applied to simulate the permanent deformation (Rutting) of HMA pavement induced by cyclic traffic loads under high-temperatures. In order to verify the binder test results and assess the high-temperature stability of PMN modified asphalt mixture, the WTT was conducted on 300x300x50 mm slab utilizing HYCZ-1 automatic rutting tester at 60 °C. The rutting test results are presented in Figure 15, in term of dynamic stability (DS) and rut depth and it is identified as effective and reasonable techniques to evaluate the high-temperature performance of asphalt mixture. From Figure 14, it can be seen that the usage of PMN significantly increased the DS and reduced the rut depth of HMA mixtures. Hence, The DS of base asphalt is increased by 69.7 %, 88.1 %, 92.6 %, and 94.4 %, while the rut depth is reduced by 36.9 %, 77.6 %, 81.9 % and 85.4 % corresponding to adding 1 %, 3 %, 5 % and 7 % of PMN respectively. Meanwhile, PMN modified asphalt mixture has excellent rutting resistance. This may be due to the fact that the gel structure damage of PMN is reduced under the mixing and rolling condition due to improves the viscosity of asphalt binder. Additionally, the flow deformation resistance of mixture was enhanced while the shear strength of the asphalt mixture is reduced under the same load. Therefore, PMN had effectively improved the resistance permanent deformation of asphalt mixtures, as well as the stiffening of the asphalt mixture. Finally, the capability of the asphalt mixture to oppose accumulated deformations due to repeated traffic loads has been increased as well.

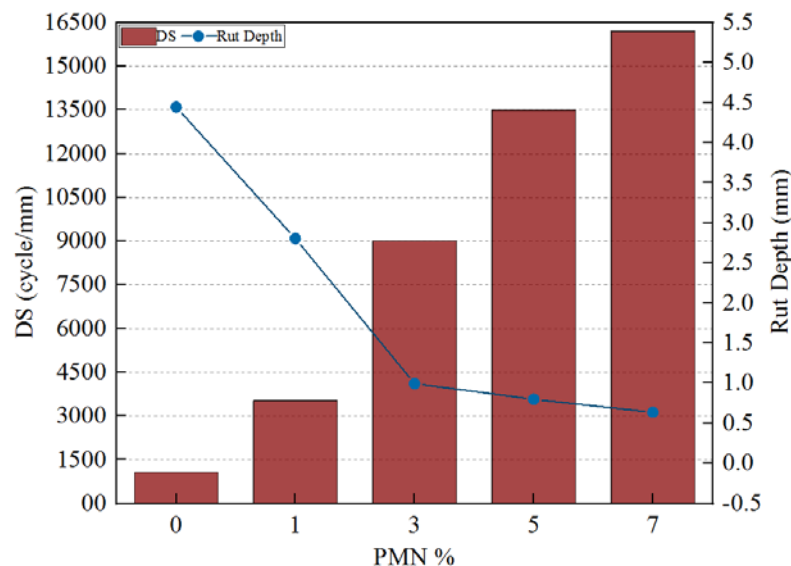


Figure 15. Effect of PMN % on dynamic stability (DS) and rut depth.

4. Conclusions

Based on the obtained results, the following specific conclusions can be drawn:

- The rheological properties of the asphalt binders at high temperatures were significantly improved via addition of PMN. Additionally, penetration index values and penetration viscosity number suggest that the addition of PMN declines the temperature susceptibility of asphalt binders.

- The rutting parameter $G^*/\sin(\delta)$ values obtained from DSR measurement were increased with increasing PMN %, while they are significantly decreased with increasing temperature. Therefore, resistance to permanent deformation and elastic response of the binder were improved. In addition, the MSCR test results demonstrate that the PMN dramatically increases the resistance of binder to permanent deformation by reducing the Jnr and increasing the recovery percent of asphalt binder. Furthermore, the PG grade base asphalt binder was improved after modification, this improvement indicated that the PMNs modified binder may be suitable for using in hot climates to develop stiff flexible mixture.

- The Marshall tests showed that the addition of PMNs increased the Marshall stability and reduced flow of the HMA mixture. Besides, the HMA mixtures which were prepared using PMN have achieved much better resistance to deformation owing to their high MQ values and Marshall stability. Thus, the PMNs modified asphalt might be suitable to use in paving places, where asphalt mixtures with minimal asphalt concentration with high stiffness were required.

- The results of the ITS test indicated that the TSR value of control mixture increased, because of the improvement of adhesion between aggregate and binder, which may reduce the stripping of HMA. Therefore, the moisture resistance of the asphalt mixture was significantly improved after PMN addition. A similar conclusion was carried out from Marshall immersion test.

- The rut depth of asphalt mixture was decreased with the increasing of PMN contents and dynamic stability. Interestingly, these indicate an improvement in permanent deformation resistance by asphalt mixtures, due to increasing stiffening of the asphalt mixture, and the capability of asphalt mixture to resist deformations at high-temperature and repeated traffic loads.

References

1. Xu, S.Y., Xiao, F.P., Amirhanian, S., Singh, D. Moisture characteristics of mixtures with warm mix asphalt technologies – a review. *Constr. Build. Mater.* 2017. 142. Pp. 148–161.
2. Ameri, M., Vamegh, M., Imaninasab, R., Rooholamini, H. Effect of nanoclay on performance of neat and sbs-modified bitumen and hma. *Petroleum Science and Technology.* 2016. 34. Pp. 1091–1097.
3. Sun, D.Q., Lu, W.M. Phase morphology of polymer modified road asphalt. *Petroleum Science and Technology.* 2006. 24. Pp. 839–849.
4. Galooyak, S.S., Dabir, B., Nazarbeygi, A.E., Moeini, A. Rheological properties and storage stability of bitumen/sbs/montmorillonite composites. *Constr. Build. Mater.* 2010. 24. Pp. 300–307.
5. Yao, H., You, Z. Effectiveness of micro-and nanomaterials in asphalt mixtures through dynamic modulus and rutting tests. *Journal of Nanomaterials.* 2016.
6. Polacco, G., Filippi, S., Paci, M., Merusi, F. Nanoclays as asphalt-binder modifiers. In *Handbook of polymernanocomposites. Processing, performance and application.* Pandey, J.K., Reddy, K.R., Mohanty, A.K., Misra, M., Eds. Springer Berlin Heidelberg: Berlin, Heidelberg, 2014. Pp. 223–245.
7. Chen, H.-X., Gang, Z.-J., Wang, Y.-L., Liang, J.-H. Temperature susceptibility indexes of sbs modified-asphalt binders. *Jianzhu Cailiao Xuebao/Journal of Building Materials.* 2010. 13. Pp. 691–696.
8. Jahromi, S.G., Khodaii, A. Effects of nanoclay on rheological properties of bitumen binder. *Constr. Build. Mater.* 2009. 23. Pp. 2894–2904.
9. Polacco, G., Stastna, J., Biondi, D., Zanzotto, L. Relation between polymer architecture and nonlinear viscoelastic behavior of modified asphalts. *Current Opinion in Colloid & Interface Science.* 2006. 11. Pp. 230–245.
10. Yuliestyan, A., Cuadri, A.A., Garcia-Morales, M., Partal, P. Selection of ethylene-vinyl-acetate properties for modified bitumen with enhanced end-performance. *Rheologica Acta.* 2018. 57. Pp. 71–82.
11. Saboo, N., Kumar, P. Optimum blending requirements for eva modified binder. *International Journal of Pavement Research and Technology.* 2015. 8. Pp. 172–178.
12. Fang, C.Q., Qiao, X.T., Yu, R.E., Yu, X., Liu, J.J., Yu, J., Xia, R.H. Influence of modification process parameters on the properties of crumb rubber/eva modified asphalt. *Journal of Applied Polymer Science.* 2016. Pp. 133.
13. Zhang, F., Hu, C.B., Zhang, Y. Influence of poly(phosphoric acid) on the properties and structure of ethylene-vinyl acetate-modified bitumen. *Journal of Applied Polymer Science.* 2018. 135. Pp. 46553.
14. Yang, J., Tighe, S. A review of advances of nanotechnology in asphalt mixtures. *Procedia-Social and Behavioral Sciences.* 2013. 96. Pp. 1269–1276.
15. Yu, J., Zeng, X., Wu, S., Wang, L., Liu, G. Preparation and properties of montmorillonite modified asphalts. *Materials Science and Engineering: A.* 2007. 447. Pp. 233–238.
16. Polacco, G., Kříž, P., Filippi, S., Stastna, J., Biondi, D., Zanzotto, L. Rheological properties of asphalt/sbs/clay blends. *European Polymer Journal.* 2008. 44. Pp. 3512–3521.
17. Yao, H., You, Z.P., Li, L., Shi, X.M., Goh, S.W., Mills-Beale, J., Wingard, D. Performance of asphalt binder blended with non-modified and polymer-modified nanoclay. *Constr. Build. Mater.* 2012. 35. Pp. 159–170.
18. Bastos, J.B.S., Babadopulos, L.F.A.L., Soares, J.B. Relationship between multiple stress creep recovery (mscr) binder test results and asphalt concrete rutting resistance in brazilian roadways. *Constr. Build. Mater.* 2017. Pp. 145, 20–27.
19. Read, J., Whiteoak, D. *The shell bitumen handbook.* Thomas Telford, 2003.
20. Siddig, E.A.A., Feng, C.P., Ming, L.Y. Effects of ethylene vinyl acetate and nanoclay additions on high-temperature performance of asphalt binders. *Constr. Build. Mater.* 2018. 169. Pp. 276–282.
21. Wu, S.-p., Li, B., Chen, Z., Huang, X. Influence of conductive additive on temperature susceptibility of asphalt binders. *Journal of Central South University of Technology.* 2008. 15. Pp. 479–482.
22. Saleh, M.F. Experimental investigation of bitumen physical properties on foamability and mechanical properties of foam bitumen stabilized mixes. 2006.

23. Khadivar, A., Kavussi, A. Rheological characteristics of sbr and nr polymer modified bitumen emulsions at average pavement temperatures. *Constr. Build. Mater.* 2013. 47. Pp. 1099–1105.
24. Li, C., Chen, Z.W., Wu, S.P., Li, B., Xie, J., Xiao, Y. Effects of steel slag fillers on the rheological properties of asphalt mastic. *Constr. Build. Mater.* 2017. 145. Pp. 383–391.
25. Zhang, J.Z., Liu, S.J., Yao, Z.Y., Wu, S.P., Jiang, H.G., Liang, M., Qiao, Y.N. Environmental aspects and pavement properties of red mud waste as the replacement of mineral filler in asphalt mixture. *Constr. Build. Mater.* 2018. 180. Pp. 605–613.
26. Fallahi Abandansari, H., Modarres, A. Investigating effects of using nanomaterial on moisture susceptibility of hot-mix asphalt using mechanical and thermodynamic methods. *Constr. Build. Mater.* 2017. 131. Pp. 667–675.

Contacts:

Elfadil Siddig, +249918171460; elfadiladmali@ymail.com

Peifeng Cheng, +8613946139402; chengpeifeng@nefu.edu.cn

Yiming Li, +8618249504717; meng.huxiyou@163.com

© Siddig, S.E., Cheng, P.C., Li, Y.L., 2019



DOI: 10.18720/MCE.91.10

Reducing alkaline corrosion of basalt fiber in concrete

L.A. Urkhanova,^a S.A. Lkhasaranov^a, S.L. Buyantuev^a, R.S. Fediuk^{b*}, A.V. Taskin^b

^a East Siberia state university of technology and management, Ulan-Ude, Russia

^b Far Eastern Federal University, Vladivostok, Russia

* E-mail: roman44@yandex.ru

Keywords: fiber reinforced materials, fiber-reinforced concrete, cements, cement-based composites, binders, concretes, mechanoactivation

Abstract. The article presents the results of studies on the development of fiber-reinforced concrete using composite binders and basalt fibers obtained in an experimental plasma reactor. To reduce the negative impact of Portland cement on the mineral fiber, composite binders based on Portland cement and fly ash were used in the study. To reduce the normal density in the composition of the binder, a polycarboxylate type superplasticizer was used in the work. The microstructure of cement stone was studied using SEM and IR-spectroscopy. The compressive strength was tested on cubes with an edge of 100 mm according to EN 12390-6, flexural strength – on prisms with a size of 100×100×500 mm according to EN 12390-3. The optimum content of fly ash (30 %) in the composite binder is evaluated, which allows to obtain high mechanical properties. It was revealed that the combined use of composite binder and fiber leads to an increase in compressive and flexural strength of fiber concrete. With the addition of fly ash, both hardening of the structure of the cement stone and a decrease in the alkaline effect of the basalt fiber binding on the surface are observed. Infrared spectroscopy of cement systems showed a change in the phase composition and a decrease in the basicity of the resulting calcium hydrosilicates upon addition of fly ash into the composition binder.

1. Introduction

Despite the proven effectiveness of fiber-reinforced concrete in comparison with traditional reinforced concrete [1–5], their use is quite rare in construction practice. This is due, inter alia, to the fact that for some types of fiber there is insufficient information about the possibility of its use in certain conditions. In particular, the study of mineral fibers remains relevant, due to the high mechanical properties of individual fibers and a lower density of these fibers compared to steel fibers [6–9]. However, Rybin [10] and Monaldo [11] report that mineral fibers corrode upon contact with the alkaline environment of Portland cement.

Alkaline solutions, which cause corrosion, affect basalt fiber, as well as glass fiber, which in turn leads to fiber destruction [12]. The resulting loss of strength causes the destruction of the composite under load during operation. Wei et al [13] proved that the alkali resistance of basalt fiber is higher than that of E-class fiber glass. There are differences in corrosion resistance of basalt fiber and fiberglass from E-class components, although the main components, SiO₂ and Al₂O₃, are the same for the two types of fibers. E-glass fiber has a much larger contribution from CaO and B₂O₃, while Fe₂O₃ and FeO are found only in basalt fiber [14].

Analyzing various approaches to solving the problem of preserving mineral fiber from the action of an alkaline medium, it can distinguished the main areas: the use of alkaline-free binders [15–18] and low-alkaline binders [19–22], the use of additives that reduce the alkalinity of the binder [23, 24], modification of fiber surface [25, 26], modification of fiber microstructure [27–30]. According to this classification, the objects of influence can be either individual fibers or fiber-reinforced concrete, and the feasibility of applying a specific method of protection from an alkaline environment is determined by the feasibility study. To protect the mineral fiber from the negative effects of the environment of Portland cement, the study decided to use fly ash to obtain

Urkhanova, L.A., Lkhasaranov, S.A., Buyantuev, S.L., Fediuk, R.S., Taskin, A.V. Reducing alkaline corrosion of basalt fiber in concrete. Magazine of Civil Engineering. 2019. 91(7). Pp. 112–120. DOI: 10.18720/MCE.91.10

Урханова Л.А., Лхасаранов С.А., Буянтуев С.Л., Федюк Р.С., Таскин А.В. Снижение щелочной коррозии базальтовой фибры в бетоне // Инженерно-строительный журнал. 2019. № 7(91). С. 112–120. DOI: 10.18720/MCE.91.10



a composite binder (CB), the effectiveness of which was previously proven, for example, for resistance of glass fiber [31, 32].

The scientific novelty lies in the use for dispersed reinforcement of concrete the mineral fiber obtained by the electrothermal method in a plasma-arc reactor and different from the known types of mineral fibers (basalt roving, thin staple fiber) with lower energy consumption during production.

The purpose of the article is to develop basalt fiber concrete and study their mechanical properties and corrosion resistance of fibers obtained by the electrothermal method.

2. Materials and Methods

The studies used follow materials: Portland cement (OPC) CEM I 32.5 N (Spasskement, Russia), fiber based on basalts of the Selendum deposit (Russia) and fly ash.

Composite binders were obtained by joint grinding of fly ash (0–50 % by weight of the OPC) with Portland cement to a specific surface area of 430–450 m²/kg. To reduce the water-binding ratio and increase the physicomechanical parameters of CB, Sika Viscocrete 5 New (Switzerland) in the amount of 0.6 % by weight of the binder was added into its composition with mixing water.

Fly ash obtained by burning coal at the Gusinozersk thermal power plant (Russia). The results of determining the main characteristics of fly ash show that it can be used without restrictions for the production of building materials and products (Table 1).

Table 1. The main characteristics of fly ash.

Characteristics	ASTM C618 – 19 requirements	Value obtained
Free calcium oxide content, wt. %	≤10	0.05
Magnesium oxide content, wt. %	≤5	1.9
Total content oxides of silicon, aluminum and iron, wt. %	≥70	84.97
Sulfur and sulfate compounds content, wt. %	≤3	0.34
Alkaline oxides content, wt. %	≤3	2.7
Specific surface area, m ² /kg	≥300	350

Fiber production was carried out in the experimental reactor, the design features of which made it possible to obtain a pure melt, free of occluded gases and reduced metals, which makes it possible to produce better products. Thus, it was possible to organize the smelting mode in one stage, consisting of combined heating of raw materials. At start-up, plasma-electric arc heating and melting of the raw material occur, and subsequently, as the melt is melted and a conductive cup is formed, the raw materials are added and current flows through the molten aluminosilicate mass, with its simultaneous electromagnetic stirring and homogenization using electromagnets connected in series, which significantly reduces the time required to reach the operating mode and reduces the energy intensity of production. The required power required to obtain a melt with a bulk weight of up to 150 kg/h is 1.1–1.3 kW/kg (for comparison, the consumed power of working induction furnaces is 6 kW/kg) [33, 34]. The obtained mineral fibers have the following characteristics: average fiber diameter – 10 μm, tensile strength – 1350 MPa, heat resistance – 600 °C.

The microstructure of fiber cement compositions was determined using a Jeol JSM 6510 LV scanning electron microscope (Japan) with a magnification of x1000. The phase composition in the entire chamber was studied by IR analysis using an IR-Fourier spectrometer IRAffinity-1 (Shimadzu, Japan).

Concrete cubes of dimensions 100×100×100 mm were prepared for compressive strength test at the age of 2, 7 and 28 days for all mixes. The concrete specimens were unmolded after 24 hours of casting and then immersed in curing tank at room temperature and relative humidity at 65 ± 5 % until the age of testing. This test was carried out using a Shimadzu (Kyoto, Japan) tester machine with a capacity of 200 kN according to EN 12390-3. Flexural strength of the prisms with an edge length of 100×100×500 mm specimens was tested according to EN 12390-6.

3. Results and Discussion

The test results showed that the use of fly ash in the composition of composite binders leads to a change in normal density, setting time and physicomechanical parameters (Table 2, Figure 1).

Table 2. Physico-mechanical characteristics of composite binders with a water-binder ratio of 0.4.

Parameter	CBs with the SP at ash content, wt. %			Control specimen (OPC)
	10	30	50	
Standard consistence, %	27	25	24	28
Initial setting, min	140	150	160	90
Final setting, min	300	320	330	245

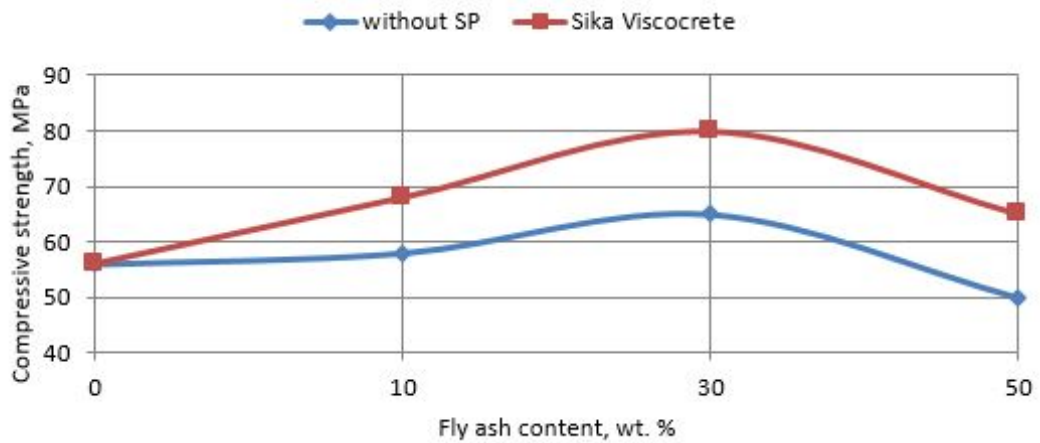


Figure 1. Compressive strength of composite binders at the age of 28 days.

The high content of SiO_2 in the fly ash (57 wt. %), when grinding with Portland cement leads to the activation of a composite binder. Fly ash acts as an active mineral additive, participating in the structure formation of cement stone. However, due to the fact that ash increases water demand, this effect is compensated by the addition of superplasticizer. Moreover, as can be seen from Figure 1, the addition of superplasticizer leads to an increase in compressive strength of composite binders by 10–15 %. In addition to the water-reducing effect, which helps to increase the mechanical characteristics of cement stone, superplasticizer significantly affects the processes occurring in the cement system through various effects, which was described by the authors earlier [28, 29]. In particular, the molecules of surfactants, adsorbed on the surface of the particles, reduce surface energy, while there is a partial saturation of free chemical bonds on the surface of the solid phase, preventing adhesion.

The change in the mechanical properties of fiber concrete occurs due to the directed formation of the structure and increase the corrosion resistance of the fiber by reducing the alkalinity of the binder. SEM results showed a change in the microstructure of Portland cement and a composite binder with basalt fiber in an amount of 4 wt. % at the age of 28 days (Figure 2).

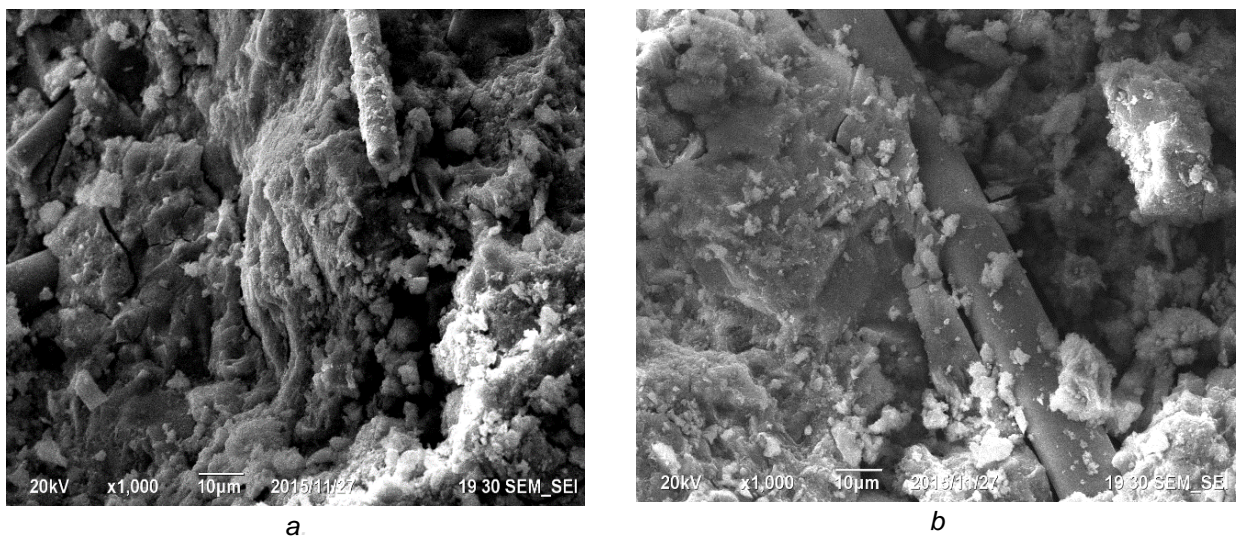


Figure 2. SEM images (x1000) of the surface of Portland cement with basalt fiber (a) and the composite binder with basalt fiber (b) at the age of 28 days.

Analysis of the microstructure allows us to conclude that the fiber surface in the sample with conventional Portland cement contains inclusions indicating the interaction of the fiber and Portland cement. This leads to a decrease in the reinforcing effect, in comparison with the composition of fiber concrete with a composite binder. The addition of fly ash contributes to the directional formation of a high-strength stone structure from low-basic calcium hydrosilicates and a decrease in the content of calcium hydroxide. Reducing the content of calcium hydroxide helps to maintain the surface strength of the mineral fiber and high mechanical properties. The change in the phase composition of the cement stone is confirmed by IR spectral analysis (Figure 3).

An analysis of the IR spectra showed that with the addition of fly ash there is a change in the intensity of the absorption band in the frequency range $1000\text{--}1100\text{ cm}^{-1}$, which correspond to vibrations of Si-O bonds, which is associated with the formation of calcium hydrosilicates. This indicates a change in the process of hydration of Portland cement with the addition of fly ash and the formation of an additional amount of calcium hydrosilicates. The shift in the frequencies of the absorption bands corresponding to calcium hydrosilicates

also suggests that the resulting structures with the use of the CBs differ from the traditional ones in the direction of increasing the number of low-basic hydrosilicates.

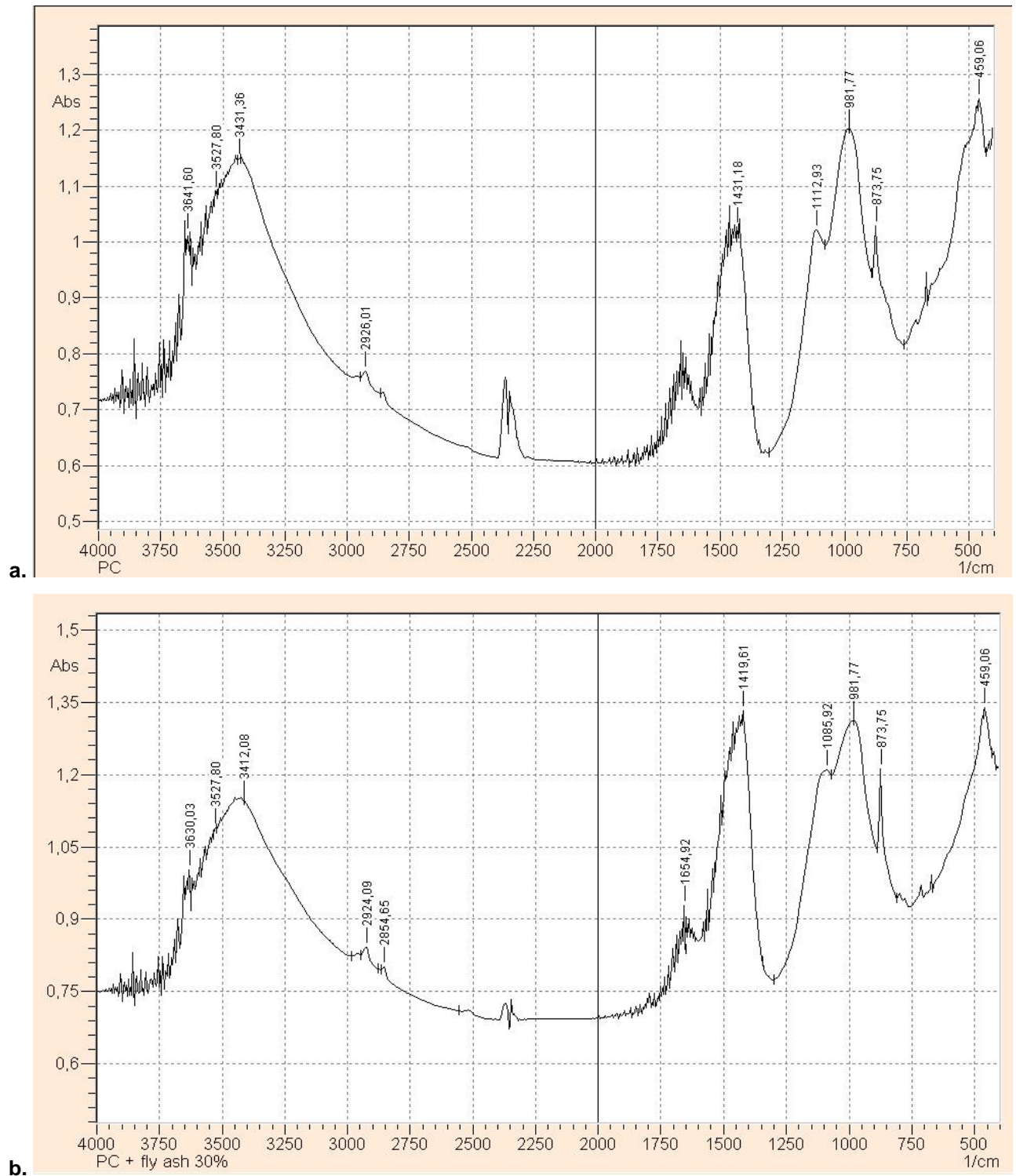


Figure 3. IR spectra of cement stones: on Portland cement (a) and on the CB (fly ash – 30 %) (b).

Development of fiber-reinforced concrete using the composite binder with an ash content of 30 wt. % and basalt fiber in an amount of 4 wt. % led to an increase both in compressive and flexural strength by 10–15 % (Figure 4).

The high mechanical properties of fiber-reinforced concrete are due to the reinforcing effect of basalt fibers, which is manifested to a greater extent in compositions with a composite binder.

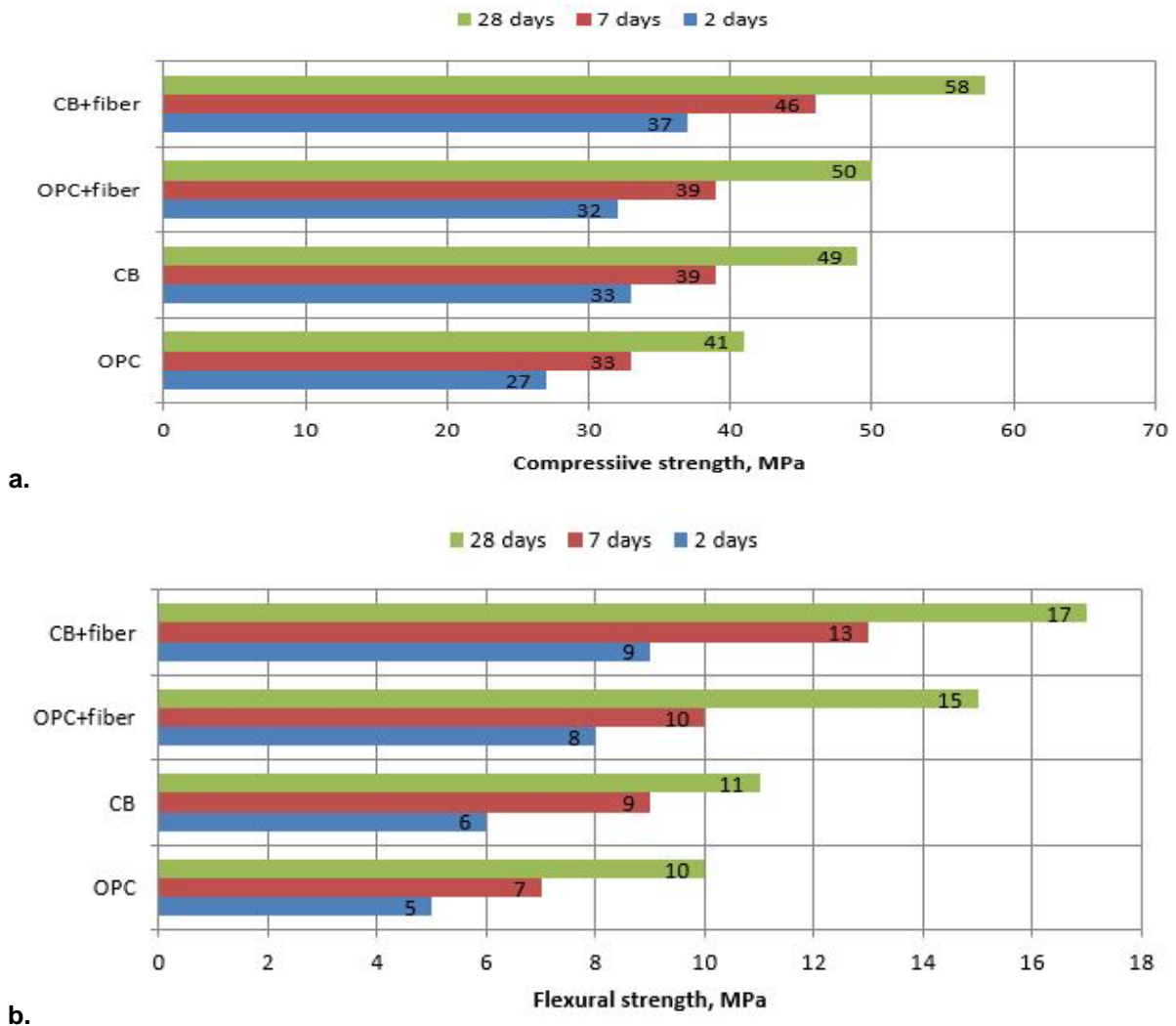


Figure 4. Effect of basalt fiber on compressive strength (a) and flexural strength (b) of fiber-reinforced concrete.

4. Conclusion

Based on the results obtained, the following conclusions can be drawn:

- the effectiveness of the use of basalt fiber obtained by the innovative electrothermal method (provided that the alkaline environment of the cement stone is reduced) has been proved;
- the reduction of the negative effect of alkaline medium on the mineral fiber was shown by the composition of fiber concrete using fly ash, in addition, showing higher both compressive and flexural strength due to the binding of additional $\text{Ca}(\text{OH})_2$;
- the study of the cement stone microstructure and IR spectroscopy allow us to conclude that the addition of fly ash contributes to the directional formation of a high-strength stone structure from low-basic calcium hydrosilicates and a decrease in the content of calcium hydroxide;
- the use of fly ash in the binder helps to increase the corrosion resistance of the mineral fiber and maintain the reinforcing effect of its addition.

Given the low energy intensity of the equipment for producing basalt fiber using the electrothermal method (proved earlier in [35]), this technology can be competitive. After additional calculations, fiber production can be implemented in industrial volumes.

5. Acknowledgements

1. The article was prepared in the framework of the project part of the state task in the field of scientific activity No. 13.6716.2017 on the topic “Innovative resource- and energy-saving technologies using plasma-energy processes and technologies”.

2. This work was financially supported by the Ministry of Education and Science of the Russian Federation, state task in the field of scientific activity No. 10.3706.2017 / 4.6.

References

1. Yoo, D.-Y., Banthia, N. Impact resistance of fiber-reinforced concrete – A review. *Cement and Concrete Composites*. 2019. 104. Article 103389.
2. Buka-Vaivade, K., Sliseris, J., Serdjusks, D., Pakrastins, L., Vatin, N.I. Rational use of HPSFRC in multi-storey building. *Magazine of Civil Engineering*. 2018. 84(8). Pp. 3–14. DOI: 10.18720/MCE.84.1
3. Park, S.H., Kim, D.J., Kim, S.W. Investigating the impact resistance of ultra-high-performance fibre reinforced concrete using an improved strain energy impact test machine. *Constr. Build. Mater.* 2016. 125. Pp. 145–159.
4. Klyuev, S.V., Klyuev, A.V., Vatin, N.I. Fiber concrete for the construction industry. *Magazine of Civil Engineering*. 2018. 84(8). Pp. 41–47. DOI: 10.18720/MCE.84.4.
5. Abirami, T., Loganaganandan, M., Murali G., Fediuk, R., Vickhram Sreekrishna, R., Vignesh, T., Janupriya, G., Karthikeyan K. Experimental research on impact response of novel steel fibrous concretes under falling mass impact. *Construction and Building Materials*. 2019. 222. Pp. 447–457.
6. Fediuk, R., Smoliakov, A., Muraviov, A. Mechanical Properties of Fiber-Reinforced Concrete Using Composite Binders [Online]. *Advances in Materials Science and Engineering*. 2017. 2017. Article 2316347. URL: <https://doi.org/10.1155/2017/2316347>
7. Sun, X., Gao, Z., Cao, P., Zhou, C. Mechanical properties tests and multiscale numerical simulations for basalt fiber reinforced concrete. *Construction and Building Materials*. 2019. 202. Pp. 58–72.
8. Wang, D., Ju, Y., Shen, H., Xu, L. Mechanical properties of high performance concrete reinforced with basalt fiber and polypropylene fiber. *Construction and Building Materials*. 2019. 197. Pp. 464–473.
9. Khan, M., Cao, M., Ali, M. Effect of basalt fibers on mechanical properties of calcium carbonate whisker-steel fiber reinforced concrete. *Construction and Building Materials*. 2018. 192. Pp. 742–753.
10. Rybin, V.A., Utkin, A.V., Baklanova, N.I. Corrosion of uncoated and oxide-coated basalt fibre in different alkaline media. *Corrosion Science*. 2016. 102. Pp. 503–509.
11. Monaldo, E., Nerilli, F., Vairo, G. Basalt-based fiber-reinforced materials and structural applications in civil engineering. *Composite Structures*. 2019. 214. Pp. 246–263.
12. Li, Z., Xiao, T., Pan, Q., Cheng, J., Zhao, S. Corrosion behaviour and mechanism of basalt fibres in acidic and alkaline environments. *Corrosion Science*. 2016. 110. Pp. 15–22.
13. Wei, B., Cao, H.L., Song, S.H. Degradation of basalt fibre and glass fibre/epoxyresin composites in seawater, *Corrosion Science*. 2011. 53. Pp. 426–431.
14. Fiore, V., Scalici, T., Di Bella, G., Valenza, A. A review on basalt fibre and its composites, *Composites Part B Engineering*. 2015. 74. Pp. 74–94.
15. Xiang, Y., Xie, Y., Long, G. Effect of basalt fiber surface silane coupling agent coating on fiber-reinforced asphalt: From macro-mechanical performance to micro-interfacial mechanism. *Construction and Building Materials*. 2018. 179. Pp. 107–116.
16. Klyuev, S.V., Klyuev, A.V., Khezhev, T.A., Pucharenko Yu.V. Technogenic sands as effective filler for fine-grained fibre concrete. *Journal of Physics: Conference Series*. 2018. 1118. 012020.
17. Zagorodnyuk L.Kh., Lesovik V.S., Sumskey D.A. Thermal insulation solutions of the reduced density. *Construction Materials and Products*. 2018. 1(1). Pp. 40 – 50.
18. Riaz Ahmad, M., Chen, B., Yu, J. A comprehensive study of basalt fiber reinforced magnesium phosphate cement incorporating ultrafine fly ash. *Composites Part B: Engineering*. 2019. 168. Pp. 204–217
19. Lee, T.W., Lee, S., Park, S.-M., Lee, D. Mechanical, thermomechanical, and local anisotropy analyses of long basalt fiber reinforced polyamide 6 composites. *Composite Structures*. 2019. 222. Article 110917.
20. Ralph, C., Lemoine, P., Boyd, A., Archer, E., McIlhagger, A. The effect of fibre sizing on the modification of basalt fibre surface in preparation for bonding to polypropylene. *Applied Surface Science*. 2019. 475. Pp. 435–445.
21. Cherevatova, A.V., Zhernovskaya, I.V., Alehin, D.A., Ko-zhukhova, M.I., Kozhukhova, N.I., Yakovlev, E.A. Theoretical aspects of development of composite nanostructured gypsum binder characterized by increased heat resistance. *Construction Materials and Products*. 2019. Vol. 2. No. 4. Pp. 5–13.
22. Klyuev, S.V., Klyuev, A.V., Vatin, N.I. Fine-grained concrete with combined reinforcement by different types of fibers. *MATEC Web of Conferences*. 2018. 245. 03006
23. Wu, H., Fang, Q., Chen, X.W., Gong, Z.M., Liu, J.Z. Projectile penetration of ultrahigh performance cement based composites at 510–1320 m/s. *Constr. Build. Mater.* 2015. 74. Pp. 188–200.
24. Ravi, R., Li V.C., Heard W.F., Williams B.A. Impact resistance of high strength-high ductility concrete. *Cem. Concr. Res.* 2017. 98. Pp. 24–35.
25. Tonoli, G.H.D., Rodrigues Filho, U.P., Savastano Jr, H., Bras, J., Belgacem, M.N., Rocco Lahr, F.A. Cellulose modified fibres in cement based composites. *Composites Part A: Applied Science and Manufacturing*. 2009. 40(12). Pp. 2046–2053.
26. Huang, D., Zhao, X. Novel modified distribution functions of fiber length in fiber reinforced thermoplastics. *Composites Science and Technology*. 2019. 182. Article 107749.
27. Kundu, S.P., Chakraborty, S., Chakraborty, S. Effectiveness of the surface modified jute fibre as fibre reinforcement in controlling the physical and mechanical properties of concrete paver blocks. *Construction and Building Materials*. 2018. 191. Pp. 554–563.
28. Sappakittipakorn, M., Sukontasukkul, P., Higashiyama, H., Chindaprasirt, P. Properties of hooked end steel fiber reinforced acrylic modified concrete. *Construction and Building Materials*. 2018. 186. Pp. 1247–1255.
29. Klyuev, S.V., Khezhev, T.A., Pucharenko, Yu.V., Klyuev, A.V. The fiber-reinforced concrete constructions experimental research. *Materials Science Forum*. 2018. 931. Pp. 598–602.
30. Lesovik, V.S., Absimetov, M.V., Elistratkin, M.Yu., Pospelova, M.A., Shatalova, S.V. For the study of peculiarities of structure formation of composite binders for non-autoclaved aerated concrete. *Construction Materials and Products*. 2019. Vol. 2. No. 3. Pp. 41–47.
31. Cheng, C., He, J., Zhang, J., Yang, Y. Study on the time-dependent mechanical properties of glass fiber reinforced cement (GRC) with fly ash or slag. *Construction and Building Materials*. 2019. 217. Pp. 128–136.
32. Güneş, E., Atewi, Y.R., Hasan, M.F. Fresh and rheological properties of glass fiber reinforced self-compacting concrete with nanosilica and fly ash blended. *Construction and Building Materials*. 2019. 211. Pp. 349–362.

33. Mucsi, G., Szenczi, A., Nagy, S. Fiber reinforced geopolymer from synergetic utilization of fly ash and waste tire. *Journal of Cleaner Production*. 2018. 178. Pp. 429–440.
34. Buyantuev. S.L., Kondratenko A.S. Issledovaniye fiziko-khimicheskikh svoystv mineral'nykh volokon, poluchennykh s pomoshch'yu elektromagnitnogo tekhnologicheskogo reaktora [Physical and chemical properties of mineral fibres obtained by electromagnetic process reactor] *Vestnik VSGUTU – Bulletin of ESSUTM*. 2013. 44(5). Pp. 123–129. (rus)
35. Fediuk, R.S., Lesovik, V.S., Liseitsev, Yu.L., Timokhin, R.A., Bituyev, A.V., Zaiakhanov, M.Ye., Mochalov, A.V. Composite binders for concretes with improved shock resistance. *Magazine of Civil Engineering*. 2019. 85(1). Pp. 28–38. DOI: 10.18720/MCE.85.3

Contacts:

Larisa Urkhanova, +7(902)1685168; urkhanova@mail.ru

Solbon Lkhasaranov, +7(950)3871856; solbon230187@mail.ru

Sergey Buyantuev, +7(950)2817945; buyantuevsl@mail.ru

Roman Fediuk, +7(950)2817945; roman44@yandex.ru

Andrei Taskin, +79242410125; taskin@yandex.ru

© Urkhanova, L.A., Lkhasaranov, S.A., Buyantuev, S.L., Fediuk, R.S., Taskin, A.V., 2019



DOI: 10.18720/MCE.91.10

Снижение щелочной коррозии базальтовой фибры в бетоне

Л.А. Урханова^а, С.А. Лхасаранов^а, С.Л. Буянтуев^а, Р.С. Федюк^б, А.В. Таскин^б

^а Восточно-Сибирский государственный университет технологий и управления, г. Улан-Удэ, Россия

^б Дальневосточный Федеральный Университет, г. Владивосток, Россия

* E-mail: roman44@yandex.ru

Ключевые слова: фиброармированные материалы, фибробетон, цементы, цементные композиты, вяжущие, бетоны, механоактивация

Аннотация. В статье представлены результаты исследований по получению фибробетона с использованием композиционных вяжущих и базальтовых волокон, полученных в экспериментальном плазменном реакторе. Для снижения негативного воздействия среды портландцемента на минеральное волокно в исследовании были использованы композиционные вяжущие вещества на основе портландцемента и золы уноса. Для снижения нормальной плотности в составе вяжущего в работе использован суперпластификатор поликарбоксилатного типа. Исследована микроструктура цементного камня с помощью СЭМ и ИК-спектроскопии. Прочность на сжатие исследовалась на кубах с ребром 100 мм согласно EN 12390-6, прочность на растяжение – на призмах размером 100×100×500 мм согласно EN 12390-3. Установлено оптимальное содержание золы уноса (30 %) в составе композиционного вяжущего, позволяющего получить высокие механические показатели. Выявлено, что совместное использование композиционного вяжущего и фибры приводит к повышению прочности при сжатии и изгибе фибробетона. При введении золы уноса наблюдается как упрочнение структуры цементного камня, так и снижение щелочного воздействия вяжущего на поверхность базальтового волокна. Инфракрасная спектроскопия цементных систем показала изменение фазового состава и снижение основности образующихся гидросиликатов кальция при введении в состав вяжущего золы уноса.

Литература

1. Yoo D.-Y., Banthia N. Impact resistance of fiber-reinforced concrete – A review // *Cement and Concrete Composites*. 2019. № 104. Article 103389.
2. Бука-Вайваде К., Шлисерис Я., Сердюк Д.О., Пакрастиньш Л., Ватин Н.И. Возможность рационального использования HPSFRC в многоэтажном строительстве // *Инженерно-строительный журнал*. 2018. № 8(84). С. 3–14. DOI: 10.18720/MCE.84.1
3. Park S.H., Kim D.J., Kim S.W. Investigating the impact resistance of ultra-high-performance fibre reinforced concrete using an improved strain energy impact test machine // *Constr. Build. Mater.* 2016. № 125. Pp. 145–159.
4. Клюев С.В., Клюев А.В., Ватин Н.И. Фибробетон для строительной индустрии // *Инженерно-строительный журнал*. 2018. № 8(84). С. 41–47. DOI: 10.18720/MCE.84.4
5. Abirami T., Loganaganandan M., Murali G., Fediuk R., Vickhram Sreekrishna, R., Vignesh, T., Januppriya, G., Karthikeyan K. Experimental research on impact response of novel steel fibrous concretes under falling mass impact // *Construction and Building Materials*. 2019. № 222. Pp. 447–457.
6. Fediuk R., Smoliakov A., Muraviov A. Mechanical Properties of Fiber-Reinforced Concrete Using Composite Binders [Электронный ресурс] // *Advances in Materials Science and Engineering*. 2017. № 2017, Article 2316347. URL: <https://doi.org/10.1155/2017/2316347>
7. Sun X., Gao Z., Cao P., Zhou C. Mechanical properties tests and multiscale numerical simulations for basalt fiber reinforced concrete // *Construction and Building Materials*. 2019. № 202. Pp. 58–72.
8. Wang D., Ju Y., Shen H., Xu L. Mechanical properties of high performance concrete reinforced with basalt fiber and polypropylene fiber // *Construction and Building Materials*. 2019. № 197. Pp. 464–473.
9. Khan M., Cao M., Ali M. Effect of basalt fibers on mechanical properties of calcium carbonate whisker-steel fiber reinforced concrete // *Construction and Building Materials*. 2018. № 192. Pp. 742–753.
10. Rybin V.A., Utkin A.V., Baklanova N.I. Corrosion of uncoated and oxide-coated basalt fibre in different alkaline media // *Corrosion Science*. 2016. № 102. Pp. 503–509.
11. Monaldo E., Nerilli F., Vairo G. Basalt-based fiber-reinforced materials and structural applications in civil engineering // *Composite Structures*. 2019. № 214. Pp. 246–263.
12. Li Z., Xiao T., Pan Q., Cheng J., Zhao S. Corrosion behaviour and mechanism of basalt fibres in acidic and alkaline environments // *Corrosion Science*. 2016. № 110. Pp. 15–22.
13. Wei B., Cao H.L., Song S.H. Degradation of basalt fibre and glass fibre/epoxyresin composites in seawater // *Corrosion Science*. 2011. № 53. Pp. 426–431.

14. Fiore V., Scalici T., Di Bella G., Valenza A. A review on basalt fibre and its composites // *Composites Part B Engineering*. 2015. № 74. Pp. 74–94.
15. Xiang Y., Xie Y., Long G. Effect of basalt fiber surface silane coupling agent coating on fiber-reinforced asphalt: From macro-mechanical performance to micro-interfacial mechanism // *Construction and Building Materials*. 2018. № 179. Pp. 107–116.
16. Klyuev S.V., Klyuev A.V., Khezhev T.A., Pucharenko Yu.V. Technogenic sands as effective filler for fine-grained fibre concrete // *Journal of Physics: Conference Series*. 2018. № 1118, 012020.
17. Загороднюк Л.Х., Лесовик В.С., Сумской Д.А. Теплоизоляционные растворы пониженной плотности // *Строительные материалы и изделия*. 2018. Т. 1. № 1. С. 40–50.
18. Riaz Ahmad M., Chen B., Yu J. A comprehensive study of basalt fiber reinforced magnesium phosphate cement incorporating ultrafine fly ash // *Composites Part B: Engineering*. 2019. № 168. Pp. 204–217
19. Lee T.W., Lee S., Park S.-M., Lee D. Mechanical, thermomechanical, and local anisotropy analyses of long basalt fiber reinforced polyamide 6 composites // *Composite Structures*. 2019. № 222. Article 110917.
20. Ralph C., Lemoine P., Boyd A., Archer E., McIlhagger A. The effect of fibre sizing on the modification of basalt fibre surface in preparation for bonding to polypropylene // *Applied Surface Science*. 2019. № 475. Pp. 435–445.
21. Череватова А.В., Жерновская И.В., Алехин Д.А., Кожухова М.И., Кожухова Н.И., Яковлев Е.А. Теоретические аспекты создания композиционного наноструктурированного гипсового вяжущего повышенной жаростойкости // *Строительные материалы и изделия*. 2019. Т. 2. № 4. С. 5–13.
22. Klyuev S.V., Klyuev A.V., Vatin N.I. Fine-grained concrete with combined reinforcement by different types of fibers // *MATEC Web of Conferences*. 2018. № 245, 03006
23. Wu H., Fang Q., Chen X.W., Gong Z.M., Liu J.Z. Projectile penetration of ultrahigh performance cement based composites at 510–1320 m/s // *Constr. Build. Mater.* 2015. № 74. Pp. 188–200.
24. Ravi R., Li V.C., Heard W.F., Williams B.A. Impact resistance of high strength-high ductility concrete // *Cem. Concr. Res.* 2017. № 98. Pp. 24–35.
25. Tonoli G.H.D., Rodrigues Filho U.P., Savastano Jr, H., Bras J., Belgacem M.N., Rocco Lahr F.A. Cellulose modified fibres in cement based composites // *Composites Part A: Applied Science and Manufacturing*. 2009. № 40(12). Pp. 2046–2053.
26. Huang D., Zhao X. Novel modified distribution functions of fiber length in fiber reinforced thermoplastics // *Composites Science and Technology*. 2019. № 182. Article 107749.
27. Kundu S.P., Chakraborty S., Chakraborty S. Effectiveness of the surface modified jute fibre as fibre reinforcement in controlling the physical and mechanical properties of concrete paver blocks // *Construction and Building Materials*. 2018. № 191. Pp. 554–563.
28. Sappakittipakorn M., Sukontasukkul P., Higashiyama H., Chindaprasirt P. Properties of hooked end steel fiber reinforced acrylic modified concrete // *Construction and Building Materials*. 2018. № 186. Pp. 1247–1255.
29. Klyuev S.V., Khezhev T.A., Pukharenko Yu.V., Klyuev, A.V. The fiber-reinforced concrete constructions experimental research // *Materials Science Forum*. 2018. Vol. 931. Pp. 598 – 602.
30. Лесовик В.С., Абсиметов М.В., Елистраткин М.Ю., Поспелова М.А., Шаталова С.В. К вопросу изучения особенностей структурообразования композиционных вяжущих для неавтоклавных газобетонов // *Строительные материалы и изделия*. 2019. Т. 2. № 3. С. 41–47.
31. Cheng C., He J., Zhang J., Yang Y. Study on the time-dependent mechanical properties of glass fiber reinforced cement (GRC) with fly ash or slag. *Construction and Building Materials*. 2019. № 217. Pp. 128–136.
32. Güneysi E., Atewi Y.R., Hasan M.F. Fresh and rheological properties of glass fiber reinforced self-compacting concrete with nanosilica and fly ash blended // *Construction and Building Materials*. 2019. № 211. Pp. 349–362.
33. Mucsi G., Szenczi A., Nagy S. Fiber reinforced geopolymer from synergetic utilization of fly ash and waste tire // *Journal of Cleaner Production*. 2018. № 178. Pp. 429–440.
34. Буянтуев С.Л., Кондратенко А.С. Исследование физико-химических свойств минеральных волокон, полученных с помощью электромагнитного технологического реактора // *Вестник ВСГУТУ*. 2013. № 5. С. 123–129.
35. Федюк Р.С., Лесовик В.С., Лисейцев Ю.Л., Тимохин Р.А., Битуев А.В., Заяханов М.Е., Мочалов А.В. Композиционные вяжущие для бетонов повышенной ударной стойкости // *Инженерно-строительный журнал*. 2019. № 1(85). С. 28–38. DOI: 10.18720/MCE.85.3

Контактные данные:

Лариса Алексеевна Урханова, +7(902)1685168; эл. почта: urkhanova@mail.ru

Солбон Александрович Лхасаранов, +7(950)3871856; эл. почта: solbon230187@mail.ru

Сергей Лубсанович Буянтуев, +7(950)2817945; эл. почта: buyantuevsl@mail.ru

Роман Сергеевич Федюк, +7(950)2817945; эл. почта: roman44@yandex.ru

Андрей Васильевич Таскин, +79242410125; taskin@yandex.ru



DOI: 10.18720/MCE.91.11

An improved membrane element for high-rise building with shear walls

Z.-Q. Liu^{a*}, J. Zhang^b, F. Li^c, H.-P. Jin^a, Z.-Y. Zong^a

^a Yancheng Institute of Technology, Yancheng, China

^b Guizhou Minzu University, Guiyang, China

^c Chongqing University, Chongqing, China

* E-mail: zhaoqiliu@sina.com

Keywords: finite element method, structural design, numerical models, wall-beam connection, computational accuracy, high-rise building

Abstract. Although a high computational accuracy can be obtained when a membrane element with rotational degrees of freedom is used for the numerical analysis of wall-beam connection of high-rise building, this method often leads to some weak analysis results because of the vague relation between rotational degrees of freedom and displacement field compared with beam or slab element. In this paper, a constraint relation was established between the rotational displacement field with independent interpolation and the rotational angle of rigid body through adopting a penalty function method, and then an improved membrane element with rotational degrees of freedom was constructed based on the work of ALLMAN. The improved membrane element was added in the standard analysis module of ANSYS through using a second development interface named UPFs (User Programming Features). Also, a curved wall was adopted as the example to test the performance of improved membrane element. The preliminary results show the improved membrane element can pass most of patch tests with no extra zero energy mode. To further verify the performance of improved membrane element used for the analysis of wall-beam connection, a high-rise building with coupled shear walls was also adopted to compare the numerical analysis results produced by four different simulation elements. The results show the improved membrane element is a reliable and superior type with some advantages including simple data preparation, convenient programming and insensitive penalty parameter.

1. Introduction

In the numerical analysis of high-rise building, the development of simulation element for shear wall has experienced three stages including thin-walled bar, membrane and shell. In the practical application, a flat slab element that based on the theories of slab and membrane is often adopted in the finite element method to replace the shell element [1–4]. In the high-rise building with shear walls, except some arc-shaped walls for good appearance, most of shear walls often adopt flat shape. For the few arc-shaped walls, the refined flat slab element is often used to simulate the curved surface, and the calculation results are also more accurate when the element is refined enough [5–7].

Stiffness matrix is an essential characteristic of the simulation element, for the flat slab element, it is formed by superposing plane stress element and bending element. If adopting the linear superposition method formed by membrane and slab, two problems may be occur. One is the poor computational accuracy, although this problem can be solved by setting up rotational degrees of freedom or adding additional displacement shape function. The other is that no definite solution can be drawn for analyzing some shear wall structures as the membrane element that built by usual rotational degrees of freedom is combined with slab element [8–11].

Although ALLMAN membrane element has been widely used in the major finite element applications, a redundant zero-energy mode is often produced for the structural analysis, as well as the above two problems

Liu, Z.-Q., Zhang, J., Li, F., Jin, H.-P., Zong, Z.-Y. An improved membrane element for high-rise building with shear walls. Magazine of Civil Engineering. 2019. 91(7). Pp. 121–128. DOI: 10.18720/MCE.91.11

Лиу Ч.-К., Чанг Дж., Ли Ф., Джин Х.-П., Чонг Ч.-Ю. Мембранный элемент для высотных зданий связевой системы // Инженерно-строительный журнал. 2019. № 7(91). С. 121–128. DOI: 10.18720/MCE.91.11



[12–14]. To solve these problems, the ALLMAN membrane element was improved in this paper by using the User Programming Features (UPFs), which is a second development interface of ANSYS. A curved wall was adopted to test the performance of improved membrane element through setting in a FORTRAN subroutine in the standard analysis module of ANSYS. The test contents included eigenvalue inspection, fragmentation inspection, high-order fragmentation inspection, and coordination inspection of degrees of freedom. The preliminary results show the improved membrane element can pass most of patch tests and has a preferable computational accuracy when combining with slab element for the analysis of curved wall. To further confirm the analysis accuracy of improved membrane element used in the wall-beam connection, a high-rise building with coupled shear walls was analyzed by adopting four different simulation elements. The calculation results show the improved membrane element is a reliable and superior type with some advantages including simple data preparation, convenient programming and insensitive penalty parameter.

2. Methods

2.1. ALLMAN Membrane Element

To build the early membrane element with rotational degrees of freedom, engineers have paid more attention to the physical significance of rotational angle. The conventional practice is to set a cubic function for the additional displacement field of element. With using this method, however, some numerical experiments have proved that the matrix formula of membrane element is very complicated, and the computational accuracy is also not high. Many research works have been conducted to solve this problem during the past decades, and big progress has been achieved [15–19]. One of the most typical methods is the formation way of rotational degrees of freedom suggested by ALLMAN.

ALLMAN's method is suitable for triangular element shown in Figure 1. The accuracy of triangular element with rotational degrees of freedom is between linear strain triangular element with six nodes and constant strain triangular element with three nodes. The key to success of this method is to set up a reasonable relationship of node displacement between line midpoint and angular point.

Based on the work of ALLMAN, COOK expanded the formation way of rotational degrees of freedom from triangular element with three nodes to quadrilateral element with four nodes and arbitrary shape (shown in Figure 2) [20]. With high computational accuracy is the biggest advantage of this method compared with conventional membrane element with four nodes, and it can be easily combined with slab element with four nodes. As shown in Figure 3, however, a redundant zero-energy mode is often produced by using COOK's method. Therefore, the following parts of this paper focus on improving the ALLMAN membrane element and testing the application effects of improved membrane element.

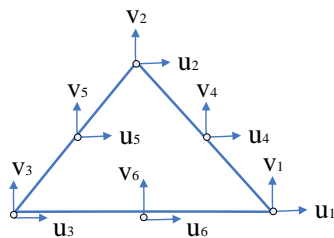


Figure 1. Triangle ALLMAN membrane element with three nodes.

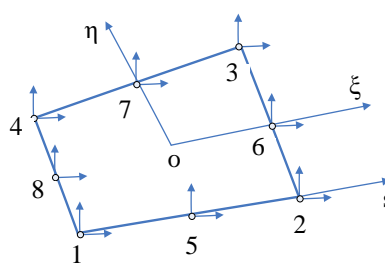


Figure 2. Quadrilateral membrane element with four nodes.

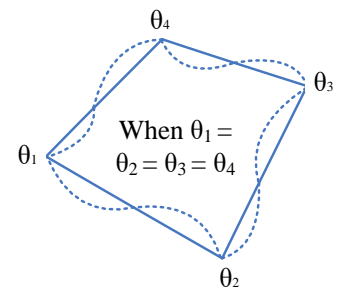


Figure 3. A redundant zero-energy mode of ALLMAN membrane element.

2.2. ALLMAN-based Improved Membrane Element

To solve the redundant zero-energy mode of ALLMAN membrane element and the problems addressed in the introduction, a penalty function method is adopted to represent the equivalence relation between the field of rotational degrees of freedom with independent interpolation and the rotational angle of rigid body in the element energy functional. The selected displacement field is shown as follows:

$$u = u_c + u_\lambda, \tag{1}$$

where u_c represents the bilinear compatible displacement field, and u_λ represents the incompatible displacement item. The rotational angle of rigid body of membrane element can be obtained from the theories of elastic mechanics, that is:

$$\omega^0 = \frac{1}{2} \begin{pmatrix} -\frac{\partial}{\partial y} & \frac{\partial}{\partial x} \end{pmatrix} \begin{Bmatrix} u \\ v \end{Bmatrix} = D_2 \begin{Bmatrix} u \\ v \end{Bmatrix}. \tag{2}$$

Considering the equal relationship of rotational angle between node and rigid body, the energy functional can be represented as follows:

$$\Pi = \int_V \frac{1}{2} \varepsilon^T C_1 \varepsilon dV + \int_V \frac{1}{2} C_2 (\omega^0 - \omega)^2 dV - W. \quad (3)$$

The matching stiffness matrix is:

$$K = \int_V [B_c \quad B_\lambda]^T C_1 [B_c \quad B_\lambda] dV + \int_V [H_c \quad H_\lambda]^T C_2 [H_c \quad H_\lambda] dV, \quad (4)$$

where $H_c = D_2^T N - N_\omega$, in the Cartesian coordinates:

$$D_2^T N = \begin{bmatrix} -\frac{\partial}{2\partial y} & \frac{\partial}{2\partial x} \end{bmatrix} \begin{bmatrix} N_1 & 0 & H_1 & N_2 & 0 & H_3 & N_3 & 0 & H_5 & N_4 & 0 & H_7 \\ 0 & N_1 & H_2 & 0 & N_2 & H_4 & 0 & N_3 & H_6 & 0 & N_4 & H_8 \end{bmatrix}. \quad (5)$$

A method of independent bilinear interpolation is adopted in the field of rotational degrees of freedom of node, that is:

$$\omega = \sum_1^4 N_i w_i = [0 \quad 0 \quad N_1 \quad 0 \quad 0 \quad N_2 \quad 0 \quad 0 \quad N_3 \quad 0 \quad 0 \quad N_4] \{u\}_{12 \times 1} = [N_\omega] \{u\}_{12 \times 1}. \quad (6)$$

The above method is also adopted for coordinate conversion between physical space and mapping space, namely:

$$\begin{Bmatrix} x \\ y \end{Bmatrix} = \begin{bmatrix} N_1 & 0 & N_2 & 0 & N_3 & 0 & N_4 & 0 \\ 0 & N_1 & 0 & N_2 & 0 & N_3 & 0 & N_4 \end{bmatrix} \begin{Bmatrix} x_1 \\ y_1 \\ x_2 \\ y_2 \\ x_3 \\ y_3 \\ x_4 \\ y_4 \end{Bmatrix}. \quad (7)$$

In the Formula 7, x_i and y_i ($i = 1, 2, 3, 4$) are coordinate values of four angular nodes in the Cartesian coordinate system. The partial derivatives of field variables are used in the calculation, which corresponds to x and y coordinates of physical space and ξ and η coordinates of mapping space respectively. Normally, the derivative for x and y coordinates is difficult to get. Therefore, the derivative for ξ and η coordinates can be obtained by using the derivability rule, namely:

$$\begin{Bmatrix} \frac{\partial \varphi}{\partial \xi} \\ \frac{\partial \varphi}{\partial \eta} \end{Bmatrix} = [J] \begin{Bmatrix} \frac{\partial \varphi}{\partial x} \\ \frac{\partial \varphi}{\partial y} \end{Bmatrix}, \quad (8)$$

where $[J]$ represents the Jacobi matrix, and for slab element with four nodes, the following formula can be obtained easily:

$$\begin{Bmatrix} \frac{\partial \varphi}{\partial x} \\ \frac{\partial \varphi}{\partial y} \end{Bmatrix} = [J]^{-1} \begin{Bmatrix} \frac{\partial \varphi}{\partial \xi} \\ \frac{\partial \varphi}{\partial \eta} \end{Bmatrix} = \frac{1}{|J|} \begin{bmatrix} J_{22} & -J_{12} \\ -J_{21} & J_{11} \end{bmatrix} \begin{Bmatrix} \frac{\partial \varphi}{\partial \xi} \\ \frac{\partial \varphi}{\partial \eta} \end{Bmatrix} = \begin{bmatrix} \Gamma_{11} & \Gamma_{12} \\ \Gamma_{21} & \Gamma_{22} \end{bmatrix} \begin{Bmatrix} \frac{\partial \varphi}{\partial \xi} \\ \frac{\partial \varphi}{\partial \eta} \end{Bmatrix}. \quad (9)$$

The correction matrix produced by compatible displacement is as follows:

$$H_c = D_2 \{u\} = \frac{1}{2} \begin{bmatrix} 0 & 0 & 0 & 0 \\ 0 & 0 & 0 & 0 \\ 0 & -1 & 1 & 0 \end{bmatrix} \begin{Bmatrix} u_{,x} \\ u_{,y} \\ v_{,x} \\ v_{,y} \end{Bmatrix}. \quad (10)$$

To make the element pass through the patch tests of displacement, a B-bar method is adopted to solve the $[H_\lambda]$ strain matrix [21]. Therefore, the solved strain matrix is described as follows

$$\left(H_{B\text{-bar}} = \int_V D_2^T M dV \right):$$

$$H_\lambda = D_2^T M - \frac{1}{V} \int_V D_2^T M dV. \quad (11)$$

Although the above improved membrane element can pass through the patch tests of displacement and no longer has a redundant zero-energy mode, it cannot pass through the patch tests of boundary. Therefore, the strain matrix that corresponds to displacement of coordination part should be further handled as follows:

$$G_{\theta M} = G_\theta - \frac{1}{V^e} \int_{V^e} G_\theta dV. \quad (12)$$

Based on the above formula, the improved membrane element not only can pass through the patch tests of displacement and boundary, but also can direct connect with the frame beam. However, the connection stiffness is too weak. So it is recommended to delete the displacement of incompatible part when the second part of stiffness matrix is calculated in formula (4), and the stiffness matrix of element adopts 3×3 way of Gauss integral. After the above amendments, the improved membrane element can achieve actual connection stiffness as direct connects with the frame beam. As shown in Figure 4, the element stiffness is calculated through a FORTRAN program, and the improved membrane element is planted into the software of ANSYS by the secondary development interface (namely, the UPFs).

```
*deck, UserElem  USERDISTRIB
  subroutine UserElem (elID, matID, keyMtx, lumpm, nDim, nNodes,
&      Nodes, nIntPnts, nUsrDof, kESTress,
&      KeyAnsMat, keySym, nKeyOpt, KeyOpt,
&      temper, temperB, tRef, kTherm,
&      nPress, Press, kPress, nReal, RealConst,
&      nSaveVars, saveVars, xRef, xCur,
&      TotValDofs, IncValDofs, ItrValDofs,
&      VelValDofs, AccValDofs,
&      kfstps, nlgeom, nrkey, outkey, elPrint, iott,
&      keyHisUpd, Idstep, isubst, ieqitr, timval,
&      keyEleErr, keyEleCnv,
&      eStiff, eMass, eDamp, eSStiff,
&      fExt, fInt, elVol, elMass, elCG,
&      nRsltBsc, RsltBsc, nRsltVar, RsltVar,
&      nElEng, elEnergy)
c*****
c
c*** Primary function: General User Element Subroutine
```

Figure 4. A user-defined subroutine.

3. Results and Discussion

3.1. Performance test for a curved wall

Based on the secondary development interface of UPFs provided by ANSYS, a curved wall (shown in Figure 5) is adopted as the example to test the performance of improved membrane element. The test contents include eigenvalue inspection, fragmentation inspection, high-order fragmentation inspection, and coordination inspection of degrees of freedom.

A concentrated force (100kN) is exerted on the upper two corner points of curved wall along the negative direction of X and Y-axes. Three types of grids including 3×5 , 5×7 and 7×10 are calculated respectively, and the displacements of upper two corner points are listed in Table 1. To facilitate a comparative study, a shell element named SHELL63 is adopted in the software of ANSYS. The displacement shape function is represented by additional incompatible mode, and the ALLMAN method is used to form the rotational degrees of freedom. All the calculated results of displacements are shown in Table 1, it can be seen the calculated displacements of three types of grids are rather close.

Table 1. A comparison table for the calculated displacements of load point (Unit: mm).

Grid	improved membrane element		SHELL63 element of ANSYS	
	U_{x1}	U_{y2}	U_{x1}	U_{y2}
3×5	-2.558	-2.558	-2.4091	-2.4091
5×7	-2.582	-2.584	-2.4839	-2.4839
7×10	-2.594	-2.600	-2.5152	-2.5152

The preliminary results show the improved membrane element can pass most of patch tests with no extra zero-energy mode compared with traditional ALLMAN element. In addition, it can direct connect with frame beam element with no extra changes, and transfer forces accurately.

3.2. Case study for a high-rise building with coupled shear walls

The wall-beam connection is common in the high-rise building with shear walls. Therefore, to further verify the accuracy of improved membrane element used for the analysis of wall-beam connection, a high-rise building with coupled shear walls is adopted (shown in Figure 6). The concrete strength grade of shear wall is C25 (Chinese standard, which represents the compressive strength standard value of concrete cube is 25 N/mm²), and the thickness of shear wall is 200 mm. With 3 m storey height, the opening height of shear wall is 2.4 m, and the height of coupling beam located in middle layers is 0.6 m. A horizontal concentrated load (200 kN) is applied to the position of each floor height respectively. Four different simulation elements are adopted as follows to calculate this high-rise building with coupled shear walls. (1) Opening hole is adopted on shear wall to create coupling beam, and shell element is used to simulate wall-column and wall-beam (shell-shell); (2) The coupling beam is created in the manner of frame structure, and constrain equation is adopted to simulate the continuous relationship of rotational angles between beam and shell (shell-beam); (3) The coupling beam is also created in the manner of frame structure, and penalty element is adopted to simulate the continuous relationship of rotational angles between beam and shell (SATWE uses this method, which is a Chinese finite element analysis software); (4) The coupling beam is still created in the manner of frame structure, and the improved membrane element is adopted to simulate the continuous relationship of rotational angles between beam and shell (this paper).

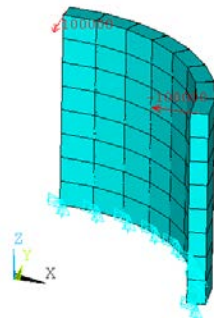
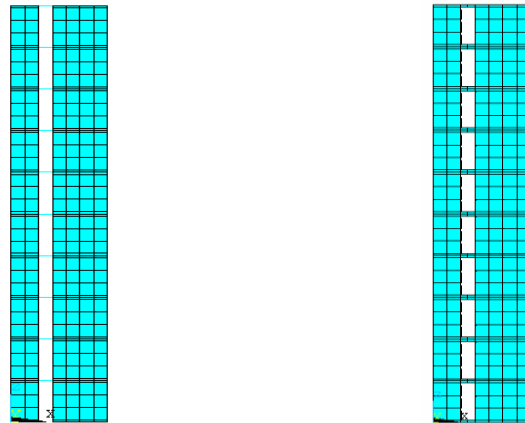


Figure 5. A structural model of curved wall.



a) Modeling by frame beam

b) Modeling by shear wall with openings

Figure 6. A model of high-rise building with coupled shear walls.

To avoid drawing a one-sided conclusion, three models with different span-depth ratios are designed. The span-depth ratios vary from 2, 4 to 6 by keeping unchanged section height of wall and column and increasing the width of opening. The calculated results show that displacement, shear force, and bending moment of each layer with different span-depth ratios are rather close. Among them, the results of constrain equation and shell element are closest, and the connection strength of wall-beam of improved membrane element is slightly soft. From Figure 7 to Figure 9 show the comparison of calculation results of displacement, shear force, and bending moment.

4. Conclusions

1. Based on the amendment of ALLMAN membrane element, an improved membrane element was proposed in this paper to solve the problems including redundant zero-energy mode, poor computational accuracy and ambiguous solution, which often occur when the traditional ALLMAN membrane element is used for the structural analysis of high-rise building with shear walls.

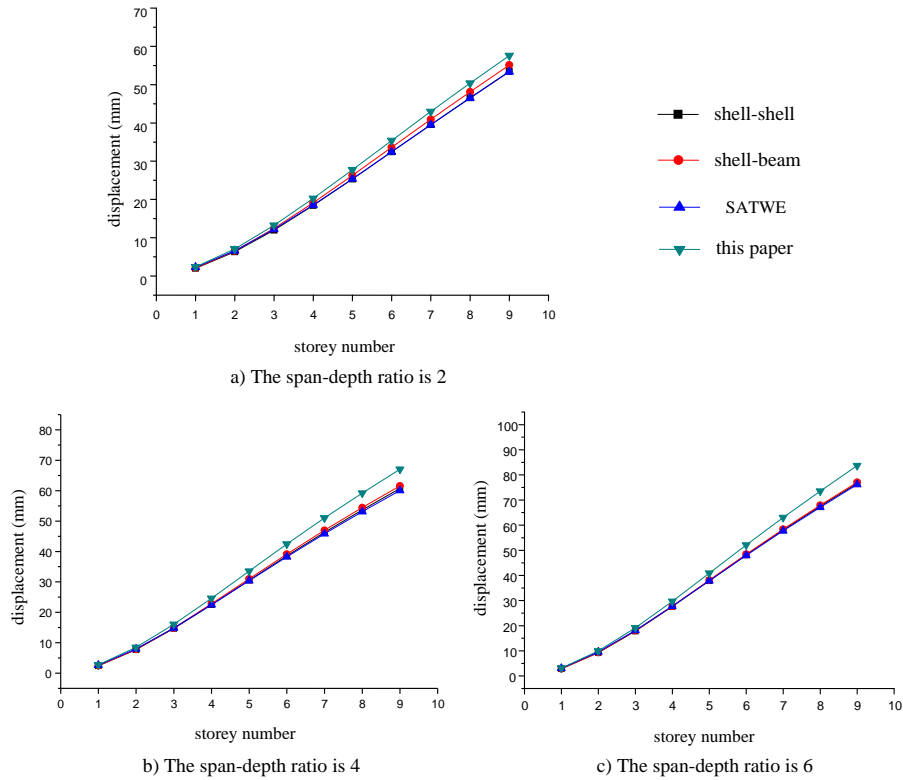


Figure 7. Comparison chart of displacement of each layer with different span-depth ratios.

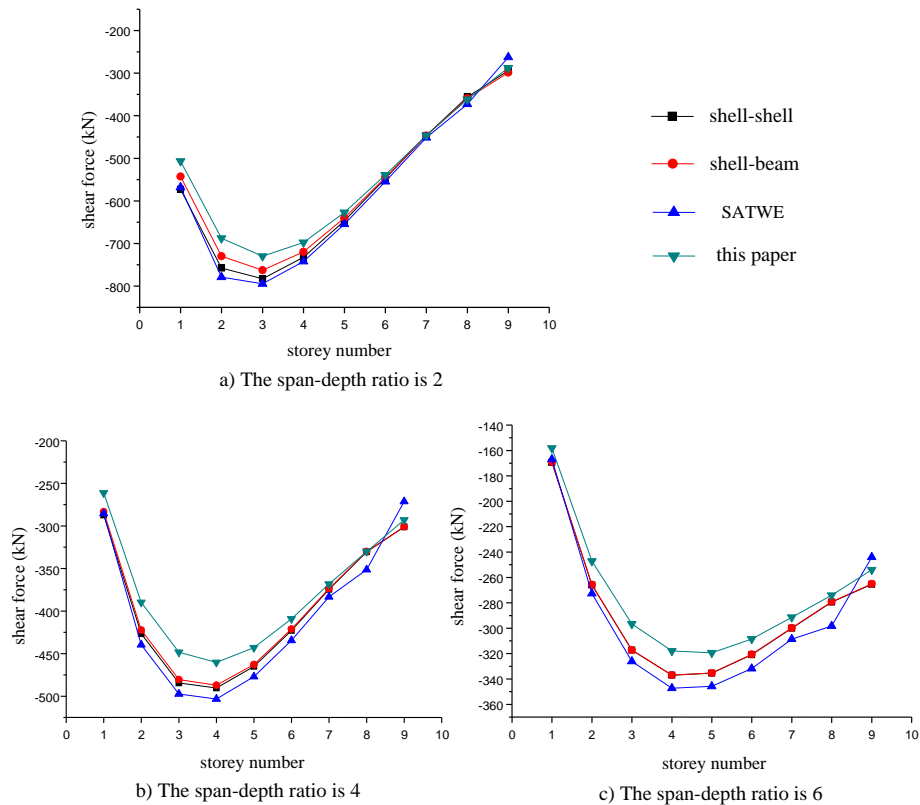


Figure 8. Comparison chart of shear force of each layer with different span-depth ratios.

2. By using the UPFs (User Programming Features, a second development interface), a FORTRAN subroutine of improved membrane element was added in the standard analysis module of ANSYS. A curved wall was adopted to test the performance of improved membrane element for structural component. The preliminary results show the improved membrane element can pass most of patch tests with no extra zero-energy mode compared with traditional ALLMAN membrane element.

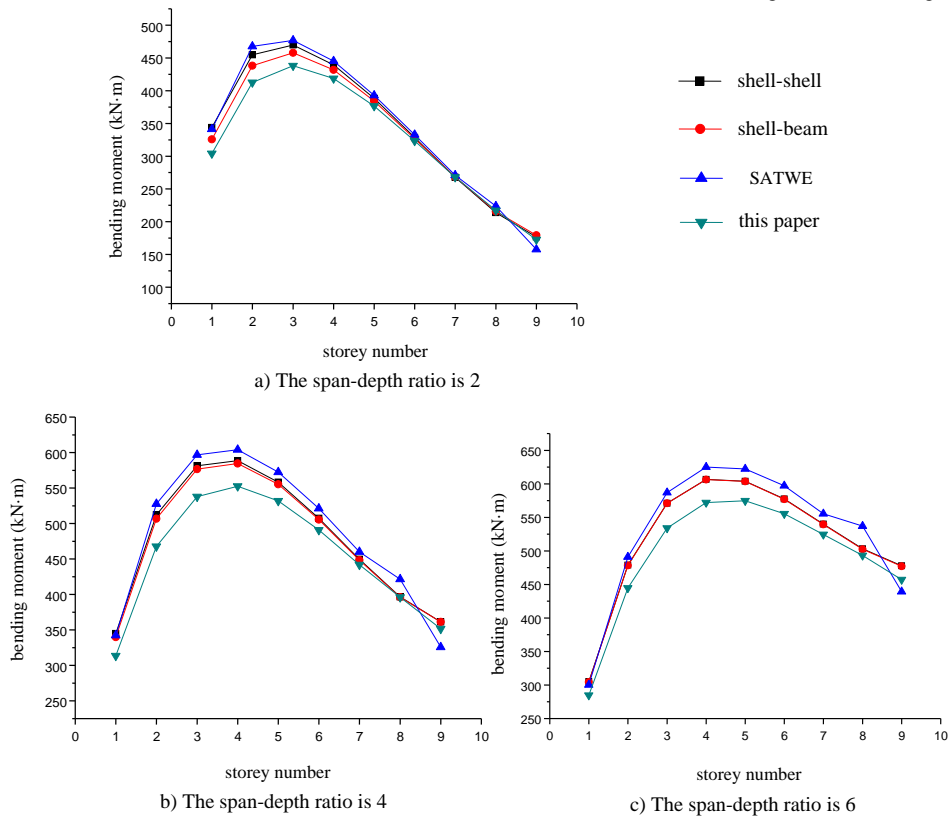


Figure 9. Comparison chart of bending moment of each layer with different span-depth ratios.

3. A high-rise building with coupled shear walls was also adopted to test the performance of improved membrane element for wall-beam connection. The results show the improved membrane element has preferable computational accuracy compared with other methods for the analysis of wall-beam connection, and is a reliable and effective type.

4. On the basis of UPFs function of ANSYS platform, currently only the preprocessor module including modeling, meshing, static and dynamic solver can be used to invoke the key data of displacement, stress and period. Since the postprocessor module of ANSYS cannot be fully used, the following work aims to improve the access of postprocessor module and take advantage of the powerful post-processing capacities.

References

- Kim, H.S., Lee, D.G. Analysis of Shear Wall with Openings Using Super Elements. *Engineering Structures*. 2003. 25(8). Pp. 981–991. DOI: 10.1016/S0141-0296(03)00041-5
- Kim, H.S., Lee, D.G., Kim, C.K. Efficient Three-dimensional Seismic Analysis of a High-rise Building Structure with Shear Walls. *Engineering Structures*. 2005. 27(6). Pp. 963–976. DOI: 10.1016/j.engstruct.2005.02.006
- Worsak, K.N. A Simple and Efficient Finite Element for General Shell Analysis. *International Journal for Numerical Methods in Engineering*. 1979. 14(2). Pp. 179–200. DOI: 10.1002/nme.162014020
- Lu, X.Z., Xie, L.L., Guan, H. A Shear Wall Element for Nonlinear Seismic Analysis of Super-tall Buildings Using OpenSees. *Finite Elements in Analysis and Design*. 2015. No. 98. Pp. 14–25. DOI: 10.1016/j.finel.2015.01.006
- Bozdogan, K.B., Ozturk, D. Vibration Analysis of Asymmetric Shear Wall and Thin Walled Open Section Structures Using Transfer Matrix Method. *Structural Engineering and Mechanics*. 2009. 33(1). Pp. 95–107. DOI: 10.12989/sem.2009.33.1.095
- Li, Y.G., Nie, Q. The Short-leg Shear Wall Element Based on the Analytical Trial Function Method. *Engineering Mechanics*. 2009. 26(4). Pp. 181–186. DOI: 10.1109/CLEOE-EQEC.2009.5194697
- Ding, J.G., Zhu, Y. An Elastic-plastic Analysis of Short-leg Shear Wall Structures During Earthquakes. *Earthquake Engineering and Engineering Vibration*. 2012. 11(4). Pp. 525–540. DOI: 10.1007/s11803-012-0139-8
- Pekau, O.A., Huttelmaier, H.P. A Versatile Panel Element for the Analysis of Shear Wall Structures. *Computers and Structures*. 1980. 12(3). Pp. 349–359. DOI: 10.1016/0045-7949(80)90032-2
- Cheng, M.Y., Fikri, R., Chen, C.C. Experimental Study of Reinforced Concrete and Hybrid Coupled Shear Wall Systems. *Engineering Structures*. 2015. 82(1). Pp. 214–225. DOI: 10.1016/j.engstruct.2014.10.039
- Cen, S., Zhou, M.J., Fu, X.R. A 4-node Hybrid Stress-function (HS-F) Plane Element with Drilling Degrees of Freedom Less Sensitive to Severe Mesh Distortions. *Computers and Structures*. 2011. 89(5). Pp. 517–528. DOI: 10.1016/j.compstruc.2010.12.010
- Jalali, A., Dashti, F. Nonlinear Behavior of Reinforced Concrete Shear Walls Using Macroscopic and Microscopic Models. *Engineering Structures*. 2010. 32(9). Pp. 2959–2968. DOI: 10.1016/j.engstruct.2010.05.01
- Chen, H.C. Evaluation of Allman Triangular Membrane Element Used in General Shell Analyses. *Computers and Structures*. 1992. 43(5). Pp. 881–887. DOI: 10.1016/0045-7949(92)90302-G

13. Allman, D.J. A Compatible Triangular Element Including Vertex Rotations for Plane Elasticity Analysis. *Computers and structures*. 1984. 19(2). Pp. 1–8. DOI: 10.1016/0045-7949(84)90197-4
14. Tian, R., Yagawa, G. Allman's Triangle Rotational DOF and Partition of Unity. *International Journal for Numerical Methods in Engineering*. 2007. 69(4). Pp. 837–858. DOI: 10.1002/nme.1790
15. Robinson, J. Four-node Quadrilateral Stress Membrane Element with Rotational Stiffness. *International Journal for Numerical Methods in Engineering*. 1980. 15(10). Pp. 1567–1569. DOI: 10.1002/nme.1620151012
16. Paknahad, M., Noorzaei, J., Jaafar, M.S. Analysis of Shear Wall Structure Using Optimal Membrane Triangle Element. *Finite Elements in Analysis and Design*. 2007. 43(11). Pp. 861–869. DOI: 10.1016/j.finel.2007.05.010
17. Sze, K.Y., Pan, Y.S. Hybrid Stress Tetrahedral Elements with Allman's Rotational D.O.F.s. *International Journal for Numerical Methods in Engineering*. 2000. 48(7). Pp. 1055–1070. DOI: 10.1002/(SICI)1097-0207(20000710)48:73.O.CO;2-P
18. Wen, Y., Zeng, Q.Y. Algorithm for Deriving Explicitly the Analytical Expression of Geometric Stiffness Matrix of the 4-node, 24 Degrees of Freedom Flat Shell Element. *Chinese Journal of Computational Mechanics*. 2013. 30(6). Pp. 796–801. DOI: 10.7511/jslx201306008
19. Rebiai, C., Belouar, L. A New Strain Based Rectangular Finite Element with Drilling Rotation for Linear and Nonlinear Analysis. *Archives of Civil and Mechanical Engineering*. 2013. 13(1). Pp. 72–81. DOI: 10.1016/j.acme.2012.10.001
20. Cook, R.D. On the Allman Triangular and a Related Quadrilateral Element. *Computers and structures*. 1986. 22(6). Pp. 1065–1067. DOI: 10.1016/0045-7949(86)90167-7
21. Reissner, E. A Note on Variational Principles in Elasticity. *International Journal of Solids and Structures*. 1965. 1(1). Pp. 93–95. DOI: 10.1016/0020-7683(65)90018

Contacts:

Zhao-Qiu Liu, +86(0515)88168215; zhaoqiuliu@sina.com

Ji Zhang, +86(0851)83613490; jizhang@163.com

Feng Li, +86(023)65120720; 773859023@qq.com

Hao-Peng Jin, +86(0515)88168215; 2812706964@qq.com

Zhen-Yu Zong, +86(0515)88168215; 1642833684@qq.com

© Liu, Z.-Q., Zhang, J., Li, F., Jin, H.-P., Zong, Z.-Y., 2019



DOI: 10.18720/MCE.91.12

Dynamic deformation of a beam at sudden structural transformation of foundation

V.I. Travush^a, V.A. Gordon^b, V.I. Kolchunov^{c*}, E.V. Leontiev^d

^a Russian academy of architecture and construction science, Moscow, Russia

^b Orel State University named after I.S. Turgenev, Orel, Russia

^c Southwest State University, Kursk, Russia

^d Main State Expertise of Russia, Moscow, Russia

* E-mail: asiorel@mail.ru

Keywords: beam, foundation, natural vibrations, forced vibrations, mode, frequency, accidental impact, structural transformation

Abstract. The article presents a methodic for analytical determining forces, displacements, modes and frequencies of natural flexural vibrations of a beam on elastic foundation. The beam consists of two sections: the first one supports on Winkler elastic foundation, and next one is free. Equations for flexural natural and forced vibrations were written in dimensionless variables and parameters and solved using the initial parameters method and Krylov functions. At the same time second and higher frequencies of natural vibrations of the beam were determined assuming unknown frequency is higher than “conventional” frequency which characterizes generalized stiffness of a system “beam–foundation”. Using numerical analysis, authors showed dependencies between the first three dimensionless frequencies of natural vibrations of the beam and a generalized stiffness of the system “beam–foundation” when foundation suddenly partially failure under the beam. Investigation established that effect of a sudden structural transformation leads to five-time moment increasing in the system “beam–foundation” at sudden foundation failure under the second half of the beam.

1. Introduction

Number of investigations on defense of buildings and structures against progressive destruction increases permanently [1] and most of these works deal with load redistribution in structural systems when a constructive element is removed from a building frame [2–4]. Investigations on deformation features of structures in a system “structure–foundation” under accidental impacts caused by sudden damage of a foundation are practically absent [13, 24]. A negligible number of studies [5–12] describes dynamic performance of beams and piles partially supported by an elastic base or partially imbedded into such a base. At the same time, it is usually assumed that a free structural segment is initially designed as a quasi-static body disregarding the inertia force [7–12]. In this regard, a problem of dynamical effects appearing when damage of a part of the system “beam–foundation” (such a partial destruction, boundary condition changing, crack formation, layers separation, reinforcement rupture) occurs suddenly, is of theoretical and practical interest [2, 25–27]. In this paper, we formulate and solve a problem on determination of dynamical force increment in a beam supported by an elastic base of Winkler’s type during forced transverse oscillations of the beam due to sudden partial damage of the base. The paper presents results on analytical determination of forces, modes, and frequencies of a beam supported by elastic foundation when sudden partial destruction of foundation does occur.

Travush, V.I., Gordon, V.A., Kolchunov, V.I., Leontiev, E.V. Dynamic deformation of a beam at sudden structural transformation of foundation. Magazine of Civil Engineering. 2019. 91(7). Pp. 129–144. DOI: 10.18720/MCE.91.12

Травуш В.И., Гордон В.А., Колчунов В.И., Леонтьев Е.В. Динамическое деформирование балки при внезапном структурном изменении упругого основания // Инженерно-строительный журнал. 2019. № 7(91). С. 129–144. DOI: 10.18720/MCE.91.12



This work is licensed under a [CC BY-NC 4.0](https://creativecommons.org/licenses/by-nc/4.0/)

2. Methods

The paper presents a formulation of the problem on determination of modes and frequencies of natural transverse oscillations for a beam of length L with flexural stiffness EI and distributed mass ρA and consisting of two segments (Figure 1): the first segment of length L_1 is supported by an elastic foundation of Winkler's type and the second one of length $L - L_1$ is free. Solutions of the vibration problem for these two segments are constructed separately. Integration constants for proper differential equation can be determined owing to the conjunction conditions between beam's segments along with the boundary conditions at beam's endpoints.

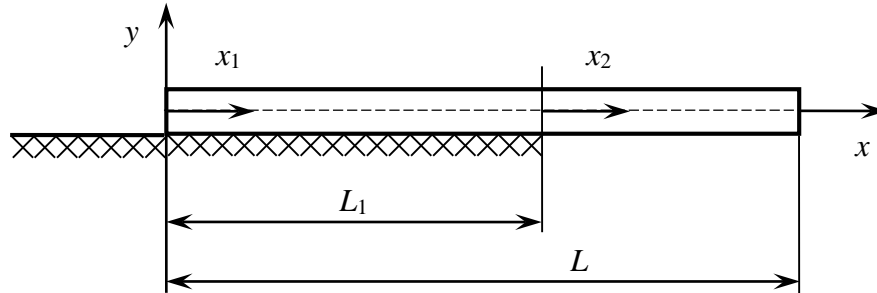


Figure 1. Beam partially supported by elastic foundation.

Transverse oscillations of the first segment $0 \leq \xi_1 \leq \nu$

Let us introduce dimensionless variables and parameters

$$\xi_i = \frac{x_i}{L} \quad (i = 1, 2); \quad w_i = \frac{v_i}{L}; \quad \tau = \omega_0 t; \quad \nu = \frac{L_1}{L}; \quad \omega_0 = \sqrt{\frac{K}{\rho A}}; \quad \alpha = \sqrt[4]{\frac{KL^4}{4EI}}; \quad \bar{\omega} = \frac{\omega}{\omega_0},$$

where x_i – axial coordinate for i -th segment ($i = 1, 2$);

$v_i = v_i(x_i, t)$ is deflection field of i -th segment ($i = 1, 2$);

ν is relative length of the segment supported by foundation;

$K = kb$ is foundation stiffness;

k is modulus of subgrade reaction,

b is width of cross section;

α is generalized stiffness of the system «beam is foundation»;

ω_0 is “conventional” frequency parameter that takes dimension of frequency [s^{-1}];

t is physical time;

ω is frequency of natural oscillations.

The equation of natural oscillations for the first section takes the form [25, 26]

$$\frac{\partial^4 w_1}{\partial \xi_i^4} + 4\alpha^4 \left(w_1 + \frac{\partial^2 w_1}{\partial \tau^2} \right) = 0. \quad (1)$$

Let us find the solution of the equation (1) assuming that oscillations are harmonic and using separation of variables:

$$w_1(\xi_1, \tau) = W_1(\xi_1) \sin \frac{\tilde{\omega}}{\bar{\omega}_0} \tau, \quad (2)$$

where $\bar{\omega} = \frac{\omega}{\omega_e}$ is dimensionless frequency;

$\bar{\omega}_0 = \frac{\omega_0}{\omega_e}$ is dimensionless “conventional” frequency;

$\omega_e = \frac{1}{L^2} \sqrt{\frac{EI}{\rho A}}$ is "reference" frequency. Further, we use the dimensionless «conventional» frequency $\bar{\omega}_0$, as a generalized stiffness of the system "beam–foundation" instead of parameter α which has a physical meaning. Reducing the base stiffness K by means of the relationships

$$\omega_0 = \sqrt{\frac{K}{\rho A}} \quad \text{and} \quad \alpha = \sqrt[4]{\frac{KL^4}{4EI}},$$

and taking into account the reference frequency ω_e we obtain

$$4\alpha^4 = \frac{\omega_0^2}{\frac{1}{L^4} \frac{EI}{\rho A}} = \left(\frac{\omega_0}{\omega_e} \right)^2 = \bar{\omega}_0^2.$$

Substituting (2) into (1), we obtain the equation for modes of natural oscillations

$$W_1^{IV} + (\bar{\omega}_0^2 - \tilde{\omega}^2)W_1 = 0. \quad (3)$$

The structure of equation (3) yields the following three possible solutions:

1) if $\tilde{\omega} > \bar{\omega}_0$, then, writing the equation (3) in the form

$$W_1^{IV} - (\tilde{\omega}^2 - \bar{\omega}_0^2)W_1 = 0 \quad (4)$$

and solving the last equation by Euler's substitution

$$W_1 = Ae^{r\xi_1}, \quad (5)$$

we obtain the characteristic equation

$$r^4 - (\tilde{\omega}^2 - \bar{\omega}_0^2) = 0,$$

the roots of which are as follow:

$$r_{1,2} = \pm\beta_1; \quad r_{3,4} = \pm i\beta_1; \quad \beta_1 = \sqrt[4]{\tilde{\omega}^2 - \bar{\omega}_0^2}. \quad (6)$$

Then the solution of equation (4) takes the form

$$W_1(\xi_1) = W_{10}R_4(\beta_1\xi_1) + W'_{10}R_3(\beta_1\xi_1) + W''_{10}R_2(\beta_1\xi_1) + W'''_{10}R_1(\beta_1\xi_1), \quad (7)$$

where $W_{10}, W'_{10}, W''_{10}, W'''_{10}$ are initial parameters;

$R_i = R_i(\beta_1\xi_1)$ is Krylov's function;

$$R_1 = \frac{\text{sh}\beta_1\xi_1 - \sin\beta_1\xi_1}{2\beta_1^3}; \quad R_2 = \frac{\text{ch}\beta_1\xi_1 - \cos\beta_1\xi_1}{2\beta_1^2};$$

$$R_3 = \frac{\text{sh}\beta_1\xi_1 + \sin\beta_1\xi_1}{2\beta_1}; \quad R_4 = \frac{\text{ch}\beta_1\xi_1 + \cos\beta_1\xi_1}{2}; \quad R'_4 = \beta_1^4 R_1.$$

The matrix equation for the state of arbitrary cross section ξ_1 in the first segment reads as

$$\bar{W}_1(\xi_1) = V_{11}(\beta_1\xi_1)\bar{W}_{10}, \quad (8)$$

where $\bar{W}_1(\xi_1) = \{W_1(\xi_1) W'_1(\xi_1) W''_1(\xi_1) W'''_1(\xi_1)\}^T$ is state vector of an arbitrary cross section ξ_1 ;

$\bar{W}_{10} = \{W_{10} W'_{10} W''_{10} W'''_{10}\}^T$ is initial parameters vector;

$$V_{11}(\xi_1) = \begin{pmatrix} R_4(\beta_1 \xi_1) & R_3(\beta_1 \xi_1) & R_2(\beta_1 \xi_1) & R_1(\beta_1 \xi_1) \\ \beta_1^4 R_1(\beta_1 \xi_1) & R_4(\beta_1 \xi_1) & R_3(\beta_1 \xi_1) & R_2(\beta_1 \xi_1) \\ \beta_1^4 R_2(\beta_1 \xi_1) & \beta_1^4 R_1(\beta_1 \xi_1) & R_4(\beta_1 \xi_1) & R_3(\beta_1 \xi_1) \\ \beta_1^4 R_3(\beta_1 \xi_1) & \beta_1^4 R_2(\beta_1 \xi_1) & \beta_1^4 R_1(\beta_1 \xi_1) & R_4(\beta_1 \xi_1) \end{pmatrix} \quad (9)$$

is a functional matrix describing the initial parameters influence on the state of cross section ξ_1 in the first segment.

2) if $\tilde{\omega} < \bar{\omega}_0$, then, substituting equation (5) into (3), we obtain the characteristic equation

$$r^4 + (\bar{\omega}_0^2 - \tilde{\omega}^2) = 0$$

with the complex roots

$$r_{1-4} = (\pm i \pm 1) \beta_2; \quad \beta_2 = \sqrt[4]{\frac{\bar{\omega}_0^2 - \tilde{\omega}^2}{4}} \quad (10)$$

and the solution of the equation (3) reads as

$$W_1 = W_{10} K_4(\beta_2 \xi_1) + W_{10}' K_3(\beta_2 \xi_1) + W_{10}'' K_2(\beta_2 \xi_1) + W_{10}''' K_1(\beta_2 \xi_1), \quad (11)$$

where $K_i = K_i(\beta_2 \xi_1)$ are Krylov's functions that are of the form

$$K_1 = \frac{\text{sh} \beta_2 \xi_1 \text{ch} \beta_2 \xi_1 - \cos \beta_2 \xi_1 \text{sh} \beta_2 \xi_1}{4 \beta_2^3}; \quad K_2 = \frac{\sin \beta_2 \xi_1 - \text{sh} \beta_2 \xi_1}{2 \beta_2^2};$$

$$K_3 = \frac{\text{sh} \beta_2 \xi_1 \text{ch} \beta_2 \xi_1 + \cos \beta_2 \xi_1 \text{sh} \beta_2 \xi_1}{2 \beta_2}; \quad K_4 = \cos \beta_2 \xi_1 + \text{ch} \beta_2 \xi_1; \quad K_4' = -4 \beta_2^4 K_1.$$

In this case, the state of an arbitrary cross section ξ_1 of the first segment can be described in the following matrix form:

$$\bar{W}_1(\xi_1) = V_{12}(\xi_1) \bar{W}_{10},$$

where

$$V_{12}(\xi_1) = \begin{pmatrix} K_4(\beta_2 \xi_1) & K_3(\beta_2 \xi_1) & K_2(\beta_2 \xi_1) & K_1(\beta_2 \xi_1) \\ -4 \beta_2^4 K_1(\beta_2 \xi_1) & K_4(\beta_2 \xi_1) & K_3(\beta_2 \xi_1) & K_2(\beta_2 \xi_1) \\ -4 \beta_2^4 K_2(\beta_2 \xi_1) & -4 \beta_2^4 K_1(\beta_2 \xi_1) & K_4(\beta_2 \xi_1) & K_3(\beta_2 \xi_1) \\ -4 \beta_2^4 K_3(\beta_2 \xi_1) & -4 \beta_2^4 K_2(\beta_2 \xi_1) & -4 \beta_2^4 K_1(\beta_2 \xi_1) & K_4(\beta_2 \xi_1) \end{pmatrix}. \quad (12)$$

3) if $\tilde{\omega} = \bar{\omega}_0$, then by using the serial integration of the equation

$$W_1^{IV} = 0,$$

we obtain the function

$$W_1 = W_{10} + W_{10}' \xi_1 + W_{10}'' \frac{\xi_1^2}{2} + W_{10}''' \frac{\xi_1^3}{6}$$

and the matrix equation

$$\bar{W}_1(\xi_1) = V_{13}(\xi_1) \bar{W}_{10}, \quad (14)$$

where

$$V_{13}(\xi_1) = \begin{pmatrix} 1 & \xi_1 & \frac{\xi_1^2}{2} & \frac{\xi_1^3}{6} \\ 0 & 1 & \xi_1 & \frac{\xi_1^2}{2} \\ 0 & 0 & 1 & \xi_1 \\ 0 & 0 & 0 & 1 \end{pmatrix}.$$

Thus, the strain-stress state of the first segment is described by equations (8), (11) and (14) that all together can be expressed in the form

$$\bar{W}_{1j}(\xi_1) = V_{1j}(\xi_1)\bar{W}_{10}, \quad j = 1, 2, 3. \quad (15)$$

Transverse vibrations of 2-nd segment $0 \leq \xi_2 \leq 1 - \nu$

Natural transverse oscillations of this segment can be described by the equation [25–27]

$$\frac{\partial^4 w_2}{\partial \xi_2^4} + 4\alpha^4 \frac{\partial^2 w_2}{\partial \tau^2} = 0. \quad (16)$$

Separating variables by the representation

$$w_2(\xi_2, \tau) = W_2(\xi_2) \sin \bar{\omega} \tau, \quad (17)$$

we obtain

$$W_2^{IV} - \tilde{\omega}^2 W_2 = 0,$$

from where, assuming

$$W_2(\xi_2) = A e^{s \xi_2}, \quad (18)$$

we deduce the characteristic equation

$$s^4 - \tilde{\omega}^2 = 0,$$

the roots of which are of the form

$$s_{1,2} = \pm \beta_3; \quad s_{3,4} = \pm i \beta_3; \quad \beta_3 = \sqrt{\tilde{\omega}}. \quad (19)$$

Express the state of an arbitrary cross section ξ_2 of the 2-nd segment by the corresponding vector

$$\bar{W}_2 = \{W_2(\xi_2) \ W_2'(\xi_2) \ W_2''(\xi_2) \ W_2'''(\xi_2)\}^T$$

and the matrix equation

$$\bar{W}_2 = V_{11}(\beta_3 \xi_2) \bar{W}_{20}, \quad (20)$$

where $\bar{W}_{20} = \{W_{20} \ W_{20}' \ W_{20}'' \ W_{20}'''\}^T$ is initial parameters vector for the 2-nd segment. Using the conjunction condition between the segments, we obtain

$$\bar{W}_{20} = \bar{W}_2(0) = \bar{W}_1(\nu),$$

since the matrix $v_{11}(0)$ is unit. Then the vector $\bar{W}_{20} = V_{1j}(\nu) \bar{W}_{10}$ ($j = 1, 2, 3$) and the state vector for both the segments can be expressed via the initial parameters for the first segment

$$\begin{aligned} \bar{W}_1(\xi_1) &= V_{11}(\beta_1 \xi_1) \bar{W}_{10} \quad (\tilde{\omega} > \bar{\omega}_0) \\ \bar{W}_1(\xi_1) &= V_{12}(\beta_2 \xi_1) \bar{W}_{10} \quad (\tilde{\omega} < \bar{\omega}_0) \\ \bar{W}_1(\xi_1) &= V_{13}(\xi_1) \bar{W}_{10} \quad (\tilde{\omega} = \bar{\omega}_0) \\ \bar{W}_2(\xi_2) &= V_{11}(\beta_3 \xi_2) V_{1j}(\nu) \bar{W}_{10}. \end{aligned} \quad (21)$$

Transverse oscillations of a beam with free endpoints

A beam resting on an elastic foundation without restrictions at the endpoints can be described as a proper model of spread footing. In this case, the boundary conditions read:

$$\begin{aligned} W_{10}'' &= W_{10}''' = 0 \\ w_2''(1-\nu) &= w_2'''(1-\nu) = 0, \end{aligned} \quad (22)$$

From here it follows that

$$\begin{aligned} \bar{W}_{10} &= \{W_{10} \ W'_{10} \ 0 \ 0\}^T \\ \bar{w}_2(1-\nu) &= \{w_2(1-\nu) \ w'_2(1-\nu) \ 0 \ 0\}^T. \end{aligned} \tag{23}$$

1. At first, we accept a condition according to which the unknown frequency $\tilde{\omega}$ for a partially supported beam equals to “conventional” frequency $\bar{\omega}_0$. Then, according to (21) and (14), we have

$$\begin{aligned} \bar{W}_1(\xi_1) &= V_{13}(\xi_1)\bar{W}_{10} \\ \bar{W}_2(\xi_2) &= V_{11}(\xi_2)V_{13}(\nu)\bar{W}_{10}. \end{aligned} \tag{24}$$

Let us write the second equation (24) in the expanded form by taking into account (23) and $\xi_2 = 1 - \nu$

$$\begin{pmatrix} w_2(1-\nu) \\ w'_2(1-\nu) \\ 0 \\ 0 \end{pmatrix} = \begin{pmatrix} R_4(\beta_3(1-\nu)) & R_3(\beta_3(1-\nu)) & R_2(\beta_3(1-\nu)) & R_1(\beta_3(1-\nu)) \\ \beta_3^4 R_1(\beta_3(1-\nu)) & R_4(\beta_3(1-\nu)) & R_3(\beta_3(1-\nu)) & R_2(\beta_3(1-\nu)) \\ \beta_3^4 R_2(\beta_3(1-\nu)) & \beta_3^4 R_1(\beta_3(1-\nu)) & R_4(\beta_3(1-\nu)) & R_3(\beta_3(1-\nu)) \\ \beta_3^4 R_3(\beta_3(1-\nu)) & \beta_3^4 R_2(\beta_3(1-\nu)) & \beta_3^4 R_1(\beta_3(1-\nu)) & R_4(\beta_3(1-\nu)) \end{pmatrix} \times \\ \times \begin{pmatrix} 1 & \nu & \frac{\nu^2}{2} & \frac{\nu^3}{6} \\ 0 & 1 & \nu & \frac{\nu^2}{2} \\ 0 & 0 & 1 & \nu \\ 0 & 0 & 0 & 1 \end{pmatrix} \begin{pmatrix} W_{10} \\ W'_{10} \\ 0 \\ 0 \end{pmatrix}.$$

From here, we obtain the homogenous system of equations relatively the unknown initial parameters W_{10} and W'_{10} :

$$\begin{cases} R_2(\beta_3(1-\nu))W_{10} + (\nu R_2(\beta_3(1-\nu)) + R_1(\beta_3(1-\nu)))W'_{10} = 0 \\ R_3(\beta_3(1-\nu))W_{10} + (\nu R_3(\beta_3(1-\nu)) + R_2(\beta_3(1-\nu)))W'_{10} = 0. \end{cases}$$

The condition of existing of nonzero roots for this system is the equality to zero the determinant

$$\begin{vmatrix} R_2(\beta_3(1-\nu)) & R_2(\beta_3(1-\nu)) + R_1(\beta_3(1-\nu)) \\ R_3(\beta_3(1-\nu)) & \nu R_3(\beta_3(1-\nu)) + R_2(\beta_3(1-\nu)) \end{vmatrix} = 0.$$

Expanding this determinant, we obtain the frequency equation

$$\text{ch}(\beta_3(1-\nu))\cos(\beta_3(1-\nu)) = 1,$$

the roots of which are [17]

$$\beta_{31}(1-\nu) = 0; \beta_{32}(1-\nu) = 4,73; \beta_{33}(1-\nu) = 7,853; \beta_{34}(1-\nu) = \frac{2n+1}{2}\pi \text{ at } n > 3 \text{ gives}$$

physically impossible results at $\nu = 1$

$$\lim_{\nu \rightarrow 1} \beta_{32} = \lim_{\nu \rightarrow 1} \sqrt{\tilde{\omega}} = \lim_{\nu \rightarrow 1} \frac{4,73}{1-\nu} = \infty \text{ and etc.}$$

Consequently, the accepted condition $\tilde{\omega} = \bar{\omega}_0$ is not realized.

2. As is known [25], a free (i.e., without foundation) beam without constrains at its endpoints has two null frequencies corresponding to translational and rotational motion of the beam as a rigid body in addition to

the frequencies of free oscillations that coincide with the frequencies of the beam with clamped endpoints. Consequently, the rigid body motion should be added to the deflections caused by beam's vibrations. Such complex motion is described by the function

$$W = C_1 + C_2\xi.$$

Following to the accepted model of the system «beam-foundation», the existence of small length $\nu \neq 0$ of beam's part interacting with foundation excludes the possibility of beam's motion as a rigid body. At the same time, calculation of the basic first frequency of natural oscillations can be performed according to (10)–(11) that is when the condition $\tilde{\omega} < \bar{\omega}_0$, holds, beginning from $\omega_1 = 0$ at $\nu = 0$ and $\omega_0 \neq 0$. Let us accept this condition, that is the unknown frequency $\tilde{\omega}$ is smaller than the «conventional» frequency $\bar{\omega}_0$. Then, according to (21) and (12) we have:

$$\bar{W}_1(\xi_1) = V_{12}(\beta_2\xi_1)\bar{W}_{10}; \quad \bar{W}_2(\xi_2) = V_{11}(\beta_3\xi_2)V_{12}(\beta_2\nu)\bar{W}_{10}. \quad (25)$$

Let us write the second equation (25) using the expanded form for $\xi_2 = 1 - \nu$

$$\begin{pmatrix} w_2(1-\nu) \\ w_2'(1-\nu) \\ 0 \\ 0 \end{pmatrix} = \begin{pmatrix} R_4(\beta_3(1-\nu)) & R_3(\beta_3(1-\nu)) & R_2(\beta_3(1-\nu)) & R_1(\beta_3(1-\nu)) \\ \beta_3^4 R_1(\beta_3(1-\nu)) & R_4(\beta_3(1-\nu)) & R_3(\beta_3(1-\nu)) & R_2(\beta_3(1-\nu)) \\ \beta_3^4 R_2(\beta_3(1-\nu)) & \beta_3^4 R_1(\beta_3(1-\nu)) & R_4(\beta_3(1-\nu)) & R_3(\beta_3(1-\nu)) \\ \beta_3^4 R_3(\beta_3(1-\nu)) & \beta_3^4 R_2(\beta_3(1-\nu)) & \beta_3^4 R_1(\beta_3(1-\nu)) & R_4(\beta_3(1-\nu)) \end{pmatrix} \times \begin{pmatrix} K_4(\beta_2\nu) & K_3(\beta_2\nu) & K_2(\beta_2\nu) & K_1(\beta_2\nu) \\ -4\beta_2^4 K_1(\beta_2\nu) & K_4(\beta_2\nu) & K_3(\beta_2\nu) & K_2(\beta_2\nu) \\ -4\beta_2^4 K_2(\beta_2\nu) & -4\beta_2^4 K_1(\beta_2\nu) & K_4(\beta_2\nu) & K_3(\beta_2\nu) \\ -4\beta_2^4 K_3(\beta_2\nu) & -4\beta_2^4 K_2(\beta_2\nu) & -4\beta_2^4 K_1(\beta_2\nu) & K_4(\beta_2\nu) \end{pmatrix} \begin{pmatrix} W_{10} \\ W_{10}' \\ 0 \\ 0 \end{pmatrix}. \quad (26)$$

Also, the two linear homogenous equations relatively the unknown initial parameters W_{10} and W_{10}' can be found from the matrix equation (26) as it was done in the Section 1 of the paper:

$$\begin{cases} U_1 W_{10} + U_2 W_{10}' = 0 \\ U_3 W_{10} + U_4 W_{10}' = 0, \end{cases} \quad (27)$$

where

$$\begin{aligned} U_1 &= \beta_3^4 R_2(X)K_4(Y_1) - 4\beta_2^4 (\beta_3^4 R_1(X)K_1(Y_1) + R_4(X)K_2(Y_1)) + R_3(X)K_3(Y_1); \\ U_2 &= \beta_3^4 (R_2(X)K_4(Y_1) + R_1(X)K_4(Y_1)) - 4\beta_2^4 (R_4(X)K_1(Y_1) + R_3(X)K_2(Y_1)); \\ U_3 &= \beta_3^4 (R_3(X)K_4(Y_1) - 4\beta_2^4 (R_2(X)K_1(Y_1) + R_1(X)K_2(Y_1))) - 4\beta_2^4 R_1(X)K_3(Y_1); \\ U_4 &= \beta_3^4 (R_3(X)K_3(Y_1) + R_2(X)K_4(Y_1) - 4\beta_2^4 R_1(X)K_1(Y_1)) - 4\beta_2^4 R_4(X)K_2(Y_1); \\ X &= \beta_3(1-\nu); \quad Y_1 = \beta_2\nu. \end{aligned}$$

Now, obtain the frequency equation by equating the determinant value of the system (27) with zero:

$$U_1 U_4 - U_2 U_3 = 0. \quad (28)$$

The deflection functions $w_i(\xi_i)$ ($i = 1, 2$) along with the bending moments $w_i''(\xi_i)$ in arbitrary cross sections are found from the matrix equations (25). For the first segment ($0 \leq \xi_1 \leq \nu$) we obtain

$$w_1(\xi_1) = W_{10} (K_4(\beta_2\xi_1) - UK_3(\beta_2\xi_1)); \quad w_1''(\xi_1) = W_{10} (-K_2(\beta_2\xi_1) - UK_1(\beta_2\xi_1))$$

and the same for the second one ($0 \leq \xi_2 < 1 - \nu$):

$$w_2(\xi_2) = W_{10} \sum_{n=1}^4 R_n(\beta_2 \xi_2) P_n; \quad w_2''(\xi_2) = W_{10} \sum_{n=1}^4 R_n''(\beta_3 \xi_2) P_n,$$

where

$$P_1 = 4\beta_2^4 (-K_3(Y_1) + UK_2(Y_1)); \quad P_2 = 4\beta_2^4 (-K_2(Y_1) + UK_1(Y_1));$$

$$P_3 = -4\beta_2^4 K_1(Y_1) - UK_4(Y_1); \quad P_4 = K_4(Y_1) - UK_3(Y_1); \quad U = \frac{U_3}{U_4}.$$

The second and higher frequencies and modes of natural vibrations of a beam with free endpoints resting on elastic foundation should be evaluated by assuming that the “conventional” frequency $\bar{\omega}_0$ is smaller than the unknown one $\tilde{\omega}$ in accordance with the variant (6)–(7). It is determined by the requirement that the second frequency (following the first null) of a free beam (i.e., a beam without foundation, when $\bar{\omega}_0 = 0$) equals to 4.73 [25]. Then, according to (21) and (9) we have:

$$\bar{W}_1(\xi_1) = V_{11}(\beta_1 \xi_1) \bar{W}_{10}; \quad \bar{W}_2(\xi_2) = V_{11}(\beta_3 \xi_2) V_{11}(\beta_1 \nu) \bar{W}_{10}. \quad (29)$$

From here, we obtain the frequency equation by performing the actions similar to ones in Section 1 and 2

$$Z_1 Z_4 - Z_2 Z_3 = 0, \quad (30)$$

where

$$Z_1 = b_3^4 R_2(X) R_4(Y_2) + b_1^4 (b_3^4 R_1(X) R_1(Y_2) + R_4(X) R_2(Y_2) + R_3(X) R_3(Y_2));$$

$$Z_2 = b_3^4 (R_2(X) R_3(Y_2) + R_1(X) R_4(Y_2)) + b_1^4 (R_4(X) R_1(Y_2) + R_3(X) R_2(Y_2));$$

$$Z_3 = \beta_3^4 (R_3(X) R_4(Y_2) + \beta_1^4 (R_2(X) R_1(Y_2) + R_1(X) R_2(Y_2))) + \beta_1^4 R_4(X) R_3(Y_2);$$

$$Z_4 = \beta_3^4 (R_3(X) R_3(Y_2) + R_2(X) R_4(Y_2) + \beta_1^4 R_1(X) R_1(Y_2)) + \beta_1^4 R_4(X) R_2(Y_2);$$

$$Y_2 = \beta_1 \nu.$$

The deflection functions $w_i(\xi_i)$ ($i = 1, 2$) and the bending moments $w_i''(\xi_i)$ in arbitrary cross section of the first segment ($0 \leq \xi_1 \leq \nu$) are found from equation (29) as this was done in Section 1:

$$w_1(\xi_1) = W_{10} (R_4(\beta_1 \xi_1) - ZR_3(\beta_1 \xi_1))$$

$$w_1''(\xi_1) = W_{10} (R_2(\beta_1 \xi_1) - ZR_1(\beta_1 \xi_1))$$

and the same for the second segment ($0 \leq \xi_2 \leq 1 - \nu$):

$$w_2(\xi_2) = W_{10} \sum_{n=1}^4 R_n(\beta_3 \xi_2) S_n; \quad w_2''(\xi_2) = W_{10} \sum_{n=1}^4 R_n''(\beta_3 \xi_2) S_n,$$

where

$$S_1 = \beta_1^4 (R_3(Y_2) - ZR_2(Y_2)); \quad S_2 = \beta_1^4 (R_2(Y_2) - ZR_1(Y_2));$$

$$S_3 = \beta_1^4 R_1(Y_2) - ZR_4(Y_2); \quad S_4 = R_4(Y_2) - ZR_3(Y_2); \quad Z = \frac{Z_3}{Z_4}.$$

3. Results and Discussion

Table 1 shows the values of the first three dimensionless natural frequencies which are obtained from equations (28) and (30) for different combinations of “conventional” frequency values $\bar{\omega}_0$, that characterize generalized stiffness of the system “beam–foundation” and ν is segment’s length after partial destruction of the foundation.

Table 1. The first three frequencies of beam's natural oscillations.

$\bar{\omega}_0$	$\tilde{\omega}_1 (\tilde{\omega} < \bar{\omega}_0)$			$\tilde{\omega}_3 (\tilde{\omega} > \bar{\omega}_0)$			$\tilde{\omega}_3 (\tilde{\omega} = \bar{\omega}_0)$		
	$\nu = 0.25$	$\nu = 0.5$	$\nu = 0.75$	$\nu = 0.25$	$\nu = 0.5$	$\nu = 0.75$	$\nu = 0.25$	$\nu = 0.5$	$\nu = 0.75$
2	0.038	0.268	0.889	22.4	22.42	22.44	61.68	61.685	61.7
6	0.195	1.245	3.309	22.61	22.77	22.94	61.75	61.83	61.89
10	0.412	2.31	4.991	23.08	23.48	23.961	61.86	62.08	62.28
14	0.664	3.25	6.985	23.87	24.53	25.48	62.05	62.47	62.87
18	0.937	4.04	8.174	25.11	25.92	27.46	62.25	63	63.65
22	1.219	4.69	9.078	26.94	27.67	29.83	62.57	63.68	64.61
26	1.498	5.25	9.772	29.27	29.87	32.52	63.04	64.51	65.76
30	1.772	5.76	10.24	32.03	32.59	35.47	63.52	65.5	67.06
34	2.031	6.25	11.15	35.16	35.8	38.6	64	66.63	68.53

Figure 2 shows the dependencies of frequency on parameter $\bar{\omega}_0$ for various lengths ν of the supported segment.

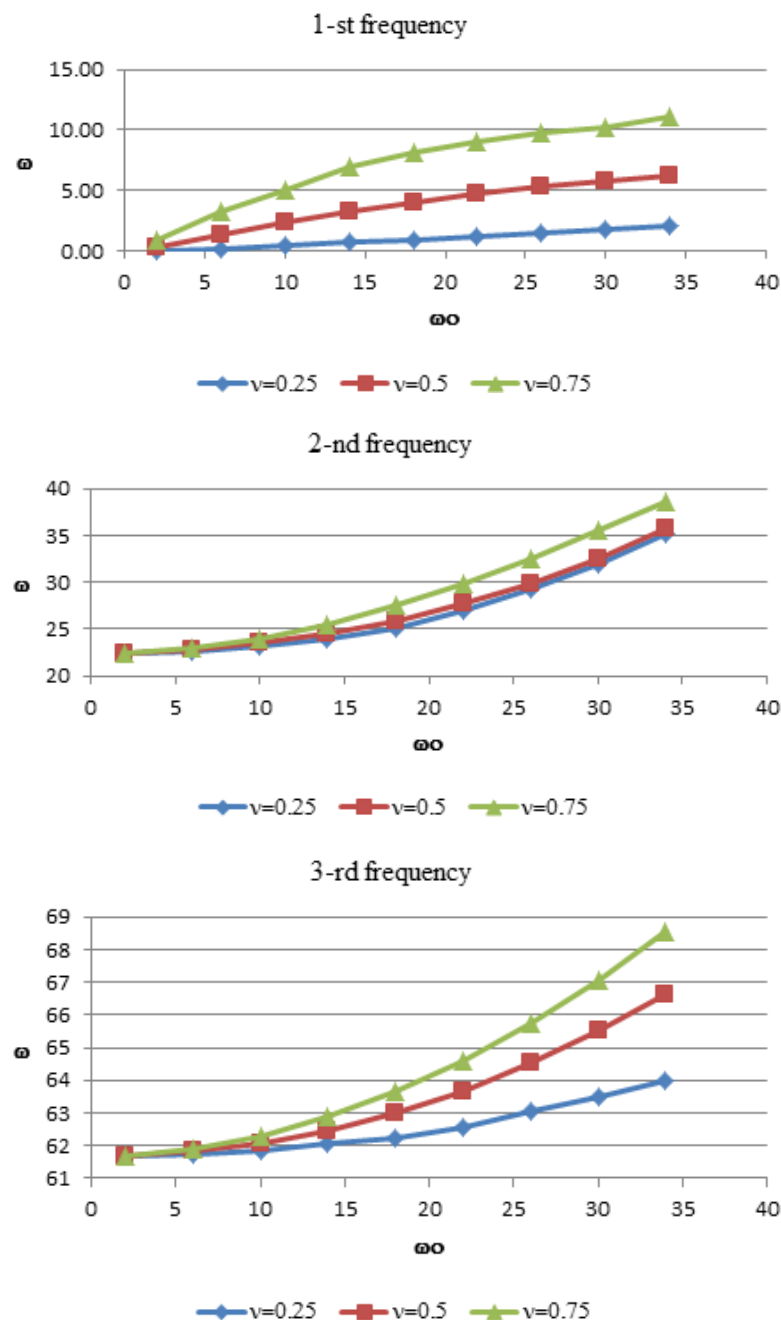


Figure 2. Dependency between frequency of vibrations and generalized stiffness $\bar{\omega}_0$.

Figure 3 presents modes of natural oscillations corresponding to these frequencies for $\bar{\omega}_0 = 18$ and $\nu = 0.5$.

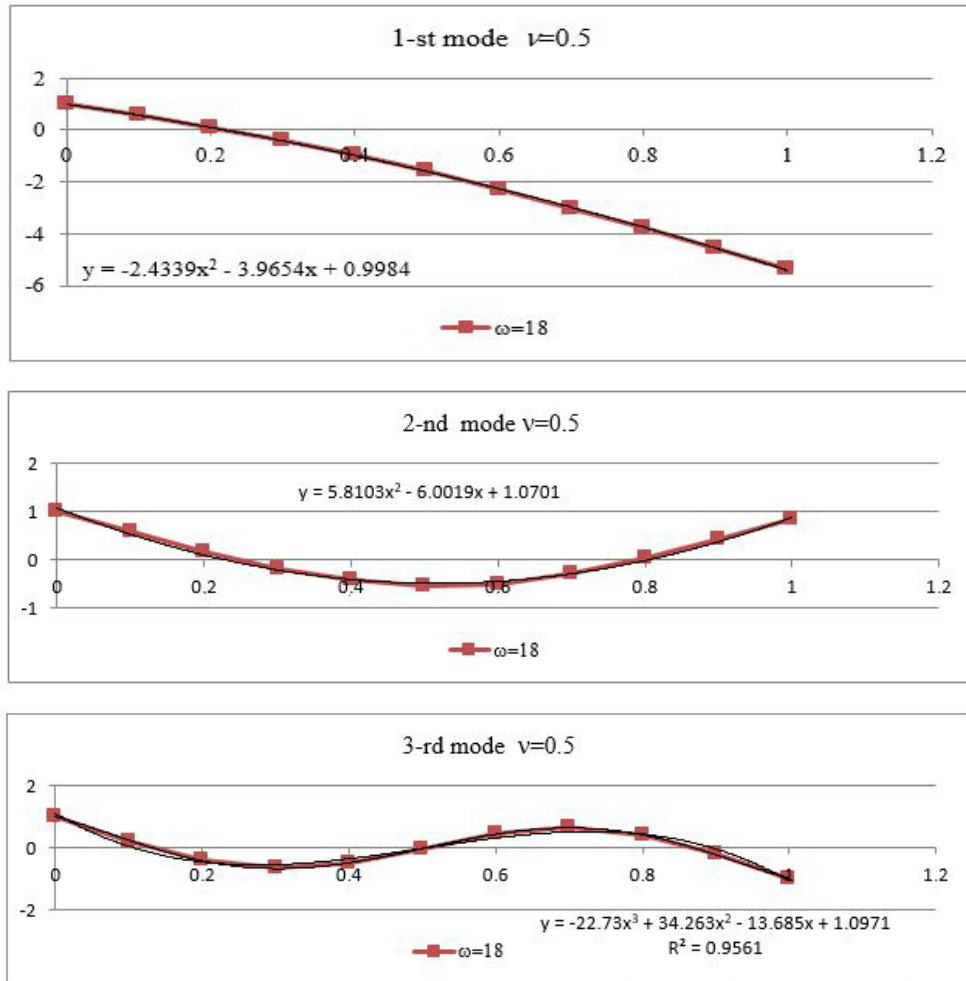


Figure 3. The first three modes of beam’s vibrations.

The following equation describes beam’s forced oscillations caused by sudden partial damage of a foundation which supports a loaded beam [27]

$$\frac{\partial^4 w_{dyn}}{\partial \xi^4} + 4\alpha^4 \left(w_{dyn} + \frac{\partial^2 w_{dyn}}{\partial \tau^2} \right) = \bar{q}, \tag{31}$$

where $\bar{q} = \frac{ql^3}{EI}$ is dimensionless intensity of an evenly distributed load;

$w_{dyn} = w_{dyn}(\xi, \tau)$ is deflection function for an arbitrary cross section ξ ($0 \leq \xi \leq 1$);

τ is physical time. Let us separate variables in equation (31) using the series

$$w_{dyn} = \sum_{n=1}^{\infty} Q_n(\tau) W_n(\xi), \tag{32}$$

where $W_n = W_n(\xi)$ is eigen function obtained by conjunction of eigen functions $W_{1m}(\xi_1)$ and $W_{2m}(\xi)$; for both the segments;

$Q_n = Q_n(\tau)$ is unknown time function.

We obtain the equations that allow determining the functions $Q_n(\tau)$:

$$\frac{d^2 Q_n}{d\tau^2} + \bar{\omega}_n^2 Q_n = R_n, \tag{33}$$

where

$$R_n = \frac{1}{\bar{\omega}_0^2} \frac{\int_0^1 \bar{q} W_n(\xi) d\xi}{\int_0^1 W_n^2(\xi) d\xi}.$$

The common solution of the equation (31) takes the form [25]

$$w_{dyn} = \sum_{n=1}^{\infty} \left(D_{1n} \cos \bar{\omega}_n \tau + D_{2n} \sin^2 \bar{\omega}_n \tau + \frac{R_n}{\bar{\omega}_n^2} \right) W_n(\xi). \quad (34)$$

The integration constants D_{1n} and D_{2n} can be determined from the initial conditions

$$\begin{aligned} w_{dyn}(\xi, 0) &= w_{st}(\xi), \\ \left. \frac{\partial w_{dyn}}{\partial \tau} \right|_{\xi, 0} &= 0, \end{aligned} \quad (35)$$

where $w_{st}(\xi)$ is static deflection of a beam entirely supported by an elastic foundation. This deflection can be determined from the equation [27] taking into account the constraints at the endpoints of the beam:

$$\frac{\partial^4 w_{st}}{\partial \xi^4} + 4\alpha^4 w_{st} = \bar{q}.$$

For a beam simply supported by an elastic foundation of Winkler's type and loaded with evenly distributed load $\bar{q} = \text{const}$, the deflection in the foundation (without flexure) descends versus the depth according to the law

$$w_{st}(\xi) = \frac{\bar{q}}{4\alpha^4}. \quad (36)$$

From 2-nd condition (35), it follows

$$D_{2n} = 0. \quad (37)$$

From 1-st condition (35), we obtain

$$\sum_{n=1}^{\infty} \left(D_{1n} + \frac{R_n}{\bar{\omega}_n^2} \right) W_n(\xi) = w_{st}. \quad (38)$$

Multiplying both the parts of (37) by $W_n(\xi)$ and integrating by ξ from 0 to 1 we obtain

$$D_{1n} = B_n - \frac{R_n}{\bar{\omega}_n^2}, \quad B_n = \frac{\int_0^1 w_{st} W_n(\xi) d\xi}{\int_0^1 W_n^2(\xi) d\xi}. \quad (39)$$

Substituting (37) and (39) into the series (34) and taking into account the equality

$$1 - \cos \bar{\omega}_n \tau = 2 \sin^2 \frac{\bar{\omega}_n}{2} \tau,$$

we obtain

$$w_{dyn}(\xi, \tau) = \sum_{n=1}^{\infty} \left(B_n \cos \bar{\omega}_n \tau + C_n \sin^2 \frac{\bar{\omega}_n}{2} \tau \right) W_n(\xi), \quad (40)$$

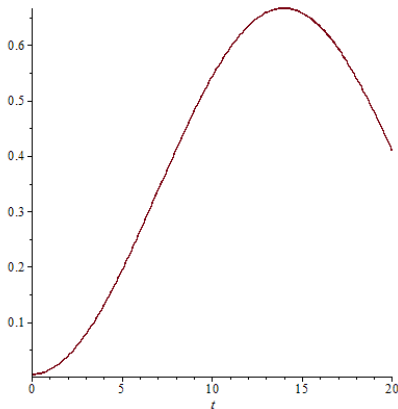
where

$$C_n = \frac{2\bar{q} \int_0^1 W_n(\xi) d\xi}{\tilde{\omega}_n^2 \int_0^1 W_n^2(\xi) d\xi}.$$

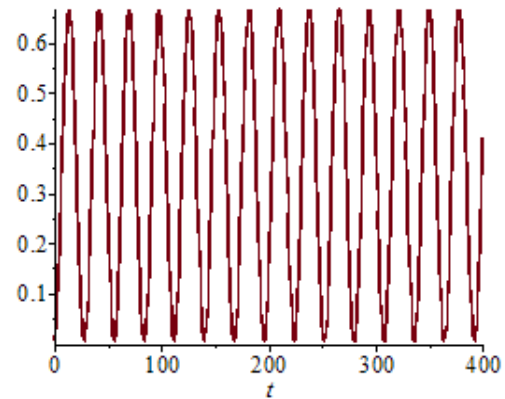
Using a similar transformation, we obtain the series for bending moments

$$M_{dyn} = w''_{dyn} = \sum_{n=1}^{\infty} \left(B_n \cos \bar{\omega}_n \tau + C_n \sin^2 \frac{\bar{\omega}_n}{2} \tau \right) W_n''(\xi). \tag{41}$$

Figure 4 presents the bending moment behavior in the cross section $\zeta = 0.43$ at the beginning of the dynamic process in the beam after sudden foundation destruction under a half of the beam ($\nu = 0.5$) when the generalized stiffness of the system “beam–foundation” is $\bar{\omega}_0 = 18$ ($\alpha = 3$) (Figure 4 a) and the graph of stationary vibrations at $\tau > 14$ (Figure 4 b). The bending moment reaches its maximum value $M_{max}^{dyn} = 0.666$.



a) The beginning of bending moment increasing in the cross section $\zeta = 0.43$



b) stationary oscillations of bending moment in the same cross section

Figure 4. Bending moment after sudden damage of foundation ($\nu = 0.5$).

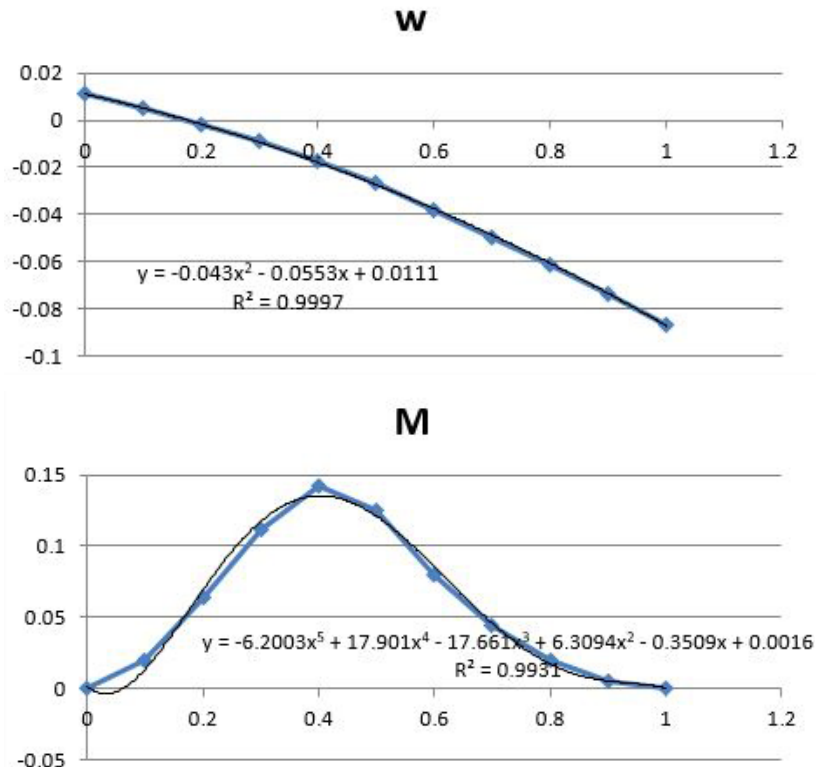


Figure 5. Distribution of deflection and bending moment caused by quasi-static damaging of foundation.

When quasi-static appearing of such a damage, the bending moment reaches its maximum value in the same cross section $\zeta = 0.43$ and is equal to $M_{\max}^{qs} = 0.143$ (Figure 5) while the external load $\bar{q} = 1$ is unit. One can see that the effect of sudden damage exhibits as the five-time increase in the internal bending moment.

4. Conclusions

The obtained analytical solution of the problem on determination forces, modes and frequencies of natural and forced flexural vibrations of a beam supported by an elastic foundation can be applied to verification of mathematical models of static-dynamic and quasi-static deforming of complex structural systems «beam – foundation» under accidental impacts caused by sudden destruction a part of foundation. Besides, this analytical solution can be applied to problems on defense of buildings and structures against progressive destruction when, according to the scenario of a special accidental impact, an additional dynamic force due to sudden subsidence of a base in the system «strip footing – structure» plays an important role.

References

1. Pearson, C., Delatte, N. Ronan Point Apartment Tower Collapse and its Effect on Building Codes. *Journal of Performance of Constructed Facilities*. 2005. 19(2). Pp. 172–177. doi:10.1061/(asce)0887-3828(2005)19:2(172)
2. Travush, V.I., Fedorova, N. V. Survivability of structural systems of buildings with special effects. *Magazine of Civil Engineering*. 2018. 81(5). Pp. 73–80. doi:10.18720/MCE.81.8
3. Fedorova, N., Savin, S. Structural transformation of reinforced concrete structural system at sudden loss of stability of one of its elements. *IOP Conference Series: Materials Science and Engineering*. 2018. 365(5). Pp. 052018. doi:10.1088/1757-899X/365/5/052018
4. Li, J., Zhou, H. Energy-based collapse assessment of complex reinforced concrete structures with uncertainties. *Procedia Engineering*. 2017. 199. Pp. 1246–1251. doi:10.1016/j.proeng.2017.09.262
5. Utkin, V.S. Calculation of the reliability of the earth foundations of buildings and structures according to the deformation criteria with limited information on the soils and loads. *Magazine of Civil Engineering*. 2016. 61(1). Pp. 4–13. doi:10.5862/MCE.61.1
6. Utkin, V.S., Borisova, O.L. Calculation of the reliability of the slit foundation by the criterion of the bearing capacity of the foundation soil at the stage of operation. *Construction of Unique Buildings and Structures*. 2017. 57(6). Pp. 7-17. doi: 10.18720/CUBS.57.1
7. Motaghian, S.E., Mofid, M., Alanjari, P. Exact solution to free vibration of beams partially supported by an elastic foundation. *Scientia Iranica*. 2011. 18(4 A). Pp. 861–866. doi:10.1016/j.scient.2011.07.013
8. Motaghian, S., Mofid, M., Akin, J.E. On the free vibration response of rectangular plates, partially supported on elastic foundation. *Applied Mathematical Modelling*. 2012. 36(9). Pp. 4473–4482. doi:10.1016/j.apm.2011.11.076
9. Rezaei, E., Dahlberg, T. Dynamic behaviour of an in situ partially supported concrete railway sleeper. *Proceedings of the Institution of Mechanical Engineers, Part F: Journal of Rail and Rapid Transit*. 2011. 225(5). Pp. 501–508. doi:10.1177/2041301710392492
10. Eisenberger, M., Yankelevsky, D.Z., Clastornik, J. Stability of beams on elastic foundation. *Computers and Structures*. 1986. 24(1). Pp. 135–139. doi:10.1016/0045-7949(86)90342-1
11. Liu, Y., Shu, D.W. Analytical Solution of the Vibration of Delaminated Bimaterial Beams Fully or Partially Supported by Elastic Foundation. *Applied Mechanics and Materials*. 2013. 394. Pp. 75–79. doi:10.4028/www.scientific.net/amm.394.75
12. Attar, M., Karrech, A., Regenauer-Lieb, K. Dynamic response of cracked Timoshenko beams on elastic foundations under moving harmonic loads. *JVC/Journal of Vibration and Control*. 2017. 23(3). Pp. 432–457. doi:10.1177/1077546315580470
13. Tsai, M.H., Huang, T.C. Progressive collapse analysis of an RC building with exterior non-structural walls. *Procedia Engineering*. 2011. 14. Pp. 377–384. doi:10.1016/j.proeng.2011.07.047
14. Amiri, S., Saffari, H., Mashhadi, J. Assessment of dynamic increase factor for progressive collapse analysis of RC structures. *Engineering Failure Analysis*. 2018. 84. Pp. 300–310. doi:10.1016/j.engfailanal.2017.11.011
15. Al-Salloum, Y.A., Abbas, H., Almusallam, T.H., Ngo, T., Mendis, P. Progressive collapse analysis of a typical RC high-rise tower. *Journal of King Saud University - Engineering Sciences*. 2017. 29(4), Pp. 313–320. doi:10.1016/j.jksues.2017.06.005
16. Weng, J., Tan, K.H., Lee, C.K. Adaptive superelement modeling for progressive collapse analysis of reinforced concrete frames. *Engineering Structures*. 2017. 151. Pp. 136–152. doi:10.1016/j.engstruct.2017.08.024
17. Fedorova, N. V., Savin, S.Y. Ultimate State Evaluating Criteria of RC Structural Systems at Loss of Stability of Bearing Element. *IOP Conference Series: Materials Science and Engineering*. 2018. 463. Pp. 032072. doi:10.1088/1757-899X/463/3/032072
18. Bažant, Z.P., Verdure, M. Mechanics of Progressive Collapse: Learning from World Trade Center and Building Demolitions. *Journal of Engineering Mechanics*. 2007. 133(3). Pp. 308–319. doi:10.1061/(ASCE)0733-9399(2007)133:3(308)
19. Khandelwal, K., El-Tawil, S. Pushdown resistance as a measure of robustness in progressive collapse analysis. *Engineering Structures*. 2011. 33(9). Pp. 2653–2661. doi:10.1016/j.engstruct.2011.05.013
20. Szyniszewski, S., Krauthammer, T. Energy flow in progressive collapse of steel framed buildings. *Engineering Structures*. 2012. 42. Pp. 142–153. doi:10.1016/j.engstruct.2012.04.014
21. Botez, M., Bredean, L., Ioani, A.M. Improving the accuracy of progressive collapse risk assessment: Efficiency and contribution of supplementary progressive collapse resisting mechanisms. *Computers and Structures*. 2016. 174. Pp. 54–65. doi:10.1016/j.compstruc.2015.11.002
22. Belostotsky, A.M., Penkovoy, S.B., Scherbina, S.V., Akimov, P.A., Kaytukov, T.B. Correct numerical methods of analysis of structural strength and stability of high-rise panel buildings part 2: Results of modelling. *Key Engineering Materials*. 2016. 685. Pp. 221–224. doi:10.4028/www.scientific.net/KEM.685.221
23. Travush, V. I., Fedorova, N.V. Survivability parameter calculation for framed structural systems. *Russian Journal of Building Construction and Architecture*. 2017. 33(1). Pp. 6–14. vestnikvgasu.wmsite.ru/ftpgetfile.php?id=564.
24. Gei, M., Misseroni, D. Experimental investigation of progressive instability and collapse of no-tension brickwork pillars. *International Journal of Solids and Structures*. 2018. 155. Pp. 81–88. doi:10.1016/j.ijsolstr.2018.07.010

25. Travush, V.I., Gordon, V.A., Kolchunov, V.I., Leontiev, E. V. The response of the system 'beam - Foundation' on sudden changes of boundary conditions. IOP Conference Series: Materials Science and Engineering. 2018. 456(1). Pp. 012130. doi:10.1088/1757-899X/456/1/012130
26. Gordon, V.A., Pilipenko, O. V., Trifonov, V.A. The reactions of the «beam – foundation» system to the sudden change of the boundary conditions. MATEC Web of Conferences. 2018. 188. Pp. 03008. doi:10.1051/mateconf/201818803008
27. Travush, V.I., Gordon, V.A., Kolchunov, V.I., Leontiev, Y.V. Dynamic effects in the beam on an elastic foundation caused by the sudden transformation of supporting conditions. International Journal for Computational Civil and Structural Engineering. 2018. 14(4). Pp. 27–41. doi:10.22337/2587-9618-2018-14-4-27-47

Contacts:

Vladimir Travush, +7(495)625-79-67; travush@mail.ru

Vladimir Gordon, +7(486)2419802; gordon@ostu.ru

Vitaly Kolchunov, +7(471)2222461; asiorel@mail.ru

Evgeny Leontiev, +7(495)6259595; e.leontyev@gge.ru

© Travush, V.I., Gordon, V.A., Kolchunov, V.I., Leontiev, E.V., 2019



DOI: 10.18720/MCE.91.12

Динамическое деформирование балки при внезапном структурном изменении упругого основания

В.И. Травуш^a, В.А. Гордон^b, В.И. Колчунов^{c*}, Е.В. Леонтьев^d

^a Российская академия архитектуры и строительных наук, г. Москва, ул. Россия

^b Орловский государственный университет имени И.С. Тургенева, г. Орел, Россия

^c Юго-Западный государственный университет, г. Курск, Россия

^d Главгосэкспертиза России, г. Москва, Россия

* E-mail: asiorel@mail.ru

Ключевые слова: система «балка – основание», собственные и вынужденные колебания, формы и частоты, аварийное воздействие, структурная перестройка

Аннотация. Приведена методика аналитического определения усилий, перемещений, форм и частот собственных поперечных колебаний балки на упругом основании, состоящей из двух участков: один опирается на упругое основание Винклера, второй свободен. Уравнения поперечных собственных и вынужденных колебаний балки записаны в безразмерных координатах и решены методом начальных параметров с использованием функций Крылова. При этом вторая и высшие частоты и формы собственных колебаний балки определяются в предположении, что искомая частота больше «условной» частоты, характеризующей обобщенную жесткость системы «балка – основание». Численным анализом показаны зависимости трех первых безразмерных частот собственных колебаний балки от обобщенной жесткости системы «балка – основание» после частичного разрушения основания под балкой. Установлено, что при внезапном разрушении основания под половиной балки при некотором значении обобщенной жесткости системы «балка – основание» эффект внезапной структурной перестройки системы приводит почти к пятикратному увеличению момента.

Литература

- Pearson C., Delatte N. Ronan Point Apartment Tower Collapse and its Effect on Building Codes // J. Perform. Constr. Facil. 2005. № 2(19). Pp. 172–177.
- Травуш В.И., Федорова Н.В. Живучесть конструктивных систем сооружений при особых воздействиях // Инженерно-строительный журнал. 2018. № 5(81). С. 73–80. doi:10.18720/MCE.81.8
- Fedorova N., Savin S. Structural transformation of reinforced concrete structural system at sudden loss of stability of one of its elements // IOP Conf. Ser. Mater. Sci. Eng. 2018. № 5(365). 052018.
- Li J., Zhou H. Energy-based collapse assessment of complex reinforced concrete structures with uncertainties // Procedia Eng. 2017. № 199. Pp. 1246–1251.
- Уткин В.С. Расчет надежности грунтовых оснований фундаментов зданий и сооружений по критерию деформации при ограниченной информации о нагрузках и грунтах // Инженерно-строительный журнал. 2016. № 1(61). С. 4–13. doi:10.5862/MCE.61.1
- Уткин В.С., Борисова О.Л. Расчет надежности целевого фундамента по критерию несущей способности грунта основания на стадии эксплуатации // Строительство уникальных зданий и сооружений. 2017. № 6(57). С. 7–17. doi: 10.18720/CUBS.57.1
- Motaghian S.E., Mofid M., Alanjari P. Exact solution to free vibration of beams partially supported by an elastic foundation // Sci. Iran. 2011. № 4 A(18). Pp. 861–866.
- Motaghian S., Mofid M., Akin J.E. On the free vibration response of rectangular plates, partially supported on elastic foundation // Appl. Math. Model. 2012. № 9(36). Pp. 4473–4482.
- Rezaei E., Dahlberg T. Dynamic behaviour of an in situ partially supported concrete railway sleeper // Proc. Inst. Mech. Eng. Part F J. Rail Rapid Transit. 2011. № 5(225). Pp. 501–508.
- Eisenberger M., Yankelevsky D.Z., Clastornik J. Stability of beams on elastic foundation // Comput. Struct. 1986. № 1(24). Pp. 135–139.
- Liu Y., Shu D.W. Analytical Solution of the Vibration of Delaminated Bimaterial Beams Fully or Partially Supported by Elastic Foundation // Appl. Mech. Mater. 2013. № 394. Pp. 75–79.
- Attar M., Karrech A., Regenauer-Lieb K. Dynamic response of cracked Timoshenko beams on elastic foundations under moving harmonic loads // JVC/Journal Vib. Control. 2017. № 3(23). Pp. 432–457.
- Tsai M.H., Huang T.C. Progressive collapse analysis of an RC building with exterior non-structural walls // Procedia Eng. 2011. № 14. Pp. 377–384.

14. Amiri S., Saffari H., Mashhadi J. Assessment of dynamic increase factor for progressive collapse analysis of RC structures // Eng. Fail. Anal. 2018. № 84. Pp. 300–310.
15. Amiri S., Saffari H., Mashhadi J. Assessment of dynamic increase factor for progressive collapse analysis of RC structures // Eng. Fail. Anal. 2018. № 84. Pp. 300–310.
16. Weng J., Tan K.H., Lee C.K. Adaptive superelement modeling for progressive collapse analysis of reinforced concrete frames // Eng. Struct. 2017. № 151. Pp. 136–152.
17. Fedorova N. V., Savin S.Y. Ultimate State Evaluating Criteria of RC Structural Systems at Loss of Stability of Bearing Element // IOP Conf. Ser. Mater. Sci. Eng. 2018. № 463. 032072.
18. Bažant Z.P., Verdure M. Mechanics of Progressive Collapse: Learning from World Trade Center and Building Demolitions // J. Eng. Mech. 2007. № 3(133). Pp. 308–319.
19. Khandelwal K., El-Tawil S. Pushdown resistance as a measure of robustness in progressive collapse analysis // Eng. Struct. 2011. № 9(33). Pp. 2653–2661.
20. Szyniszewski S., Krauthammer T. Energy flow in progressive collapse of steel framed buildings // Eng. Struct. 2012. № 42. Pp. 142–153.
21. Botez M., Bredean L., Ioani A.M. Improving the accuracy of progressive collapse risk assessment: Efficiency and contribution of supplementary progressive collapse resisting mechanisms // Comput. Struct. 2016. № 174. Pp. 54–65.
22. Belostotsky A.M. Correct numerical methods of analysis of structural strength and stability of high-rise panel buildings part 2: Results of modelling // Key Eng. Mater. 2016. № 685. Pp. 221–224.
23. Travush V. I., Fedorova N.V. Survivability parameter calculation for framed structural systems // Russ. J. Build. Constr. Archit. 2017. № 1(33). Pp. 6–14.
24. Gei M., Misseroni D. Experimental investigation of progressive instability and collapse of no-tension brickwork pillars // Int. J. Solids Struct. 2018. № 155. Pp. 81–88.
25. Travush V.I., etc. The response of the system «beam - Foundation» on sudden changes of boundary conditions // IOP Conf. Ser. Mater. Sci. Eng. 2018. № 1(456). 012130.
26. Gordon V.A., Pilipenko O. V., Trifonov V.A. The reactions of the «beam – foundation» system to the sudden change of the boundary conditions // MATEC Web Conf. 2018. № 188. 03008.
27. Travush V.I., Gordon V.A., Kolchunov V.I., Leontiev Y.V. Dynamic effects in the beam on an elastic foundation caused by the sudden transformation of supporting conditions // International Journal for Computational Civil and Structural Engineering. 2018. 14 (4). Pp. 27–41. DOI: 10.22337/2587-9618-2018-14-4-27-47

Контактные данные:

Владимир Ильич Травуш, +7(495)625-79-67; travush@mail.ru

Владимир Александрович Гордон, +7(486)2419802; gordon@ostu.ru

Виталий Иванович Колчунов, +7(471)2222461; asiorel@mail.ru

Евгений Владимирович Леонтьев, +7(495)6259595; e.leontyev@gge.ru

© Травуш В.И., Гордон В.А., Колчунов В.И., Леонтьев Е.В., 2019



ПОЛИТЕХ
Санкт-Петербургский
политехнический университет
Петра Великого

Инженерно-строительный институт
Центр дополнительных профессиональных программ

195251, г. Санкт-Петербург, Политехническая ул., 29,
тел/факс: 552-94-60, www.stroikursi.spbstu.ru,
stroikursi@mail.ru

Приглашает специалистов проектных и строительных организаций,
не имеющих базового профильного высшего образования
на курсы профессиональной переподготовки (от 500 часов)
по направлению «Строительство» по программам:

П-01 «Промышленное и гражданское строительство»

Программа включает учебные разделы:

- Основы строительного дела
- Инженерное оборудование зданий и сооружений
- Технология и контроль качества строительства
- Основы проектирования зданий и сооружений
- Автоматизация проектных работ с использованием AutoCAD
- Автоматизация сметного дела в строительстве
- Управление строительной организацией
- Управление инвестиционно-строительными проектами. Выполнение функций технического заказчика

П-02 «Экономика и управление в строительстве»

Программа включает учебные разделы:

- Основы строительного дела
- Инженерное оборудование зданий и сооружений
- Технология и контроль качества строительства
- Управление инвестиционно-строительными проектами. Выполнение функций технического заказчика и генерального подрядчика
- Управление строительной организацией
- Экономика и ценообразование в строительстве
- Управление строительной организацией
- Организация, управление и планирование в строительстве
- Автоматизация сметного дела в строительстве

П-03 «Инженерные системы зданий и сооружений»

Программа включает учебные разделы:

- Основы механики жидкости и газа
- Инженерное оборудование зданий и сооружений
- Проектирование, монтаж и эксплуатация систем вентиляции и кондиционирования
- Проектирование, монтаж и эксплуатация систем отопления и теплоснабжения
- Проектирование, монтаж и эксплуатация систем водоснабжения и водоотведения
- Автоматизация проектных работ с использованием AutoCAD
- Электроснабжение и электрооборудование объектов

П-04 «Проектирование и конструирование зданий и сооружений»

Программа включает учебные разделы:

- Основы сопротивления материалов и механики стержневых систем
- Проектирование и расчет оснований и фундаментов зданий и сооружений
- Проектирование и расчет железобетонных конструкций
- Проектирование и расчет металлических конструкций
- Проектирование зданий и сооружений с использованием AutoCAD
- Расчет строительных конструкций с использованием SCAD Office

П-05 «Контроль качества строительства»

Программа включает учебные разделы:

- Основы строительного дела
- Инженерное оборудование зданий и сооружений
- Технология и контроль качества строительства
- Проектирование и расчет железобетонных конструкций
- Проектирование и расчет металлических конструкций
- Обследование строительных конструкций зданий и сооружений
- Выполнение функций технического заказчика и генерального подрядчика

По окончании курса слушателю выдается диплом о профессиональной переподготовке
установленного образца, дающий право на ведение профессиональной деятельности

